VASCULAR STIFFENING IN ATHEROSCLEROSIS: CELL CONTRACTILITY AND MATRIX MECHANICAL HETEROGENEITIES MEDIATE BARRIER INTEGRITY

A Dissertation

Presented to the Faculty of the Graduate School

of Cornell University

In Partial Fulfillment of the Requirements for the Degree of

Doctor of Philosophy

by

Marsha Christine Lampi

August 2017

VASCULAR STIFFENING IN ATHEROSCLEROSIS: CELL CONTRACTILITY AND MATRIX MECHANICAL HETEROGENEITIES MEDIATE BARRIER INTEGRITY

Marsha Christine Lampi, Ph.D.

Cornell University 2017

Cardiovascular pathologies are a leading cause of death in the Western world. Atherosclerosis is the development of lipid-rich plaques within the arterial wall, and is considered the major underlying pathology that contributes to cardiovascular disease development. Intriguingly, age is a primary risk factor for atherosclerosis, and increased artery stiffness increases with advanced age and atherosclerosis. It is now established that endothelial cell feedback to mechanical stimuli on the cellular level, including age-related arterial stiffness can promote a pro-atherogenic endothelium. In response to increased matrix rigidity, endothelial cells exert increased RhoA-mediated contractile forces that disrupt monolayer barrier function and increase endothelium permeability. Identifying therapeutic approaches to overcome the cellular response to extracellular matrix stiffness cues and understanding how the altered mechanical properties of the arteries associated with aging contribute to endothelium disruption is important to the prevention of atherosclerosis.

Using hydrogel scaffolds with tunable crosslinking, I fabricated physiologically relevant models to study the effects of age-related matrix mechanical cues on endothelial cell behaviors in the translational context of atherosclerosis. I identified that therapeutically targeting the Rho GTPase family members RhoA and Rac1 with the available statin,

simvastatin, attenuated the endothelial cell response to increased matrix stiffness. Importantly, the altered GTPase activity was associated with endothelial cell-cell junction reorganization and decreased intercellular junction tension to promote an atheroprotective endothelium. Motivated by the increased spatial stiffness heterogeneity observed in the aged arterial intima, I then developed and characterized a second hydrogel platform that employed photocrosslinking to vary the presentation of matrix stiffness. My data demonstrated that increased complexity of a heterogeneously stiff substrate in addition to a mean increase in the elastic modulus was deleterious to monolayer integrity and disrupted cell-cell junctions. Collectively, these two studies identified a pharmacological approach to overcome the cellular response to extracellular matrix stiffening and identified a novel matrix mechanical factor that has implications for the development of age-related atherosclerosis. Finally, because pathological matrix stiffening drives disease progression, I investigated the emerging field of mechano-medicine and potential therapeutic approaches to overcome stiffness-mediated pathologies.

BIOGRAPHICAL SKETCH

Marsha Christine Lampi was born in Portland, Oregon on January 19th, 1989 to Eugene and Yomaira Lampi and grew up with her three siblings, Clara, Benjamin, and Jacob. She completed the rigorous International Baccalaureate diploma program at Lincoln High School and graduated as valedictorian in 2007. Marsha then attended Oregon State University where she received an athletic scholarship to run Division I cross country and track for the Beavers. At Oregon State, Marsha was part of the University Honors College where she majored in bioengineering and minored in chemistry. Her undergraduate summers were filled with internships that fostered her interest in biomedical research. Marsha earned numerous PAC-12 First Team All-Academic honors for her achievements off the track and graduated summa cum laude from Oregon State in 2012. Marsha entered the Ph.D. program in Biomedical Engineering at Cornell University in the fall of 2012 with a Sloan Foundation Fellowship. Immediately after arriving at Cornell, Marsha joined the lab of Professor Cynthia Reinhart-King and began her research studying the role of extracellular matrix stiffness cues on endothelial monolayer integrity in the context of atherosclerosis. She was awarded a National Science Foundation Graduate Research Fellowship in 2013 as well as a Ford Foundation Predoctoral Fellowship, also in 2013. Marsha completed her Ph.D. in summer 2017. In addition to spending time in the lab, Marsha also enjoys cooking and spending time outdoors.

To my family.

ACKNOWLEDGMENTS

A well-known African proverb states, “It takes a village to raise a child.” I am forever indebted to all those who offered their mentorship, support, and love throughout my Ph.D. journey.

I would like to express my deepest thanks to my research advisor, Dr. Cynthia Reinhart-King. You welcomed me into your lab when I first arrived at Cornell even though I was coming from an entirely different background and had a steep learning curve ahead—endothelial cells, extracellular matrix, and microscopes were all foreign to me. You provided unyielding support as we navigated projects and transitions in the lab. Under your mentorship I became a scientist: I learned to think critically, ask questions, and design experiments, and was given the opportunity to develop an expansive scientific toolbox. I am continually inspired by your dedication to science and steadfast determination. Thank you Cindy, for being my advisor, mentor, and friend from day one. This is not a goodbye, but rather the beginning of a new chapter.

I would also like to thank Drs. Barbara Baird and Christopher Ober for graciously being a part of my dissertation committee. In addition, thank you to Dr. Dave Putnam for stepping in as a proxy during my defense and dissertation submission. Your thoughtful feedback has strengthened my work.

I would like to thank the Reinhart-King lab for being my science family. Thank you to Drs. Casey Kraning-Rush, Brooke Mason, and Shawn Carey for answering endless questions,

teaching me countless techniques, and serving as excellent role models. Thank you to Dr. Francois Bordeleau for being a scientific sounding board day in and day out, and your eagerness to always lend a hand. Julie Kohn, we are almost there. Thank you for your friendship and support. Danielle LaValley, Aniqua Rahman, Jacob VanderBurgh, Lauren Hapach, Emmanuel Lollis, Matthew Zanotelli, Adam Muñoz, Marianne Lintz, and Johana Uribe, I am better for having known you. We will always be part of the Reinhart-King lab family and best of luck in all your future endeavors. Thank you to the undergraduates I mentored: Jeffrey Ly, Jack Pollack, and Angelia Laudermilch, you taught me so much, and I wish you success.

Thank you to all those whom I have collaborated with both within and external to Cornell. I would especially like to acknowledge Drs. Jason Burdick and Murat Guvendiren for inviting me to the University of Pennsylvania and training me on making photocrosslinking hydrogels.

Special thanks to my undergraduate research mentors at Oregon State, Drs. Skip Rochefort and Joe McGuire. Skip, you believed in me and saw research potential long before I ever did. Without your guidance, I never would have survived CBEE 101, let alone embarked on the path that I am on today. Dr. McGuire, you helped me get a running start into graduate school by overseeing my honors thesis project and first scientific publication. Thank you for your continued mentorship and support, and never ending positive energy. Thank you to my college track coach Kelly Sullivan, for teaching me how to see the positive in the negative, and to pick myself up after disappointment—research can be a roller coaster, but

it is so worth it when you finally collect that one piece of data you have been working towards.

I would be remiss if I left out the glue that holds together the Cornell biomedical engineering department. Thank you to the department administrators and Weill Hall building staff for your tireless work. Thank you to Diversity Programs in Engineering, and especially Sara Hernandez and Jami Joyner for providing community during my time at Cornell. Thank you to the Sloan Foundation, the National Science Foundation, and the Ford Foundation for financial support of my graduate studies. It is an incredible privilege to be earning a Ph.D.

Many, many thanks to my parents Yomaira and Eugene, and my siblings Clara, Benjamin, and Jacob for being a constant source of love, support, and encouragement.

And finally, thank you to my husband Dan, for everything.

TABLE OF CONTENTS

LIST OF FIGURES

Chapter 4: Additional Data

LIST OF TABLES

Chapter 1: Introduction

LIST OF ABBREVIATIONS

α-tub	Alpha tubulin
α-SMA	Alpha smooth muscle actin
AFM	Atomic force microscopy
AGE	Advanced glycation end product
ANOVA	Analysis of variance
A.U.	Arbitrary units
BAPN	B-aminopropionitrile
CO_2	Carbon dioxide gas
DAPI	4',6-diamidino-2-phenylindole
DPI	Dots per inch
DTT	Dithiothreitol
EC	Endothelial cell
ECM	Extracellular matrix
EDA-FN	Extra domain-A (EDA) type III repeat fibronectin
EDB-FN	Extra domain-B (EDB) type III repeat fibronectin
FA	Focal adhesion
FAK	Focal adhesion kinase
FDA	Food and Drug Administration
FRET	Förester resonance energy transfer
G''	Loss modulus
G'	Storage modulus
GAP	GTPase-activating protein

GDP	Guanosine diphosphate
GEF	Guanine nucleotide exchange factor
GTP	Guanosine triphosphate
HA	Hyaluronic acid
HMG-CoA	3-hydroxy-3-methylglutaryl coenzyme A
HRP	Horseradish peroxidase
I2959	Irgacure 2959 photoinitiator
ICAM-1	Intercellular adhesion molecule-1
JAIL	Junction associated intermittent lamellipodia
LAP	Lithium acylphosphinate photoinitiator
LDL	Low density lipoprotein
LINC complex	Linker of nucleoskeleton and cytoskeleton complex
LOX	Lysyl oxidase
LSM	Laser scanning confocal microscope
LS-Means	Least squares means
MeHA	Methacrylated hyaluronic acid
MEM	Minimal essential medium supplement
MRTF-A	Myocardin related transcription factor-A
MLC	Myosin light chain
MMP	Matrix metalloproteinase
MWCO	Molecular weight cutoff
$NaHCO_3$	Sodium bicarbonate
NIH	National Institutes of Health

NO	Nitric oxide
PA	Polyacrylamide
PECAM-1	Platelet and endothelial cell adhesion molecule-1
PBS	Phosphate buffered saline
PDGF	Platelet derived growth factor
pMLC	Phosphorylated myosin light chain
PVDF	Polyvinylidene difluoride
ROCK	Rho-associated coiled-coil kinase
SDS-PAGE	Sodium dodecyl sulfate – polyacrylamide gel electrophoresis
SEM	Standard error of the mean
SIP	Sphingosine-1-phosphate
SR	Serine-arginine rich
SRF	Serum response factor
TB-PET	Total body positron emission
TG2	Tissue transglutaminase
TIMP	Tissue inhibitor of matrix metalloproteinases
Triton	Octyl phenol ethoxylate
Tween	Polyoxyethylene 20 sorbitan monolaurate
UV	Ultraviolet
VCAM-1	Vascular cell adhesion molecule-1
VE	Vascular endothelial
VGLL4	Vestigial like family member 4
VSMC	Vascular smooth muscle cell

RGD	L-arginine, glycine, and L-aspartic acid amino acid sequence
TCP	Tissue culture plastic
YAP/TAZ	Yes-associated protein/Transcriptional coactivator with PDZ-binding motif

LIST OF SYMBOLS

Symbol	Description	Units
°C	Degrees Celsius	Degrees
wt%	Weight Percent	Dimensionless
E	Young's Modulus	Pascal (N/m^2)
F	Force	N

CHAPTER 1

INTRODUCTION

Portions of this chapter were published in *Frontiers in Genetics*

(Kohn,* Lampi,* and Reinhart-King, 2015, *denotes equal contribution)

1.1 Introduction to Atherosclerosis

Cardiovascular diseases are a leading cause of death in the United States and atherosclerosis is often the underlying pathology that contributes to their development *(1)*. During atherogenesis, the accumulation of lipid rich plaques in the arterial wall narrows the vessel lumen and impedes blood flow (Figure 1.1) *(2)*. These changes in artery structure impose increased stress on the heart muscle that can lead to cardiac failure *(3, 4)*.

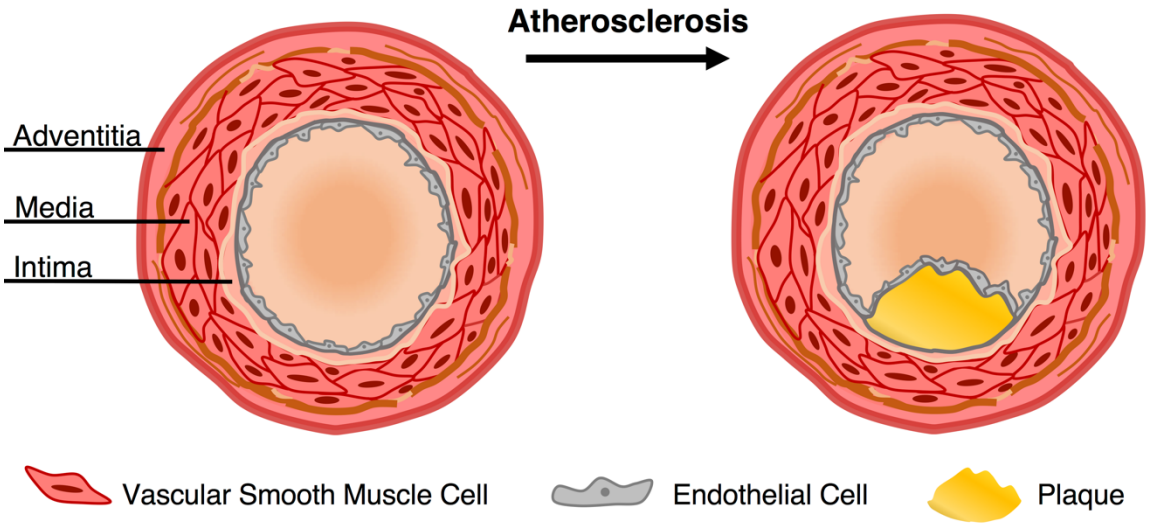

Figure 1.1. Large artery structure and atherosclerotic plaque development. Arteries are composed of three concentric layers: the adventitia, the media, and the intima. Atherosclerotic plaque development begins in the innermost artery layer, the intima and hinders blood flow through the vessel lumen.

In addition, a fraction of atherosclerotic plaques become unstable and release debris into the circulation that can cause thrombus, heart attacks, and strokes *(4, 5)*. Thus, research efforts to mitigate atherosclerosis have important clinical health implications.

Increased age is a primary risk factor for atherosclerosis and nascent asymptomatic lesions know as fatty streaks that are found during childhood develop into plaques throughout adulthood *(6–8)*. Endothelial cells line the arterial lumen and help to maintain vascular homeostasis by acting, in part, as a semi-permeable barrier preventing circulating macromoelcules, such as lipids from entering the arteries *(9–11)*. When endothelium integrity becomes compromised, apoB-lipoproteins, primarily low density lipoprotein (LDL) cholesterol, can permeate into the artery wall and initiate a chronic inflammatory immune response that culminates in atherosclerotic plaque development *(12, 13)*. Lipids are retained in the arterial wall through interactions with subendothelial extracellular matrix proteoglycans and subsequently oxidized by reactive oxygen species, enzymes, and lipases *(13–15)*. Oxidized LDL triggers endothelial cells to express chemokines and adhesion molecules that recruit monocytes into the arterial wall *(16–19)*. Once within the arterial wall, monocytes differentiate into macrophages that recognize oxidized LDL through scavenger receptors *(20, 21)*. Subsequent macrophage uptake of oxidized LDL leads to lipid-filled foam cells that comprise the characteristic fatty streaks of early atherosclerosis *(22, 23)*. Macrophages also secrete chemokines to recruit additional monocytes and sustain the inflammatory response that drives plaque formation *(24, 25)*.

During intermediate atherogenesis, vascular smooth muscle cells (VSMCs) are stimulated by endothelial and macrophage secreted growth factors, namely platelet derived growth factor (PDGF) to migrate to the plaque site *(26, 27)*. Here, they adopt a synthetic phenotype and produce large amounts of extracellular matrix that, in combination with increased proliferation, cause localized vessel thickening *(28, 29)*. Matrix proteoglycans synthesized by VSMCs contribute to increased retention of lipids, and the production of additional matrix is stimulated when these lipids become oxidized *(30, 31)*. Thus, VSMCs play an important role in plaque growth through a feed forward cycle of lipid retention, oxidation, and extracellular matrix production. VSMCs also participate in lipid uptake to become foam cells and release cytokines that further drive immune cell recruitment and atherogenesis *(32–34)*.

In advanced atherosclerosis, a characteristic necrotic core within developed plaques arises when excess foam cell apoptosis exceeds phagocytic clearance rates, and is deleterious to plaque stability *(35)*. In addition, VSMC death occurs at high rates and causes a significant reduction in collagen matrix synthesis. A lack of extracellular matrix production in concert with increased matrix metalloproteinase activity thins the protective fibrous cap on the surface of atherosclerotic lesions *(36, 37)*. Advanced atherosclerotic plaques pose a serious patient health risk because they are prone to rupture, particularly at weakened cap sites in close proximity to the necrotic core *(38)*. Upon rupture, thrombus at the plaque surface and released debris can cause heart attacks and strokes *(2, 4)*.

1.2 Large Artery Structure

Arteries are composite materials, containing multiple concentric layers, each with a distinct composition and function (Figure 1.1). The intima is the innermost artery layer and is a composite of two layers. The luminal layer, known as the basal lamina, is comprised of a thin basement membrane with a proteoglycan rich matrix and small amounts of collagen *(39, 40)* Endothelial cells (ECs) attach to the intimal basement membrane and exist as a monolayer lining the arterial lumen. The second intimal layer is musculoelastic and consists of elastin fibers, individual smooth muscle cells, and collagen *(41)*. Continuing inwards from the lumen, a collection of organized fenestrated elastin fibers known as the internal elastic lamina separates the intima from the media, the middle artery layer. Elastin within the internal elastic lamina is oriented longitudinally in the direction of luminal blood flow, while in the medial layer it is oriented circumferentially *(42)*. The media is composed of lamellar units that are composites of elastin fibers, circumferentially oriented VSMC layers, collagen fibers, and a mucopolysaccharide viscoelastic gel, commonly referred to as a "ground substance" *(41)*. The characteristic lamellae of the media comprise the majority of the arterial wall bulk and are responsible for its elastic properties, allowing for the artery to expand and contract with the blood pulse. The outermost artery layer is the adventitia. The adventitia is composed of circumferentially arranged, wavy collagen fibrils intermixed with elastin and is surrounded by loose connective tissue. Fibroblasts are dispersed within the adventitia, but are generally absent from the intima and media artery layers *(43)*.

1.3 Arterial Mechanics

When analyzed as a composite material, large arteries exhibit a non-linear stress-strain pattern, and therefore, are best described in terms of an elastic modulus evaluated at a given physiological stress along the stress-strain curve, termed the incremental elastic modulus *(44)*. The extracellular matrix (ECM) proteins collagen and elastin account for approximately half of the vessel dry weight, and play a crucial role in artery mechanics *(45)*. Overall, Type I and Type III collagens account for 60% of the artery wall, and elastin 30% *(46, 47)*. At low degrees of stretch, the compliant elastin fibers dominate the mechanics, while at higher levels of deformation, helically oriented collagen fibers are recruited *(48, 49)*. Collagen fibers are 100–1,000 times stiffer than elastin which causes a sharp increase in the incremental elastic modulus at higher levels of circumferential stretch *(50–53)*. Under physiological strain loads, the incremental elastic modulus is a function of strain and the combined contributions of elastin and collagen *(53)*.

The distinct composition of each artery layer lends itself to layer-specific mechanical properties that can vary from person to person, and also between large and small arteries *(54, 55)*. For example, measured under axial stretch and using non-axisymmetric deformations, the media is significantly less compliant than the adventitia *(56, 57)*. The media and adventitia also have different load bearing proportions. Under circumferential tension, the media bears ~60% of the load and the adventitia bears 40%. Longitudinal tension is primarily assumed by the adventitia which bears ~75% of the load *(58)*. It is important to note that cells only sense the mechanical properties of their microenvironment

to a depth of 5 μm *(59, 60)*. As such, measurements and analysis of each individual layer is essential when considering cellular level mechanobiology.

Intima

The mechanical properties of the healthy intima are not well-established largely because artery mechanics are traditionally studied on the macroscale, where properties of the media and adventitia dominate. Several studies have analyzed the aorta as a two-layer construct consisting of a combined intima-media layer surrounded by the adventitial layer *(61, 62)*. Because recent evidence has shown that endothelial cells are mechanosensitive to matrix stiffness and that increased intimal stiffness promotes endothelial dysfunction; the mechanical properties of the intima alone may be important factors in cardiovascular disease progression and warrant further investigation *(63, 64)*. The healthy human intima has been reported to have an elastic modulus of 34.4 kPa and is considered a compliant material, with an elastic modulus similar to adipose tissue and lower than muscle *(65–68)*.

Media

Medial mechanics are dominated by elastin within the lamellar units at physiological pressures *(69)*. When the artery is subjected to a transmural pressure, the elastin fibers which possess high entropically driven recoil properties are initially stretched, followed by the stretching of stiffer collagen fibers *(70)*. The number of concentric lamellae layers in the media remains constant with age but scales with arterial radius and vessel wall tensional strength *(71)*. The mechanical contribution of VSMCs dispersed within the aortic lamellae is still somewhat unclear. Contractile activation of VSMCs has been shown to increase the

medial elastic modulus; but separate studies have shown that lamellar mechanical properties are unchanged after VSMC activation with noradrenaline *(72–74)*.

Adventitia

The mechanics of the adventitia are attributed to collagen organization. In the zero-load state, the fibers assume a crimped morphology *(75)*. As an axial load is placed on the vessel, the collagen fibers deform and straighten, exhibiting their high tensile strength. In the inner adventitia, collagen fibers are oriented, thin, and intermixed with elastin allowing for vessel distension and protection against rupture, whereas the outer adventitia is primarily composed of thick, non-oriented collagen fibers that support the vessel *(76)*.

1.4 Causes of Age-Related Arterial Stiffening

It is well established that the aorta stiffens with age, and that increased aortic stiffness is correlated with increased cardiovascular risk and mortality *(7, 77, 78)*. Clinical studies report a 1% increase in bulk artery stiffness, followed by more rapid stiffening after age 55 in otherwise healthy adults, independent of sex or other cardiovascular risk factors *(7, 79–81)*. Age-related stiffening within the aorta is primarily caused by changes to elastin and collagen, the primary constituents of the vessel wall.

Elastic fibers have an extremely low turnover rate *in vivo,* and this longevity allows for fragmentation, calcification, and MMP-degradation effects to accumulate over the lifespan *(82)*. As elastin fibers decay, they lose functionality and shift load bearing onto stiffer collagen fibrils, which directly contributes to significant increases in bulk arterial stiffness.

Fatigue failure from pulsatile wall stress can also cause elastin fragmentation *(83–85)*. Moreover, calcium in the arterial wall increases with age facilitating the direct binding of calcium ions to elastin fibers causing calcification *(86–88)*. Animal models that induce elevated elasto-calcinosis have demonstrated increased medial elastin fragmentation and arterial stiffness *(89, 90)*.

Enzymatic degradation of elastin is mediated by matrix metalloproteinases which have low basal activity in healthy arteries to balance the absence of new elastin synthesis. The dysregulation of MMPs is already known to play a role in the cardiovascular pathologies hypertension and aneurysm *(91, 92)*. With age, increased activity of the elastases MT1-MMP and MMP-2 has been observed, and MMP-2 has been found near fragmented elastin fibers within the aorta *(92–94)*. Notably, even though the absolute elastin content in the aorta remains relatively stable with age, the elastin concentration decreases and is accompanied by a substantial increase in collagen concentration *(55, 95–97)*. Age is also associated with changes on the amino acid scale that can contribute to decreased arterial compliance caused by a loss of elastin functionality. The compounds desmosine and isodesmosine are formed from four lysine amino acids and are critical for crosslinking elastin fibers to give them their elastic properties *(98)*. The concentrations of desmosine and isodesmosine and their crosslinks decrease with age *(99, 100)*.

In contrast to elastin, the collagen concentration in all three layers of the arterial wall increases with age, shifting the optimal elastin:collagen balance that governs healthy arterial mechanics. Aged endothelial cells have morphological changes resembling a VSMC phenotype and express alpha smooth muscle actin and collagen I, indicating they

may deposit collagen that contributes to intimal thickening *(101)*. In the media, collagen fibers replace VSMCs causing medial fibrosis *(82)*. Furthermore, in general, in individuals over the age of 50, collagen redistributes within the media to bundle near lamellae units *(82, 102)*. Finally, within the adventitia, collagen I and III deposition by fibroblasts increases with age and is accompanied by vessel stiffening *(103)*.

In concert with increased collagen concentrations, collagen crosslinking by non-enzymatic glycation causes age-related arterial stiffening *(104, 105)*. Glycation is a reaction between reducing sugars and proteins, and directly stiffens tissues in addition to producing deleterious end products. Advanced glycation end products (AGEs) accumulate through the Maillard reaction. Amino groups on proteins react with aldehydes or ketones on the reducing sugars to form shift bases that rearrange to Amadori products and are further modified to produce AGEs *(106, 107)*. In addition to collagen crosslinking, AGEs are harmful to vascular health because they reduce nitric oxide availability, an important vasodilator used to maintain vascular tone that also has anti-inflammatory effectors on the endothelium *(108–111)*. AGEs also interact with the receptor for advanced glycation end products (RAGE) which results in downstream effects that include the production of reactive oxygen species, NF-κB inflammatory signaling, and endothelial hyperpermeability *(112–116)*.

1.5 Clinical Interventions to Mitigate Arterial Stiffening

Because increased arterial stiffness is a negative indicator of cardiovascular health, clinical interventions to prevent or reverse arterial stiffening have been explored. Assuming an

active lifestyle remains one of the safest, most successful, and cost-effective interventions to prevent cardiovascular diseases *(1)*. Numerous human studies have demonstrated that habitually active adults have more compliant arteries when compared to their age-matched sedentary peers and that moderate aerobic exercise interventions successfully increased macroscale arterial compliance in healthy aged populations *(117–119)*. Brisk walking can improve arterial compliance in as little as 3 months in healthy middle aged men *(117)*. Notably, the protective benefits of exercise appear to be most effective as a preventative precaution prior to the onset of cardiovascular pathologies. In two separate studies of individuals with hypertension, arterial stiffness did not improve after short-term aerobic exercise interventions *(120, 121)*. In addition to improvements in macroscale arterial compliance, it has also been demonstrated that layer specific microscale intima stiffening is attenuated by exercise in aged mouse populations *(122)*. The mechanism by which exercise restores arterial compliance is not fully understood and appears to vary with the type of exercise. Mouse studies show that voluntary wheel running decreases Type I collagen levels in the media and adventitia of old mice, while studies involving swimming and treadmill running did not detect altered arterial collagen compositions *(103, 123, 124)*. Exercise may increase collagen turnover, thus preventing the accumulation of AGEs. However, while increased markers of collagen synthesis and turnover have been found in response to exercise for cardiac, tendon, and bone collagens, studies with arterial collagen still need to be completed *(67, 125, 126)*. It is important to note that collagen deposition in bone and tendon in response to exercise is indicative of beneficial strengthening while collagen deposition in the arteries contributes to pathological stiffening; therefore, it is possible that the effects of exercise on collagen deposition may be tissue specific.

Pharmacological interventions for arterial stiffening can be primarily organized into two categories that are targeted at preventing or breaking AGE crosslinks in collagen. Several chemical compounds to prevent arterial stiffening by inhibiting AGE accumulation have been studied, but thus far, none have made it past clinical trials. Aminoguanidine was the first well-studied inhibitor of AGEs. Early studies in diabetic rats showed that it was able to inhibit AGE formation by blocking carbonyl reactivity on early glycation products even when animals were fed high glucose diets *(127)*. Later studies with an aged, non-diabetic rat model showed aminoguanidine prevented arterial stiffening in 24-month old, end-of-life rats without altering collagen content *(128)*. Despite the early promise of aminoguanidine, clinical trials were terminated when it caused impaired liver functionality and the initiation of lupus-like illnesses in patients *(129)*. An alternative AGE inhibitor, 2,3 diaminophenazine (2,3 DAP) did not make it past pre-clinical toxicity tests *(130)*. ALT-946 and OPB-9195 are other examples of AGE blockers that possess similar hydrazine structures to aminoguanidine, that have not yet reached clinical trials *(131)*. The continued failure of the AGE inhibitors mentioned here, and others, to succeed in clinical trials highlights the difficulty of safely and effectively reducing AGE accumulation *in vivo*.

The second class of pharmaceutical interventions used to overcome arterial stiffness are compounds that break AGE crosslinks. The most widely studied of these is a thiazelium based compound, ALT-711 (alagebrium chloride). ALT-711 was discovered as a more stable form of the very first AGE breaker, n-phenacylthiazolium bromide (PTB) *(132)*. AGE breakers are commonly designed to be nucleophilic compounds that break carbon–carbon bonds between adjacent carbonyl groups in crosslinked proteins *(132, 133)*. ALT-

711 showed efficacy *in vitro* and *in vivo* at cleaving AGE crosslinks. The resulting collagen fragmentation increased the elasticity of cardiac and arterial tissue *(132, 134, 135)*. However, despite multiple Phase 2 and Phase 3 clinical trials, a randomized factorial study comparing the interaction between ALT-711 and exercise in older sedentary adults showed the treatment did not decrease arterial stiffness. Additionally, cardiovascular health measured using the Lifetime Risk Score (LRS) improved with exercise, but not the drug intervention *(136)*. All ongoing clinical trials for ALT-711 were terminated by Synvista Therapeutics Inc. for financial reasons *(131)*. The safety, pharmacokinetics, and tolerance of another AGE crosslink breaking compound, TRC4186, were established during a successful phase 1 clinical trial and published in 2009 *(137)*. However, the necessary phase 2 and 3 clinical trials showing efficacy and continued safety have not been completed. Preliminary studies on a safer AGE breaker, C36 (3-benzyloxycarbonylmethyl-4-methyl-thiazol-3-ium bromide) showed decreased systemic arterial stiffness and improved collagen composition in diabetic rats *(138)*. There currently are no AGE blockers or breakers on the market today, indicating the difficulty of successfully and safely overcoming the effects of tissue stiffening that occur with age.

Table 1.1. Selected interventions with humans to reduce arterial stiffness.

Intervention Type	Intervention	Study	Outcome	Reference
Lifestyle	Aerobic exercise	Brisk walking in healthy sedentary male adults	Increased central arterial compliance	Tanaka *et al*. (2000)
Pharmaceutical AGE blocker	Aminoguanidine	Phase III clinical trial	Early termination due to safety and efficacy	Freedman *et al*. (1999) Thornalley (2003)
Pharmaceutical AGE breaker	Alagebrium chloride (ALT-711)	Phases II & III clinical trials	No increase in cardiovascular health; Clinical trials terminated	Oudegeest-Sander *et al*. (2013) clnicaltrials.gov
Pharmaceutical AGE breaker	TRC4186	Phase I clinical trial	Safety, tolerance, and kinetics established	Chandra *et al*. (2009)

1.6 Vascular Stiffening and Atherosclerosis

Bulk measurements of vessel stiffness measurements using pulse wave velocity and ultrasound are widely used in the clinic as indicators of vascular health, but the importance of vascular stiffening, especially on the microscale, in promoting disease is not well-understood *(139)*. Layer specific heterogeneous stiffening of the arterial intima occurs with age and may contribute to atherogenesis *(63, 122)*. The combined effects of increased mean stiffness and increased spatial stiffness heterogeneity with in the arterial intima with age remain to be elucidated. However, recent studies have provided evidence for a paradigm

shift in the role of vascular stiffness in cardiovascular diseases as a contributing cause rather than an outcome of the pathologies *(140–142)*.

It has been shown in both clinical studies and animal models that arterial stiffening precedes hypertension, and that preventing arterial stiffening can attenuate atherosclerosis *(140–142)*. Kothapalli and colleagues demonstrated that treatment with the lysyl oxidase inhibitor BAPN (B-aminopropionitrile) to prevent collagen crosslinking reduced luminal arterial stiffness and decreased plaque size by ~50% in an atherosclerotic mouse model *(142)*. In addition, the more compliant arteries exhibited decreased deposition of a pro-atherogenic extracellular matrix by VSMCs and had reduced monocyte infiltration. *Ex vivo* studies have also revealed that arteries with stiffer intima layers exhibit disrupted endothelial cell-cell junctions and increased permeability *(63)*. Reducing arterial stiffness in the lumen where endothelial cells reside resulted in a significant reduction in atherosclerotic plaque formation *(142)*. Conversely, when bulk artery stiffness was reduced by changing elastin within the lamellar units of the media, the same reduction in atherosclerotic burden was not achieved *(143)*. These conflicting reports describing the effects of artery stiffness on atherosclerosis underscore the importance of localized artery mechanics on cell behaviors that contribute to atherogenesis.

1.7 Rho GTPase Family

One avenue by which localized age-related arterial stiffening is thought to contribute to atherogenesis is the activation of Rho family signaling cascades in endothelial cells. The Rho family of GTPases are small G-protein signaling molecules that are involved in a

multitude of cellular processes and pathologies *(144)*. GTPase activity is dependent on guanine nucleotide exchange factors (GEF)s and GTPase-activating proteins (GAPs) for rapid switch-like signaling. GEFs catalyze the exchange of GDP for GTP in the conversion to an active GTPase state that interacts with downstream effectors. Conversely, GAPs catalyze the hydrolysis of GTP to GDP to turn off GTPase signaling. Because GTPases have high, nearly equal affinities for GTP and GDP and slow intrinsic exchange rates, GEFs and GAPs are necessary for quick cellular responses. Importantly, GEFs and GAPs are critical to initiating G-protein signaling cascades; therefore, their spatiotemporal regulation is an underlying mechanism regulating G-protein signaling *(145)*. Cellular localization on the GTPase level is regulated by post-translational modifications with lipid anchors used for membrane and organelle targeting *(146)*. Within the Rho family, RhoA, Rac1, and Cdc42 are the most well studied, and have important functions regulating the cytoskeleton that contribute to endothelial barrier formation, stability, and disruption *(147)*. Deletion of RhoA, Rac1, or Cdc42 is embryonic lethal which underscores their overall importance to cellular function *(148)*.

RhoA is primarily associated with endothelial barrier disruption, although basal levels of RhoA activity are necessary for junction integrity *(149)*. The formation of actin stress fibers and myosin mediated contraction of actin filaments are primary outputs of RhoA activation that disrupt endothelial barriers. Briefly, GTP-bound RhoA activates Rho-associated coiled-coil kinase (ROCK). ROCK directly phosphorylates myosin light chain (MLC) and also inhibits myosin light chain phosphatase to increase the overall concentration of active myosin (Figure 1.2) *(150, 151)*. Increased extracellular matrix stiffness is a mechanical cue

that activates RhoA, and thrombin is a pharmacological agent that activates RhoA. In response to both stimuli, cell contractility is increased and elevated intercellular tension disrupts cell-cell junctions *(152, 153)*.

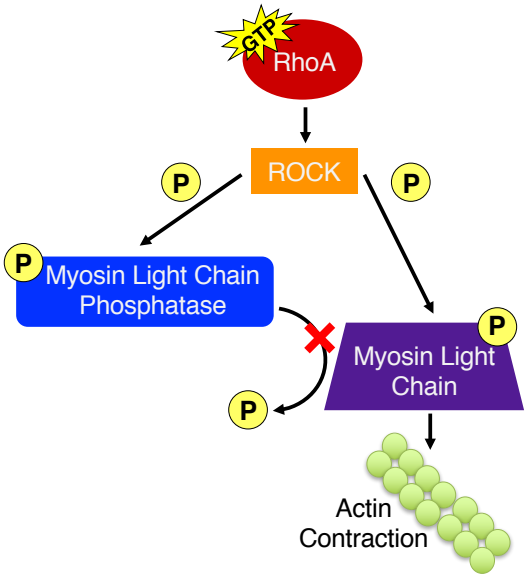

Figure 1.2. RhoA cell contractility pathway. GTP-bound RhoA activates its major downstream effector ROCK. Kinase activity by ROCK results in elevated levels of phosphorylated myosin light chain contributing to actin contraction and cellular force generation.

Rac1 is primarily associated with endothelial barrier protection and repair, although its effect on endothelial junctions can vary based on the activation of other co-current signaling cascades *(154, 155)*. Consistent with their phenotypic functions, an inverse relationship exists between RhoA and Rac1 where active RhoA downregulates Rac1 and vice versa *(156, 157)*. Rac1 is activated during lamellipodia formation and membrane ruffling, and as such, is integral to the annealing of cell membranes to form adherens junctions *(151, 158)*. Thrombin challenges that destabilized endothelial barriers by elevating RhoA activity were followed by Rac1 activation during endothelium recovery

(147). In mature endothelial cell-cell junctions, GTP-bound Rac1 caused VE-cadherin clustering, stabilized VE-cadherin conformations that favored stable adhesions, and decreased junction tension *(159)*. Active Rac1 also stimulates cortactin localization and actin rearrangement to form cortical actin structures that enhance endothelial junction integrity *(160, 161)*.

Cdc42 is also associated with endothelial barrier strengthening and restoring. More generally, Cdc42 is activated during filopodia formation *(162)*. In both cell and mouse models, decreased Cdc42 levels caused disorganized actin organization and prevented actin protrusions that are necessary for nascent and mature junction formation *(163)*. In confluent endothelial monolayers, membrane localization and activation of Cdc42 coincided with junction repair after thrombin challenges, and Cdc42 depletion impaired endothelium recovery *(164)*. It has been proposed that Cdcd42 controls basal endothelial adherens junction tension, and therefore, integrity. Downstream effectors of Cdc42 contribute to myosin filament assembly, actin polymerization, and moderate myosin phosphorylation *(155)*.

1.8 Matrix Stiffness and Endothelial Cell Behavior

It is now well accepted that numerous cell types respond to extracellular matrix stiffness and that stiffness can promote stem cell differentiation, tissue morphogenesis, gene expression and tumor malignancy *(165–169)*. Cells also respond to temporal stiffening or softening of their matrix *(170, 171)*. Intimal stiffening, which occurs with age, promotes aberrant endothelial cell behaviors *(63, 172)*.

Cells adhere to, sense, and exert forces against their extracellular matrix using transmembrane proteins, namely integrin complexes. External signals are integrated in an outside→in→outside signaling mechanism *(173)*. In the extracellular space, integrin heterodimers cluster and bind ECM ligands. Within the cytoplasm, integrins bind to scaffolding proteins that link to actin filaments. Collectively these adhesion protein complexes are termed focal adhesions and act to mechanically couple ECM cues and cytoskeletal responses *(174)*. Cellular forces generated by actin polymerization or myosin mediated actin contraction within the cytoplasm are transmitted to the extracellular matrix via integrins. Integrin conformational changes are dependent on force dissipation to the ECM, thus allowing for local rigidity sensing on a subcellular scale *(175, 176)*. Scaffolding proteins within focal adhesions also undergo force-dependent conformational changes in response to extracellular matrix stiffness to induce cellular responses. Specifically, talin unfolds under tension to expose a cryptic vinculin binding site, and subsequent vinculin binding stabilizes nascent focal adhesions *(177, 178)*. As described by clutch models of cell-matrix adhesion, contractile force is needed to form and strengthen focal adhesions, but excessive force loading leads to matrix detachment *(176)*. In response to increased extracellular matrix rigidity, RhoA signaling cascades that mediate actin stress fiber formation and cell contractility are activated *(179)*. The resulting contractile forces exerted against the extracellular matrix are known as traction forces and are traditionally calculated from substrate deformations on compliant matrices *(180, 181)*. Polyacrylamide gels and micropillar elastomer arrays are the most widespread platforms used to measure traction forces, and represent both continuous and discrete matrices, respectively *(182)*. Because

cellular force transmission can occur over long distances within a cell, matrix mechanical cues can have cell-wide implications including altering cytoskeletal tugging forces at cell-cell adhesions *(183)*.

Endothelial cell studies have previously established that age-related increased extracellular matrix stiffness alone may play a significant pathogenic role in promoting atherogenesis by compromising endothelial barrier integrity (Figure 1.3). In the absence of other cues, increased matrix stiffness elevated RhoA-mediated cell contractility that contributed to disrupted cell-cell junctions and increased permeability both *in vitro* and *in vivo (63)*. Endothelial barrier recovery after pharmacological disruption was also impaired by increased extracellular matrix stiffness *(184)*. Moreover, increased matrix mechanics were also identified as detrimental during later stages of atherogenesis as demonstrated by *in vitro* models showing elevated leukocyte recruitment, transmigration, and persistent monolayer gap formation that were associated with increased matrix stiffness *(63, 185, 186)*. Endothelial expression of the adhesion molecules VCAM-1, ICAM-1, and E-selectin were unaffected by substrate stiffness *in vitro*, suggesting the changes in endothelium integrity were largely driven by mechanics *(63)*.

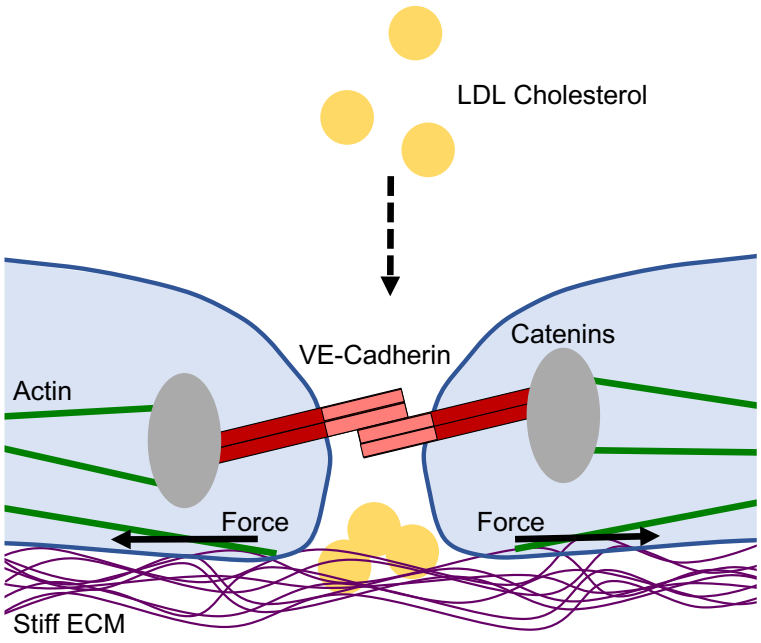

Figure 1.3. Matrix stiffness-mediated cell contractility destabilizes endothelial cell-cell junctions. Endothelial cells exert increased contractile forces with increasing extracellular matrix (ECM) stiffness. Traction forces against the matrix are proportional to cell-cell tensional forces that destabilize intercellular junctions and promote increased endothelium permeability.

1.9 Endothelial Cell Adherens Junctions and Mechanotransduction at Cell-Cell Contacts

A critical function of endothelial cells within the vasculature is to exist as a semi-permeable barrier lining the arterial lumen. As such, endothelial cells exist as part of a monolayer and adherens junctions connect neighboring cells to give the endothelium its integrity *(11)*. Cellular force that is generated in response to matrix mechanical cues is transmitted across the cytoskeletal network and results in cell-cell junction tension *(187, 188)*. Importantly, adhesions between adjacent cells are also mechanosensitive and transmit forces that result in global endothelial monolayer responses *(189)*.

Vascular endothelium cadherin (VE-cadherin) is the primary component of endothelial adherens junctions and exists as a dimer with intercellular and extracellular domains. The extracellular domain of VE-cadherin dimers from adjacent cells form homotypic bonds at cell-cell contacts to give the endothelium its integrity *(11)*. Intracellularly, the cytoplasmic tail of VE-cadherin forms a complex with scaffolding proteins, primarily catenins. VE-cadherin directly binds p120 catenin, beta catenin, and gamma catenin. A fourth catenin, alpha catenin is the only catenin known to have an actin binding domain, and thus links VE-cadherin to the actin cytoskeleton through beta catenin binding *(155, 190)*. Alpha catenin undergoes force-dependent conformation changes under tension that alter junction stability *(191)*.

Vinculin, which has already been identified as a critical component of force sensing through focal adhesions, is also associated with cadherin mediated mechanotransduction *(192–194)*. Junction tension, for example from increased cytoskeletal contractility, induces the stretching of alpha catenin to expose a hidden vinculin binding site *(191)*. Subsequent vinculin recruitment and binding to the complex protects the adherens junction adhesion from opening *(191)*. Consistent with a junction strengthening function, vinculin localization to focal adhesions or intercellular junctions is associated with endothelial barrier disruption or strengthening, respectively *(195)*. Other junctional proteins that regulate actin polymerization, are also recruited to adherens junctions in a tension dependent manner *(196)*.

Despite a role for force in mediating VE-cadherin adhesions and endothelial junction integrity, mechanotransduction by VE-cadherin at cellular junctions was not immediately established *(159, 188)*. A force sensing role for VE-cadherin was first revealed when it was identified as part of the mechanosensory complex that in concert with PECAM-1 mediated the endothelial cell response to fluid shear stress. Data now indicate that cadherins at cell-cell junctions are mechanosensitive *(193)*. Force is transmitted to adjacent cells through VE-cadherin and actin filaments that extend between cells *(193)*. Direct force application to VE-cadherin using magnetic twisting cytometry resulted in ROCK dependent cytoskeletal remodeling and most notably, caused monolayer disruption and gap formation distant from the site of the applied force *(189)*.

Many of the same scaffolding proteins found at focal adhesions are also components of adherens junction complexes suggesting that spatial and temporal regulation is necessary to maintain integrity at both cell-matrix and cell-cell adhesions *(197)*. Indeed, significant crosstalk exists between the two cellular events, as already demonstrated by their direct cytoskeletal linkages and studies showing that intercellular junction forces are an output of chemical and mechanical substrate cues *(187)*. Understanding how localized matrix cues contribute to aberrant endothelial behaviors that are transmitted across adherens junctions into monolayer responses may elucidate how the altered mechanical properties of the intima associated with aging contribute to a disrupted endothelial barrier.

1.10 Organization of the Dissertation

The objective of this work is to investigate the integration of extracellular matrix stiffness cues by endothelial cells within the context of compromised endothelium barrier integrity that contributes to age-related atherogenesis. Because vessel stiffening that occurs as part of aging may contribute to atherogenesis and pharmacological efforts to overcome arterial stiffness have had poor clinical success; an alternative approach is to modulate the cellular response to matrix mechanics. Herein, I present data demonstrating that pharmacologically interrupting endothelial cell contractility on stiff matrices or presenting a substrate with heterogeneous stiffness cues, restores or disrupts endothelium integrity. I then discuss clinically relevant approaches to attenuate matrix stiffness-mediated pathologies.

CHAPTER 2

SIMVASTATIN AMEOLIORATES MATRIX STIFFNESS-MEDIATED ENDOTHELIAL MONOLAYER DISRUPTION

Portions of this chapter were published in *PLoS One* (Lampi *et al*., 2016).

2.1 Abstract

Arterial stiffening accompanies both aging and atherosclerosis, and age-related stiffening of the arterial intima increases RhoA activity and cell contractility contributing to increased endothelium permeability. Notably, statins are 3-hydroxy-3-methylglutaryl coenzyme A (HMG-CoA) reductase inhibitors whose pleiotropic effects include disrupting small GTPase activity; therefore, it was hypothesized the statin simvastatin could be used to attenuate RhoA activity and inhibit the deleterious effects of increased age-related matrix stiffness on endothelial barrier function. Using polyacrylamide gels with stiffnesses of 2.5, 5, and 10 kPa to mimic the physiological stiffness of young and aged arteries, endothelial cells were grown to confluence and treated with simvastatin. RhoA and phosphorylated myosin light chain activity increased with matrix stiffness, but were attenuated when treated with the statin. Readouts of intercellular tension that increased with matrix stiffness, and are correlated with matrix stiffness-dependent increases in monolayer permeability, also decreased with the statin treatment. Furthermore, simvastatin increased activated Rac1 levels that contributed to endothelial barrier enhancing cytoskeletal reorganization. Simvastatin, which is prescribed clinically due to its ability to lower cholesterol, altered the endothelial cell response to increased matrix stiffness and restored endothelial

monolayer barrier function; and therefore, presents a possible therapeutic intervention to prevent atherogenesis initiated by age-related arterial stiffening.

2.2 Introduction

Age is a primary risk factor for atherosclerosis, and vascular stiffness increases with age due to changes in the extracellular matrix that include increased elastin fragmentation, collagen deposition, and collagen crosslinking by advanced glycation end products (AGEs) *(63, 198–200)*. While the connection between macroscale arterial stiffness and cardiovascular diseases is well characterized, the relationship between increased vessel stiffness and endothelium behavior on a cellular level is less clear *(201, 202)*.

Within the vasculature, endothelial cells maintain vascular homeostasis, in part, by forming a monolayer barrier along the arterial lumen. Endothelium integrity is dependent upon extracellular VE-cadherin interactions between adjacent cells and intracellular VE-cadherin anchoring to the actin cytoskeleton through catenins *(11)*. Cellular mechanotranduction occurs at both cell-matrix and cell-cell contacts *(183)*. Our group and others have shown that the mechanical stiffness of the cellular microenvironment plays a key role in dictating endothelial cell behaviors including cell area, adhesion, spreading, network formation, and sprouting *(64, 203–206)*. Permeability of the endothelium is a key feature of atherosclerosis, as cholesterol flux across the vessel wall is an initiating step in atherogenesis *(207–209)*. Using *in vitro* and *ex vivo* models of vessel stiffness and aging, we previously showed that increasing substrate stiffness alone promoted RhoA/ROCK mediated endothelial monolayer disruption and increased endothelium permeability *(63)*.

RhoA-mediated actomyosin contractility is increased on stiff matrices, with increasing substrate stiffness leading to increased traction stresses *(63, 206, 210, 211)*. Increased cellular traction stresses leads to the disruption of cell-cell junctions. As such, inhibition of cellular contractility is one potential avenue for the prevention of increased endothelial permeability in response to the matrix stiffening that occurs with age and atherosclerosis progression.

Interestingly, statins are 3-hydroxy-3-methylglutaryl coenzyme A (HMG-CoA) reductase inhibitors that are traditionally prescribed to lower blood cholesterol levels by inhibiting the production of the intermediate mevalonate during cholesterol synthesis, but are now recognized to have pleiotropic cardiovascular benefits *(212–214)*. Clinically, improvements in patient cardiovascular health that are not correlated to decreased cholesterol levels have been observed in as little as 4 weeks after initiating a statin regimen *(215)*. Statins improve vascular inflammation and reduce the risk of myocardial infarction and stroke *(216, 217)*. Statins also reduce all-cause mortality in patients with and without histories of coronary artery disease *(218, 219)*. It is now evident that inhibiting cholesterol biosynthesis with statins leads to aberrant activity of small GTPase signaling molecules. Mechanistically, it is well established that statins prevent the synthesis of isoprenoids that are post-translationally added to G-proteins *(212–214)* and it has been demonstrated that the addition of mevalonate or the isoprenoids directly rescues the effect of statins *(220, 221)*. Within the Rho family of G-proteins, RhoA, Rac1, and Cdc42 are post-translationally prenylated with a geranylgeranyl pyrophosphate lipid anchor that is important for membrane localization, anchoring, and activation *(222, 223)*. The statin, simvastatin,

originally marketed by Merck under the brand name Zocor®, has been shown to attenuate RhoA activity and increase cytosolic activation of Rac1 by disrupting geranylgeranyl pyrophosphate synthesis to improve endothelial barrier function *(221, 224)*. Notably, although also geranylgeranylated, altered Cdc42 activity does not contribute to the significant improvements in endothelial barrier function after simvastatin treatment *(221)*.

In this study, we investigate the use of simvastatin to restore endothelial barrier integrity by altering pathways that contribute to increased RhoA-mediated cell contractility on stiff matrices. We also investigate Rac1 activity and cytoskeletal reorganization in response to simvastatin treatment. To date, previous studies have demonstrated that simvastatin pre-treatment attenuates barrier disruption caused by the known endothelial agonists thrombin and lipopolysaccharide *(221, 224, 225)*, but have not accounted for physiological biomechanical stimuli such as extracellular matrix stiffness, which is altered with age and also disrupts the arterial endothelium *(63)*. To investigate the effects of statin treatment on the disruption of endothelial barrier function due to matrix stiffness, we grew endothelial cell monolayers on polyacrylamide gels ranging in stiffness from 2.5 to 10 kPa to mimic the young and aged arterial intima respectively *(172)*. Our data indicate that simvastatin treatment altered the cellular response to substrate mechanics and attenuated increased RhoA activity caused by increased matrix stiffness to restore endothelial barrier integrity. Simvastatin also increased Rac1 activity and correlated with barrier enhancing cytoskeletal reorganization. These results indicate that using simvastatin treatment to interrupt pathways that affect RhoA and Rac1 activity may be one method to mitigate endothelium

hyperpermeability that occurs in response to age-related arterial stiffening and prevent atherosclerosis.

2.3 Materials and Methods

Cell Culture and Polyacrylamide Gel Synthesis

Bovine aortic endothelial cells purchased from VEC Technologies (Rensselaer, NY) were used from passages 7-12. Endothelial cells were maintained at 37 ºC and 5% CO_2 in Medium 199 (Invitrogen, Carlsbad, CA) with 10% Fetal Clone III (HyClone, Logan, UT), 1% MEM amino acids (Invitrogen), 1% MEM vitamins (Medtech, Manassas, VA), and 1% penicillin-streptomycin (Invitrogen) (complete Medium 199). Polyacrylamide (PA) gels with stiffnesses of 2.5, 5 and 10 kPa were made with bisacrylamide:acrylamide ratios of 5:0.1, 7.5:0.175, and 7.5:0.35, respectively. The PA gels and glass controls were coated with 0.1 mg/mL rat tail type I collagen (BD Biosciences), as described previously *(63, 203)*.

Simvastatin Treatments

Simvastatin (Sigma-Aldrich) was activated as previously described *(226–228)*. Briefly, simvastatin prodrug was dissolved in 200-proof ethanol and incubated with 0.1 N NaOH for 2 hours at 50 °C followed by the addition of MilliQ water. The solution was brought to a final pH of 7.0 using 0.1 N HCl and stored at 4 °C. Simvastatin was diluted to final concentrations of 1 μM and 10 μM in complete M199 for cell studies. Simvastatin treatment was 24 hours based on previous time course studies demonstrating greater effects on barrier enhancement with longer incubation times *(221, 229)*.

RhoA and Rac1 Activity Assays

The colorimetric RhoA and Rac1 activity assays (Cytoskeleton #BK124 and #BK128) were carried out according to the manufacturer protocol. Lysate was collected from endothelial cell monolayers on 2.5, 5, and 10 kPa PA gels and glass controls treated with 0 or 10 μM simvastatin for 24 hours, two days post-confluence. The lysate from two gels at each condition was pooled and RhoA or Rac1 activity was normalized to the total protein content of the sample using the included Precision Red Protein Assay (#ADV02).

Western Blotting

Two days post-confluence, endothelial cell monolayers on 2.5, 5, and 10 kPa PA gels and glass controls were treated with 0 or 10 μM simvastatin for 24 hours. Samples for phosphorylated myosin light chain (pMLC) analysis were lysed directly into boiling 2x Laemmli buffer, followed by immediate heating of the lysate at 95 °C and heavy vortexing to disrupt nucleic acid structure. Lysate collected for the RhoA and Rac1 assays were used for quantifying total GTPase protein expression. Lysate was separated using sodium dodecyl sulfate polyacrylamide gel electrophoresis (SDS-PAGE) followed by protein transfer onto a polyvinylidene difluoride (PVDF) membrane (Bio-Rad). Total RhoA was probed with a mouse monoclonal antibody against full-length RhoA (1:100) (Abcam, No. ab54835). Phosphorylated myosin light chain (pMLC) was probed with a polyclonal rabbit antibody against pMLC at threonine-18 and serine-19 (1:50) (Cell Signaling Technology, No. 3674). Total Rac1 was probed with a mouse monoclonal antibody against full-length Rac1 (1:00) (Millipore, No. 23A8). Alpha tubulin was probed as a loading control with a

mouse polyclonal primary antibody (1:2000) (Sigma, No. T3559). Horseradish peroxidase (HRP) conjugated anti-rabbit and anti-mouse secondary antibodies were used (1:2000) (Rockland, No. 611-103-122 and Rockland, No. 610-103-121, respectively). The signal was developed with SuperSignal West Pico Chemiluminescent Substrate (Thermo Scientific). The membranes were exposed and imaged with a FujiFilm Image-Quant LAS-4000, followed by protein quantification using ImageJ software (v2.0.0-rc-41/1.50d, National Institutes of Health, Bethesda, MD, USA). The pMLC, RhoA, and Rac1 signals were normalized to the alpha tubulin loading control at each condition.

Vinculin Focal Adhesion Quantification and Cell-Cell Junction Localization

Endothelial cells were seeded on 2.5, 5, and 10 kPa PA gels and allowed to adhere for 16 hours (single cells) or cultured 2 days post-confluence (monolayers). The growth media was then removed and replaced with complete M199 containing 0 or 1 μM simvastatin for 24 hours. Cells were fixed and permeabilized with 3.2% paraformaldehyde (EMS) and 1% Triton (VWR), respectively. Immunostaining was done with a mouse monoclonal vinculin antibody (1:100) (Santa Cruz, No. sc-59803) and a goat polyclonal VE-cadherin antibody (1:100) (Santa Cruz, No. sc-6458). Alexa Fluor 488 donkey anti-mouse (1:200) (Invitrogen, No. A21202) and Alexa Fluor 568 donkey anti-goat (1:200) (Invitrogen, No. A11057) secondary antibodies were used.

A z-stack image of each sample was captured using a Zeiss LSM700 microscope (v. 2010, Carl Zeiss MicroImaging GmbH, Jena, Germany) using a 40X/1.1 NA water immersion objective and 488 nm and 568 nm excitation laser lines, for vinculin and VE-cadherin,

respectively. Images were then opened in ImageJ and converted into image sequences followed by automated image analysis performed with MatLab. To extract adhesion labeled structures, individual images were subjected to an adaptive Wiener filter filtering window (0.8 μm for vinculin and 0.6 μm for VE-cadherin) to remove background noise. Image sections presenting structures with a signal to noise ratio greater than 3:1 for vinculin and 2:1 for VE-cadherin where then subjected to a top-hat filter (1 μm diameter disk). Filtered images were further subjected to a median filter (0.48 μm filtering window) to correct for intensity variations while keeping necessary structures. To quantify FA length and area, confocal sections from vinculin stained single cells were used. To quantify vinculin:VE-cadherin overlap, corresponding vinculin and VE-cadherin stained endothelial cell monolayer confocal image stacks were filtered as described and then overlaid to generate the 3D overlapping volume data.

Cell Circularity and Actin and Cortactin Arrangement

Two days post-confluence, endothelial cell monolayers on 10 kPa PA gels were treated with 0, 1, and 10 μM simvastatin for 24 hours. Cells were fixed and permeabilized with 3.7% formaldehyde (VWR) and 1% Triton (VWR), respectively. Immunostaining was done with a rabbit polyclonal cortactin primary antibody (1:100) (Santa Cruz, No. sc-11408) and Alexa Fluor 488 donkey anti-rabbit secondary (1:200) (Invitrogen, No. A21206). Actin was visualized with 594 FITC-conjugated phalloidin (1:100) (Invitrogen, No. A12381). Fluorescent images were captured on a Zeiss Axio Observer.Z1m microscope equipped with a Hamamatsu ORCA-ER camera using a 20x objective. Cell perimeters were outlined and cell circularity was calculated in ImageJ software where

$circularity = \frac{4\pi(Area)}{(Perimeter)^2}$ and a perfect circle has a value of 1. Cortactin organization was quantified using MatLab code to quantify the number of linear segments at cell-cell junctions.

Statistical Analysis

Statistical analysis was conducted in JMP v. 10. All data is mean ± SEM (standard error of the mean). Analysis of variance (ANOVA) followed by a Tukey's Honestly Significant Difference (HSD) test were used for total RhoA expression, total Rac1 expression, focal adhesion size and length, cell circularity, cortactin arrangement, and vinculin localization analyses. Within stiffness changes in RhoA and Rac1 expression and vinculin localization were analyzed with a two-tailed Student's t-test. Focal adhesion and vinculin localization data was log transformed to meet normality assumptions. Least squares means (LS-Means) regression was used to analyze Western blotting and RhoA-GTP activity using experiment as a random effect to account for differences in baseline values between experimental replicates. Rac1-GTP activity was analyzed using a linear mixed effects model accounting for within experiment dependence.

2.4 Results

Simvastatin Alters the RhoA Pathway

To investigate the effect of simvastatin on endothelial barrier disruption associated with elevated RhoA activity caused by increased matrix stiffness, we probed RhoA activity and markers of endothelium integrity in response to both substrate stiffness and simvastatin treatments. We also investigated the effect of simvastatin on Rac1 activity, noting that Rac1

is reported to have inverse activation when compared to RhoA, and that Rac1 is also altered by simvastatin to improve endothelial barrier function *(151, 221, 224)*.

To modulate substrate stiffness and maintain physiological relevance, we grew bovine aortic endothelial cells on polyacrylamide gels with a lower stiffness level of 2.5 kPa to match the reported Young's modulus of 2.7 ±1.1 kPa for the stiffness of the subendothelial matrix of healthy bovine carotid arteries *(172)*. Higher stiffness 5 and 10 kPa gels were used as models of aged arteries. As matrix stiffness increased, RhoA activity increased (Figure 2.1A). At each stiffness level, simvastatin treatment resulted in a significant decrease in active RhoA levels. Interestingly, while total cellular RhoA showed no significant change in expression over the stiffness range tested in control conditions, there was a robust increase in total RhoA across all stiffnesses with simvastatin treatment (Figures 2.1B,C). These results suggest a compensatory cellular response to the production of unprenylated RhoA and indicate the decrease in active RhoA-GTP caused by the statin treatment is not a result of lower expression levels. To further assess the effect of simvastatin on the RhoA/ROCK contractility pathway, we probed endothelial monolayers for phosphorylated myosin light chain (pMLC) which is activated downstream of RhoA (Figure 2.1D). Similar to RhoA activity, activation of myosin light chain increased with stiffness, and the effect of matrix mechanics was attenuated with simvastatin treatment (Figure 2.1E). The significant decreases in active RhoA and phosphorylated myosin light chain levels suggest that simvastatin interferes with cell contractility pathways.

Figure 2.1. Simvastatin disrupts the RhoA pathway. The RhoA/ROCK pathway activity was elevated in endothelial monolayers with increased matrix stiffness but was attenuated with 10 μM simvastatin treatment. (A) Bar graphs of RhoA-GTP activity in response to matrix stiffness and simvastatin treatment normalized to total protein of lysate (n = 2, performed in triplicate). (B) Representative Western blot probing for total cellular RhoA expression and alpha tubulin (α-tub) loading control. (C) Quantification of total RhoA normalized to alpha tubulin loading control demonstrating that RhoA expression was significantly increased by the simvastatin treatment (n = 5). (D) Representative Western blot probing for phosphorylated myosin light chain (pMLC) and alpha tubulin loading control. (E) Western blot quantification normalized to alpha tubulin loading control demonstrating simvastatin attenuated increased pMLC caused by increased substrate stiffness, (n = 4). Data are presented as means ± standard error of the mean, *$p<0.05$, **$p<0.01$, ***$p<0.001$ when compared to the untreated control at each stiffness.

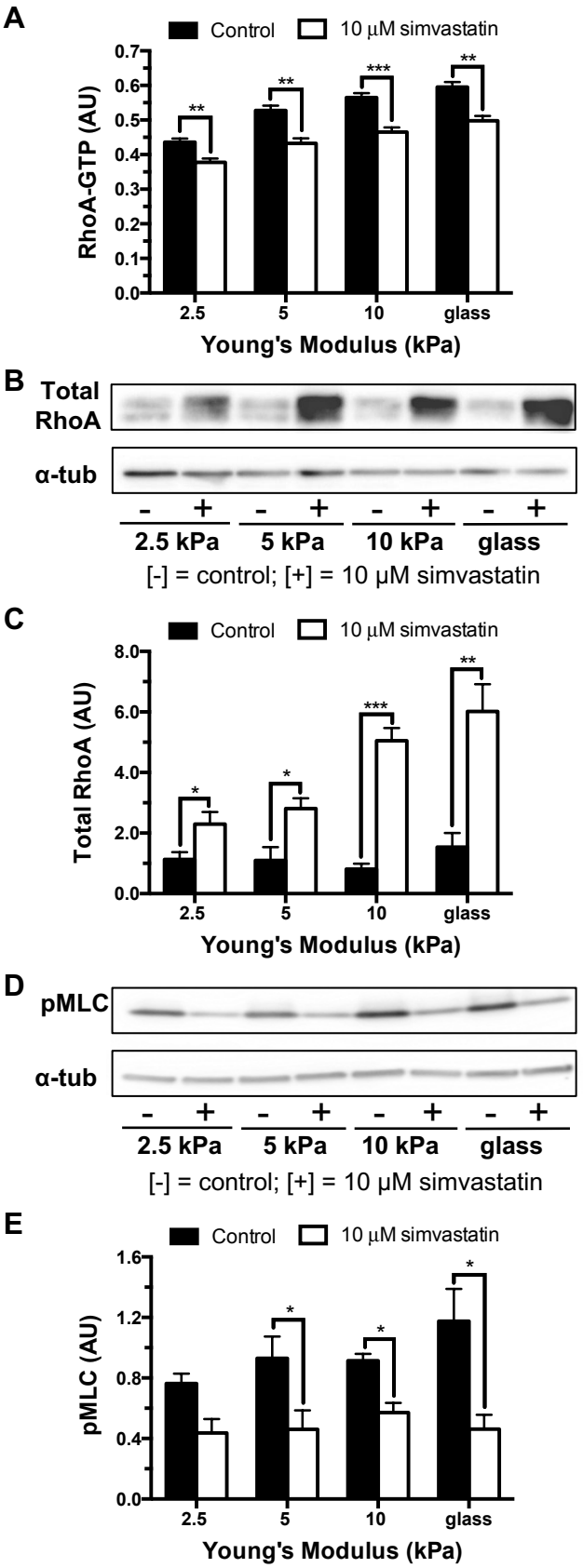
A
Control
10 μM simvastatin
RhoA-GTP (AU)
0.7
0.6
0.5
0.4
0.3
0.2
0.1
0.0
**
**
***
**
2.5
5
10
glass
Young's Modulus (kPa)
B
Total RhoA
α-tub
- + - + - + - +
2.5 kPa
5 kPa
10 kPa
glass
[-] = control; [+] = 10 μM simvastatin
C
Control
10 μM simvastatin
Total RhoA (AU)
8.0
6.0
4.0
2.0
0.0
*
*
***
**
2.5
5
10
glass
Young's Modulus (kPa)
D
pMLC
α-tub
- + - + - + - +
2.5 kPa
5 kPa
10 kPa
glass
[-] = control; [+] = 10 μM simvastatin
E
Control
10 μM simvastatin
pMLC (AU)
1.6
1.2
0.8
0.4
0.0
*
*
*
2.5
5
10
glass
Young's Modulus (kPa)

Simvastatin Alters Endothelial Cell Focal Adhesions

RhoA-mediated cell contractility is necessary for focal adhesion assembly *(230)* and both focal adhesion size and traction forces increase with increased matrix stiffness *(173, 231)*; therefore, we treated endothelial cells with and without 1 μM simvastatin and stained for vinculin to quantify individual cell-matrix interactions using length and area as metrics (Figure 2.1A). As predicted from a prior study where RhoA-mediated traction forces increased with increased matrix stiffness, focal adhesion length and area increased with increasing substrate stiffness, but were attenuated with simvastatin, most notably on the stiffer matrices (Figures 2.1B, C) *(63)*. Since focal adhesion formation relies on feedback loops transmitting matrix cues from integrins to the cytoskeleton *(192)*, and it is established that stable focal adhesions are elevated on stiff matrices *(173)*, our data demonstrate that simvastatin treatment is altering how mechanical signals from the underlying matrix are integrated into cellular responses.

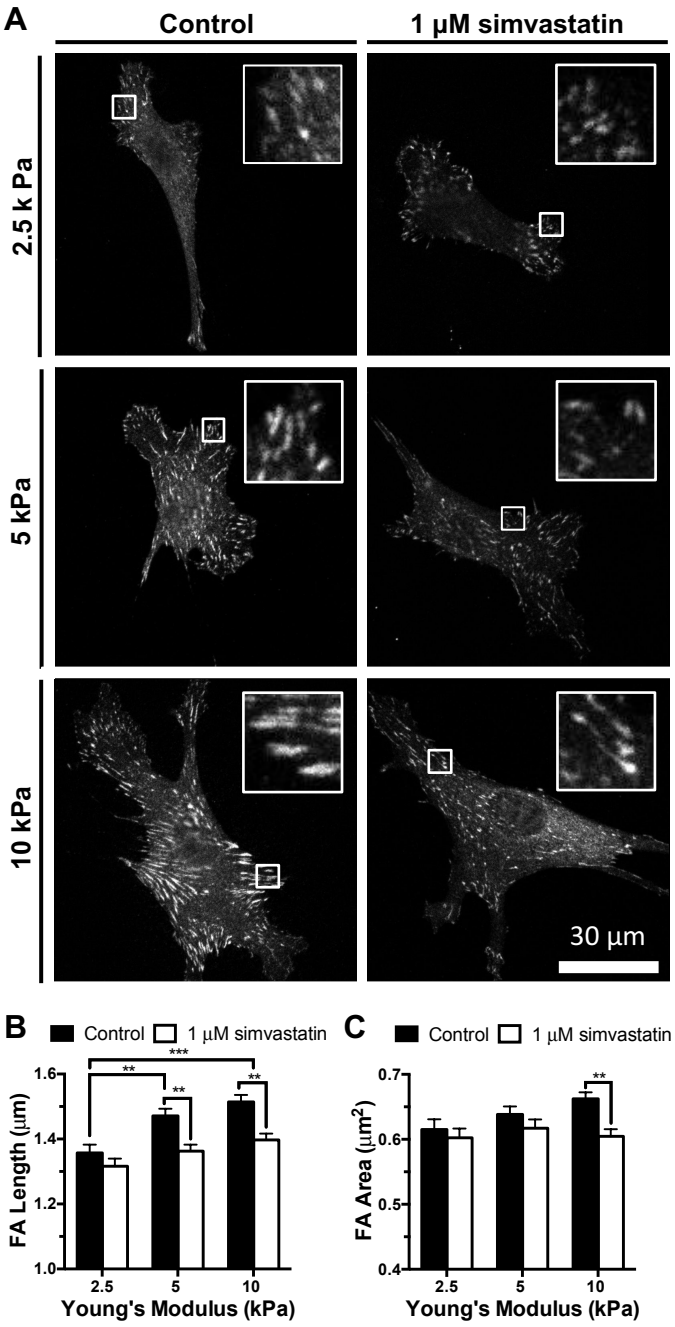

Figure 2.2. Simvastatin decreases endothelial cell focal adhesion length and area. Endothelial cell focal adhesion length and area increased with matrix stiffness but decreased with 1 μM simvastatin treatment demonstrating that statins alter cell-matrix interactions. (A) Representative images of vinculin stained focal adhesions in individual endothelial cells with increasing matrix stiffness and 1 μM simvastatin treatment. Inset shows individual vinculin stained focal adhesions. (B) Focal adhesion (FA) length and (C) area increased with substrate stiffness but decreased with the statin treatment (n = 3, 38-56 cells per condition). Data are presented as means ± standard error of the mean,**p<0.01, ***p<0.001.

Simvastatin Alters Endothelial Cell Cytoskeletal Organization and Rac1 Activity

Since simvastatin had the greatest effect on focal adhesion formation on stiff matrices, and transverse actin stress fibers anchored at focal adhesions are used to exert contractile forces that are endothelial barrier disrupting, we investigated the effects of simvastatin on the cytoskeleton using 10 kPa polyacrylamide gels where high matrix stiffness-dependent contractile forces have been measured *(63, 232)*. Previous work has shown that enhanced endothelial integrity by simvastatin treatment is associated with distinct patterns of actin reorganization from stress fibers into an endothelial barrier enhancing cortical actin ring *(224)*. The formation of a cortical actin ring has also been associated with known barrier enhancing stimuli such as shear stress and sphingosine-1-phospate (S1P) *(160, 233)*. As such, we were interested in whether simvastatin could attenuate the formation of prominent actin stress fibers and instead promote a barrier protective phenotype on stiff matrices. Endothelial cell monolayers on 10 kPa polyacrylamide gels were treated with 0, 1, or 10 μM simvastatin and actin was visualized (Fig. 2.3A). Consistent with our RhoA activation data, we observed prominent actin stress fibers in the control monolayers that decreased in a dose-dependent manner with simvastatin treatment. At higher simvastatin concentrations, a cortical actin ring defined cell-cell junctions suggesting improved barrier integrity. Cortactin activates the Arp 2/3 complex for actin assembly *(234)* and its translocation to the cell periphery is necessary for cortical actin organization resulting in improved endothelial barrier integrity by S1P *(160)*. Similarly, cortactin translocation to cell edges has been reported in endothelial cells after simvastatin treatment *(224)*. Therefore, we fluorescently stained endothelial cell monolayers treated with 0, 1, or 10 μM simvastatin to determine if cortactin translocation could be an underlying mechanism mediating the

barrier protective cytoskeletal reorganization we observed on stiff matrices in response to simvastatin (Figure 2.3A). Whereas cortactin in control cells was found in concentrated puncta around the cell periphery, it was linearly organized along the entire perimeter in cells treated with 10 μM simvastatin. Cortactin reorganization, measured by quantifying the number of linear segments along the cell perimeter, significantly increased with the statin treatment (Figure 2.3B). Cytoskeletal changes were accompanied by a distinct change in cell shape to a more elongated morphology with increasing statin treatment. The change in cell morphology was quantified using cell circularity where a perfectly circular cell has a value of 1 (Figure 2.3C).

Since Rac1 has been identified as the upstream effector mediating cortactin translocation *(235)*, and it is also a prenylated G-protein that regulates cytoskeletal dynamics in concert with RhoA *(151)*, we investigated whether simvastatin was also altering Rac1 activity. While there was no significant difference in activated Rac1 with increasing physiological matrix stiffness, across all stiffnesses, endothelial cell monolayers receiving the statin treatment exhibited increased active Rac1-GTP levels that were consistent with the cortactin translocation we observed (Figure 3D). Expression of total cellular Rac1 was unchanged by either matrix stiffness or simvastatin treatment (Figures 2.3E, F). Interestingly, although both RhoA and Rac1 are post-translationally modified with a geranygeranyl moiety, our results demonstrate that simvastatin differentially affects RhoA and Rac1 pathways to alter downstream indicators of cellular mechanosensing such as cytoskeletal organization, stress fiber formation, and contractility.

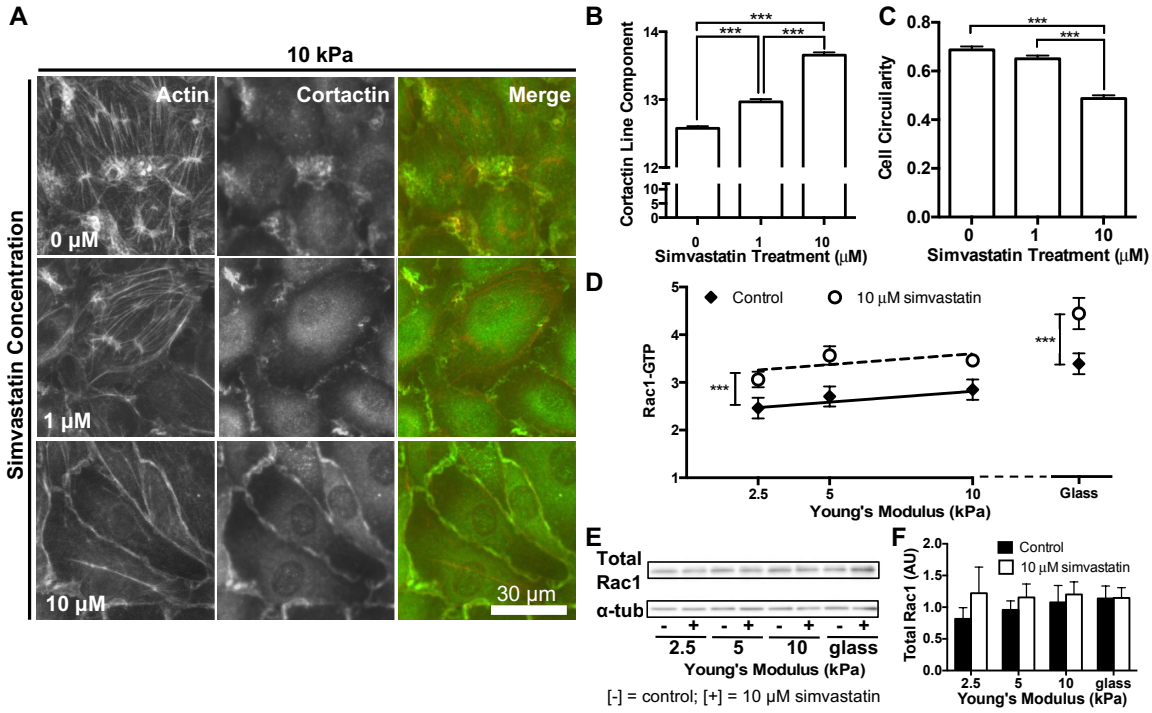

Figure 2.3. Simvastatin alters actin organization, cell morphology, and Rac1 activity in endothelial monolayers. Cytoskeletal organization and Rac1 activity in endothelial monolayers was altered by simvastatin treatment. (A) Representative images of endothelial monolayers demonstrating prominent actin stress fibers in control cells and a barrier enhancing cortical actin ring that formed with increasing simvastatin concentration. Cortactin changed from puncta to organized linear segments around the cell periphery and localized with actin with increasing statin treatment. (B) Cortactin organization, measured by quantifying linear segments at cell-cell junctions, increased with simvastatin (n = 3, 30 fields of view per condition). (C) Endothelial cells adopted an elongated morphology as actin stress fibers diminished with increasing simvastatin treatment. Cell circularity, where a perfectly circular cell has a value of 1, decreased with increasing simvastatin concentration (n = 3, 50-54 cells per condition). (D) Rac1-GTP activity normalized to total protein of lysate increased across all stiffness levels with simvastatin treatment (n = 5, performed in duplicate or triplicate). (E) Representative Western blot probing for total cellular Rac1 expression and alpha tubulin (α-tub) loading control. (F) Quantification of total Rac1 normalized to alpha tubulin loading control demonstrated no significant change in expression with stiffness or statin treatment (n = 5) Data are presented as means ± standard error of the mean, ***p<0.001.

Simvastatin Attenuates Intercellular Tension in Monolayers

Our prior studies have demonstrated that increased matrix stiffness elevates RhoA-mediated cell contractility disrupting endothelial cell-cell junctions and decreasing barrier function. Here, we have demonstrated that simvastatin treatment decreased RhoA activity and resulted in barrier strengthening cortical actin arrangement. To further characterize the role of simvastatin in attenuating the effect of increased matrix stiffness on cell-cell junctions in endothelial monolayers, the mechano-sensitive protein vinculin was used as a readout of intercellular junction tension. It has been established that vinculin localizes at adherens junctions under tension and during remodeling to prevent junction opening, but is absent from mature cell-cell contacts *(193, 194)*. Furthermore, Huveneers *et. al* demonstrate that stable endothelial junctions are converted into remodeling, vinculin positive junctions after adding thrombin, thereby connecting endothelium permeability to RhoA activation, vinculin localization and cell-cell junction tension *(194)*. Endothelial monolayers grown on polyacrylamide gels of increasing stiffness were treated with control or 1 μM simvastatin and fluorescently stained for vinculin and VE-cadherin (Figures 2.4A,B). Vinculin localization was measured using confocal microscopy and automated image analysis to quantify the volume of vinculin per monolayer overlapping with VE-cadherin at cell-cell junctions. Increased matrix stiffness correlated with a significant increase in vinculin at cell-cell contacts that is decreased at higher stiffnesses with simvastatin treatment (Figures 2.4C). These data indicate that cell-cell adhesions within endothelial monolayers on stiff matrices are under increased tension and are less-stable, but have improved integrity after simvastatin treatment.

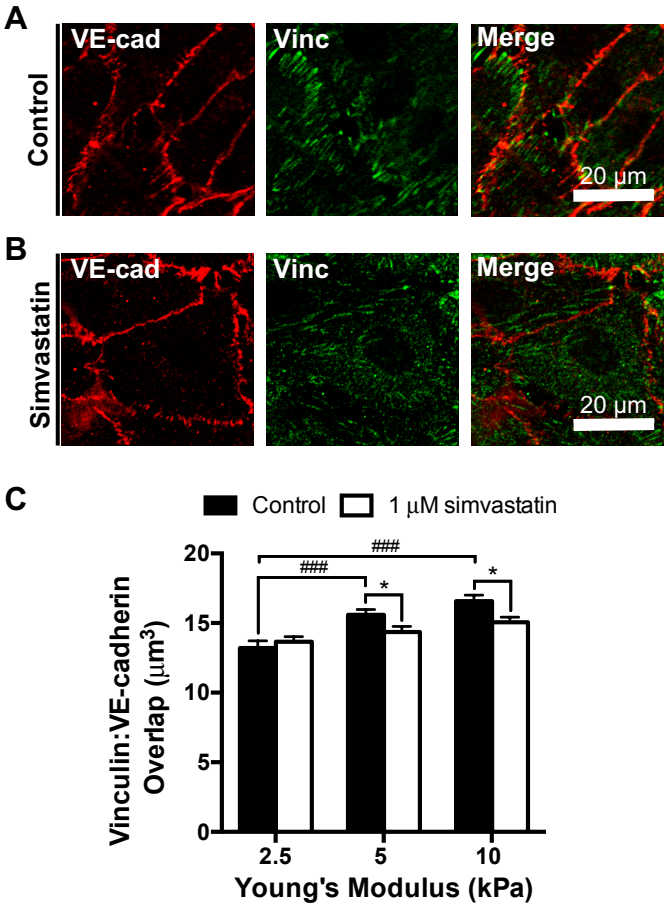

Figure 2.4. Simvastatin reduces vinculin localization at cell-cell adhesions in endothelial monolayers. Endothelial monolayers treated with control and 1 μM simvastatin were stained for vinculin and VE-cadherin, and the vinculin volume overlapping with VE-cadherin was quantified. Representative images of endothelial cell-cell junctions within a confluent monolayer fluorescently stained for VE-cadherin and vinculin on a 10 kPa polyacrylamide gel after 24 hour (A) control and (B) 1 μM simvastatin treatment demonstrating vinculin positive and vinculin negative junctions, respectively. (C) Vinculin localization per monolayer at cell-cell adhesions, a readout of intercellular junction tension, was quantified and increased with matrix stiffness but was significantly decreased with the statin treatment at higher matrix stiffnesses (n = 3, 70-90 fields of view per condition). Data are presented as means ± standard error of the mean, ###$p<0.001$ compared to matrix stiffness, *$p<0.05$ compared to the untreated control.

Collectively, our data suggests that simvastatin may provide age-related atheroprotective benefits by altering pathways that disrupt RhoA and Rac1 activity to contribute to restored endothelium integrity and barrier function on stiff matrices.

2.5 Discussion

To date, there are no FDA-approved therapeutics to reverse age-related vessel stiffening even though arterial stiffness is well accepted to occur with age and is a negative predictor of cardiovascular health *(236, 237)*. Stiffening of the arterial intima disrupts endothelium integrity, and the flux of cholesterol across the endothelium is the first-step in atherogenesis, suggesting that maintaining or restoring endothelial barrier function may be one method to mitigate atherosclerosis *(63)*. Notably, the small GTPase RhoA is known to play a critical role in disrupted endothelial adherens junctions and its activity is elevated in response to increased matrix stiffness *(63, 147, 210)*. Here, we demonstrate the use of simvastatin to inhibit the endothelial cell response to substrate stiffness and show that simvastatin alters RhoA and Rac1 pathways to restore endothelial monolayer integrity.

An altered endothelium is known to precede atherosclerotic lesion development *(238)*, and increased collagen crosslinking by advanced glycation end products (AGEs) is a major contributor to stiffening of the vascular wall *(239)*. Therapeutics to reverse arterial stiffening by breaking AGE crosslinks or preventing AGE formation have been met with limited success despite reaching clinical trials *(200)*. Therefore, new approaches to target vascular stiffening or the cellular response to stiffening are required. Our data suggest that statins may be one approach to preventing the aberrant endothelial cell response to vascular stiffening.

Numerous pleiotropic effects of statins can be attributed to the inhibition of isoprenoid production which disrupts post-translational prenylation of the Rho family of GTPases:

RhoA, Rac1, and Cdc42. Specific attention has been placed on RhoA because of its role in regulating contractility of the actin cytoskeleton and the importance of post-translational prenylation for its localization and activation at the cell membrane *(147)*. In agreement with other studies, we report that simvastatin decreases RhoA activity. We also report attenuated cell-cell junction tension that suggests increased monolayer stability and integrity with simvastatin treatment. Furthermore, we report elevated Rac1 activity after the statin treatment that is correlated with barrier enhancing cytoskeletal rearrangements. This paradoxical activation of Rac1 has been previously attributed to the inability of unprenylated Rac1 to associate with its GDI *(240)*, upstream activation of the AMP-activated protein kinase (AMPK) pathway *(241)*, and the inverse activation relationship between RhoA and Rac1 *(151)*. To date, improved barrier integrity by simvastatin has not been associated with altered Cdc42 activity, and therefore, was not included in this study *(221)*. The pleiotropic effects of statins are not limited to altering the RhoA family of GTPases and there is significant crosstalk between cellular mechanotransduction pathways that continue to be elucidated, therefore, we acknowledge that simvastatin may also be acting through additional pathways to ameliorate the effects of increased matrix stiffness (for reviews on the pleiotropic effects of statins see references *(212–214)*. While other groups have shown the efficacy of simvastatin in response to exogenous chemical agonists such as thrombin or in diabetic disease models, we are the first to show that statins can counteract the deleterious effects of matrix stiffening that occurs with normal aging *(221, 224)*. Our results suggest that statins have the potential to benefit otherwise healthy adults as they age by maintaining endothelial barrier integrity to prevent the onset of atherosclerosis and subsequent cardiovascular diseases.

RhoA activity has generally been regarded as detrimental to endothelial barrier function *(147)*; however, basal RhoA activity is required for intact endothelial junctions and VE-cadherin expression *(149)*. Szulcek and colleagues reported its role in promoting the formation of endothelial cell-cell junctions *(242)*. Hotspots of RhoA activity were identified in regions of the cell membrane where endothelial protrusions were creating new junctions after spontaneous small gap formation. Interestingly, coordinated RhoA activity is also necessary for cell polarization and alignment in response to shear stress, hallmarks of a healthy endothelium *(243, 244)*. Similarly, Rac1 can have barrier protective or disruptive effects depending on its specific localization and activation. Membrane bound Rac1 can produce deleterious reactive oxygen species at cell-cell adhesions *(245)*, but also stabilizes adherens junctions by retaining VE-cadherin *(159)*. Cytosolic Rac1, in agreement with our data, is necessary for cortactin shuttling and cortical actin polymerization *(220)*. Since precise regulation of RhoA and Rac1 are necessary for endothelial functionality, developing barrier-restoring therapeutics presents a particular challenge and should not focus on complete suppression or amplification of their activity.

Endothelial cells are modulators of vascular homeostasis and exhibit improved functionality after statin treatment. Notably, endothelial cells are also mechanosensitive, incorporating matrix signals from basal integrins and flow stimuli from the apical glycocalyx *(246, 247)*. The crosstalk between mechanical cues and statin treatment is not well understood. Previous work has shown that a synergistic response between statins and mechanical force exists, where laminar shear stress with statin treatment provided

enhanced protection against oxidative stress. However, under disturbed flow conditions, the protective benefit of the statin was diminished *(248)*. This prior work lays the foundation to suggest that there is an intersection in mechanotransductive effects of shear stress and the signaling pathways affected by statin treatment. Our data furthered this work by demonstrating that other mechanical cues, specifically matrix stiffening, also exhibit crosstalk with the pathways targeted by statins.

Cardiovascular stiffening is well known to occur with age, and the role of vascular stiffening as a cause rather than a consequence of cardiovascular diseases has been demonstrated in several recent studies *(236)*. Weisbrod and colleagues recently demonstrated that microscale vessel stiffening preceded hypertension in a mouse model of diet-induced obesity *(140)*, and clinical trials have shown that macroscale arterial stiffening also precedes hypertension *(249)*. Our group has shown that intimal stiffness causes endothelial barrier disruption due to increased RhoA-mediated cell contractility, and that the endothelial response to increased matrix stiffness, and not adhesion molecule expression, contributed to enhanced leukocyte transmigration *(63)*. Moreover, endothelial monolayers cultured on stiff matrices, are unable to recover from leukocyte transmigration events leading to persistent gaps in the endothelial layer *(185)*, through which subsequent leukocytes can transmigrate at increased rates *(250)*. *In vivo*, delayed repair of the endothelium could promote a local inflammatory response and drive atherosclerotic plaque formation. These recent advances in the literature indicate that vascular stiffening may be a potential target to mitigate cardiovascular disease pathologies associated with a compromised endothelium. As such, preventing the aberrant cellular response to age-

related arterial stiffening to restore endothelial barrier function using statins, for example, as was done here, may be a promising approach to inhibiting atherosclerosis.

CHAPTER 3

PHOTOPATTERNED HYDROGELS TO INVESTIGATE THE ENDOTHELIAL CELL RESPONE TO MATRIX STIFFNESS HETEROGENEITY

Portions of this chapter were published in

ACS Biomaterials and Engineering (Lampi *et al.*, 2017)

3.1 Abstract

Age-related intimal stiffening is associated with increased endothelium permeability, an initiating step in atherosclerosis. Notably, in addition to a bulk increase in matrix stiffness, the aged intima also exhibits increased spatial stiffness heterogeneity; therefore, the effect of heterogeneous matrix stiffness on endothelial cells was investigated. Methacrylated hyaluronic acid hydrogels were fabricated and photopatterned to create substrates with 50 and 100 μm squares containing soft and stiff matrix regions of 2.7 ± 0.7 and 10.3 ± 3.9 kPa. On the patterned matrices, endothelial cells integrated subcellular matrix stiffness cues at stiffness interfaces, and focal adhesions were increased in the cell body adhered to stiff matrix regions. Increased matrix stiffness heterogeneity disrupted cell−cell junctions in confluent endothelial monolayers (Figure 3.1). Together, this work indicated that the spatial presentation of matrix mechanical cues, in addition to bulk substrate compliance, plays a role in governing endothelial single cell and monolayer behaviors.

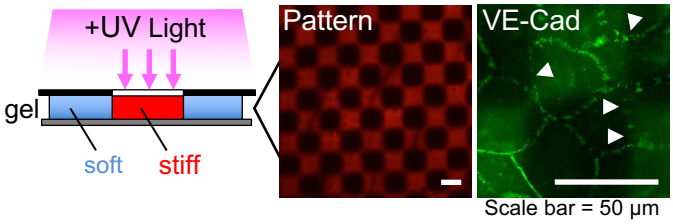

Figure 3.1. Graphical abstract. Hydrogels with heterogeneous stiffness were patterned by photocrosslinking and used to investigate the endothelial cell response to spatial matrix stiffness cues. Endothelial cells responded to subcellular changes in matrix stiffness and endothelial monolayer cell-cell junction integrity was disrupted on the heterogeneous stiffness substrates.

3.2 Introduction

Extracellular matrix stiffening is associated with a diverse array of pathologies including cancer, diabetes, and cardiovascular diseases, and matrix mechanical cues can alter cellular behaviors to contribute to disease progression *(173, 200, 251–253)*. Increased bulk artery stiffness is a hallmark of both aging and atherosclerosis and is used as a clinical marker to assess cardiovascular health *(254, 255)*. Notably, macroscale measurements of arterial stiffness do not reflect the cell−scale matrix mechanics of the microenvironment where endothelial cells reside lining the arterial intima lumen and act in part, as a semipermeable barrier that maintains vascular homeostasis *(256)*. Compromised endothelial adherens junctions that contribute to increased endothelial permeability and the accumulation of LDL cholesterol in the intima are initiating steps in atherosclerosis *(2, 11)*. Endothelial junction integrity relies on a critical balance between tensional forces and Rho family GTPase activity to promote the formation of stable junctional complexes without leading to their disassembly *(149, 151, 152, 159, 221, 257)*. Evidence that intimal stiffening precedes cardiovascular disease, combined with prior reports that increased matrix stiffness elevates cell contractility and stress fiber formation, disrupts endothelial cell−cell

junctions, and inhibits endothelium barrier recovery, suggests that extracellular matrix mechanics may play a critical role in atherogenesis *(63, 140, 149, 153, 184, 185, 230, 258)*.

In addition to increased average intima stiffness with age, *ex vivo* mechanical characterization of murine aortas revealed that aged vessels also exhibit increased mechanical spatial heterogeneity within the intima over an area where a single endothelial cell would reside *(122, 172)*. Within a 100 by 100 μm area, stiffness "hotspots" were detected, and intima stiffness increased as much as 50-fold from 2 to 100 kPa. Because focal adhesions individually probe the extracellular environment and *in vitro* models have shown that cells can discern subcellular differences in matrix compliance that alter cell polarization, local traction stresses, and durotactic behaviors, we hypothesize that endothelial cells *in vivo* are integrating distinct matrix mechanical cues from their extracellular environment that alter junction integrity *(175, 179, 259, 260)*. Although increased bulk matrix stiffness is recognized to compromise endothelium integrity, the role of spatially heterogeneous matrix mechanics on endothelial cells remains unknown and is important to understanding how the altered mechanical properties of the intima associated with aging contribute to a disrupted endothelium.

Here, we used methacrylated hyaluronic acid hydrogels that undergo sequential polymerization to fabricate and characterize substrates with regions of patterned crosslinking *(171, 261)*. Motivated by the increased spatial heterogeneity and abrupt increases in extracellular matrix stiffness within the aged arterial intima, these stiffness patterned substrates were then used to study the endothelial cell response to stepwise spatial

changes in matrix stiffness. On the basis of the location of focal adhesion formation, within an individual endothelial cell, there was a local response to multiple matrix stiffness cues. Furthermore, matrix stiffness heterogeneity affected monolayer formation and disrupted cell−cell junction integrity. Average intercellular gap size increased with increased matrix stiffness heterogeneity, and the greatest cell−cell junction disruption occurred at stiffness interfaces. These findings suggest the spatial presentation of extracellular matrix mechanical cues, in addition to the average bulk modulus, contribute to atherogenesis caused by age related intimal stiffening.

3.3 Materials and Methods

Methacrylated Hyaluronic Acid Synthesis

Methacylated hyaluronic acid (MeHA) was synthesized as described previously *(171, 262)*. Sodium hyaluronate (51 kDa, Lifecore Biomedical, Chaska, MN) was dissolved in DI water at 1 wt% and reacted with 2.4 mL of methacrylic anhydride (Sigma-Aldrich, St. Louis, MO) per gram HA on ice at pH 8.0 for 8 h. The reaction mixture was incubated overnight at 4 °C followed by the introduction of an additional 1.2 mL of methacrylic anhydride per gram HA on ice at pH 8.0 for 4 h. The reaction product was dialyzed against DI water (6−8 kDa MWCO, SpectraPor, Rancho Dominguez, CA) and lyophilized. MeHA modification was determined to be ~100% by 1H NMR (600 MHz Varian).

Photopatterned MeHA Gel Fabrication

MeHA hydrogels were synthesized as described previously *(171, 261)*. Briefly, substrates were fabricated by dissolving the synthesized MeHA polymer in 0.2 M triethanolamine

(Sigma Aldrich, St. Louis, MO) in PBS, at pH 10.25 at 3 wt%. A custom synthesized RGD cell-binding peptide, GCGRGDSPG (Genscript, Piscataway, NJ) was added to the polymer solution at a final concentration of 1 mM and reacted for 45 min. Gels were then polymerized between two glass coverslips by Michael-type addition using dithiothreitol (DTT) (Sigma-Aldrich, St. Louis, MO) to consume 13% of the available methacrylates. Polymerized hydrogels were incubated overnight at room temperature in PBS prior to use or characterization. These hydrogels were used as uniform soft controls. To fabricate substrates with stiffness patterns, polymerized hydrogels were incubated in solutions of 0.05 wt% Irgacure 2959 (BASF, Overland Park, KS) photoinitiator and 200 μM methacrylated rhodamine (Polysciences, Inc., Warrington, PA) in PBS for 30 min at 37 °C. Custom 24,500 DPI photomasks (CAD/Art Services, Bandon, OR) were then overlaid on the gel surface followed by immediate exposure to 320−500 nm collimated UV light at an intensity of 10 mW/cm^2 for 4 min using an Omnicure S1500 (Excelitas Technologies, Waltham, MA). Gels were thoroughly rinsed with PBS prior to cell studies to remove excess photoinitiator and unreacted methacrylated rhodamine. Uniform stiff control hydrogels were fabricated by substituting the patterned photomask with a clear film of the same material.

Atomic Force Microscopy

Hydrogel elastic moduli of uniform gels were measured using an Asylum MFP-3D (Asylum Research, Santa Barbara, CA) AFM in contact mode at locations distributed throughout the gel surface. Elastic moduli of 50 and 100 μm patterned gels were measured in 10 μm increments over 100 or 200 μm distances, respectively, perpendicular to stiffness

interfaces. The gel surface was indented with a 1.0 μm diameter spherical silicon dioxide particle on a silicon nitride cantilever with a manufacturer precalibrated spring constant of 0.06 N/m (Novascan Technologies, Ames, IA) *(263)*. The resulting force vs. indentation curves were fit to the Hertz model assuming a Poisson's ratio of 0.5 to extract the Young's modulus using the Asylum software *(264)*. Measurements taken at the interface point were excluded from the mean stiffness values calculated for the soft and stiff patterned regions.

Patterned Hydrogel Characterization

Stiffness pattern fidelity was assessed using a Zeiss LSM700 microscope using a 10x objective and the 568 nm excitation laser line to visualize the covalently bound rhodamine fluorophore in the stiffened gel regions. Color intensity profiles to distinguish soft and stiffened gel regions were obtained using ImageJ software (National Institutes of Health, Bethesda, MD). To visualize gel topographical features, phase contrast images of patterned hydrogels were acquired using a Zeiss Axio Observer.Z1m microscope using a 10x objective. For gel topography measurements, gels were incubated overnight at room temperature in 10 μM, 40 kDa FITC-dextran (Sigma Aldrich, St. Louis, MO) in PBS, and XZ confocal z-slices were acquired using a Zeiss LSM700 microscope using a 40x objective and the 488 nm excitation laser line. The distance between the highest and lowest z-positions at the gel surface within each field of view were measured using ImageJ. Because the width of the stripe pattern exceeded a single field of view, tile scans combining 5 images were used.

Cell Culture

Bovine aortic endothelial cells (VEC Technologies, Rensselaer, NY) from passages 7−12 were used. Cells were maintained in Medium 199 (Invitrogen, Carlsbad, CA) supplemented with 10% Fetal Clone III serum (HyClone, Logan, UT), 1% MEM amino acids (Invitrogen), 1% MEM vitamins (MedTech, Manassas, VA), and 1% penicillin−streptomycin (Invitrogen) at 37 °C and 5% CO_2.

Immunofluorescence

Endothelial cells were fixed with 3.2% paraformaldehyde (Electron Microscopy Sciences, Hatfield, PA) and permeabilized with 1% Triton (VWR, Radnor, PA). For focal adhesion studies, a mouse monoclonal vinculin primary antibody (Santa Cruz Biotechnology, Dallas, TX) and an Alexa Fluor 488 donkey antimouse secondary (Invitrogen) were used. Confocal z-stack images were acquired using a LSM700 microscope equipped with a 40x objective and the 488 nm and 568 excitation laser lines to visualize vinculin and the rhodamine marked stiffness patterns, respectively. For subconfluent monolayer studies, actin was visualized with Alexa Fluor 488 conjugated phalloidin (Invitrogen). Images were captured using a LSM700 microscope equipped with a 20x objective and the 488 nm and 568 excitation laser lines to visualize actin and the rhodamine marked stiffness patterns, respectively. For confluent monolayer studies, a goat polyclonal VE-cadherin primary antibody (Santa Cruz Biotechnology) was used with an Alexa Fluor 488 donkey antigoat secondary antibody (Invitrogen). Actin was visualized using Alexa Fluor 350 phalloidin (Invitrogen). Fluorescent images were captured using a Zeiss Axio Observer.Z1m microscope with a 20x objective.

Quantification of Focal Adhesion Length and Area

Focal adhesion length and area were quantified as described previously *(258)*. Briefly, confocal z-stack images of endothelial cells stained for vinculin and the rhodamine labeled stiffness patterns were captured. Vinculin images were converted to maximum intensity z-projections and subjected to an adaptive Wiener filter, a top-hat filter, and a median filter to extract focal adhesion structures using MatLab. Maximum intensity z-projections of the stiffness pattern images were converted to binary images to create a mask of the stiff hydrogel areas. The pattern mask was multiplied by the extracted focal adhesion image to quantify structures on the stiff substrate regions. To quantify focal adhesions on the soft substrate regions, a soft pattern mask was obtained from the complement image of the stiff pattern mask and multiplied by the extracted focal adhesion image.

Quantification of Monolayer Intercellular Gap Size

Intercellular gap size was quantified using ImageJ software and corresponding fluorescent images of VE-cadherin, actin, and the substrate stiffness pattern. Areas of endothelial cell−cell junction disruption were identified using the VE-cadherin images, and the corresponding actin image was used to trace and measure the gap area. The corresponding stiffness patterned image was used to identify the location of the monolayer disruption.

Statistics

Statistical analysis was conducted using GraphPad Prism, version 6.0d. All data in graphical form are presented as the mean ± standard error of the mean, and all numerical

values in the text are presented as the mean ± standard deviation. Statistical significance was evaluated using analysis of variance (ANOVA) with a Tukey's Honestly Significant Difference (HSD) test for AFM and monolayer data. Two-tailed Student's t-tests were used for focal adhesion data. Statistical significance was considered with a p-value <0.05. All images are representative of a minimum of 3 replicate studies.

3.4 Results

Hydrogel Fabrication and Photopatterning Approach

To create substrates with stiffness heterogeneity, hyaluronic acid based hydrogels that had been modified to contain methacrylate groups on the polymer backbone were synthesized. Briefly, the addition of methacrylates permitted the synthesis of hyaluronic acid hydrogel substrates using a simple, two-step sequential crosslinking method, where a portion of the methacrylates were first crosslinked by a Michael-type addition reaction with DTT followed by radical polymerization using a photoinitiator and UV light *(171)*. To create spatial stiffness patterns, high resolution photomasks were overlaid on the gel during the radical polymerization to spatially control UV light exposure and stiffening. Three photomask patterns were designed to vary the presentation of matrix stiffness heterogeneity: 50 by 50 μm checkerboard squares, 100 by100 μm checkerboard squares, and 500 μm stripes (Figure 3.2).

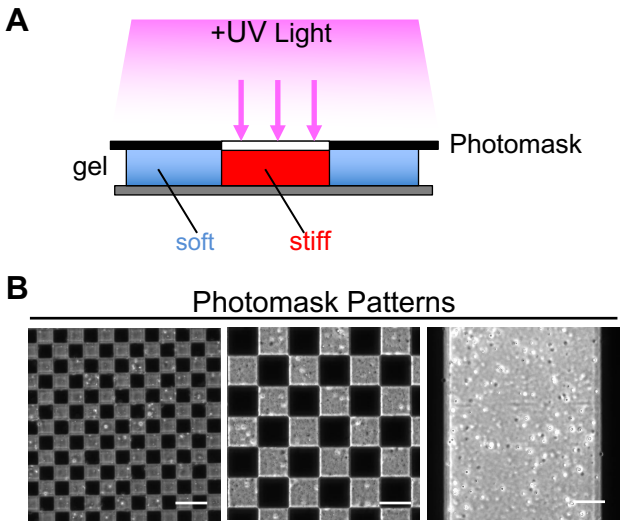

Figure 3.2. Photopatterning approach. (A) Methacrylated hyaluronic acid hydrogels were photopatterned to create substrates with stiffness heterogeneity. (B) Photomasks with 50 by 50 μm squares, 100 by 100 μm squares, and 500 μm stripes were used to control the gel regions exposed to UV light and crosslinked; scale bar = 100 μm.

Stiffness Patterned Hydrogel Characterization

Base hydrogels containing an RGD cell-binding motif were fabricated at an initial gel stiffness of 2.2 ± 0.7 kPa to maintain physiological relevance and approximate the Young's modulus of 2.7 ± 1.1 kPa that has been reported for the healthy bovine intima *(172)*. Precise regions of the hydrogel substrates were then stiffened with exposure to 4 min of UV light through the photomask patterns. A clear photomask was used to fabricate uniform stiff control gels. Prior to UV cross linking, the gels were incubated with 200 μM methacrylated rhodamine. The rhodamine covalently incorporated into the hydrogel backbone only in regions where gel-stiffening radical polymerization had occurred and allowed for stiffness pattern visualization using fluorescence microscopy *(261)*. Gel stiffening to 18.5 ± 2.9 kPa was confirmed using atomic force microscopy to measure the Young's moduli of uniform control and UV stiffened gels (Figure 3.3A). Prior rheological characterization

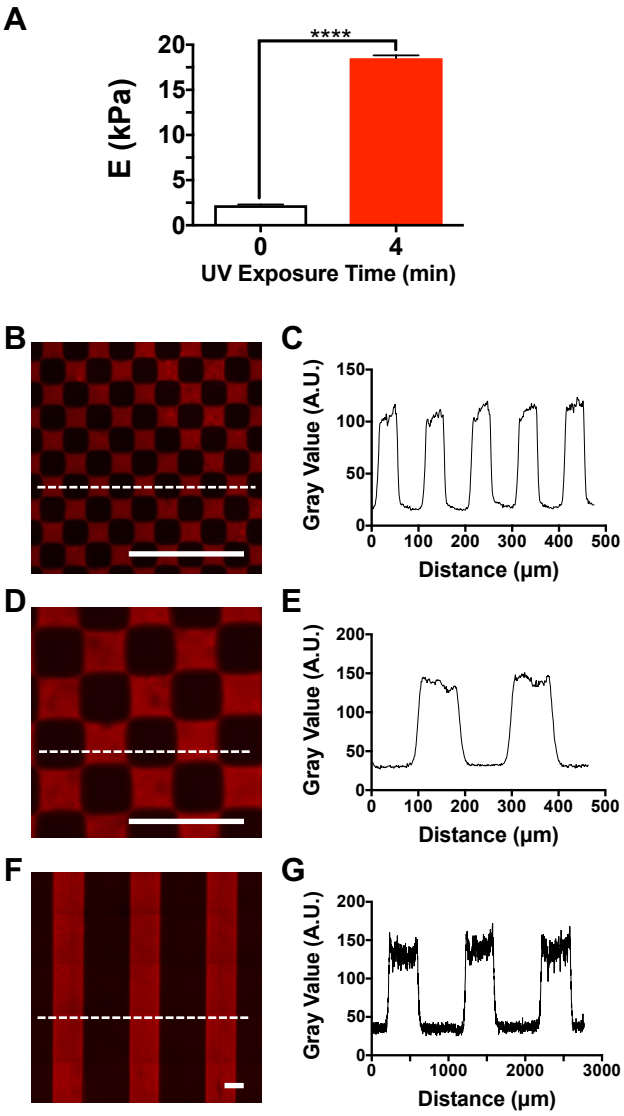

Figure 3.3. Characterization of gel stiffening and pattern fidelity. (A) Atomic force microscopy measurements of hydrogel Young's moduli in uniform control and UV stiffened gels (n = 3, 70−77 indentations per condition). Representative confocal images of the hydrogel stiffness patterning where rhodamine (red) was covalently bound to the gel backbone after radical polymerization in stiffened regions for the (B) 50 μm square, (D) 100 μm square, and (F) 500 μm stripe patterns. Color intensity profiles of the confocal images at the white line demonstrated the photopattern feature size was conserved when transferred to the gel for (C) 50 μm square, (E) 100 μm square, and (G) 500 μm stripe patterns. Data are presented as the means ± standard error of the mean; ****$p < 0.0001$; scale bar = 250 μm.

demonstrated no change in loss modulus (G″) was accompanied by an increase in storage modulus after UV stiffening (G′) *(171)*. Confocal imaging of the methacrylated rhodamine conjugated hydrogels and color intensity profiles revealed high pattern fidelity across all the patterns and conservation of the photomask feature sizes (Figures 3.3B-G).

Noting that increased network crosslinking affected gel swelling, the effect of stiffness patterning on hydrogel surface topography was evaluated. Stiffened regions of the gels exhibited decreased swelling, and topographical features were visible using phase-contrast imaging (Figure 3.4A,C,E). No cracks or gel separation at interface regions were found in any of the stiffness patterned substrates. To quantify the swelling behavior of the patterned hydrogels, the substrates were saturated with a FITC-dextran solution, and confocal XZ slices were obtained to measure the maximum change in Z height for each pattern within a single field of view (Figure 3.4B,D,F). Gel swelling increased with pattern size, and the gel surface height varied by 4.5 ± 2.6 μm, 6.7 ± 3.5 μm, and 37 ± 7.0 μm for the 50 μm square, 100 μm square, and 500 μm stripe patterns, respectively (Figure 3.4G). Because topographical surface cues can also influence cell behaviors and cannot be decoupled from the stiffness patterned substrate, the remainder of the study focused on the substrates patterned with 50 and 100 μm squares of stiffness heterogeneity where minimal surface swelling was detected *(265)*.

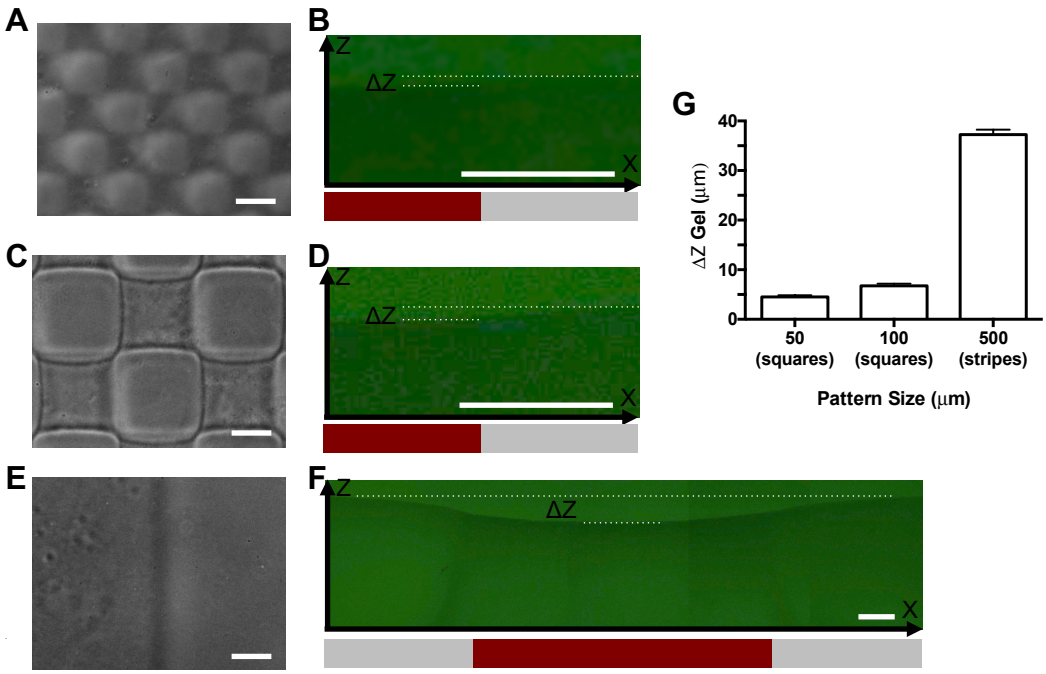

Figure 3.4. Characterization of stiffness patterned hydrogel topography. Representative phase-contrast images of patterned hydrogels revealed gel surface topography caused by decreased swelling in stiffened regions for the (A) 50 μm square, (C) 100 μm square, and (E) 500 μm stripe patterns. Topographical features were quantified using XZ confocal scans of FITC dextran saturated gels to measure the maximum change in Z height for the (B) 50 μm square, (D) 100 μm square, and (F) 500 μm stripe patterns in a single field of view. The red bar indicates stiffened gel regions. (G) Changes in gel surface height increased with stiffness pattern feature size (n = 3, 50−60 fields of view). Data are presented as the means ± standard error of the mean; scale bar = 50 μm.

De-swelling behavior caused by increased matrix crosslinking that began at stiffness interfaces and reached minima in the pattern centers indicated possible stiffness variation within the photocrosslinked gel regions. Starting at an interface, AFM stiffness measurements were collected at 10 μm intervals along a perpendicular line across soft and stiff gel regions (Figure 3.5A, B). Minimal variation in stiffness was measured in soft gel regions for both the 50 and 100 μm square patterned gels, and the mean Young's moduli of 2.7 ± 0.7 of the soft patterned regions was not significantly different when compared to uniformly soft control gels (Figure 3.5C). Despite a uniform rhodamine signal which only

identified UV crosslinked regions and not the extent of crosslinking, stiffened gel areas exhibited spatial stiffness variation. Gel stiffness in UV crosslinked regions increased with increasing distance away from the stiffness interface, and maxima occurred in the pattern centers. These data are consistent with the surface topography data where maximal de-swelling also occurred in the pattern centers. A much smaller interface effect was present within the 50 μm stiffness patterned region compared to that of the larger 100 μm pattern but may be partially explained by the lateral measurement sensitivity where 5 measurements were collected for the smaller pattern compared with 10 for the larger pattern size. Although spatial characterization across soft and stiffened gel regions indicated that abrupt stepwise stiffening did not occur at pattern edges, increased stiffening still occurred over the length scale of an individual endothelial cell. Average stiffness in the photocrosslinked patterned regions significantly increased to 10.3 ± 3.9 compared to that of the soft gel regions (Figure 3.5C). Stiffened regions of the patterned substrates had lower mean stiffness when compared to that of uniformly stiff control gels (Figure 3.4C). The large standard deviation in the Young's modulus of the stiffened gel areas resulted from the spatial variations in stiffness, especially near the interface regions.

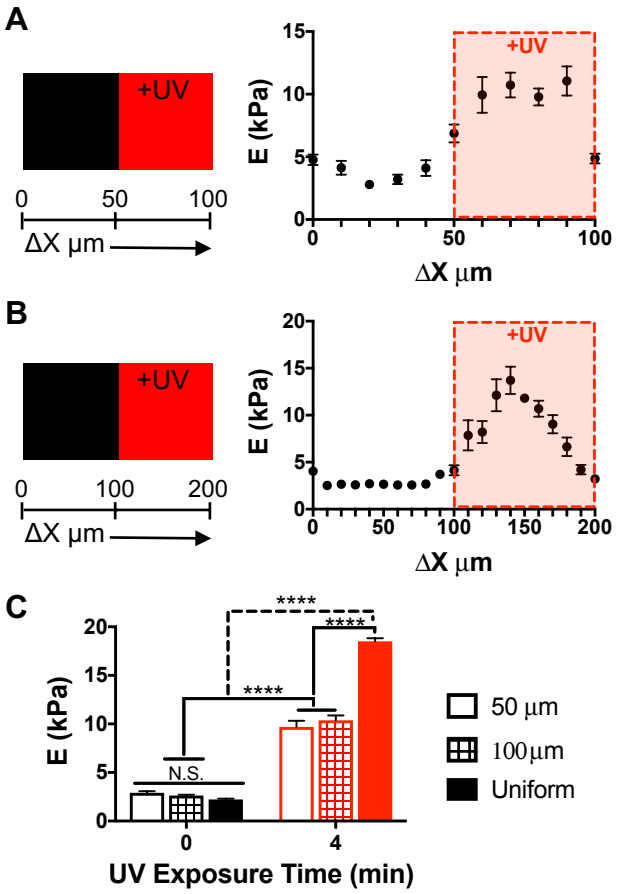

Figure 3.5. AFM mechanical characterization of 50 and 100 µm square stiffness patterned hydrogels. Gel stiffness was measured at 10 µm increments beginning at a stiffness interface across soft and stiff gel regions on (A) 50 and (B) 100 µm square stiffness patterned gels (n = 3, 10 interface regions per condition). (C) Average hydrogel stiffness increased in UV stiffened regions when compared to soft gel regions on the patterned and uniform substrates (n = 3, 40−90 indentations per condition). Data are presented as the means ± standard error of the mean; ****$p < 0.0001$.

Focal Adhesions Localize to Stiff Regions on Substrates Containing Subcellular Matrix Stiffness Heterogeneities

Previous studies have demonstrated that an individual cell spanning a single substrate stiffness interface can sense and respond to the mechanical cues of their matrix by locally altering traction forces *(175)*. Therefore, the integration of more complex substrate

mechanical cues, such as an endothelial cell spanning multiple matrix stiffness interfaces, was investigated. Because focal adhesions are mechanosensitive complexes that link cell-ECM interactions to the cytoskeleton and are incorporated in feedback loops where increased traction forces are generated in response to increased matrix stiffness, focal adhesion formation was used as a readout of matrix stiffness sensing *(192)*. Bovine aortic endothelial cells on 50 and 100 μm checkerboard patterned hydrogels were stained with vinculin to evaluate focal adhesions and compared to cells grown on uniformly soft and stiff hydrogels (Figure 3.6). On the uniformly soft matrices (2.2 ± 0.7 kPa), focal adhesions were small and sparse, while on the uniformly stiff matrices (18.5 ± 2.9 kPa), mature focal adhesions were greater in both size and number. Notably, in endothelial cells on the hydrogels patterned with matrix stiffness heterogeneity, focal adhesion localization was dependent on the underlying matrix stiffness. Mature focal adhesions were found on the stiff substrate regions (10.3 ± 3.9 kPa) and were largely absent in areas where the cell body was adhered to a soft matrix (2.7 ± 0.7 kPa). In addition to localization, focal adhesion length and area significantly increased on stiff matrix regions in cells adhered across stiffness interfaces and further indicated subcellular matrix stiffness sensing (Figure 3.6D,E).

Figure 3.6. Endothelial cell focal adhesion localization and size were dependent on subcellular matrix stiffness. Representative confocal images of endothelial cells stained for vinculin to visualize focal adhesions on (A) uniform control, (B) 50 μm square, and (C) 100 μm square patterned gels. Focal adhesion (D) length and (E) area within a single endothelial cell significantly increased on stiffened matrix regions for both the 50 and 100 μm patterns (n = 3, 24−33 cells per condition). White dashed lines indicate stiffness pattern boundaries, and stiffened regions of the gel are red. Data are presented as the means ± standard error of the mean; $^{**}p < 0.01$, $^{*}p < 0.05$; scale bar = 50 μm.

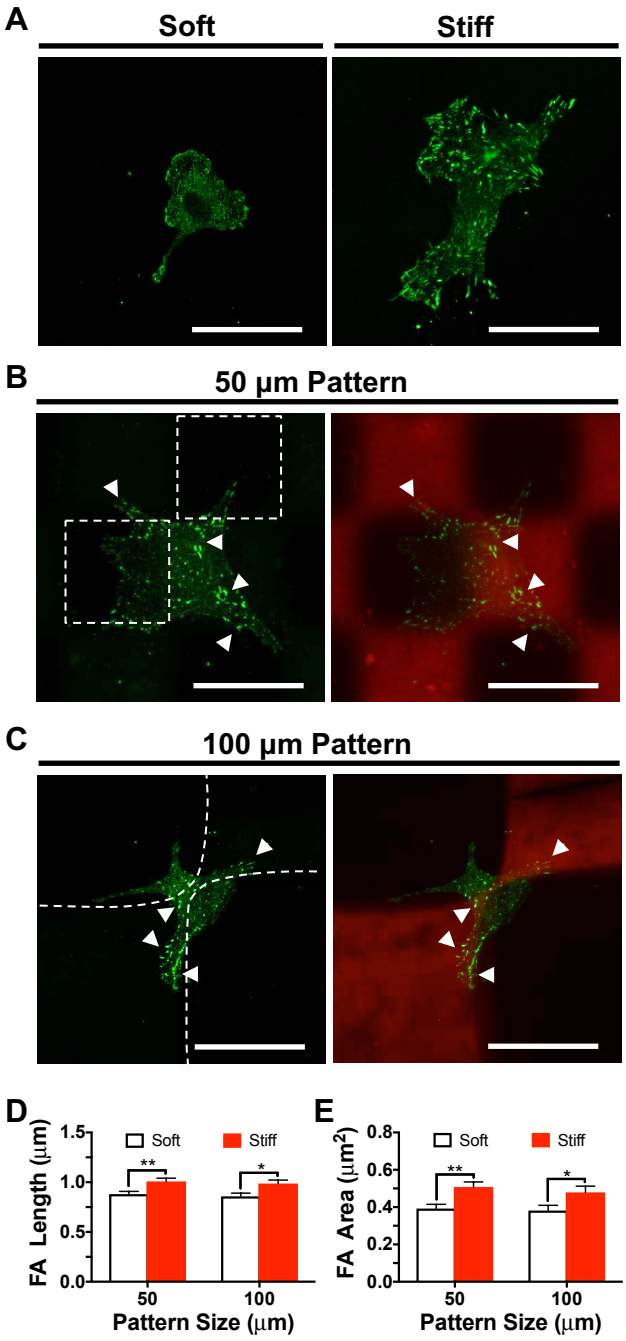
A
Soft
Stiff
B
50 μm Pattern
C
100 μm Pattern
D
FA Length (μm)
1.5
1.0
0.5
0.0
Soft
Stiff
**
*
50
100
Pattern Size (μm)
E
FA Area (μm²)
0.8
0.6
0.4
0.2
0.0
Soft
Stiff
**
*
50
100
Pattern Size (μm)

Endothelial Monolayer Formation and Junction Integrity is Disrupted by Spatial Matrix Stiffness Heterogeneity

In vivo, endothelial cells lining the arterial intima exist as a monolayer, and cell−cell junction integrity is paramount to preventing cholesterol flux into the arterial wall where it can initiate atherosclerotic plaque formation. Therefore, the effect of spatial matrix stiffness heterogeneity on endothelial monolayer formation and integrity using the patterned hydrogel substrates was investigated. During monolayer growth, subconfluent endothelial cells preferentially grew on regions of stiff matrix, while cell growth on the soft regions was dramatically reduced (Figure 3.7).

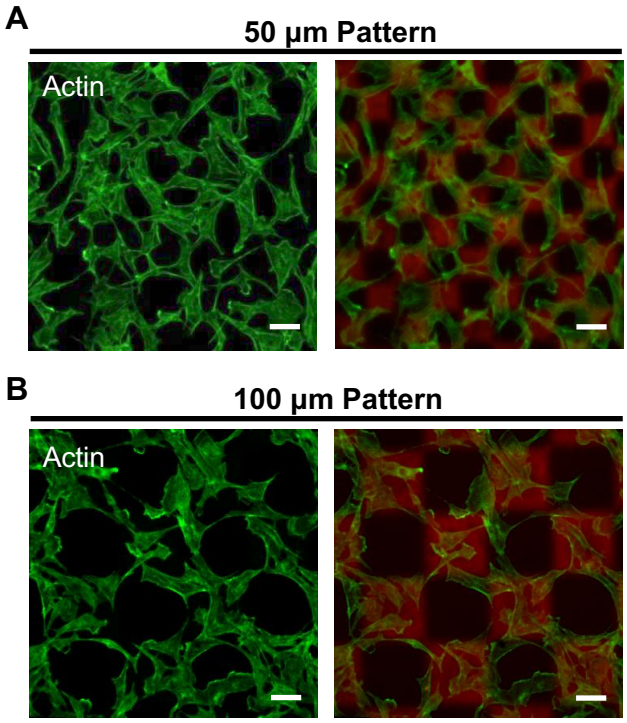

Figure 3.7. Endothelial cells preferentially grew on stiff matrix regions during monolayer formation. Representative confocal images visualizing actin in subconfluent monolayers on (A) 50 and (B) 100 μm square stiffness patterned gels where red areas indicate stiffened gel regions. Scale bar = 50 μm.

These data could have important in vivo implications where circulating debris in the blood can denude the endothelium, and efficient recellularization is important to prevent permeability.

To directly assess the effects of matrix stiffness heterogeneity on endothelium integrity, confluent endothelial monolayers were stained for the cell−cell junctional protein VE-cadherin, and the actin cytoskeleton was visualized with phalloidin. Consistent with our prior studies, on uniformly stiff matrices, VE-cadherin staining revealed disrupted cell−cell junctions and intercellular gaps *(63, 258)*. Increased endothelial cell−cell junction disruption occurred on the heterogeneous stiffness matrices. Average intercellular gap size increased with increasing matrix stiffness heterogeneity when gap area on 50 μm square, 100 μm square, and uniformly stiff patterned substrates was measured (Figure 3.8A). Notably, intercellular gaps on the heterogeneous matrices were significantly greater in area when compared to that of the monolayer disruption that occurred on a uniformly stiff substrate with a greater overall bulk modulus. Intercellular gaps were predominantly located at matrix stiffness interfaces on the 50 μm square patterned substrates but were approximately evenly distributed among soft, stiff, and interface regions on the less heterogeneous 100 μm square patterned substrates (Figure 3.8B). On both of the heterogeneous stiffness substrates, the largest areas of monolayer disruption were found at stiffness interfaces, when compared to those of soft and stiff gel regions (Figure 3.8C-E). The increased intercellular gap size measured at stiffness interfaces and with increased matrix stiffness heterogeneity provides evidence that balancing distinct matrix cues within one cell compromises endothelial monolayer cell−cell junction stability. Cutiongco and

colleagues demonstrated that micron sized surface topographies on hydrogels enhanced endothelial monolayer formation compared to that of planar controls; therefore, although we cannot decouple the topographical surface swelling features characterized in Figure 3.3, we assume matrix stiffness heterogeneities and not the surface topographies are the dominant extracellular matrix cues contributing to endothelial cell−cell junction disruption on the stiffness patterned substrates *(266)*.

Together, our data indicate that endothelial cells are able to sense and respond to subcellular spatial stiffness cues from their substrate and that spatial stiffness heterogeneity in addition to a bulk increase in matrix stiffness disrupts endothelial cell−cell junction integrity.

Figure 3.8. Matrix stiffness heterogeneity disrupted endothelial monolayer junction integrity. Endothelial monolayers were stained for VE-cadherin, and the actin cytoskeleton was visualized with phalloidin. (A) Average intercellular gap area increased with increasing matrix stiffness heterogeneity (n = 3, 10−12 fields of view per condition). (B) Monolayer gaps were found with increased frequency at stiffness interfaces on the 50 μm square stiffness patterned substrates and were evenly distributed among soft, stiff, and interface regions on the less heterogeneous 100 μm square stiffness patterned substrates. Intercellular monolayer gaps found at interface regions were larger when compared to areas of monolayer disruption located at stiff and soft regions on the (C) 50 μm square and (D) 100 μm square stiffness patterned substrates (n = 3, 10−12 fields of view per condition). Representative images of intercellular gaps found at soft, stiff, and interface regions in endothelial monolayers on 50 μm square stiffness patterned substrates. Data are presented as the means ± standard error of the mean; ****$p < 0.0001$, ***$p < 0.001$, **$p < 0.01$, and *$p < 0.05$; scale bar = 10 μm.

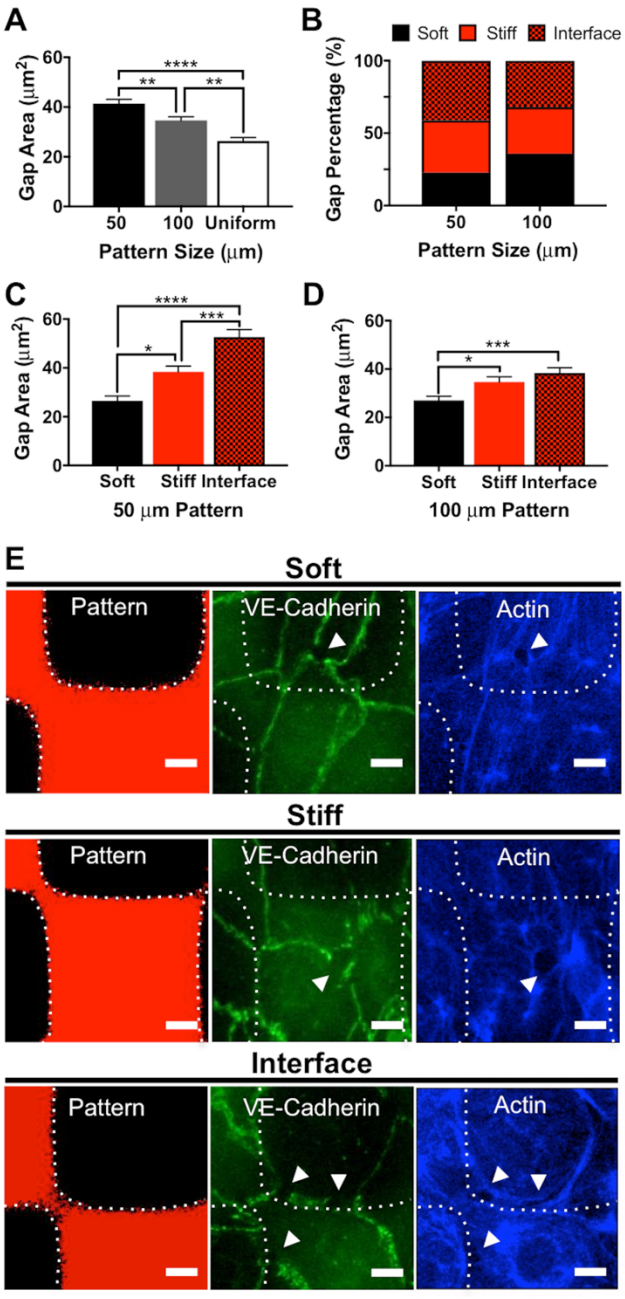
A
Gap Area (μm²)
60
40
20
0
****
**
**
50
100
Uniform
Pattern Size (μm)
B
Soft
Stiff
Interface
Gap Percentage (%)
100
50
0
50
100
Pattern Size (μm)
C
Gap Area (μm²)
60
40
20
0
****
***
*
Soft
Stiff
Interface
50 μm Pattern
D
Gap Area (μm²)
60
40
20
0
***
*
Soft
Stiff
Interface
100 μm Pattern
E
Soft
Pattern
VE-Cadherin
Actin
Stiff
Pattern
VE-Cadherin
Actin
Interface
Pattern
VE-Cadherin
Actin

3.5 Discussion

In this study, we fabricated hyaluronic acid based hydrogels with photopatterned regions of increased crosslinking to study endothelial cell behavior in response to matrix stiffness heterogeneity. The data demonstrate that endothelial cells integrate multiple subcellular matrix stiffness cues and that substrate stiffness heterogeneity disrupts endothelial monolayer junction integrity. Notably, increases in substrate stiffness from 2.7 to 10.3 kPa, which are significantly smaller than the intima stiffness heterogeneity increases that have been measured *ex vivo*, resulted in endothelium disruption and provide compelling evidence that the mechanics of the aged intima may contribute to endothelium permeability and atherogenesis. The ability of extracellular matrix stiffness to influence a diverse array of endothelial cell behaviors including cell spreading, focal adhesion formation, traction forces, and monolayer permeability has been appreciated for some time *(63, 64, 206, 258)*. However, the *in vivo* extracellular matrix of endothelial cells within the arterial intima is more complex than the synthetic uniform stiffness substrates commonly used to study these behaviors *in vitro*. Age-related mechanical heterogeneity within the aorta exists on both the macro- and microscales, and atherosclerotic plaques are associated with regions of increased arterial wall thickness *(122, 267–269)*. Intimal stiffening is a dynamic process that occurs throughout the lifespan, largely due to the combined effects of collagen crosslinking and increased extracellular matrix deposition *(200)*. Developing new *in vitro* substrates to recapitulate the *in vivo* complexity of the arterial intima, such as the stiffness patterned substrates presented here, are important to understanding how age-related intimal stiffening contributes to endothelium disruption and atherogenesis.

Single cell studies have identified many of the molecular mechanisms that underlie the mechanotransduction feedback loops between a cell and extracellular matrix stiffness sensing *(176, 270, 271)*. It is well accepted that environmental sensing through integrin complexes leads to the assembly of nascent focal adhesions, which then undergo force dependent conformational changes to bind F-actin and require RhoA-mediated contractile force generation to mature *(177, 192, 230)*. However, *in vivo*, isolated individual endothelial cells are rare, and most cells exist as part of a collective where both direct cell−cell as well as cell−matrix cues influence cellular behavior. Intercellular interactions are critical for endothelium function, which requires intact adherens junctions mediated by VE-cadherin to maintain a vascular barrier *(11, 256)*. Opposing activation of the GTPases RhoA and Rac1 are associated with stress fiber formation and cytoskeletal rearrangements that promote endothelium disruption or strengthening, respectively *(153, 160, 272)*. Importantly, the cytoskeleton is able to transmit force generated by GTPase activity over long ranges from cell−matrix to cell−cell contacts and from the cell surface to focal adhesions *(188, 273, 274)*. Within cell pairs, it has been demonstrated that RhoA and Rac1 activity affects the tugging force at cell−cell junctions and that traction forces, which are mediated in part by RhoA activity, are directly proportional to the cell−cell junction tension *(187, 188)*. Varying either matrix stiffness or chemistry to alter cell−matrix interactions and consequentially, traction forces, alters the cell−cell force *(187)*. These foundational studies demonstrate the interdependence between matrix cues and cell−cell junction tension. Within endothelial monolayers, both traction stresses and VE-cadherin junction forces increase with matrix stiffness *(210)*. Monolayer traction stresses exhibit spatial variance, and subcellular hotspots of increased traction stress are correlated with high force

fluctuation and intercellular gap formation *(275)*. Here, a localized increase in focal adhesions in subcellular regions of increased matrix stiffness is demonstrated, and endothelial cell−cell junctions in monolayers on a heterogeneously stiff matrix are disrupted, thereby suggesting that matrix mechanical cues may augment traction force hotspots that contribute to endothelium instability and disruption.

A role for aberrant traction forces contributing to endothelium disruption is also supported by work from Cai and colleagues investigating the mechanisms of cytoplasmic coherence where nonmuscle myosin-IIA crosslinks actin filaments to form a mesh networking extending across the cell cytoplasm. The actin network creates a stabilizing contractile force that counterbalances high traction forces located at the cell periphery *(276, 277)*. Within endothelial monolayers, localized cytoskeletal tension has been associated with both endothelial barrier disruption and strengthening. Pharmacological treatment with a barrier disruptive agonist caused concentrated cytoskeletal tension away from the cell periphery, and an opposite shift occurred after treatment with barrier protective agents *(278)*. Because the cytoskeleton transmits force from cell end to end to achieve equilibrium, an important requirement for cytoplasmic coherence is that traction forces located at one side of a cell are symmetrically balanced by opposing forces on the opposite side *(277)*. As already noted, we found that on a heterogeneously stiff matrix, focal adhesion sizes were dependent on the underlying matrix stiffness suggesting that traction force distribution was also altered due to localized matrix mechanical cues and therefore may not meet the symmetrically balanced criteria necessary for cytoplasmic coherence. Indeed, single cell studies on micropillar arrays have demonstrated that matrix rigidity interfaces polarize

traction forces normal to the interface and that sharp increases in cellular forces occur in migrating cells as they cross a soft to stiff boundary *(179)*. On the basis of exaggerated cell membrane spreading and fragmentation that occurred when bulk cell contractility was modulated pharmacologically and the importance of membrane tension for cadherin aggregation, a misbalance of contractile forces and disrupted cytoplasmic coherence may in part explain the disrupted endothelial monolayer junctions observed on stiffness patterned substrates *(277, 279)*.

Parallels between the mechanotransduction machinery used at cell−matrix and cell−cell contacts to anchor to the cytoskeleton suggest a prominent role for cell−cell force transmission in regulating endothelial monolayer behaviors. At focal adhesions, mechanical stretching of talin exposes a vinculin binding site, and similarly force-dependent conformational unfolding of alpha catenin at adherens junctions is necessary for vinculin recruitment to the junctional complex *(177, 191)*. Both focal adhesions and adherens junctions undergo force-dependent strengthening *(230, 280, 281)*. Although it has been known that cadherin complexes at cell−cell junctions are mechanotransducers and that VE-cadherin is an integral part of the mechanosensitive response to fluid shear stress in endothelial monolayers, only recently has VE-cadherin been directly identified as a mechanotransducer *(189, 193, 282)*. Direct force application to VE-cadherin caused global endothelial monolayer remodeling distant from the site of the applied force and demonstrated that force propagation between endothelial cells can disrupt monolayer integrity *(189)*. These results suggest that exogenous cues that cause increased cell−cell junction tension across VE-cadherin, can have global ramifications on endothelial cell−cell

monolayer integrity. Consistent with this finding, and noting that matrix stiffness alters traction stresses and cell−cell junction tension, our data indicate that localized matrix stiffness heterogeneity may contribute to aberrant VE-cadherin forces to disrupt cellular junction integrity.

The molecular mechanisms underlying force-dependent endothelial cell−cell junction maintenance and disruption continue to be elucidated; however, an overlap in important cytoskeletal regulatory proteins found at both focal adhesions and cell−cell junctions suggest a necessary role for spatial and temporal regulation *(194, 196, 270)*. It has recently been identified that vinculin localization to focal adhesions or cell−cell junctions is associated with endothelial barrier disruption or enhancement, respectively *(195)*. Increased matrix stiffness that contributes to the recruitment of shared proteins to form focal adhesions at the cell−matrix interface likely alters cell−cell adhesion dynamics. Future studies should modulate matrix heterogeneity with respect to feature size and stiffness magnitude to develop an increased understanding of the matrix mechanical cues and molecular mechanisms that are most critical to endothelium integrity.

3.6 *Conclusion*

Hyaluronic acid hydrogels with regions of patterned stiffness were fabricated to study the endothelial cell response to matrix stiffness heterogeneity. Focal adhesions were localized in regions of increased subcellular stiffness and increased matrix stiffness heterogeneity disrupted endothelial monolayer cell−cell junctions. Although bulk increases in matrix stiffness have been shown to increase the force at intercellular junctions and disrupt

endothelial monolayers, to our knowledge, our data is the first to show that the spatial presentation of matrix mechanical cues in addition to the magnitude of matrix compliance disrupts cell−cell junctions *(63, 187)*. Because intima stiffness heterogeneity increases with age, our findings have important clinical implications for understanding the mechanisms that contribute to age-related atherosclerosis.

CHAPTER 4

ADDITIONAL DATA

In addition to the data that resulted in peer-review manuscripts, there was a substantial amount of work invested into notable side projects, that ultimately were not pursued further. This chapter will discuss the motivation, methods, results, and conclusions for two of those studies.

4.1 Effects of Temporal Matrix Stiffening on Endothelial Cell Monolayers

Motivation

Cardiovascular diseases are a leading cause of death worldwide and account for 17.5 million deaths annually *(283)*. Atherosclerosis is often an underlying pathology that contributes to cardiovascular diseases and age-related arterial stiffening on the cellular scale has been recognized as a mechanical cue that compromises endothelial barrier function, an initiating step in atherosclerosis development *(2, 63, 210)*. As the stiffness of their extracellular matrix increases, endothelial cells lining the arterial lumen exhibit increased contractility leading to the disruption of cellular junctions and increased permeability *(63, 210)*. Importantly, while the importance of artery stiffness is already recognized clinically where is it used as a marker of morbidity and mortality, mounting evidence indicates that increased arterial stiffness precedes cardiovascular pathologies and contributes to their development *(77, 140)*. Understanding the endothelial cell response to temporal stiffening of the subendothelial matrix, which occurs over the lifespan may

provide important insights into the development of a compromised endothelial barrier and the prevention of atherosclerosis *(200)*.

Within the vasculature, endothelial cells reside in a highly dynamic mechanical microenvironment. Because of their location, extracellular matrix cues, hemodynamic shear and pulsatile forces from blood flow, and cyclic strain from artery contraction and relaxation are integrated into endothelial cell responses *(284)*. These cues can vary throughout the lifespan and based on location within the vasculature. Indeed, arterial compliance decreases with age and hemodynamic forces are varied throughout the arterial tree *(7, 285)*. Endothelial cells exhibit an adaptive response to fluid shear stress that includes signaling cascades and cytoskeletal reorganization that can promote or protect against atherogenesis, suggesting that an adaptive response to other mechanical cues, namely subendothelial matrix stiffening that occurs with age, may be integral to atherogenesis *(282, 286, 287)*. Current *in vitro* models to study the effects of matrix stiffness on endothelium integrity rely on static synthetic substrates, primarily polyacrylamide gels or micropillar arrays to modulate mechanics. The aim of this project was to employ a cell compatible hydrogel system that dynamically stiffened by radical crosslinking to investigate the presence of an adaptive endothelial cell response to temporal matrix stiffening and its effect on endothelial monolayer integrity.

Initial stages of the project included synthesizing a methacrylated hyaluronic acid polymer and fabricating hydrogel substrates for endothelial monolayer cell studies. The hydrogel substrate mechanics before and after UV initiated radical crosslinking were characterized.

Gel fabrication parameters were optimized to achieve an initial gel stiffness that approximated the measured Young's modulus for the healthy bovine subendothelial matrix and to maximize the covalent incorporation of an RGD cell-binding motif. Cell viability and morphology studies before-and-after *in situ* substrate stiffening with a photoinitiator and UV light were then completed to validate the system. The project was discontinued after the deleterious effects of free radicals generated to stiffen the matrix by photocrosslinking could not be overcome and persisted with two different photoinitiators.

Methods

Methacyrlated hyaluronic acid synthesis

Methacrylated hyaluronic acid (MeHA) polymer was synthesized as previously described *(171, 262)*. A 1 wt% solution of sodium hyaluronate (51 kDa, Lifecore Biomedical, Chaska, MN) in DI water was reacted with methacrylic anhydride (Sigma-Aldrich, St. Louis, MO) at a ratio of 2. 4 mL methacrylic anhydride per gram of HA on ice at pH 8 for 8 h. The reaction mixture was maintained at 4 °C overnight followed by the addition of 1.2 mL of methacrylic anhydride per gram HA on ice at pH 8.0 for 4 h. The synthesized product was dialyzed against DI water (6−8 kDa MWCO, SpectraPor, Rancho Dominguez, CA) and lyophilized. The synthesized product was confirmed by ^{1}H NMR (600 MHz Varian).

Cell Culture

Bovine aortic endothelial cells (VEC Technologies, Rensselaer, NY) from passages 7−12 were used. Base Medium 199 (Invitrogen, Carlsbad, CA) was supplemented with 10% Fetal Clone III serum (HyClone, Logan, UT), 1% MEM amino acids (Invitrogen), 1%

MEM vitamins (MedTech, Manassas, VA), and 1% penicillin−streptomycin (Invitrogen). Cells were maintained at 37 °C and 5% CO_2 and passaged at confluence.

MeHA Gel Fabrication

MeHA hydrogels were synthesized as already described *(171, 261)*. Briefly, 3% MeHA was dissolved in 0.2 M triethanolamine (Sigma Aldrich, St. Louis, MO) in PBS. A custom RGD peptide for cell attachment, GCGRGDSPG (Genscript, Piscataway, NJ) was added to the polymer solution at a final concentration of 1 mM and reacted for 45 min with continuous vortexing. The triethanolamine buffer pH was optimized to increase the reaction of the RGD peptide with the polymer backbone. Gels were polymerized between a glutaraldehyde functionalized bottom glass coverslip and an untreated top coverglass by Michael-type addition using dithiothreitol (DTT) (Sigma-Aldrich, St. Louis, MO). Hydrogels were incubated overnight at room temperature in PBS prior to use or characterization. For cell studies, the gels were sterilized with a germicidal lamp for 30 minutes followed by cell seeding. Control cell studies with a static substrate were conducted on coverglass coated with 0.1 mg/mL rat tail type I collagen (BD Biosciences, San Jose, CA).

To dynamically stiffen the gels, polymerized hydrogels with endothelial cells grown to confluence were incubated in solutions of 0.05wt% Irgacure 2959 (BASF, Overland Park, KS) photoinitiator in M199 with supplements for 30 min at 37 °C. The gels were then individually exposed to 320−500 nm collimated UV light at an intensity of 10 mW/cm^2 using an Omnicure S1500 (Excelitas Technologies, Waltham, MA) *(171)*. Gels were

immediately rinsed 3 times with PBS, followed by an additional media change 30 minutes after the reaction to remove any remaining photoinitiator or free radical products. For lithium acylphosphinate (LAP) studies, a 0.067 wt % working solution (2.2 mM) in M199 with supplements was used. Gels were incubated with the photoinitiator solution in complete media for 30 min at 37 °C followed by exposure to 470 or 320-500 nm collimated UV light at an intensity of 10 mW/cm^2 using the Omnicure S1500 *(288)*. UV stiffened MeHA gels without cells were used for mechanical characterization studies.

Steel Ball Mechanical Testing

Preliminary measurements of hydrogel elastic moduli were measured using the steel ball method as described previously *(289)*. Prior to polymerization, 0.5 μm polystyrene fluorescent beads (Invitrogen, Carlsbad, CA) were added to the gel solution. To measure hydrogel elastic modulus, steel balls (Abbott Ball Co., West Hartford, CT) with a radius of 0.32 mm and a density of 7,200 kg/m^3 were then dropped onto the gel surface. A LSM700 microscope with a 10x objective was used to locate the fluorescent bead field at the gel surface directly beneath the ball and the z-height was recorded. A magnet was then used to remove the steel ball and the surface bead field was re-located. The ball indentation depth was calculated from the change in z-height between the two bead fields and the gel elastic modulus was extracted using the Hertz model for spherical contact where a buoyancy corrected weight of the steel ball and a hydrogel Poisson's ratio of 0.5 was assumed.

Atomic Force Microscopy

Hydrogel elastic moduli were measured using an Asylum MFP-3D (Asylum Research, Santa Barbara, CA) AFM in contact mode at random locations distributed throughout the gel. Force vs. indentation curves were acquired by indenting the gel surface with a 1.0 μm diameter spherical silicon dioxide particle on a silicon nitride cantilever with a manufacturer precalibrated spring constant of 0.06 N/m (Novascan Technologies, Ames, IA) and fit to the Hertz model *(263)*. A Poisson's ratio of 0.5 was assumed and the Young's moduli were extracted using the Asylum software *(264)*.

Live/Dead Viability Assay

Cell viability was assessed using a commercial Live/Dead Viability Assay according to the manufacturer recommended protocol (Invitrogen, Carlsbad, CA). Briefly, ethidium homodimer-1 and calcein AM stocks were combined in sterile PBS to final concentrations of 4 μM and 2 μM, respectively. Cells were washed twice with sterile PBS and incubated with the reagent solution for 30 minutes at 37 °C and 5% CO_2. Cells were then rinsed with PBS and complete media, followed by immediate fluorescence imaging using a Zeiss Axio Observer.Z1m microscope.

Statistics

GraphPad Prism version 6.0d (La Jolla, CA) was used to conduct all statistical analysis. (ANOVA) with a Tukey's Honestly Significant Difference (HSD) test was used to evaluate

statistical significance and significance was considered with a p-value <0.05. Data in graphical form are presented as the means ± standard error of the mean.

Results

The synthesis of methacrylated hyaluronic acid (MeHA) polymer was confirmed by ^{1}H NMR characterization (Figure 4.1).

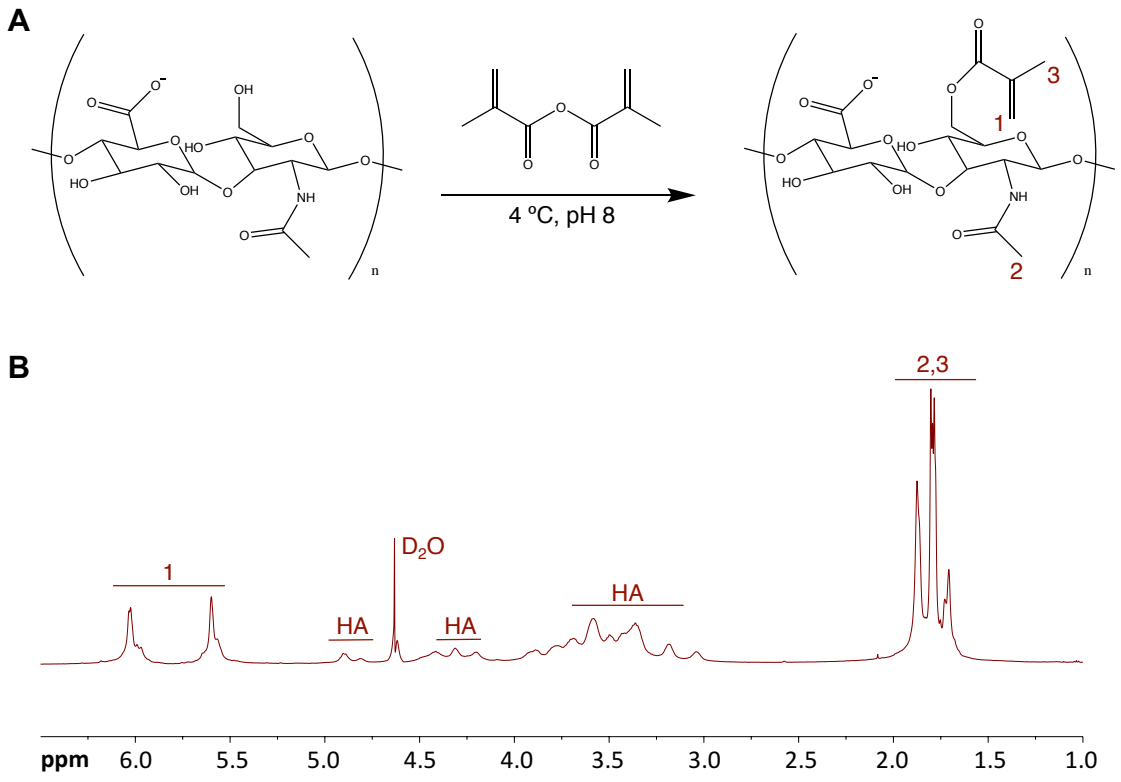

Figure 4.1. Methacrylated hyaluronic acid synthesis and ^{1}H NMR spectrum. (A) Methacrylated hyaluronic acid was synthesized and (B) confirmed by ^{1}H NMR. Spectrum peaks correspond to MeHA polymer features indicated in (A): (1) methacrylate protons, and (2,3) free methyl protons.

The synthesized polymer was then used to fabricate hydrogel substrates that were initially polymerized by a Michael-type addition reaction with dithiothreitol (DTT) followed by

sequential radical crosslinking *in situ* to increase the gel elastic modulus. Gel crosslinking occurred through methacrylate groups on the MeHA backbone, and thus, initial gel stiffness was modulated by varying the consumption of methacrylates by DTT. (Figure 4.2). A gel with 13 mol% consumption of the available methacrylates that had a Young's modulus of 2.2 ± 0.8 kPa was selected as the base gel for cell studies to match the reported value of 2.7 ± 1.1 kPa for the healthy bovine intima *(172)*.

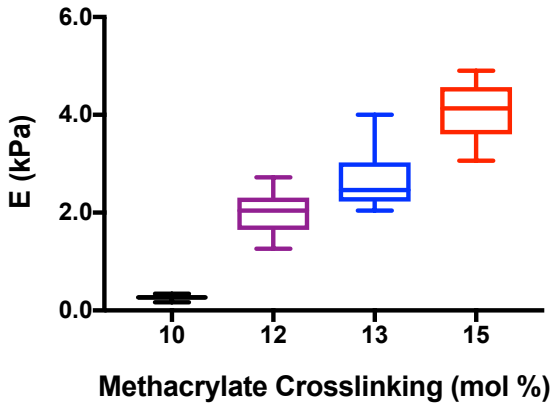

Figure 4.2. Characterization of base MeHA hydrogel elastic modulus. MeHA hydrogel elastic modulus after Michael-type addition polymerization was measured using the steel ball method *(289)*. Gel elastic modulus increased with increasing methacrylate crosslinking.

To create a temporally stiffening substrate, base hydrogels were sequentially stiffened by free radical crosslinking using the photoinitiator I2959 and UV light. UV light cleaved the photoinitiator into two radical components that then reacted with remaining methacrylate groups on the polymer backbone to further crosslink the hydrogel. Hydrogel elastic moduli increased with radical crosslinking, and the stiffness increase was time dependent because free radical generation from the photoinitiator was dependent on the UV light exposure time. The substrates underwent step-wise stiffening when exposed to sequential doses of radical crosslinking treatments, and the final gel elastic modulus was equivalent to a single

UV exposure that matched the cumulative exposure time of the individual treatments (Figure 4.3).

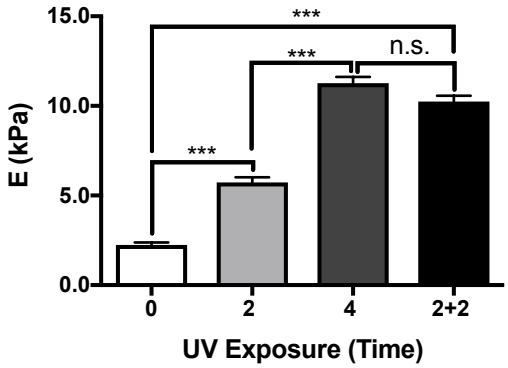

Figure 4.3. MeHA hydrogels exhibited step-wise sequential stiffening by radical crosslinking with the photoinitiator I2959. Polymerized hydrogels were sequentially stiffened by free radical crosslinking using the photoinitiator I2959 and UV light. Gel stiffening increased with increasing UV light exposure and was cumulative over multiple stiffening sessions, ***$p<0.001$.

Surface functionalization was necessary for cell adherence to the hydrogel surface because hyaluronic acid does not engage integrins; therefore, a custom synthesized RGD motif was covalently bound to the MeHA backbone prior to polymerization *(290)*. Initial cells studies were constrained by minimal cell attachment to the hydrogel surface that precluded monolayer growth. When equal seeding densities were used, tissue culture plastic (TCP) controls were confluent while cells on gels where the RGD reaction occurred at pH 9.4 with 1 mM RGD had sparse, poorly spread cells (Figure 4.4 A, D). Increasing the concentration of RGD from 1 mM to 4 mM did not significantly increase cell attachment to the gel surface suggesting that RGD incorporation into the MeHA backbone and not the reactant concentration was limiting cell adherence (Figure 4.4).

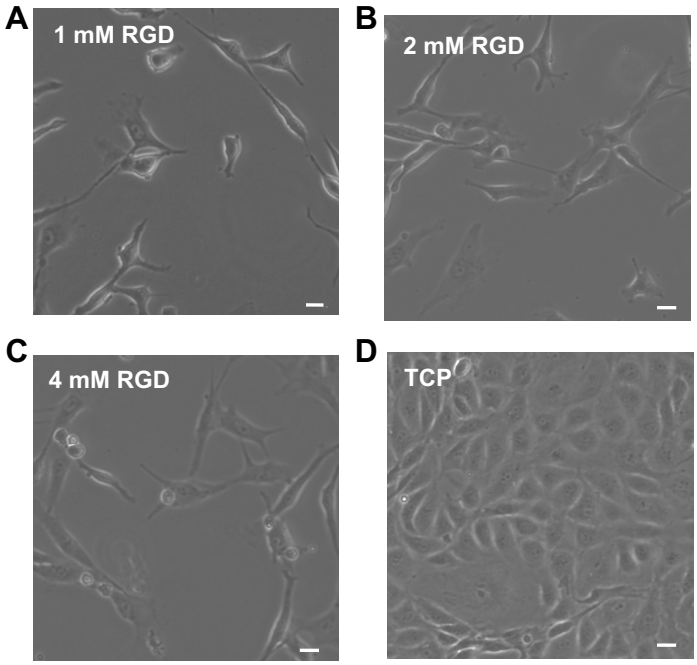

Figure 4.4. Endothelial cell adhesion to the MeHA gels did not increase with increasing RGD concentration. Representative images of low endothelial cell adhesion to the MeHA gel surface that prevented monolayer growth. Increasing the RGD concentration in the gel from 1 to 4 mM while maintaining constant seeding densities did not increase cell binding. Control cells on tissue culture plastic controls (TCP) grew to confluence; scale bar = 20 μm.

The Michael-type addition reaction to conjugate RGD onto the MeHA macromer is pH sensitive and favored under basic conditions; therefore, the reaction pH was varied between 9.4 and 10.5 to select the reaction conditions that resulted in optimal RGD incorporation for monolayer studies (Figure 4.5) *(170)*. A RGD binding reaction at pH 10.25 was determined to be optimal because it yielded a well spread cell morphology and sufficient cell adherence numbers without becoming overconfluent.

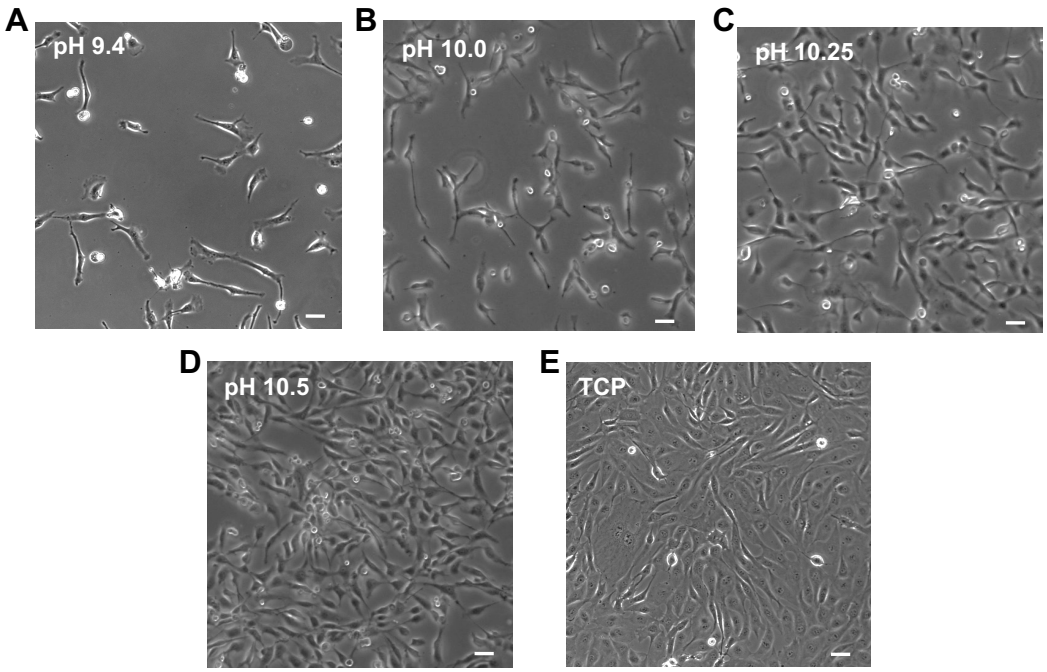

Figure 4.5. Covalent binding of RGD to the MeHA macromer and cell adhesion to the gel surface increased with increasing pH. Representative images of endothelial cells at equal seeding densities with increasing pH reaction conditions to incorporate the RGD cell binding peptide. Cell binding to the hydrogel surface increased with increasing pH and was maximal on tissue culture plastic (TCP) controls; scale bar = 40 μm.

To assess the validity of the methacrylated hyaluronic acid hydrogel system as an *in vitro* method to study the endothelial cell response to temporal substrate stiffening *in situ*, endothelial cells were grown into confluent monolayers on control collagen coated coverglass substrates to determine viability under the radical crosslinking reaction conditions. The monolayers were incubated with I2959 photoinitiator and exposed *in situ* to 2 minutes of UV light, the equivalent reaction conditions to stiffen the MeHA substrates to ~5 kPa (Figure 4.3). Cell health was assessed on the basis of a live/dead assay (Figure 4.6).

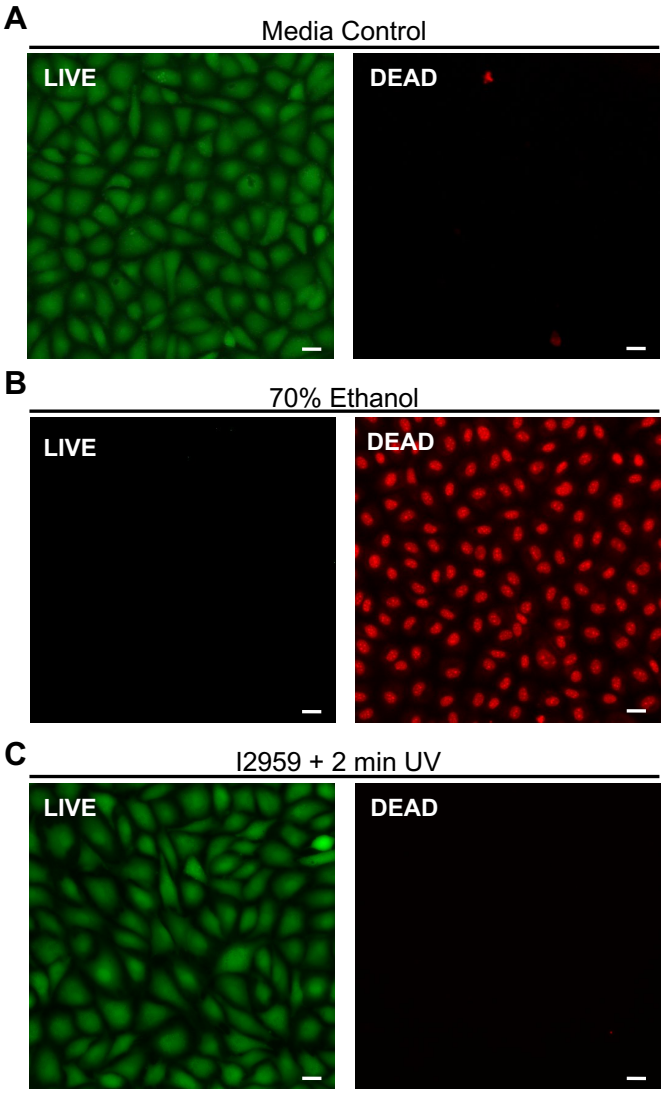

Figure 4.6. Endothelial monolayers exhibited high viability to the radical crosslinking reaction conditions. Representative images of endothelial monolayer viability where green indicates live cells and red indicates dead cells. Media (A) and ethanol controls (B) had nearly 100% live or dead cells, respectively. Endothelial monolayers also had nearly 100% viability after free radical generation with the photoinitiator I2959 and 2 min UV light exposure (C); scale bar = 20 μm.

Notably, although cell viability was high after the UV treatments, cells adopted an elongated morphology on both stiffened MeHA gels and glass controls after just one 2 minute stiffening treatment. An elongated cell morphology ocurred when the UV stiffening treatment was reduced to 1 minute. Cell elongation persisted on control glass substrates in

the presence of the UV-activated photoinitiator. UV light alone, even with repeated exposure periods, did not induce cell morphological changes indicating the elongation was occurring in response to free radical generation and was not a cellular response to increased matrix stiffness (Figure 4.7).

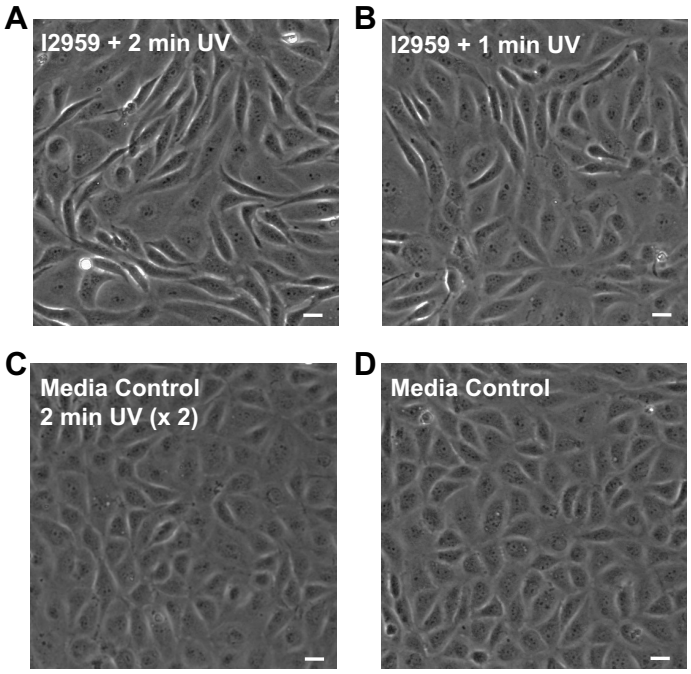

Figure 4.7. I2959 free radical species caused endothelial cell elongation. Representative images of endothelial monolayers on collagen coated coverglass after the radical stiffening reaction conditions. Endothelial cells elongated after free radicals were generated (A,B) but morphology was unchanged with UV light exposure alone (C) when compared to media controls (D); scale bar = 20 μm.

Because radical generation was necessary for the *in situ* gel crosslinking, these data indicated that changes in cell-cell junction dynamics caused by increased matrix stiffness would not occur independently from junction reorganization caused by cell elongation in response to the stiffening process. In addition, the observed change in cell morphology suggested that other cellular processes were likely being affected, thereby limiting the utility of the system.

In an effort to mitigate the effects of free radical generation on the endothelial monolayers, delivering UV light in fractionated exposures was explored, where the both UV exposure time and recovery time between treatments were modulated. The maximum amount of UV exposure for which free radical generation did not cause endothelial cell morphological changes was determined to be 30 s. However, AFM mechanical testing of MeHA hydrogels after 8, 30 s UV stiffening sessions did not detect any measureable increase in gel stiffness, compared to the unstiffened control. These results suggest that a minimum threshold of UV exposure, greater than 30 s, is necessary to cause measureable gel stiffening and that the MeHA platform with I2959 photoinitiator was not suitable for *in situ* substrate stiffening because sufficient matrix stiffening could not be achieved without altering cell morphology.

Because the free radicals generated from the I2959 photoinitiator under UV light were altering cell morphology, an alternative photoinitiator that had also been used with the MeHA gel system for radical *in situ* substrate stiffening was investigated. The photoinitiator lithium acylphosphinate (LAP) can be activated with 470 nm blue visible light which is reported to be less damaging to cells compared to lower wavelength UV light. Importantly, it was tolerated by primary hepatic stellate cells suggesting the system may also be tolerated by primary endothelial cells *(288)*. A bandpass filter was used to isolate 470 nm wavelength light and control monolayers on glass coverslips were exposed to blue light to determine endothelial tolerability to this wavelength of light (Figure 4.8). A 5 minute exposure period was reported to be well tolerated by primary stellate hepatic

cells, but caused significant endothelial cell death (Figure 5.8A). Lower exposure times caused an elongated endothelial cell morphology, similar to what was observed with the I2959 photoinitiator (Figure 4.8B). Collectively, these data indicated that 470 nm wavelength light was damaging to endothelial cells.

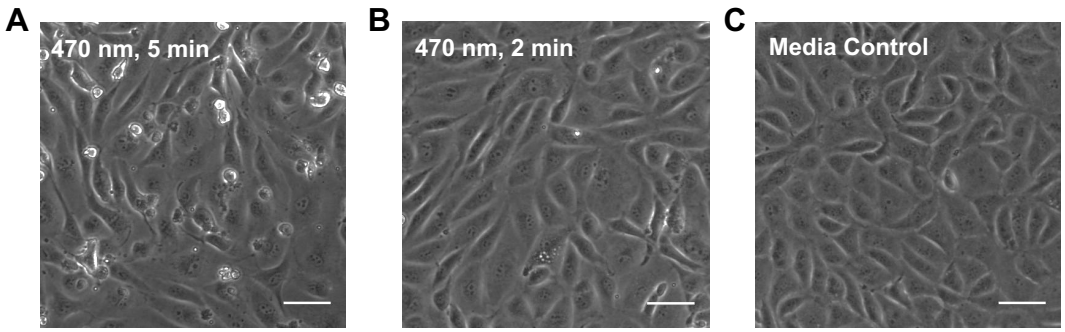

Figure 4.8. Visible blue light at 470 nm damaged endothelial cell monolayers. Endothelial monolayers exhibited (A) high cell death after 5 minutes of blue light exposure and (B) an elongated morphology at 2 minutes when compared to untreated media controls (C); scale bar = 50 μm.

The 470 nm wavelength for LAP radical crosslinking was used in prior studies because the higher wavelength is less damaging to some cell types. Notably, the absorption spectra for LAP is greater at lower wavelengths when compared to 470 nm, and 320-500 nm light was well tolerated by endothelial monolayers in the prior I2959 experiments; therefore, the application of LAP for *in situ* stiffening at 365 nm was investigated *(291)*. AFM mechanical characterization of MeHA gels stiffened by LAP initiated free-radical crosslinking yielded moderate stiffness increases with 1 min UV light exposure, and demonstrated that a step-wise increase in elastic modulus occurred with a second 1 min stiffness treatment (Figure 4.9).

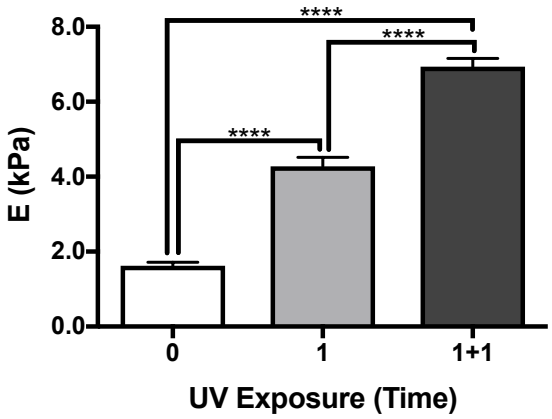

Figure 4.9. MeHA hydrogels exhibited step-wise sequential stiffening by radical crosslinking with the photoinitiator LAP. MeHA hydrogels were sequentially stiffened by free radical crosslinking using the photoinitiator LAP and 1 minute UV light exposure. Gel stiffening was cumulative over multiple stiffening sessions, ****$p<0.0001$.

Under these same conditions on glass coverslips, control tests determined that consistent with the I2959 photoinitiator, the generation of free radical species caused an elongated endothelial cell morphology (Figure 4.10).

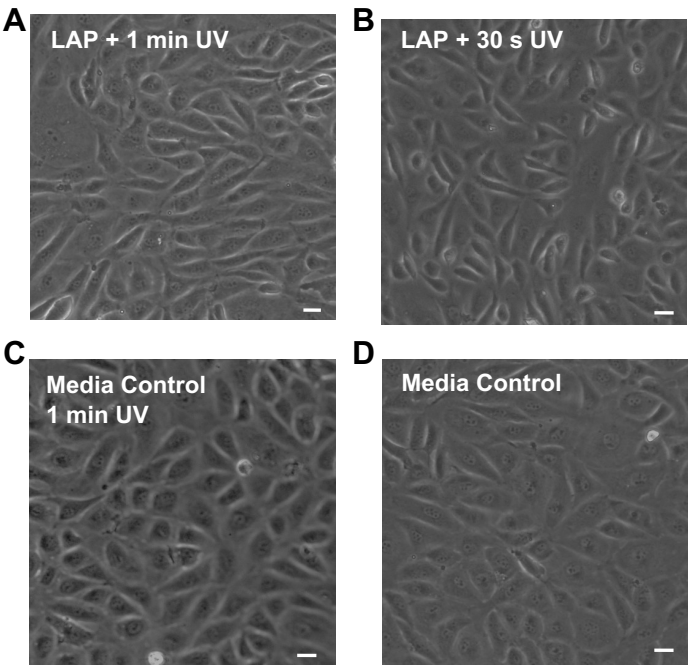

Figure 4.10. LAP free radical species caused endothelial cell elongation. Endothelial monolayers on control coverglass exhibited an elongated morphology when in the presence of hydrogel stiffening reaction conditions that generated free radicals from LAP (A,B). Cell morphology was unchanged after UV exposure alone (C) when compared to untreated controls (D); scale bar = 20 μm.

Because the conditions needed to achieve even very moderate *in situ* substrate stiffening by radical crosslinking were altering cell morphology, and more specifically, the free radicals from two different photoinitiators were damaging to endothelial cells, it was concluded that the usefulness of this *in vitro* model was limited and the project was not pursued further.

Conclusion

A significant limitation of current *in vitro* methods to study pathologies characterized by increased extracellular matrix stiffness is that static models are used to modulate

environmental stiffness. During events such as disease progression or natural aging, a compliant to stiff extracellular matrix transition occurs gradually *(200, 292)*. The development of models that incorporate temporal changes in stiffness are important to understanding the basic biological mechanisms underlying the cellular response to increased extracellular matrix mechanics, and its role in driving the progression of pathological states. Scaffolds that utilize photo-polymerization are one promising approach to *in vitro* stiffening studies because the investigator can tightly tune the degree of spatial and temporal matrix crosslinking. However, as demonstrated here, the widespread application of photo-polymerization is limited because of cell-type specific biocompatibility *(290)*. A potential method to improve the cyto-compatibility of photo-crosslinking approaches that rely on free-radical generation is to include free radical scavengers, for example, the antioxidant vitamin C, to consume excess radicals and prevent off-target cell damage *(293, 294)*.

An alternative *in vitro* approach to studying the temporal effects of matrix stiffening is the use of substrates that soften over time through hydrolytic, proteolytic, or photocleaved matrix crosslink degradation *(170, 295–297)*. Bioresponsive hydrogels are another platform that could be employed for adaptive cell studies *(298)*. Although these substrates are less relevant as a disease progression model for atherogenesis or other pathologies characterized by matrix stiffening, they still provide important biological insights on cell priming and stiffness adaptive behaviors. Stellate stem cells with a myofibroblast phenotype exhibited phenotypic regression as their matrix softened *(170)*.

A primary cause of age-related arterial stiffening is increased matrix crosslinking caused by the accumulation of advanced glycation end products (AGEs) over the lifespan *(299)*; therefore, therapeutics that break AGEs have been pursued as one method to overcome arterial stiffening *(131)*. Despite multiple candidate compounds, there are currently no products for which clinical trials were successfully completed. Softening substrates present a proof-of-concept method to validate that endothelial cells respond to matrix softening and that an AGE-breaking treatment could improve endothelium barrier integrity. In addition, significant crosstalk between cellular pathways that are altered by matrix softening and stiffening likely exist, albeit in opposite directions. Therefore, understanding the effects of matrix softening, could contribute to the identification of alternative targets to overcome the deleterious effects of matrix stiffening.

4.2 *Effects of Local Aberrant Cell Contractility on Global Endothelial Monolayer Integrity*

Motivation

Cell-cell adhesions in confluent endothelial monolayers undergo dramatic reorganization in response to external mechanical and pharmacological stimuli that have important implications for endothelium integrity *(149, 153, 160, 272)*. However, adherens junctions do not exist in a quiescent state in the absence of these exogenous cues *(300)*. VE-cadherin binds to the actin cytoskeleton through the cadherin-catenin complex, and RhoA mediated cell contractility generates a tensional force at cell-cell adhesions *(155)*. Cadherin adhesions are strengthened under force, and junctional tension contributes to conformational changes in adaptor proteins as well as their recruitment *(191, 194, 196)*. The clustering, lateral diffusion, and disassociation of VE-cadherin within junctional zones

is an ongoing dynamic process, and transient junction associated lamellipodia (JAIL) are present during active remodeling in mature endothelial monolayers *(159, 301)*. Notably, force is transmitted across adherens junctions and can alter collective cell behaviors, including migration and global monolayer barrier integrity *(189, 193, 302)*.

Endothelial junction integrity requires a balance between cell-cell and cell-matrix adhesions that are connected by intracellular cytoskeletal networks *(183, 195)*. Under both basal and elevated contractility states, cells exert myosin dependent tensional forces across cadherin junctions that are proportional to the traction forces they exert against their matrix *(188)*. RhoA activation from matrix cues, for example, increased stiffness, is one pathway that increases both traction stresses and tensional force across VE-cadherin junctions *(187, 188)*. Pathological states that alter extracellular matrix stiffness; therefore, also likely alter cell-cell junction tension.

Arterial stiffness increases with both age and atherosclerosis. Importantly, the characterization of the aged murine arterial intima revealed that in addition to an overall increase in Young's modulus, an increase in stiffness heterogeneity existed when compared to young controls. Intima stiffness increased by as much as 50-fold within a 100 by 100 μm area *(122)*. These data suggest that within the physiological arterial niche, matrix stiffness "hotspots" may result in individual endothelial cells that have a hyper contractile profile from localized RhoA activation. It has already been reported that traction forces are non-uniformly distributed within endothelial monolayers, and that inter-endothelial gaps are more numerous in regions of high force fluctuation *(275)*. Therefore, endothelial cells

with aberrant contractility profiles may further explain how the mechanical properties of the aged arterial intima contribute to atherogenesis. And because excess force across VE-cadherin disrupts distant cell adhesions, the deleterious effects of localized hyper contractility may be propagated across a monolayer *(189)*.

Here, I used endothelial monolayers and microinjection as a minimal model to investigate how the effects of an individual cell with increased contractility is propagated into a monolayer response through force transmission across VE-cadherin junctions.

Methods

Cell Culture

Bovine aortic endothelial cells (VEC Technologies, Rensselaer, NY) from passages 7−12 were cultured in Medium 199 (Invitrogen, Carlsbad, CA) supplemented with 10% Fetal Clone III serum (HyClone, Logan, UT), 1% MEM amino acids (Invitrogen), 1% MEM vitamins (MedTech, Manassas, VA), and 1% penicillin−streptomycin (Invitrogen) at 37 °C and 5% CO_2. For microinjection studies, cells were seeded onto 0.1 mg/mL rat tail type I collagen coated coverglass and grown to confluence.

Microinjection

A FemtoJet injector equipped with an Injectman NI2 microinjector (Eppendorf, Hauppauge, NY) and mounted on a Zeiss LSM700 microscope with an environmental chamber was used to deliver sub-microliter volumes of material to endothelial cells without disrupting the internal cellular environment. Endothelial morphology was assessed

immediately after microinjection and also at 3 hours post-injection for signs of cell damage. Injection needles were fabricated from filamented glass capillaries with a 1.00 mm outer diameter and a 0.50 mm inner diameter (Sutter Instrument, Novato, CA) using a P-97 micropipette puller (Sutter Instrument, Novato, CA). Cells were injected with Rho Activator II (Cytoskeleton, Denver, CO) at a final concentration of 100 μg/mL in PBS (Invitrogen). Cells were co-injected with a lysine fixable 10,000 MW Alexa Fluor 488 dextran (Invitrogen) at a final concentration of 1 mg/mL for identification. Control cells were injected with the 488 dextran in PBS only. To account for the effects of RhoA activator that leaked out of the injection needles into the culture media while approaching the cell monolayer due to back pressure, after injecting control cells, a microinjection needle filled with RhoA activator at the treatment concentration was hovered over the injected control cells for ~30 seconds. After microinjection, samples were rinsed twice and placed in fresh culture media. All assays were conducted 3 hours post-injection.

Actin Visualization

Endothelial monolayers were fixed with 3.7 % formaldehyde (VWR) and permeabilized using 1% triton (J.T. Baker, Center Valley, PA), followed by incubation with Alexa Fluor phalloidin 568 (Invitrogen) to visualize actin structures. Samples were imaged using a Zeiss LSM700 microscope equipped with a 40x water immersion objective.

Localized Permeability Assay

Localized junction permeability was assessed as described by Dubrovskyi *et al. (303)*. Briefly, biotinylated gelatin was synthesized by dissolving porcine gelatin (Sigma, St.

Louis, MO) at 10 mg/mL in 0.1 mol/L $NaHCO_3$ (VWR), pH 8.3 in a 70 ºC water bath. The gelatin solution was then clarified by centrifugation at 10,000 x g for 5 minutes at room temperature. EZ-Link NHS-LC-LC-Biotin (Thermo Scientific, Rockford, IL) was dissolved in DMSO (VWR) at a final concentration of 0.57 mg/mL and added 1:10 to the clarified gelatin solution. The biotin-gelatin conjugation reaction was allowed to proceed at room temperature for 1 hour with constant stirring. The product was then aliquoted and stored at -20 ºC. For cell experiments, the biotinylated gelatin was diluted to 0.25 mg/mL in $NaHCO_3$, pH 8.3 and activated coverglass was coated with the protein. To measure localized permeability, samples were incubated in culture media containing 25 μg/mL Alexa Fluor 568 streptavidin for 5 minutes, followed by two rinses with PBS (Invitrogen), and immediate fixation with 3.7 % formaldehyde in PBS. Samples were imaged using a Zeiss LSM700 microscope equipped with a 20x objective and permeability was evaluated by quantifying the Alexa Fluor 568 signal using ImageJ software.

Cell-Cell Junction Size Quantification

Cell-cell junction size was quantified by measuring the width of VE-cadherin signals in endothelial monolayers, as described previously *(63, 258)*. Samples were fixed with 3.7 % formaldehyde (VWR) and permeabilized using 1% triton (J.T. Baker) in PBS (Invitrogen). VE-cadherin at cell junctions was visualized by incubating with a goat polyclonal VE-cadherin primary antibody (Santa Cruz Biotechnology, Dallas, TX) followed by incubation with an Alexa Fluor 568 donkey antigoat secondary antibody (Invitrogen). Fluorescent images of the target cell and surrounding monolayer were acquired on a Zeiss Axio

Observer.Z1m microscope equipped with a Hamamatsu ORCA-ER camera using a 20x objective.

Cells surrounding the microinjected cell were categorized on the basis on their proximity the target cell. Cells sharing a junction with the microinjected cell were categorized as "Layer 1" cells, cells sharing a junction with "Layer 1" cells were categorized as "Layer 2," and cells sharing a junction with "Layer 2" cells were categorized as "Layer 3" cells. The size of cell-cell junctions were quantified using ImageJ software and a custom MatLab code. All junctions for the cells in each layer were measured at their widest point by drawing a line perpendicular to the VE-cadherin junction signal and a pixel intensity profile was obtained in ImageJ (National Institutes of Health, Bethesda, MD). The pixel intensity profiles were fit to a two-Gaussian curve and the junction size was defined as the width of the curve 20% above the baseline intensity.

Statistics

All images are representative of 3 independent experiments and ANOVA statistical analysis with a Tukey's Honestly Significant Difference (HSD) test was performed in GraphPad Prism version 6.0d (La Jolla, CA) were significance was considered with a p-value <0.05. Data is presented as the mean ± standard error of the mean,

Results

To modulate single cell contractility within an endothelial monolayer, bovine aortic endothelial cells were cultured to confluence on 0.1 mg/mL collagen coated coverglass and

individual cells within the monolayer were co-microinjected with a recombinant protein RhoA activator and a fluorescent lysine fixable dextran in PBS. Control cells were injected with the lysine fixable dextran in PBS only, and successful injections were identified on the basis of the fluorescence signal of the injected cells. Increased stress fiber formation in cells microinjected with the RhoA activator compared to surrounding cells within the monolayer were indicative of an increased contractile state (Figure 4.11).

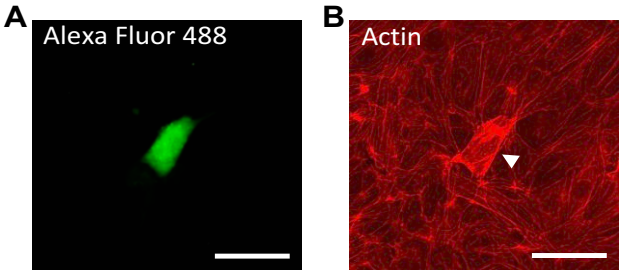

Figure 4.11. Microinjection of a RhoA activator increased stress fiber formation in the target cell. Individual cells within endothelial monolayers were co-microinjected with a RhoA activator and an Alexa Fluor 488 dextran. (A) Microinjected cells were identified using the Alexa Fluor 488 signal and (B) actin stress fibers were visualized using phalloidin. The microinjected cell (white arrowhead) exhibited increased stress fiber formation compared to surrounding cells within the monolayer; scale bar = 50 μm.

Force transmission across VE-cadherin has been shown to cause monolayer disruption distant from the applied force, and increased RhoA activation increases cell-cell junction tension; therefore, the effect of an individual cell exhibiting increased contractility on localized monolayer integrity was investigated. Local endothelial monolayer permeability was measured using a biotin-streptavidin permeability assay. Because of the strength and specificity of biotin-streptavidin interactions, fluorescently tagged streptavidin that diffuses across the monolayer binds nearly irreversibly to a biotinylated substrate below the monolayer, and the fluorescent signal in an indicator of local permeability. To validate the assay, endothelial monolayers were treated with thrombin, a well known endothelial

barrier disruptive agonist that activates RhoA. Thrombin treatment monolayers had significantly higher fluorescent streptavidin signals compared to untreated control monolayers indicating increased permeability (Figure 4.12). No permeability signal was detected in negative controls cultured without a biotinylated substrate nor controls on a biotinylated substrate that were not incubated with streptavidin.

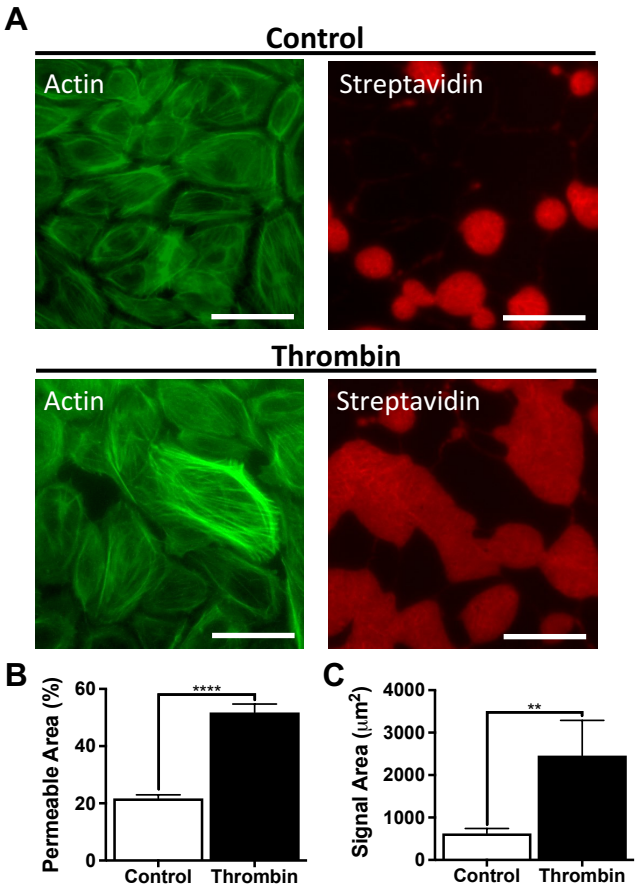

Figure 4.12. Localized endothelial monolayer permeability was measured using streptavidin immobilization to biotin beneath the endothelial monolayer. (A) Actin stress fiber formation was visualized in control and thrombin treated endothelial cells, and the signal from streptavidin that had diffused across the monolayer and bound to biotin was used to measure permeability. Monolayer permeability was increased in thrombin treated cells when the overall streptavidin area percentage (B) and the size of individual streptavidin signals (C) were compared between control and thrombin treated cells, **indicates $p<0.01$, **indicates $p<0.001$. Data are presented as means ± standard error of the mean; scale bar = 50 μm.

Individual cells within monolayers were then co-injected with RhoA activator and a green fluorescent dextran. Local monolayer permeability surrounding the hyper contractile (green) cell was measured (Figure 4.13A). Permeability was measured as a function of the radial distance from the contractile cell to determine if contractile force propagation across VE-cadherin was causing areas of increased monolayer permeability (Figure 4.13B).

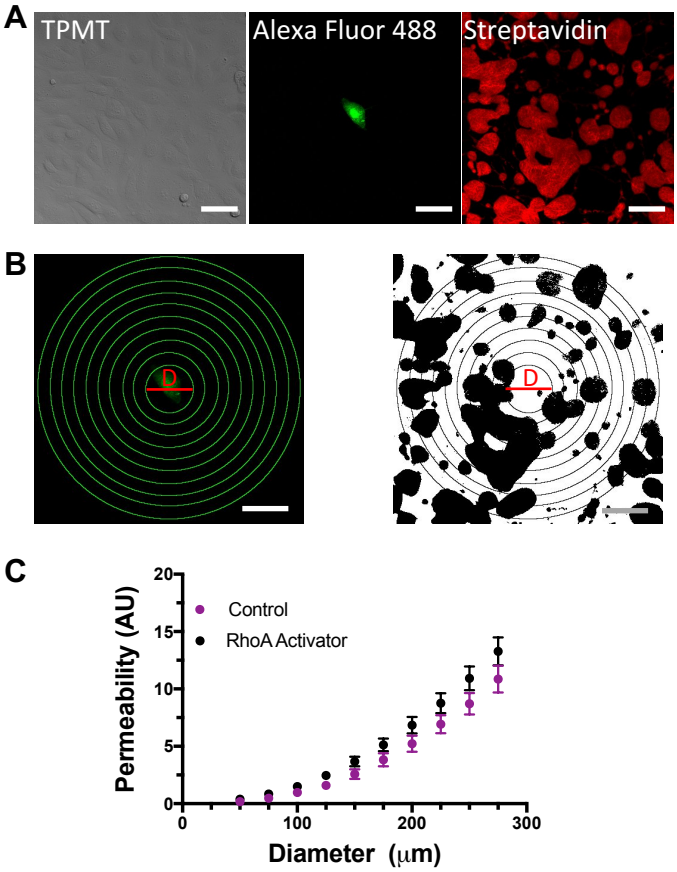

Figure 4.13. Local endothelial monolayer permeability surrounding microinjected cells was measured. (A) Isolated cells within endothelial monolayers were co-microinjected with Alexa Fluor 488 and RhoA activator or Alexa Fluor 488 alone, and permeability was evaluated. (B) Monolayer permeability was analyzed as a function of radial distance from the microinjected cells where the diameter of the measurement circle increased by 25 μm in each increment. (C) There was no statistical difference in localized permeability in monolayers surrounding control and RhoA activator injected cells. Data are presented as means ± standard error of the mean; scale bar = 50 μm.

Permeability profiles between monolayers with RhoA activator and control injected cells were not significantly different, indicating that under the injection conditions and analysis metrics used, localized contractility did not increase endothelium permeability.

To further investigate the effects of localized increased cell contractility and force propagation across VE-cadherin on endothelium integrity, cell-cell junctions between cells surrounding RhoA activator microinjected cells were measured. Previous studies have established that increased cell-cell junction size correlates with increased endothelium permeability *(63, 258)*. Monolayers containing isolated microinjected cells were stained to visualize VE-cadherin and the width of the VE-cadherin signal between adjacent cells was quantified. Monolayer cells surrounding the microinjected cell were divided into groups on the basis of their relative distance from the cell with increased contractility to investigate the propagation of contractile effects. The cells that shared a junction with the microinjected cell were categorized as "Layer 1," the cells that shared a junction with "Layer 1" cells were "Layer 2," and cells that shared a junction with "Layer 2" cells were categorized as "Layer 3" cells (Figure 4.14).

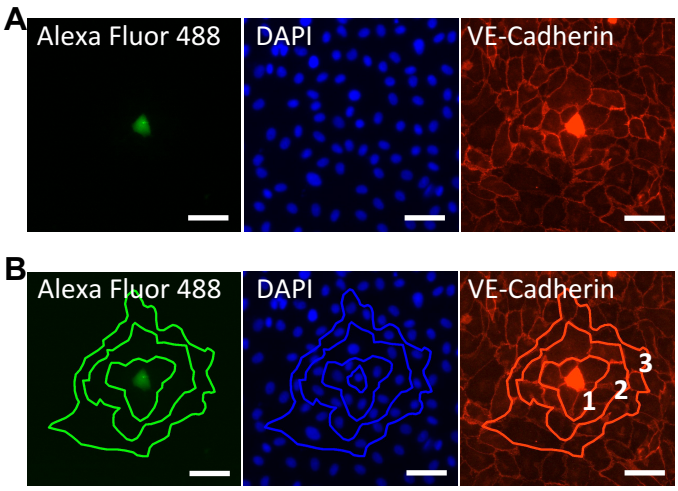

Figure 4.14. Endothelial monolayers were microinjected and VE-cadherin was visualized to measure cell-cell junctions. (A) Endothelial monolayers were co-injected with Alexa Fluor 488 and RhoA activator or Alexa Fluor 488 alone, and cell nuclei and cell-cell junctions were visualized with DAPI and VE-cadherin, respectively. (B) Monolayer cells were divided into three cell layer categorizes on the basis of the proximity of their nearest junction to the microinjected cell. Data are presented as means ± standard error of the mean; scale bar = 50 μm.

There was no statistical difference in junction size between the different cell layers (Figure 4.15A). The distributions of cell-cell junction sizes between cell layers were also investigated to determine if there was an increased prevalence of larger junction sizes within a certain layer (Figure 4.15B). Consistent with the mean junction sizes, all groups had similar junction size distribution profiles.

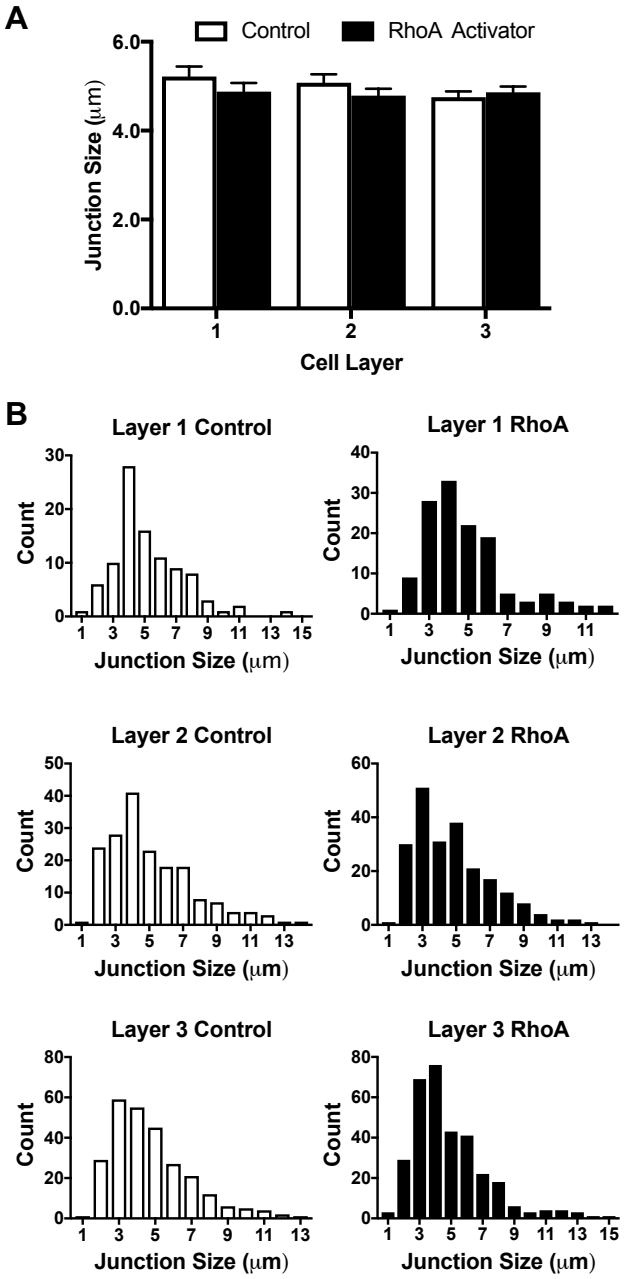

Figure 4.15. Endothelial cell-cell junction size was measured surrounding microinjected cells. (A) Cell-cell junction size was not statistically different in monolayers injected with RhoA activator or control. Cell-cell junction size was also not statistically different between cells adjacent to microinjected cells and those that did not directly share a cell border with the injected cell. (B) The distribution of cell-cell junction sizes was unchanged between monolayers with control and microinjected cells, and was also unchanged with respect to proximity to the microinjected cell. Larger junction sizes did not occur with greater frequency between the treatment and control monolayers, nor with respect to the proximity to the microinjected cell. Data are presented as means ± standard error of the mean.

Conclusion

Direct force application to VE-cadherin and force transmission across endothelial junctions have been shown to cause global endothelial monolayer disruption *(189)*. However, in the present study, using microinjection to locally increase cell contractility and tensional forces across cell-cell junctions, no change in monolayer integrity was measured. Differences in the approaches to apply a force across VE-cadherin may explain the incongruity among the two studies. Direct force application to VE-cadherin by Barry *et al*. was achieved using magnetic twisting cytometry to apply an oscillatory shear stress that increased from 0.036 to 9 Pa. However, tension between cell-cell adhesions is not oscillatory under increased contractile conditions, as studied here, and the measured cell-cell force is on the order of nanonewtons for an entire adhesion when RhoA is constitutively active *(188)*. The measured tension across an individual VE-cadherin molecule is 2.4 nN/molecule under basal conditions *(300)*. In addition, force fluctuations are associated with increased inter-endothelial gap formation, suggesting that both the magnitude of the applied force and the method of application may have attributed to the results reported by Barry and colleagues *(275)*.

The data discussed here indicate that an increase in cell contractility from the injected RhoA activator were insufficient to cause significant force changes across cell-cell junctions and elicit global monolayer effects. A suggested future study to investigate the effects of an isolated hyper contractile cell within an endothelial monolayer, such as what could occur from a hotspot of increased extracellular matrix stiffness, is to directly measure VE-cadherin tension using a FRET sensor *(300)*. Incorporating this technique into the

current microinjection approach would allow the investigator to verify that the level of microinjected RhoA activator significantly increased cell-cell junction forces. In addition, a quantitative assessment of force propagation could be analyzed in concert with localized permeability data.

Another interesting future study is to investigate the effects of VE-cadherin force propagation on matrices of decreasing compliance. Because cells within a monolayer exert forces at both cell-cell and cell-ECM adhesions, this study would determine to what extent aberrant contractile forces are dissipated or strengthened at ECM and/or intercellular contacts. Forces exerted at focal adhesions could be measured with FRET based tension sensors developed for vinculin, talin, and integrin proteins *(165, 304, 305)*. Although study complexity is increased with the introduction of matrix stiffness, physiological relevance it also increased. The effects of increased RhoA activation also have the potential to elicit a more robust response on compliant matrices because RhoA activation exists is in an elevated basal state on glass substrates *(258)*. Important clinical insights into the underlying mechanisms and the role of cellular forces that contribute to endothelial permeability caused by the mechanical properties of the aged arterial intima would be gained from these studies.

CHAPTER 5

THERAPEUTICALLY TARGETING INCREASED EXTRACELLULAR MATRIX MECHANICS TO ATTENUATE DISEASE: FROM MOLECULAR TARGETS TO CLINICAL TRIALS

5.1 Abstract

Tissue stiffening manifests during the pathological progression of cancer, fibrosis, and cardiovascular disease, and also during aging. Importantly, extracellular matrix stiffness is emerging as a prominent mechanical cue that precedes disease and drives it progression by altering cellular behaviors. As such, targeting mechanics, by preventing or reversing tissue stiffening, or interrupting the cellular response, is a novel therapeutic approach with important clinical potential. The contributions of phenotypically converted myofibroblasts, the growth factor TGFβ, and crosslinking to extracellular matrix stiffening are described. Potential pharmacological interventions to overcome extracellular matrix stiffening are then discussed with an emphasis on clinical translation. An alternative approach to mitigate the effects of increased matrix stiffness by identifying cellular targets to inhibit the deleterious response to matrix mechanical cues is also reviewed. Therapeutic interventions for each target are discussed in the context of their limitations, pre-clinical drug development efforts, and clinical trials.

5.2 Introduction

Increased tissue stiffness is associated with a diverse array of pathologies including the two leading causes of death in the United States: cancer and cardiovascular disease *(306, 307)*. Decreased extracellular matrix (ECM) compliance also occurs with fibrosis, advanced age, and diabetes *(308, 309)*. With the expansion of the mechano-biology field over the past decade, integrating techniques and results across the engineering and biological landscapes, our understanding of the contributions of increased ECM stiffness on disease has vastly increased. Although it is well established that changes in tissue mechanics are hallmarks of specific pathological states, more recently, it has become apparent that tissue stiffening can precede disease development and that mechanical cues can drive its progression *(249, 310)*. As such, mechano-medicine is an emerging field focused on therapeutically targeting mechanics, either by directly altering the mechanical cues presented to cells or disrupting the cellular response to mechanics.

The extracellular matrix (ECM) is a cell secreted network that surrounds cells and is primarily composed of proteoglycans and fibrous proteins, the most abundant being collagen. In addition to providing structural support, the ECM imparts important biochemical and mechanical cues to maintain tissue homeostasis *(311)*. The mechanical stiffness of healthy tissues is tightly controlled and exists on a continuum ranging from 200 Pa within the breast to 20 GPa for cortical bone *(292, 312)*. Importantly, tissue stiffness can regulate cell behavior and aberrant stiffening is associated with pathological states *(313)*. Increased ECM stiffness elicits a diversity of adverse cellular responses by activating integrin-mediated signaling cascades *(314)*.

Because aberrant ECM mechanical properties play a critical role in numerous pathologies, mechano-medicine, is a novel therapeutic approach to treat disease with important clinical implications. Mechanisms that cause ECM stiffening during natural aging and pathological progression are first discussed. Therapeutic approaches to prevent or reverse matrix stiffening, including their clinical relevance, are then reviewed. Potential cellular targets to disrupt the response to increased matrix mechanics are then identified, and their drug development efforts are described. Finally, translational potential is discussed in the context of available drugs, pre-clinical studies, and clinical trials.

5.3 Targeting Tissue Stiffening to Limit Pathological Progression

5.3.1 Extracellular matrix deposition

Myofibroblasts

A major cause of increased ECM stiffness during cancer and fibrotic diseases is the deposition of extracellular matrix by quiescent resident cells that have undergone epithelial to mesenchymal transition (EMT) to myofibroblasts (Figure 5.1). These dedifferentiated myofibroblast are proliferative, highly contractile, and secrete large amounts of matrix. Interestingly, myofibroblasts originate from different precursor cells depending on the pathology, and can be derived from multiple cell sources including bone marrow and immune cells *(315)*. A significant shortfall in our knowledge is a comprehensive understanding of myofibroblast origins and the respective contributions of resident and

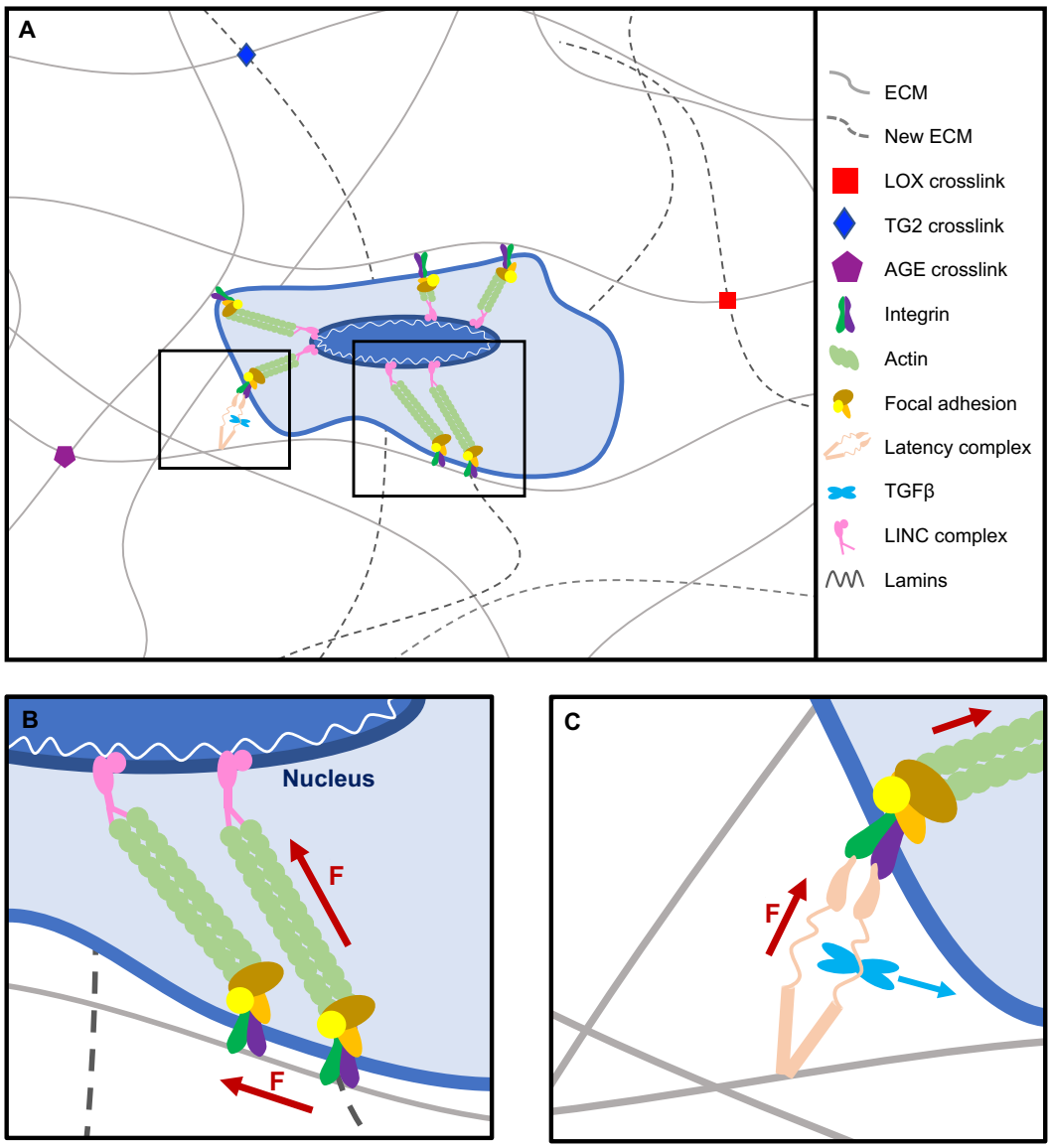

Figure 5.1. Schematic of a cell within a stiffened ECM microenvironment. (A) Matrix crosslinking by LOX (squares) TG2 (diamonds) and AGEs (pentagons) in concert with increased matrix deposition (dashed lines) are major contributors of pathological matrix stiffening. Inside-out and outside-in ECM rigidity sensing is transmitted across cell adhesions composed of integrins and focal adhesion complexes. (B) Actomyosin cell contractility forces are increased in response to elevated matrix stiffness and traction forces are exerted against the ECM. Cellular force is also propagated across the cell cytoplasm to the nucleus. (C) Stiffness-mediated traction forces transmitted across integrins cause a conformational change in the TGFβ latency complex to release TGFβ ligand and activate positive feedback cycles of ECM synthesis and stiffening.

infiltrating cells during fibrosis. Although alpha smooth muscle actin (α-SMA) expression is commonly used as a myofibroblast molecular marker, not all cells expressing α-SMA are myofibroblasts, and α-SMA negative cells also exhibit myofibroblast behaviors *(316)*. The diversity of myofibroblast precursor cells and a lack of a molecular identifier make them a difficult therapeutic target to prevent ECM deposition.

Growth factors

Common among myofibroblast driven pathologies is the prominent role of the growth factor TGFβ which is aberrantly overexpressed. TGFβ promotes myofibroblast differentiation, cell proliferation, and matrix production. Briefly, extracellular TGFβ ligand binds to its serine/threonine kinase receptor (TGFβR1) and activates canonical SMAD pathways that induce collagen and fibronectin gene expression *(317)*. Simultaneously, TGFβ signaling inhibits matrix metalloproteinase (MMP) matrix degradation by inducing the expression of tissue inhibitors of matrix metalloproteinases (TIMPs) to drive microenvironment stiffening *(318)*. Notably, cells exert increased contractile pulling forces against their matrix in response to elevated matrix stiffness which activates a vicious feed forward cycle of matrix production by releasing sequestered TGFβ from the matrix through mechanical force *(319, 320)*. Both increased stiffness and TGFβ1 activity are found at the active front of invasive tumors, and TGFβ inhibition decreases fibrotic progression *(321, 322)*.

Because of their dominant role stimulating proliferation and ECM production, growth factor therapies, especially those targeted against TGFβ, are a promising avenue to inhibit

pathological cycles of ECM synthesis. Targeting TGFβ is an active area of research for fibrosis and cancer applications, and therapeutics are in development stages ranging from *in vitro* pre-clinical studies to Phase III clinical trials *(322)*. Disrupting the pathological role of TGFβ has been approached from multiple angles including inhibiting receptor-ligand interactions, tyrosine kinase activity, and protein synthesis. These efforts have utilized peptides, antisense oligonucleotides, small molecule inhibitors, and monoclonal antibodies *(322)*. Exploiting the off-target effects of tyrosine kinase inhibitors that have already been FDA approved for other applications has also been pursued to accelerate small molecule therapies for anti-fibrotic applications *(323)*. (See Akhurst and Hata *(322)* for a review on TGFβ inhibitory drugs and their clinical translation.) Importantly, because of the central role of TGFβ in propagating fibrosis, once developed, therapeutics can have widespread applications across organ specific diseases. For example, the small molecule Pirfenidone is a breakthrough drug that inhibits TGFβ pathways and was FDA approved in 2014 to treat idiopathic lung fibrosis *(324)*. Pirfenidone is now in clinical trials to improve patient outcomes in cancer (NCT00020631), kidney fibrosis (NCT02408744, NCT00001959), and systemic sclerosis (NCT01933334, NCT03068234). Fresolimumab (GC1008) is a monoclonal antibody against TGFβ that is also being actively pursued in numerous clinical trials for its anti-fibrotic effects in cancer (NCT01401062, NCT02581787), kidney sclerosis (NCT00464321), and systemic sclerosis (NCT01284322).

Other growth factors such as PDGF and VEGF also contribute to fibrotic development, and similar to TGFβ, are potential therapeutic targets *(325, 326)*. PDGF is of particular

interest because it stimulates vascular smooth muscle cell migration and proliferation during atherogenesis *(325)*. A challenge with therapeutically targeting growth factor-mediated ECM synthesis is that the ECM imparts tissue integrity, and regulating extracellular matrix turnover is one of many downstream growth factor signaling outcomes. Indeed, despite its identification as the key regulator of fibrosis, the pleiotropic effects of TGFβ impose significant challenges to its therapeutic targeting. During cancer, TGFβ can have both pro- and anti-tumorigenic effects, and TGFβ is important for inflammatory regulation *(322)*. Paradoxical roles for growth factors underscore the challenges of using them as therapeutic targets and highlight a necessary role for spatial and temporal control in drug administration.

Aptamers may represent the future for targeted therapeutics, including growth factor inhibition. Although conceptually similar to antibody approaches, as synthetic oligonucleotides, aptamers are advantageous because they are produced without animal intermediates, and can be designed to engage in distinct, location specific protein interactions with tailored pharmacokinetics *(327)*. With continued contributions from next generation sequencing and bioinformatics, improved selection methods, and lower costs, it is anticipated that aptamers can fill a critical therapeutic niche *(328)*. Currently, Macugen (Pfizer), which targets VEGF-165 to inhibit angiogenesis related to macular degeneration is the only aptamer on the market, but nevertheless, demonstrates the successful translation of aptamer technology to the clinic for effective, isoform specific, growth factor targeting *(329)*.

Because cells respond to the mechanical cues of their microenvironment and a dense ECM inhibits the delivery of therapeutics, interventions that rely on disrupting fibrotic cascades are likely to be most effective during the earliest stages of disease before irreversible changes to ECM rigidity have occurred. Therefore, the success of these interventions will also rely on the development of new technologies that contribute to early disease detection.

A unifying thread in the approaches to inhibit ECM deposition is that they target cells after they have undergone a pathological phenotypic switch. While the contribution of the ECM in promoting cancer malignancy, atherogenesis, and fibrosis is becoming increasingly appreciated, an ongoing area of investigation is understanding the mechanisms that drive quiescent cells to adopt a myofibroblast state. Genetic, gender, and age predispositions may cause the myofibroblast conversion *(330)*. Notably, matrix stiffness may also contribute to myofibroblast phenotypes. Similar gene expression profiles are observed between cells originating from dense breast tissue and the tumor stroma *(331)*. These data provide evidence that phenotypic modulation is more complex than cytokine and growth factor crosstalk. Further implicating mechanics as a driving factor in the development of myofibroblasts is evidence that stiffening precedes fibrosis and hypertension, that proliferation and migration increase with increased matrix stiffness, and that EMT and TGFβ stimulation are matrix stiffness dependent *(140, 332–334)*. Denser tissues from genetic predisposition, aging, or diabetic complications may prime cells towards fibrotic phenotypes. If matrix stiffness is a driving factor that causes an even stiffer ECM, then what are the initial mechanisms contributing to pre-pathological increases in matrix

rigidity? As these pathways become unveiled, it is anticipated that new therapeutic targets will also be identified to interrupt matrix stiffening at earlier stages of disease development.

5.3.2 Extracellular matrix crosslinking

In concert with increased extracellular matrix deposition, increased crosslinking is also a major contributor to tissue stiffening. Collagen and elastin have low turnover rates, and covalent crosslinks by advanced glycation end products (AGEs) that occur from a reaction between reducing sugars and matrix proteins accumulate over the lifespan *(200)*. Hyperglycemic diabetic individuals have increased susceptibility to glycation, and therefore, experience accelerated tissue crosslinking *(308)*. Dysregulated enzymatic crosslinking of matrix components also contributes to stiffening. Lysyl oxidase and tissue transglutaminase (TG2) are implicated in these processes during cancer, fibrotic progression, and age-related arterial stiffening *(335, 336)*. Importantly, covalent crosslinking induces irreversible changes in matrix stiffness and prevents tissue regression back to a compliant state *(337)*.

Breaking or preventing ECM crosslinks is an attractive therapeutic approach to stall, reverse, or even prevent pathologies that are in-part, driven by increased matrix stiffness, and appear promising on the basis of reports that hepatic stellate cells respond to both the mechanical stiffening and softening of their extracellular matrix *in situ (170)*.

Advanced Glycation End Products (AGEs)

Despite initial indications of clinical potential, there are no glycation-related therapeutics on the market. The pioneering AGE breaker alagebrium and the AGE inhibitor, aminoguanidine, had contradictory clinical trial results and ultimately, toxicity risks removed them from consideration for therapeutic use *(338)*. Other therapeutics to break or inhibit glycation crosslinks have been investigated and are reviewed extensively elsewhere, but remarkably, despite a diverse range of candidate compounds, limited clinical success has been achieved *(338)*. Repeatedly, *in vitro* results are not replicated *in vivo*. Progress is hindered by poorly defined mechanisms of target compounds and the widespread use of BSA as a model protein that does not capture the diversity of glycation crosslinks found *in vivo*. Synthetic AGE-BSA compounds produced *in vitro* behave differently than native AGEs and do not represent the varied kinetics between BSA, collagen, and elastin substrates *(339, 340)*. Additionally, toxicity and low efficacy are common outcomes of clinical trials indicating that AGE therapeutics with increased specificity need to be designed.

As previously highlighted, aptamers are an emerging therapeutic technology, and preliminary studies suggest they are also effective at ameliorating the deleterious effects of AGEs *(341)*. Aptamer therapy prevented increases in serum AGE levels in an animal model of diabetes *(342)*. Importantly, long term administration was well tolerated, suggesting that aptamer translation to clinical use will not be hindered by the same toxicological limitations of small molecule AGE inhibitors and breakers. In light of the challenges to develop drugs against glycation, diet adjustments that significantly reduce circulating AGE levels and

evidence that exercise reduces AGE crosslinking in tissues should also be emphasized for their therapeutic potential and ease of implementation *(343, 344)*.

Lysyl oxidase (LOX)

Lysyl oxidase and TG2 are cell produced proteins; therefore, enzymatic crosslinking can be targeted at the transcriptional, post-translational, and catalytic levels. An ongoing pursuit is understanding the paradoxical outcomes of LOX activity, and the specific contexts in which it can be pro- or anti-pathogenic *(345)*. Increasingly, LOX is considered as a therapeutic target because of its dual role in the formation of the tumor stroma and the pre-metastatic niche, in addition to its deleterious activity during fibrosis and atherosclerosis. The effectiveness of inhibiting LOX crosslinking to reduce extracellular matrix stiffness and improve pathological outcomes has been well established using the competitive inhibitor B-aminopropionitrile (BAPN). BAPN inhibition of LOX decreased aortic stiffness and atherosclerotic plaque burden, attenuated tumor stroma stiffness and reduced metastasis, inhibited liver fibrosis and promoted its reversal, decreased lung fibrosis, and prevented renal fibrosis *(142, 346–348)*. Although BAPN is a valuable research tool and validates LOX as a clinical target to prevent pathological progression caused by matrix crosslinking, high toxicity during clinical trials preclude its clinical use *(349)*.

Monoclonal antibody inhibition of lysyl oxidase-like 2 (LOXL2) was pursued by Gilead Sciences with Simtuzumab, but the culmination of Phase II clinical trials during late 2016 revealed no benefit for cancer and fibrotic disease patients *(350, 351)*. A sizeable challenge

in the race to create effective LOX inhibitors is that the complete crystal structure, which is typically used to guide small molecule development pipelines, remains unknown for mammalian LOX *(352)*. Therefore, alternative approaches that include inhibiting the LOX transcription factor or preventing post-translational cleavage of the precursor peptide by BMP-1 have been proposed *(353)*. Notably, unparalleled clinical success in cancer has been achieved with the non-specific copper chelator tetrathiomolybdate which depletes the LOX catalytic site of the metal and lowered serum LOXL2 levels in Phase II clinical trials (NCT00195091) *(354)*. Corresponding murine models demonstrated that copper depletion reduced LOX, collagen deposition, and collagen fiber length in pre-metastatic lungs *(354)*. Tetrathiomolybdate treatment is favorable because of its simple oral administration route, excellent tolerability, and greater LOX inhibition when compared to BAPN *(354)*.

Tissue Transglutaminase (TG2)

Pharmacological inhibition of TG2 is in pre-clinical stages with classical small molecule competitive, reversible, and irreversible inhibitors *(355)*. Reportedly, a TG2 inhibitor was investigated in Canadian clinical trials where poor efficacy was demonstrated, and an irreversible TG2 inhibitor is in Phase 1b clinical trials in Europe, but limited information is available about these efforts *(355, 356)*. Interestingly, TG2 is found in almost all tissues where it exists as a cytosolic protein with catalytic, G-protein, kinase, cell survival, and transcription regulating roles *(336)*. The ubiquitous nature of TG2 and its multi-faceted impact on cell behaviors beyond ECM crosslinking make it a difficult therapeutic target. The challenge of developing effective small molecule inhibitors is exacerbated by evidence

that TG2 exists in multiple conformational states and has several structural domains *(336)*. Therefore, less conventional methods that abolish TG2 activity by limiting its expression are also being pursued. Upstream inhibitors of the ERK pathway that downregulate TG2 expression and siRNA have successfully demonstrated fibrotic reduction in animal models *(357, 358)*. Notably, TG2 siRNA coupled with liposome delivery yielded effective organ specific targeting to the liver and lungs *(358)*.

5.3.3 Proteolytic matrix degradation

Paradoxically, despite mounting evidence that increased stiffness contributes to poor patient outcomes, the proteolytic activity of MMPs also contributes to disease progression. Notably, cancer, fibrosis, and cardiovascular disease are all associated with dysregulated MMP activity *(359)*. Although MMPs are commonly affiliated with extracellular matrix proteolytic activity, matrix components only account for 20% of MMP substrates and their ability to cleave and activate growth factors, chemokines, cytokines, and receptors are associated with conflicting cell processes that promote and inhibit stiffness mediated pathologies *(360)*. For example, MMPs can release matrix-bound latent TGFβ, but their expression can also have anti-fibrotic effects, and MMPs have a critical role in fibrotic resolution *(361–363)*. There is also evidence indicating that MMP activity is mediated by substrate stiffness, suggesting that MMPs can have an evolving role during disease progression *(364)*. Because of the varied, context specific effects of MMPs, and the major clinical failure of MMP targeting for cancer treatment, strategies that rely on altering MMP activity to overcome ECM stiffness should be pursued with caution *(365)*. Therapeutics with high specificity must be developed, but present a significant challenge because of

similarities between catalytic sites and functional redundancy among the 24 mammalian MMP family members *(365)*. The success of MMP therapeutic strategies will also rely on correctly identifying the appropriate pathological stage during which to administer the drugs to avoid amplifying MMP disease-promoting effects.

Hyaluronidase

Despite significant hurdles to controlling MMP activity, enzymatic matrix degradation with hyaluronidase that improved prognostic outcomes has been achieved in pre-clinical models of cancer. Intravenous injection of hyaluronidase decreased tumor size by 50% within 4 days in mice, and co-administration of hyaluronidase is an ongoing effort to improve drug delivery to the tumor stroma *(366)*. Hyaluronidase has exceptionally high tolerability and pegylated hyaluronidase (PEGPH20) is in several late stage clinical trials as a combination cancer therapy to improve drug penetration (NCT02753595, NCT02921022, NCT02715804) *(367, 368)*. The success of hyaluronidase in the cancer sphere could crossover to other stiffness pathologies to aid drug delivery efforts.

Although targeting the ECM presents a significant challenge and is confounded by crosstalk between disparate mechanisms that contribute to stiffening, it will remain an active area of investigation as the contribution of ECM mechanics in disease progression is increasingly elucidated. Advances in mitigating matrix stiffness directly will likely draw on clinical successes from other settings such as scar and wound healing where matrix turnover is critical *(356)*.

5.4 Interrupting Cellular Responses to Increased Extracellular Matrix Stiffness

Instead of preventing ECM stiffening which occurs with advanced age and can precede disease, an alternative approach to overcome the adverse effects of microenvironment stiffening is to inhibit the cellular response to increased matrix mechanics. The extracellular matrix activates integrin-mediated signaling pathways to elicit cellular outcomes; therefore, mechanotransduction can be disrupted at the cell-ECM level as well as with downstream signaling targets.

5.4.1 Integrins

A logical first choice to interrupt ECM mechano-sensing is integrin targeting because the transmembrane adhesion proteins are conduits of bidirectional signaling directly connecting extracellular inputs to intracellular outputs. Interestingly, integrin expression alone does not drive the cellular response to increased substrate mechanics *(369)*. The judicious selection of which integrins to antagonize to specifically ameliorate matrix stiffness sensing is not straightforward and the regulation of diverse cellular events that result from integrin binding is an active area of investigation. The β integrin subunit recruits focal adhesion kinase (FAK) to initiate downstream signaling cascades that include Rho and Src, and therefore, is a potential target to mediate matrix stiffness responses *(370, 371)*. Already, antagonizing integrins is being pursued in clinical trials for cancer *(372)*. On fibronectin, rigidity sensing through α5β1stimulates Rho-mediated contractility and αv integrins activate the GEF-H1 Rho pathway, suggesting other potential targets *(373)*.

The current understanding of force sensing across focal adhesions is centered around a shared sequence of events among autonomous adhesions that begins when integrin dimers bind their ECM ligands *(174)*. Extracellular integrin deformation from cytoskeletal forces is dependent on substrate compliance which then drives the intracellular recruitment of scaffolding proteins, actin binding reinforcement, and finally, the activation of downstream effectors *(174)*. A stiffened ECM is well established to increase Rho-mediated cellular contractile forces that are necessary for protein conformational changes contributing to focal adhesion maturation, and cell-ECM adhesions are stronger on rigid matrices *(174, 246)*. However, the individual contributions of specific integrin dimer pairs to stiffness sensing and mechanotrasduction in a multi-component ECM has not been fully delineated *(174, 314)*. Fibronectin and collagen are often used interchangeably as ECM proteins during *in vitro* experiments studying cellular forces despite groundwork that ECM ligand biochemistry and thus, integrin engagement, influences cellular mechano-responses *(187)*. Further confounding efforts to target specific integrin mechanosensors is the intersection of integrin cascades with inputs from other microenvironment mechanical stimuli that are also affected by pathological stiffening, for example hemodynamic forces in the artery wall, elevated interstitial pressure in the tumor stroma, or lung parenchyma stretching during respiration *(374–376)*.

Among integrins, the αv family has been identified as a possible therapeutic target for fibrotic pathologies, not for their mechanosensitive signaling, but rather facilitating ECM deposition. Engagement of the arginine-glycine-aspartic acid (RGD) sequence on the latency associated peptide of TGFβ1 by the integrins αvβ1, αvβ3, αvβ5, αvβ6, or αvβ8

coupled with traction forces releases TGFβ1 from a latency complex *(377, 378)*. Function blocking antibodies and small molecule inhibitors that antagonized αvβ1, αvβ6, or αvβ8 to inhibit TGFβ1 activity demonstrated decreased xenograft tumor growth and fibrotic progression in pre-clinical models *(378–380)*. With these encouraging results, a Phase 2 clinical trial is currently active to evaluate the safety and tolerability of BG00011, a humanized monoclonal antibody against αvβ6 for idiopathic lung fibrosis (NCT01371305). Whether αv integrin inhibitors in development for other applications, such as Cilengitide for glioblastoma, also have efficacy against TGFβ1 remains to be established *(381)*. Integrin inhibition is championed when compared to other strategies that target TGFβ1 because it inhibits a population of TGFβ1 that becomes active as an outcome of pathological stiffening, and circumvents the inflammatory reactions that plague systemic inhibition *(377)*.

5.4.2 Cell contractility

Rho GTPase Targeting

Elevated Rho GTPase signaling and contractile traction forces activated by integrin engagement with the ECM is one of the most widely documented downstream consequences of increased ECM stiffness (Figure 5.2) *(173)*. As a critical regulator of cytoskeletal dynamics and cellular force through the formation of actin stress fibers, Rho signaling has been causally attributed to pathological cell contractility, motility, gene expression, cell cycle progression, and survival *(183, 382, 383)*. However, Rho is considered "un-druggable" from the standpoint of traditional small molecule inhibitors that directly bind their protein targets because of its globular structure. Classical small

molecule drugs are designed to fit into hydrophobic pockets, which Rho lacks *(384)*. As an intracellular protein, Rho is also inaccessible to protein biologics that do not require a defined binding pocket, but are too large to cross the plasma membrane *(384)*. Bacterial toxins that block Rho activity are used in academic research, but are not suitable for the clinic because they are non-specific and irreversible *(385)*. Therefore, with these limitations, the Rho pathway has been targeted upstream or downstream of the mature GTPase. The primary strategies are focused on inhibiting Rho localization, preventing Rho activation by guanine nucleotide exchange factors (GEFs), and targeting downstream effectors.

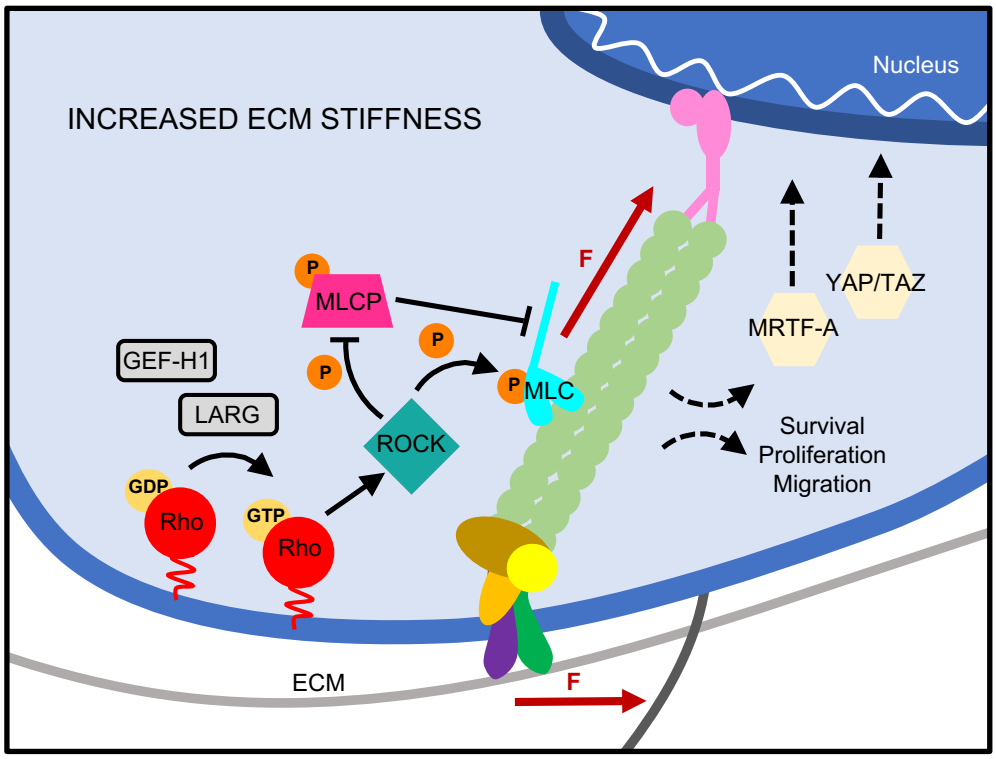

Figure 5.2. Increased ECM stiffness activates the Rho-mediated cell contractility pathway. Mechanical force on integrins activates the Rho GEFs, GEF-H1 and LARG to catalyze the exchange of GDP for GTP. The major Rho effector Rho-associated coiled-coil kinase (ROCK) induces actomyosin cell contractility by phosphorylating myosin light chain (MLC) and myosin light chain phosphatase (MLCP). Downstream of Rho activation, nuclear localization of MRTF-A and YAP/TAZ regulate gene expression, and Rho activity has pathological implications on cell survival, proliferation, and migration.

Statins

Rho localization is important to its activation and is regulated by the post-translational addition of a geranylgeranyl pyrophosphate moiety *(146)*. The lipid anchor targets Rho to the plasma membrane where it maintains close proximity to GEFs that catalyze the exchange of GDP for GTP to transform Rho from an inactive to an active state in a rapid, switch-like manner *(146)*. Intriguingly, statins, which are widely prescribed to lower serum cholesterol levels by competitive inhibition with the enzyme HMG-CoA reductase during cholesterol synthesis have been pursued to inhibit Rho *(386)*. Because statins block cholesterol synthesis, they also inhibit the synthesis of prenylated protein intermediates including geranylgeranyl pyrophosphate, thereby interfering with Rho localization and activation *(386)*. Notably, the therapeutic benefits of statins in cardiovascular disease exceed what can be attributed to their cholesterol lowering abilities *(214)*. Re-purposing statins for clinical use beyond cholesterol lowering is a potential clinical tool to overcome the effects of matrix stiffening that occurs with age or pathology. The statin simvastatin attenuated elevated Rho activity caused by increased matrix stiffness in endothelial cells to reduce cell contractility and improved endothelial barrier function *(258)*. In fibroblasts derived from fibrotic lungs, simvastatin attenuated the myofibroblast phenotype and reduced growth factor expression *(387)*. Despite common deleterious roles for increased matrix stiffness and elevated Rho, the benefits of statins in cancer are less clear, and even conflicting. Pharmacokinetic differences between lipophilic and hydrophilic statins, heterogeneity between patient cancer, and data extracted from clinical trials designed with cardiovascular endpoints rather than as cancer studies have all been cited as causes of the inconsistencies *(388)*. Nevertheless, because the off-target effects of statins extend beyond

Rho, and noting that matrix stiffness is one of many factors that compound to drive disease progression, the success or failure of statin re-purposing cannot be attributed to altered Rho activity alone.

Rho GEF Targeting

GEFs are a therapeutic target to control Rho activity because of their direct role in activating Rho signaling. In addition, because of the diversity of cellular behaviors that result from intricate upstream signaling pathways that converge at Rho, and the identification of more than 80 GEFs, GEF targeting has the potential to impart an elevated degree of specificity on Rho inhibition *(389)*.

GEF inhibitors can be designed to block GEF-Rho interactions or target the GEF catalytic site, both of which terminate forward movement of the signal cascade. For example, the compound Rhosin blocks a GEF docking site on RhoA and a class of compounds named Y16 bind to the GEF catalytic site *(390, 391)*. Importantly, within the Rho family of GTPases, Rhosin only inhibits RhoA activity without interrupting the function of other Rho GTPase family members, and Y16 binds to just three RhoA GEFs: LARG, p115, and PDZ demonstrating high specificity with GEF targeting approaches *(391)*. *In silico* methods were used to discover these two Rho GEF inhibitors, and are becoming powerful tools for rational drug discovery. Because the siRNA techniques used to study GEFs in experimental settings are not applicable for clinical translation, there is a need to develop small molecule inhibitors. However, similar to Rho, GEFs engage in protein-protein interactions and lack large structural pockets which make them poor candidates for

traditional small molecule inhibitors. The combination of computational methods with data driven structural knowledge is identifying novel surface sites that are energetically favorable on proteins that were previously deemed un-druggable, and due to the high clinical need, it is anticipated these methods will yield additional sites to target Rho signaling and the associated GEFs *(392)*. The Rho GEFs LARG and GEF-H1 have been identified as critical mediators of the cellular response to integrin force; and therefore, are ideal GEF targets for dampening cell-ECM mechanotransduction *(393)*. As the ability to target Rho signaling expands, a more complete understanding of the expression, function, regulation, and activation of individual GEFs in specific cell types will be necessary.

Rho-associated coil-coiled kinase (ROCK)

Rho-associated coil-coiled kinase (ROCK) is the major downstream effector of Rho that drives cell contractility and is a mediator of fibrotic pathologies *(394)*. ROCK phosphorylates myosin light chain and myosin light chain phosphatase to induce the generation of cellular force from actomyosin filament contraction. Recently, a stiffness dependent role for ROCK in driving fibroblast to myofibroblast conversion in pulmonary fibrosis was identified, and ROCK inhibition attenuated increased endothelial permeability caused by age-related increased intima stiffness *(63, 395)*.

As a kinase, ROCK inhibition can be readily pursued using traditional small molecule discovery efforts but is also plagued by non-specificity. Indeed, the two most prominent small molecule ROCK inhibitors, Fasudil and Y27632 target the ATP-dependent ROCK kinase domain, but also show non-specific interactions with other kinases *(396)*. It is

hypothesized that Fasudil and Y27632 effectiveness is partially due to their off-target effects with other kinases *(397)*. To overcome off-target interactions, high inhibitor concentrations in the nanomolar range are required for *in vivo* efficacy, which limits clinical translation. In addition to its pathological role, ROCK has an important function maintaining vascular tone via vascular smooth muscle cell contraction *(397)*. Thus, ROCK inhibitors, such as Fasudil, can be designed and employed with this motivation. However, drugs that are successful *in vitro* for different clinical applications of ROCK inhibition can also induce unwanted decreases in blood pressure when transferred to animal models or humans, creating a barrier to their clinical adaptation. Nevertheless, the ROCK inhibitor Fasudil has been used in Japan since 1995 for the treatment of cerebral vasospasms, and ROCK inhibitors have been widely investigated to treat a variety of pathologies either alone or as a combination treatment *(397)*. Fasudil has demonstrated an impressive record of safety and efficacy, but interestingly to date, has not been commercially marketed in the United States. The pharmaceutical company contracted to manage Fasudil in the United States was acquired by a competitor, ultimately resulting in an international lawsuit that reached the California Supreme Court (Asahi Kasei Pharma Corporation v. Actelion Ltd., No. S216123 (Cal)) and stalled Fasudil development. The composition of matter patent on Fasudil expired in early 2016, and while its commercial future is unknown, it continues to be evaluated in pre-clinical and clinical studies (U.S. Patent 5,942,505). A timely pre-clinical investigation recently reported that priming with Fasudil to inhibit Rho-pathway mediated ECM remodeling markedly improves the efficacy of the current standard-of-care pancreatic chemotherapies gemcitabine and Abraxane at both the primary tumor and metastatic sites *(398)*.

New ROCK inhibitors have emerged from the clinical need to lower ocular pressure in glaucoma *(399)*. Ripasudil, a Fasudil derivative is already approved for use in Japan for glaucoma patients *(400)*. One approach to mitigate the off-target effects of ROCK inhibitors is the development of "soft inhibitors" which are designed to degrade into inactive metabolites when not at their target site for improved patient tolerability *(401)*. For example, the soft inhibitor AMA0076 which completed Phase 2 clinical trials (NCT02136940, NCT01693315) is structurally based on Y27632, but exhibits tissue-specific hydrolysis rates in the eye *(401)*. Pharmacological efforts distinguishing the distinct roles of the two ROCK isoforms, ROCK1 and ROCK2 are also in progress *(396)*. The development of small molecule inhibitors that exhibit greater specificity towards the ROCK family kinases or its specific isoforms are using high throughput screening and fragment based approaches *(397)*. New patents for clinical siRNA inhibition of ROCK have also been filed *(397)*.

Focal adhesion kinase (FAK)

Focal adhesion kinase (FAK) is a cytosolic non-receptor tyrosine kinase that is activated by integrin clustering and is a regulator of focal adhesion dynamics and Rho activity *(402)*. FAK integrates extracellular matrix signals from integrins to activate downstream pathways that control adhesion, proliferation, motility and survival *(402)*. In addition, focal adhesions are sites of actomyosin force transmission to the extracellular matrix; therefore, FAK is a potential upstream target to inhibit cellular responses to matrix mechanical cues. Moreover, phosphorylation of FAK at Tyrosine 397 (Tyr-397) which is

necessary for Src binding followed by complete FAK activation through additional phosphorylation, is increased with increased matrix stiffness *(167, 402)*. Dysregulated FAK-Src signaling is widely appreciated for a role in cancer invasion and metastasis, and consequently, the development of FAK inhibitors is co-currently being pursued by GlaxoSmithKline, Novartis, Merck, Takeda, and Pfizer, in addition to efforts by smaller pharmaceutical companies *(403, 404)*. These inhibitors primarily target the FAK catalytic site, and several have reached clinical trials, either alone or as combination therapies *(403, 404)*. However, stiffness induced upregulated FAK activation is also deleterious in pathologies other than cancer. Constitutive phosphorylation of the kinase is found in fibrotic fibroblasts *(405)*. FAK signaling also potentiates growth factor signaling and the myofibroblast phenotype *(405, 406)*. In addition, mechanically driven FAK-ERK pathways activate the Rho GEF, GEF-H1 *(393)*.

As a druggable protein, FAK suffers from the same limitations as other kinases, namely similarity in the catalytic domain that imparts non-specific cross reactivity of small molecule inhibitors. Among a subset of kinases, improved selectivity has been demonstrated with allosteric inhibitors directed to a flexible Aps-Phe-Gly (DFG) amino acid trio at the N-terminus of the activation loop *(407)*. In these kinases, the DFG portion undergoes dramatic conformational changes as it switches between active and inactive states, and has been identified as a domain that imparts selectivity when targeted in the inactive state *(407)*. Importantly, inhibitors stabilizing a unique alpha helix conformation of the FAK DFG-domain have exhibited robust selectivity and efficacy *in vivo (408)*. Other recent efforts to target FAK signaling are designed to inhibit scaffolding interactions with

downstream effectors *(403)*. These approaches are advantageous because they target specific lineages of FAK signaling *(403)*. Another current approach to targeted FAK inhibition is preventing autophosphorylation at Tyr-397 which is particularly relevant to attenuating aberrant FAK activation caused by increased extracellular matrix stiffness *(409)*. For detailed discussions on FAK pharmacological development the reader is directed to reviews by Lee *et al*. and Golubovskaya *(403, 404)*.

5.4.3 Gene expression

YAP/TAZ

In addition to protein activation, the cellular response to increased extracellular matrix stiffness also occurs at the transcriptional level. Most prominently, the downstream effectors of the Hippo pathway yes-associated protein (YAP) and transcriptional coactivator with PDZ-binding motif (TAZ) that are known for mediating transcriptional regulation of apoptosis and proliferation, are also activated by increased matrix rigidity independent of the canonical Hippo cascade *(410)*. YAP/TAZ activation by matrix stiffness contributes to fibroblast phenotypic conversion, increased collagen deposition, and cell proliferation where feed-forward cycles that enhance microenvironment stiffening are augmented *(411, 412)*. YAP/TAZ also potentiates TGFβ signaling *(413)*. Interestingly, actomyosin contractility is necessary for stiffness-induced YAP activation, and inhibition of intercellular tension by abrogating Rho activation attenuates YAP/TAZ nuclear localization *(410)*. The ongoing efforts to develop therapeutic Rho antagonists therefore represent an indirect mechanism to inhibit stiffness mediated YAP/TAZ activation. Already, statins have been identified as strong inhibitors of YAP/TAZ nuclear localization

due to the crossover between the synthesis of cholesterol intermediates and the synthesis of geranygeranyl pyrophosphate for Rho post-translational modification *(414)*. Direct inhibition of YAP/TAZ has been pursued using small molecule inhibitors that prevent YAP/TAZ from associating with their target TEAD transcription factors in the nucleus *(415)*. The results of a small molecule screen revealed the Novartis photosensitizer Visudyne administered for macular degeneration treatment prevented YAP from interacting with TEAD, and Visudyne was confirmed to attenuate YAP mediated events *in vivo (415)*. Inhibition of YAP has also been demonstrated with a peptide designed to mimic the native inhibition of YAP-TEAD association by vestigial like family member 4 (VGLL4) *(416)*. Regulation of YAP/TAZ in both normal and pathological settings is an intense area of investigation, and undoubtedly as our understanding of the crosstalk between the Hippo and mechanotransduction pathways expands, new therapeutic approaches will build upon the proof-of-concept studies that have validated YAP/TAZ as a druggable target. Notably, YAP inhibition in hepatic stellate cells impeded the activated cell phenotype *in vitro* and prevented fibrosis, indicating that transcriptional regulation may be a method to inhibit tissue stiffening *(417)*. Screens of available drugs have already yielded strong candidates that can be re-purposed to inhibit YAP/TAZ which suggest that an accelerated track for druggable efforts may exist.

MRTF-A

Another transcriptional co-activator, myocardin related transcription factor-A (MRTF-A) also undergoes nuclear localization with increasing matrix stiffness. Through the generation of cellular force by Rho activation and actin polymerization, MRTF-A promotes

myofibroblast differentiation *(418)*. Nuclear MRTF-A activates the serum response factor (SRF) transcription factor to induce α-SMA and collagen-I expression, thereby inducing fibrogenesis *(419)*. In addition to activation by cellular tension, TGFβ intersects with MRTF-A activation and also induces its nuclear translocation, further linking matrix stiffness and TGFβ in a self-propagating cycle *(420)*. High throughput screening of 2000 compounds from the Maybridge Diverse Chemical Library led to the identification of the compound CCG-1423 that inhibited transcription along the Rho/MRTF/SRF pathway, downstream of Rho activation by binding to the MRTF-A nuclear localization sequence *(421, 422)*. Although CCG-1423 suffered from high toxicity, structural insights into the rational design of Rho-mediated transcription inhibitors were gained, and new compounds with improved cytocompatibility were subsequently developed. Attenuated matrix stiffness and TGFβ fibrosis were achieved with the second generation MRTF-A inhibitors CCG-100602 and CCG-*20397*, justifying stiffness-mediated Rho transcription as a therapeutic target *(419)*.

Alternative splicing

Variations in gene expression by alternative splicing were recently found to be regulated by extracellular matrix mechanics. Bordeleau and colleagues reported that expression of the splice variant of fibronectin including the extra domain-B (EDB) type III repeat (EDB-FN), commonly found in tumors and believed to contribute to tumorigenesis, is regulated by increased matrix stiffness *(423)*. Interestingly, the splicing event depends on Rho-mediated cell contractility. The authors also identified alternative splicing of PKC BII and VEGF 165b to be matrix-stiffness dependent. Notably, the phosphorylation of serine-

arginine rich (SR) proteins that mediate splicing increased with matrix stiffness via a PI3/AKT pathway. These data suggest that other splice variant proteins that aberrantly appear in the extracellular matrix milieu of stiffened tissues, may also be mediated by matrix mechanics through a similar pathway. For example, the extra domain-A (EDA) type III repeat fibronectin (EDA-FN) variant is found in the abnormal matrix of atherosclerotic plaques *(424)*. Furthermore, TGFβ is often upregulated in pathologically stiff microenvironments, and contributes to splicing events, suggesting that alternative splicing may involve synergistic contributions between mechanical cues and ECM components *(425)*. SR proteins or the PI3/AKT pathways are potential therapeutic targets to control stiffness-mediated splicing events, in addition to current approaches using oligonucleotides and small molecules *(426)*.

Nuclear mechanics

The cell nucleus is mechanically coupled to the actin cytoskeleton by an assembly of proteins that comprise the linker of nucleoskeleton and cytoskeleton (LINC) complex, and by extension to integrins and the extracellular matrix *(427)*. Thus, as first described by the cellular tensegrity model, externally applied force, as well as cell-generated intercellular tension is propagated to the nucleus, which itself is a mechanotransducer *(427, 428)*. Force propagation across the cytoskeleton occurs orders of magnitude faster than biochemical signaling and the nucleus is involved in the integration and response to these mechanical inputs *(427)*. Because cellular DNA is stored in the nucleus, transmitted forces that induce changes in protein conformation, protein association, or deform chromatin may have transcriptional implications *(429)*.

Lamins are nuclear intermediate filaments that create a structured protein network associated with the interior nuclear membrane and are implicated in both nuclear mechanotransduction and matrix stiffening responses *(429)*. Of interest, lamin-A expression increases with matrix stiffness altering the structure and stiffness of the nuclear envelope *(430)*. In addition to transducing force, lamins are scaffolding proteins that interact with transcription factors and bind chromatin *(429)*. Lamin-dependent regulation of the MRTF-A/SRF and YAP/TAZ pathways may explain the excessive ECM production in many laminopathies, and demonstrate another mechanism by which ECM protein transcription is regulated by matrix stiffness *(431)*. Therapeutic targets for nuclear mechanotranduction are likely to be discovered in parallel with the development of improved technologies to study subcellular processes. However, the complexity and delicacy of the nucleus, coupled with our current understanding of mechanotransduction, suggest that the best therapeutic options to intervene lie within already discussed mechanotransduction sensing components. Force transmission to the nucleus requires cells under pre-stress which can be modulated by Rho contractility *(427)*. Additionally, MRTF-A and YAP/TAZ pathways can be targeted independent of lamin regulation as already described.

5.5 Conclusion

Two key players emerge from the discussion about potential therapeutic targets to overcome pathological extracellular matrix stiffening: TGFβ and Rho. Not surprisingly, their pleiotropic effects converge as they function in concert to promote feed forward

cycles that amplify extracellular matrix production and stiffening. However, they also represent elusive therapeutic targets because of their ubiquitous expression and important functions in healthy tissues. Indeed, a common underlying theme is a need for high potency and specificity among druggable efforts. Off-target interactions are a major hurdle for developing kinase inhibitors, and high toxicities have been crippling to the development of small molecules to prevent or disrupt matrix crosslinking. Moreover, these interventions need to be localized to the organs of interest to further minimize deleterious side-effects. Improved specificity is anticipated with aptamer technologies and new approaches to small molecule drug development that employ multi-faceted approaches combining thermodynamics, structural biology, and mathematical computation to identify novel sites for small molecule-protein interactions *(392)*. The identification of inhibitor sites on previously undruggable proteins, including Rho, should vastly expand the available therapeutic library.

With the recognition of ECM stiffness as a contributing factor to multiple pathologies across diverse organs, the advancement of clinical technologies to non-invasively measure local tissue mechanics are necessary to achieve earlier diagnoses and better patient outcomes. From an academic perspective, these modalities will contribute to an increased understanding of pathological stiffening in its earliest stages, and drive research efforts to identify novel clinical targets, perhaps even preventing full disease manifestation. An example of one such platform, is non-invasive tissue stiffness quantification by measuring the propagation of shear waves using high speed ultrasound imaging. Less shear is generated in stiff tissues, allowing for healthy and pathological tissues to be distinguished.

Over the past two decades, this technology has rapidly expanded from a 1-D measurement to 3D supersonic shear wave elastography with improved resolution and accuracy, and has been validated for clinical implementation *(432)*. The recently NIH funded total body positron emission (TB-PET) scanner is also expected to expand the understanding of ECM in disease. The technology is projected to identify micro-metastases beyond the current clinical resolution limit to gain new insights into the pre-metastatic niche *(433)*.

With the strong foundation of the mechanotransduction field and the importance of microenvironment stiffness built up over the past two decades, we can now work towards applying our knowledge to mitigating the effects of increased substrate mechanics in the emerging field of mechano-medicine. As has already been discovered for other pathologies, the most successful mechano-based therapeutic interventions will likely include drug cocktails to reach more than one target and overcome cellular redundancies.

CHAPTER 6

CONCLUSIONS AND FUTURE DIRECTIONS

6.1 Conclusions

Biochemical and mechanical cues from the extracellular matrix (ECM) are increasingly being appreciated for their role in regulating cell behaviors, both during development and disease progression. Notably, increased extracellular matrix stiffness is a hallmark of diverse pathologies, including atherosclerosis. Evidence now suggests that elevated matrix rigidity is not a passive outcome of disease, but instead, a cue that drives pathological progression. Thus, both the identification of cellular targets to overcome the cellular response to stiffness and an increased understanding of extracellular matrix mechanical cues on pathological cell behaviors are of high clinical importance. This dissertation investigates the role of the altered mechanical properties of the aged arterial intima on endothelial cells behaviors that contribute to atherosclerosis, a leading cause of death in the Western world. Using *in vitro* gel systems to modulate ECM stiffness and mimic the young and aged arterial intima mechanics, this work demonstrates that the endothelial cell response to increased matrix stiffness can be pharmacologically interrupted. Moreover, the heterogeneous spatial presentation of matrix stiffness cues in addition to an overall increase in elastic modulus are deleterious to endothelial monolayer integrity. This work also explores the emerging field of mechano-medicine with a detailed discussion of pre-clinical and clinical approaches to attenuate the effects of increased ECM stiffness on disease.

In Chapter 2, I investigated re-purposing the commercially available pharmaceutical simvastatin to ameliorate the effects of increased ECM stiffness on endothelial cell behaviors that are associated with poor endothelium barrier integrity, an initial step in atherogenesis. Because elevated RhoA activity scales with matrix stiffness and disrupts the endothelium, I hypothesized that statin treatment to prevent RhoA post-translational prenylation and membrane localization near activating guanine nucleotide exchange factors (GEFs) would attenuate the deleterious cellular response to increased matrix mechanics. Polyacrylamide gels with compliances between 2.5 and 10 kPa were fabricated to mimic the compliance of the young and aged arterial intima, respectively, and endothelial cells were treated with simvastatin. The data demonstrated that GTP-bound RhoA was decreased while GTP-bound Rac1 increased in endothelial monolayers following the statin treatment. Importantly, the altered GTPase signaling occurred in concert with protein recruitment to cell-cell adhesions that is associated with enhanced endothelium integrity. Moreover, focal adhesion size was decreased with simvastatin treatment demonstrating that disrupting RhoA and Rac1 activation interrupts matrix stiffness sensing at cell-ECM adhesions that are critical sites of outside-in and inside-out signaling.

The cardiovascular protective effects of statins are known to exceed their cholesterol lowering outcomes, and my data indicates that improved endothelium integrity from attenuated RhoA activity may be one underlying mechanism, especially in aged individuals where elevated artery stiffness is prevalent *(212, 434)*. These data complement *in vivo* models that implicate arterial stiffness as a contributor to atherogenesis, and notably,

indicate the validity of a pharmacological approach to overcome the cellular response to matrix mechanical cues. Prior *in vivo* work from our group demonstrated that inhibiting Rho-associated coiled-coil kinase (ROCK), the major downstream effector of RhoA in the cell contractility pathway decreased permeability in stiffer, aged arteries. However, the inhibitor employed in these studies, Fasudil, is not FDA approved in the United States and has off-target effects with the catalytic sites of other serine/threonine kinases. Kothapalli and colleagues used the lysyl oxidase inhibitor B-aminopropionitrile (BAPN) to prevent collagen crosslinking in a mouse model of atherosclerosis and reported more compliant arteries exhibited a reduced atherosclerotic burden. Furthermore, they identified a pathological feed-forward cycle of collagen, fibronectin, and lysyl oxidase expression in response to increased matrix mechanics that was attenuated in compliant arteries, and was later attributed to RhoA activation *(142, 435)*. However, these encouraging data are not transferrable to the clinic because BAPN toxicity precludes its use in patients. Therefore, the data presented in this dissertation identify that as an FDA approved drug, simvastatin could fill an unmet clinical need and mitigate the contributions of arterial stiffness to atherogenesis.

I further explored the effects of age-related arterial stiffness on endothelial cell behaviors that contribute to atherogenesis in Chapter 3 by developing an *in vitro* model to modulate the spatial presentation of matrix mechanical cues. Characterization of the subendothelial matrix by atomic force microscopy indicated that both mean intima stiffness and spatial stiffness heterogeneity increase with age *(122)*. Motivated by age-related stiffness heterogeneity in the arterial intima and evidence of crosstalk between integrin and cadherin

adhesions, I hypothesized that subcellular matrix stiffness cues could disrupt endothelial cell-cell junction integrity *(197)*.

A methacrylated hyaluronic acid (MeHA) hydrogel that sequentially crosslinks first by Michael-type addition followed by photo crosslinking, developed by the Burdick Lab at the University of Pennsylvania, was adapted to create a physiologically relevant platform to vary the spatial presentation of matrix stiffness. The hydrogel substrate had a checkerboard grid of high and low stiffness regions, and was characterized with respect to the elastic modulus, swelling, and stiffness pattern fidelity. The stiffness patterned hydrogel platform was then applied to investigate the endothelial cell response to subcellular increases in matrix stiffness, and the data revealed that cell-ECM adhesions corresponded to the local stiffness of the underlying matrix. Additionally, integrity of endothelial monolayers decreased with increased stiffness heterogeneity (50 by 50 μm vs. 100 by 100 μm features). Importantly, this study identified the spatial presentation of ECM stiffness as a mechanical cue that disrupts endothelial cell-cell junction integrity.

Because atherosclerotic plaques preferentially develop at distinct locations within the artery wall, and endothelium permeability within a monolayer is non-uniform, identifying physiological causes of local permeability is clinically relevant. A central dogma is that increased matrix stiffness causes increased RhoA-mediated cell contractility resulting in cell-cell junction disruption and permeability *(63, 185, 210)*. However, it is now emerging that the regulation of endothelial permeability is more complex than mean monolayer traction forces. Cellular forces within a monolayer are highly dynamic and exhibit spatial

variation. High traction force fluctuations rather than absolute force magnitudes predict intercellular gap formation *(275)*. Additionally, the effects of RhoA are dependent on spatio-temporal localization. Cytoplasmic RhoA localization near actin bundles is barrier disrupting *(242)*. At the cell periphery, hotspots of RhoA activity have been associated with adhesion formation and repair *(242)*. The MeHA hydrogel platform validated in Chapter 3 expands beyond prior studies investigating the deleterious effects of elevated matrix stiffness on endothelial cell behavior by incorporating matrix stiffness heterogeneity, a distinct characteristic of the aged arterial intima *(122)*. Intriguingly, RhoA activation, subcellular traction forces, and cell-cell junction tension scale with local ECM stiffness *(175, 187, 210, 258)*. And cytoplasmic coherence indicates that traction forces must be balanced even though local matrix stiffness cues can elicit different subcellular forces *(175, 277)*. In this context, my data suggests that spatial variations in age-related matrix stiffening may contribute to enhanced endothelial permeability and atherosclerosis by stimulating unstable cellular force generation.

Although vascular stiffening is a hallmark of atherosclerosis, other pathologies including cancer, fibrosis, and diabetes are also characterized by increased ECM stiffness that alters cell behaviors and promotes disease progression. In Chapter 5, I performed a literature review that investigated the emerging field of mechano-medicine. I discussed pharmacological interventions ranging from novel pre-clinical *in vitro* approaches to clinical trials aimed to overcome either matrix stiffening or the cellular response to increased matrix mechanics. The feasibility and challenges associated with each ECM or cellular target were highlighted. Because matrix stiffening is increasingly being identified

as a driving force in disease development, the advancement of mechano-based therapeutic approaches to the clinic has important patient implications across diverse pathologies.

Collectively, this dissertation investigated the role of age-related stiffness changes in the arterial intima on endothelial cell behaviors that contribute to atherosclerosis with an emphasis on clinical translation. I demonstrated the off-target effects of the available statin, simvastatin interrupt RhoA and Rac1 pathways to attenuate the endothelial cell response to increased matrix stiffness and enhance cell-cell adhesions. I next identified increased stiffness heterogeneity as a physiologically relevant ECM mechanical cue that disrupts endothelial monolayer integrity. Finally, I discussed clinical targets and therapeutic interventions to overcome pathologies driven by the cellular response to ECM stiffening. Cardiovascular pathologies initiated by atherosclerosis continue to be a leading cause of death in the Western world; therefore, the identification of novel therapeutic strategies, such as age-related matrix stiffness targeting, are of high clinical importance.

6.2 Future Directions

The research presented in this dissertation identified a method to pharmacologically overcome the cellular response to increased matrix stiffness and developed a novel hydrogel platform to determine that matrix stiffness heterogeneity disrupts endothelial monolayer integrity. These studies contribute to our understanding of the effects of altered matrix mechanics associated with aging on atherogenesis, and future studies will build upon these findings.

In Chapter 2, my data revealed that the pleiotropic effects of statins can be used overcome the cellular response to matrix stiffness by attenuating RhoA activation and reducing intercellular junction tension. However, statins have other reported atheroprotective effects and investigating their benefits in the context of age-related intima stiffening is of interest. Nitric oxide (NO) production by endothelial cells is critical to the regulation of vascular tone and is used as a marker of endothelial dysfunction. Intriguingly, the inhibition of RhoA by statins increases NO through stabilization of endothelial nitric oxide synthase (eNOS) mRNA and phosphorylation of mature eNOS *(436, 437)*. The activation of eNOS and NO production by shear stress have also been demonstrated to be matrix stiffness-dependent with reduced early signaling on rigid matrices *(287)*. These data lead to the hypothesis that statins would enhance NO bioavailability on stiff substrates to reduce endothelial dysfunction.

This dissertation focused on endothelium integrity as a gatekeeper to prevent cholesterol entry into the arterial wall and the initiation of atherogenic cascades. However, once initiated, atherosclerosis is largely recognized as a prolonged inflammatory pathology *(2)*. *In vivo*, atherosclerosis development is a complex process with contributions from multiple cell types; therefore, investigating the dual effects of ECM stiffness and statins on other cell types within the atherosclerotic plaque milieu is necessary for a comprehensive understanding of statins as a mechano-based therapeutic approach. Notably, immune cell transmigration is regulated via the Rho/ROCK/pMLC pathway, suggesting that statin inhibition of RhoA would interrupt this behavior and attenuate an inflammatory response *(438, 439)*. Moreover, because immune cell transmigration events across the endothelium

are substrate stiffness-dependent and are attributed to increased cell contractility that reduces endothelium barrier resistance *(63, 185)*; statins could have synergistic effects when acting on multiple cell types by combining enhanced endothelial integrity with reduced immune cell migration behaviors. Statins could also attenuate the mechanically driven pathological behavior of vascular smooth muscle cells that migrate to the arterial intima and contribute to atherosclerotic plaque progression. ECM stiffness-mediated MLC phosphorylation and cell contractility promoted the formation of migration associated circular dorsal ruffles in VSMC *(440)*. My data demonstrated that statins attenuated RhoA/pMLC activation caused by matrix mechanics, suggesting that VSMC migration would be suppressed by statins. VSMC proliferation also increases with matrix stiffness and proliferation caused by matrix stiffness is a RhoA-dependent process, implying another potential atheroprotective benefit of statin treatment in stiff, aged arteries *(441, 442)*.

In chapter 3, I developed and characterized a photocrosslinked hydrogel platform that was used to study endothelial single cell and monolayer responses to subcellular matrix stiffness cues. From the conclusion that spatial stiffness heterogeneity observed *in vivo* with advanced age is a monolayer disrupting cue when modeled *in vitro*, new questions arise to discern the underlying mechanistic processes.

An advantage of employing a photocrosslinking approach to create a stiffness patterned substrate is that feature size and presentation are easily tunable with new photomasks. My data demonstrated that decreasing the feature size to 50 by 50 μm squares to increase stiffness heterogeneity caused increased monolayer disruption. Future studies should

further reduce the feature size to determine a biophysical resolution of monolayer stiffness sensing heterogeneity. Data from single cell studies suggest that subcellular matrix mechano-sensing occurs at multiple length scales ranging from sub-focal adhesion nanometer sensing to cell-scale global responses *(443, 444)*. At cell-ECM adhesions a 58-73 nm separation is proposed as a universal length scale for integrin clustering and signaling, which suggests that much smaller subcellular mechanical features than investigated in this dissertation, can be discerned by monolayer cells *(445)*. At the same time, cytoplasmic coherence proposes a global mechano-sensitive contractile cellular response *(276, 277)*. Modulating stiffness pattern feature size across length scales could determine at which threshold subcellular and cellular scale sensing mechanisms dominate the monolayer response. The stiffness dependent nuclear localization of the transcriptional activators YAP/TAZ, which are also associated with a pro-atherogeneic mechanically stimulated inflammatory response, could be used as indicators of overall cell sensing of a compliant or rigid substrate *(410, 446)*.

In addition to changing the size of stiffness pattern features in the ECM, changing their spatial presentation is also interesting for future studies. Because arterial stiffening is a progressive and dynamic process, this data would provide insight into the degree of localized ECM stiffening that is necessary for monolayer disruption. Instead of creating a photomask of repeating stiffness patterns, stiffness islands of different sizes could be patterned. Matrix stiffness cues that cause cell contractile forces are transmitted into cell-cell junction tension, and Barry *et al*. have demonstrated that force transmission across VE-cadherin results in long range monolayer disruption *(187, 189)*. Thus, with stiffness islands

the dissipation of localized stiffness effects could also be evaluated. Finally, recognizing that more than two compliance levels exist *in vivo*, heterogeneity of stiffness levels within the substrate could be investigated by creating patterned gradient photomasks. For greater *in vivo* relevance, the stiffness profile of representative intimas from young and aged animals could be mapped using atomic force microscopy and recapitulated *in vitro* using a photomask with different opacities to match the magnitude and spatial presentation of the *ex vivo* measurements.

Studies to determine the underlying cellular mechanisms contributing to monolayer disruption caused by endothelial matrix stiffness heterogeneity would nicely extend the work presented in this dissertation. Mechanistic parallels between adhesion complexes at cell-matrix and cell-cell interfaces, and conserved scaffolding proteins used at both sites lead to questions related to the spatial regulation that governs adhesion integrity *(177, 191, 197)*. Interestingly, vinculin is paradoxically associated with both focal adhesion strengthening and cell-cell adhesion reinforcement, and its phosphorylation is adhesion specific *(197)*. In endothelial cells pharmacologically treated to enhance or disrupt monolayer integrity, vinculin localized to either cell-cell junctions or focal adhesions, respectively *(195)*. VASP, zyxin, and TES are also traditional focal adhesion proteins that are recruited in a tension dependent manner to adherens junctions, and together with vinculin, represent initial candidate proteins to investigate adhesion regulation *(196)*. A body of work has demonstrated that matrix stiffness promotes focal adhesion maturation and reinforcement *(173)*; therefore, it is hypothesized that stiff matrix regions would recruit shared adhesion strengthening proteins to the cell-ECM interface and destabilize cell-cell

contacts. Modulating the stiffness pattern feature size and compliance would elucidate at what threshold shared proteins are recruited to each adhesion type.

In concert with adhesion protein localization studies, quantitative measurements of force would contribute to an increased understanding of crosstalk between cell-ECM and cell-cell adhesions that contribute to matrix stiffness-mediated junction disruption. The FRET based tension sensors developed by the Schwartz group for vinculin and VE-cadherin could be used to simultaneously measure forces at focal adhesions and cell-cell junctions, respectively *(300, 304)*. These studies would elucidate how adhesion tensional force patterns within monolayers change with both uniform and heterogeneous matrix mechanics, and could be correlated with monolayer integrity. Additionally, because tension-dependent conformational changes in protein structure recruits scaffolding proteins, the recruitment of adhesion strengthening proteins could be quantitatively assessed with respect to adhesion tension and matrix rigidity *(177, 191)*. Monolayer traction force studies on mechanically heterogeneous substrates are also of interest to investigate the physiologically relevant multi-cell response that includes cell-cell force transmission through both the ECM and cell-cell junctions *(189, 275, 447)*.

The data presented in this dissertation identified a pharmacological approach to mitigate the cellular response to age-related arterial stiffening and determined that matrix stiffness heterogeneity in addition to a bulk increase in rigidity alters endothelial behaviors towards an atherogenic phenotype. Because cardiovascular diseases initiated by atherosclerosis continue to be prevalent and deadly, novel therapeutic methods beyond lipid lowering

strategies are needed. The experiments described in the future directions will provide useful insight into the clinical utility of targeting the age-related mechanical properties of the intima from a biophysical perspective.

APPENDIX A

PROTOCOL FOR METHACRYLATED

HYALURONIC ACID POLYMER SYNTHESIS

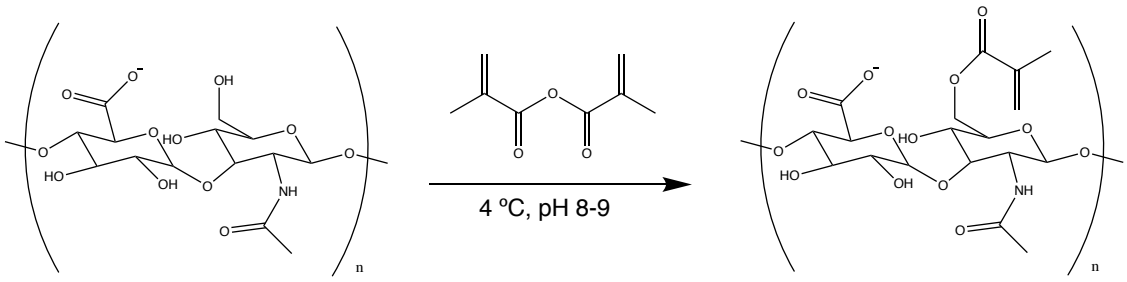

Materials:

Sodium hyaluronate (HA) (Lifecore Biomedical, 59 kDa)

50 mL conical tubes

Methacrylic anhydride

5 N NaOH

Three neck round bottom flask

Ice bucket

Ice

Stir plate and stir bar

pH meter

Parafilm

Cell strainers (70μm)

4 L Glass beaker

Dialysis tubing (6-8 kDa MWCO)

Protocol for Methacrylated Hyaluronic Acid Polymer Synthesis:

Day 1:

1. Weigh out 0.5 g HA in 6- 50 mL conical tubes (total 3 g HA).
2. Add 50 mL of DI water to each conical tube (300 mL total).
3. Vortex to dissolve the HA.
4. Place the round bottom flask in a container of ice and place the set-up on a stir plate.
5. Pour the dissolved 1 wt% HA solution from the conical tubes into the round bottom flask on ice.
6. Insert the pH probe into one of the round bottom flask openings and secure it with a clamp.
7. Turn on the stir plate and set it to a fast stir rate to create a vortex.
8. Slowly dissolve 7.66 mL methacrylic anhydride drop-wise into the HA solution. Adjust the pH with 5 N NaOH to maintain a reaction pH of ~8-9.
9. Continue the polymerization reaction for 8 hours monitoring the pH and adding 5 N NaOH dropwise as necessary to maintain a pH of ~8-9.
10. Remove the pH probe and seal the openings of the round bottom flask with Parafilm.
11. Store the polymer reaction solution at 4 °C overnight.

Day 2:

12. Set-up the round bottom flask on ice with the pH probe and stir plate as was done the previous day.

13. Add 3.6 mL methacrylic anhydride (1.2 mL/g HA), drop-wise. Adjust the pH with 5 N NaOH to maintain a reaction pH of ~8-9.
14. Continue the polymerization reaction for 4 hours monitoring the pH and adding 5 N NaOH drop-wise as necessary to maintain a pH of ~8-9. Note: Goal is ~100 mol% HA modification with methacrylates.
15. Soak dialysis tubing in DI water.
16. Filter the reaction product solution through cell strainers into the dialysis tubing.
17. Fill a 4 L beaker with DI water and dialyze the polymer solution against water at room temperature.

Days 3-9:

18. Change the dialysis DI water at least 1x per day. Continue the dialysis at least 1 week at room temperature.

Day 10:

19. Remove the MeHA polymer solution from the dialysis tubing and place it in 50 mL conical tubes
20. Freeze the polymer solution at -20 ºC.

Day 11

21. Lyophilize the polymer product.
22. Store the final product in desiccant protected from light.
23. Perform NMR characterization to confirm MeHA synthesis and modification %.

APPENDIX B

PROTOCOL FOR METHACRYLATED HYALURONIC ACID HYDROGEL FABRICATION

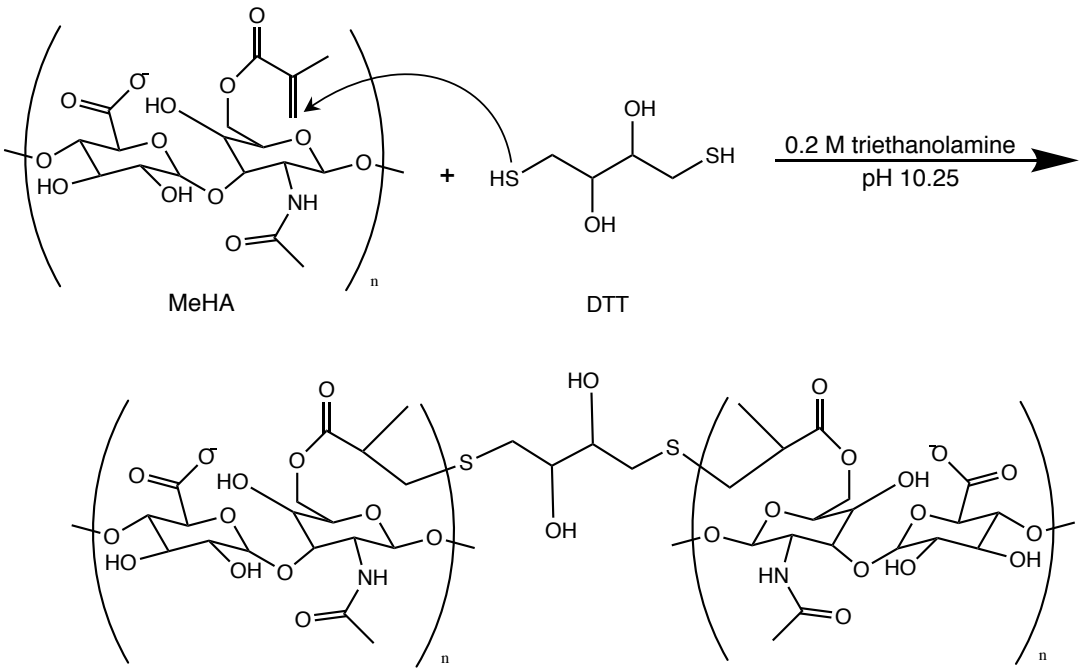

Materials:

22 x 22 mm activated coverglass

22 x 22 mm non-activated coverglass

50 mL conical tubes

15 mL conical tube caps

RGD peptide (GCGYGRGDSPG, Custom Synthesis, Genscript), aliquoted to 50 mg/mL in PBS and frozen

0.2 M triethanolamine (TE) buffer in PBS**,** pH 10.25

Synthesized methacrylated hyaluronic acid (MeHA)

Dithiothreitol (DTT)

Reagents per 50 mL conical tube reaction:

MeHA	22.0 mg
TE buffer, pH 10.25	687 μL
RGD, 50 mg/mL in PBS	15 μL
DTT, 25 mg/mL	31 μL

Protocol for Methacrylated Hyaluronic Acid Hydrogel Fabrication:

1. Remove DTT from the freezer.
2. Weigh out MeHA and place it in a 50 mL conical tube.
3. Dissolve MeHa in the TE buffer using the vortexer to create a 3 wt% solution.
4. Add the RGD peptide (sterile aliquots – 50 mg/mL in PBS) at a final concentration of 1 mM.
5. Vortex the mixture.
6. Change the vortex platform to the conical tube foam inserts.
7. Vortex the mixture 45 minutes on medium. The Michael-type addition reaction of the RGD peptide is pH controlled – pH≥8.
8. Prepare a 25 mg/mL DTT solution in TE buffer and vortex ~45 seconds. Make this fresh every time and use it immediately because it is reactive with air. Note:

Initial gel stiffness can be modulated by varying the DTT concentration to increase or decrease crosslinking.

9. Place an activated 22 x 22 mm coverslip with the activated side facing up on top of a 15 mL falcon tube lid to create a “pedestal” to polymerize the gel.
10. Change the vortex platform back to the standard cup fitting.
11. Add DTT to the gel solution and vortex to mix. Use immediately. Note: Polymerization starts immediately and is controlled by the % DTT and reaction pH.
12. Make gels by pipetting 80 μL of the gel solution directly onto the activated coverslip.
13. Carefully slide a clean (non-activated) coverslip over the gel drop. The gel will polymerize between the two coverslips.
14. Protect the gels from light during polymerization by covering with an upside-down tray or tented foil.
15. Polymerize gels 2 hours.
16. Peel off the top coverslip using a razor blade.
17. Place gels in a 6 well-plate and swell in 3-4 mL of sterile PBS overnight before use. Can be stored up to 2 days if necessary.

APPENDIX C

PROTOCOL FOR METHACRYLTED HYALURONIC ACID HYDROGEL PHOTOCROSSLINKING

A. Free Radical Generation:

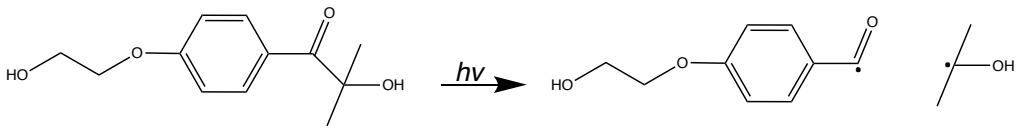

I2959 Initiator Radical Species (I)

B. Radical Polymerization:

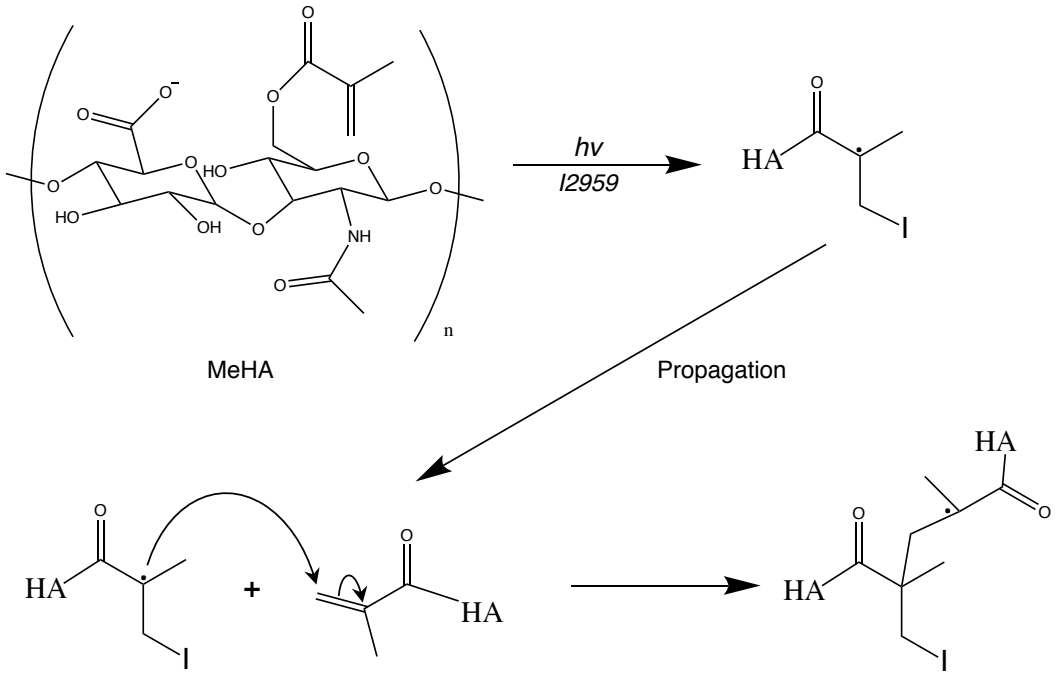

Materials:

Polymerized methacrylated hyaluronic acid (MeHA) hydrogels

Irgacure 2959 (I2959) photoinitiator

1x PBS

Warm 1x PBS buffer for rinses (4 mL per sample)

Cell culture media

UV lamp (320-500 nm, 100 watt mercury bulb)

UV light meter

Protocol for Methacrylated Hyaluronic Acid Hydrogel Photocrosslinking:

Day 0

1. Prepare a 0.5 wt% I2959 stock solution in 1x PBS. Vortex overnight to fully dissolve, sterile filter, and store protected from light in foil at 4 ºC.

Day 1

2. Dilute the 0.5 wt% I2959 stock solution 1:10 to 0.05 wt% in media or sterile PBS for cell or mechanical testing studies, respectively.
3. Transfer gels to sterile 35 mm Petri dishes.
4. Add 2 mL of the 0.05 wt% photoinitiator solution to each dish.
5. Incubate the gels with the photoinitiator for 30 minutes at 37 ºC and 5% CO_2.
6. Turn on the UV lamp and allow it to warm-up.

7. Adjust the vertical height of the light guide so the light intensity at the gel surface is 10 mW/cm^2. Note: Make sure the UV light meter probe is calibrated at the same vertical height as the gels in the Petri dish.
8. Expose an individual hydrogel to the desired amount (time) of UV light. The media color will turn purple in the presence of free radicals.
9. Immediately rinse the gel 2x with warm PBS, and add fresh media.
10. Return the gel to the cell incubator.
11. Repeat steps 8 and 9 for all remaining gels.
12. Refresh the cell culture media after UV crosslinking has been completed for all the samples.

APPENDIX D

PROTOCOL FOR MICROINJECTION OF ADHERENT CELLS

Materials:

Eppendorf FemtoJet injector

Eppendorf Injectman NI2 microinjector

Femtotips injection tips (Eppendorf Cat #930000035) or custom pulled tips

Microloader tips (Eppendorf Cat #930001007)

Cells to inject in a traction chamber

Lysine fixable 10,000 MW Alexa Fluor 488 dextran

Microcentrifuge or 0.22 μm syringe filter

Solution for microinjection—Should be 10-20x the optimal *in vitro* concentration

Parameters to adjust for microinjection

These parameters can be adjusted using the knobs on the FemtoJet injector unit. The volume delivered to the cells is a product of the (injection pressure) x (injection time).

- Pc (Compensating pressure): The constant back pressure to prevent capillary action from pulling media from the sample dish into the injection needle. If Pc is not stable your needle is broken or a gasket needs replacement.
- Pi (Injection pressure): The pressure used to inject your solution.
- Ti (Injection time): The amount of time the injection needle is inside a cell at the set injection pressure delivering your solution.

Good starting parameters are: Pc: 30 hPa, Pi: 170 hPa, and Ti: 0.1-0.3 s, but can be empirically determined for each system based on the literature for specific cells, reagents, and needle geometry combinations.

Protocol for Microinjection of Adherent Cells:

1. Turn on the LSM microscope, fluorescent bulb, CO_2, and heat, and allow the environmental chamber to stabilize at 37 °C and 5% CO_2.
2. Place the cell sample in an assembled traction chamber on the microscope and bring the cells into focus using the 20x objective and the TPMT LSM mode.
3. Turn on the FemtoJet injector unit using the switch on the back of the module and allow it to warm-up and complete a self-check. Make sure the pressure tubing is detached at this point.
4. Press the menu button on the FemtoJet injector unit to temporarily turn off the pressure and wait until a message prompting you to change the capillary appears.
5. Attach the pressure tubing to the injector unit on one end and the metal shaft of the injection needle holder on the other end.
6. Press the menu button. Note: The Cp pressure will not stabilize unless the injection capillary is attached.
7. Prepare the microinjection sample:

    Note: The sample will dry out quickly and clog the injection needle tip if you let it sit for a long period of time, so have your cells ready to go on the microscope and the microinjection unit set-up before loading the tips.

a. Prepare the injection solution in PBS or other physiological buffer at 10-20x the optimal *in vitro* concentration.
b. Add a co-injection fluorescent marker at a 1-10 mg/mL final concentration. The lysine fixable Alexa Fluor 488 dextran works well at 10 mg/mL. If you want to fix, permeabilize and stain your cells after microinjection, make sure you use a fixable fluorescent dextran. Normal FITC will wash out of the cells during permeabilization and washing.
c. Filter the final microinjection solution through a 0.22 μm syringe filter or centrifuge it for 15 minutes at the highest speed and remove the supernatant.
d. Using a microloader tip, pick up 3 μL of the solution to be injected, and thread the microloader into the top of a glass injection needle all the way to the bottom.
e. Release the injection solution at the bottom of the capillary as you are removing the pipette.
f. If air bubbles are present, vigorously flick your wrist repeatedly to remove the bubbles and force the liquid solution to the bottom of the microinjection capillary.

8. Press the menu button on the FemtoJet injector unit and wait until a message prompting you to change the capillary appears.
9. Attach the loaded glass capillary needle to the free end of the injection needle holder.

10. Press the menu button on the FemtoJet injector unit to resume pressure through the tubing. The Cp (compensating pressure) on the FemtoJet injector screen should be constant. An unstable Cp indicates that a gasket should be changed or your needle is broken. Note: If there is no back pressure in your needle as you lower it into the cell media to inject, capillary action can pull media into the needle tip and will dilute your injection solution.
11. Press the clean button on the FemtoJet injector unit to push a high pressure burst through your needle tip to clear it.
12. Tilt the injection motor unit (black casing attached to the microscope) downwards into the load position.
13. Wake-up the Injectman NI2 microinjector joystick unit by pushing the standby button.
14. Press the coarse adjustment button on the joystick unit and lower the microinjection tip into your sample by rotating the joystick until you can visually see that it is beneath the liquid surface.
15. Turn on the appropriate fluorescent channel for your co-injection marker and visually move the tip in the x-y plane using the joystick to the general vicinity of the objective center.
16. Press the fine adjustment button to slow the speed of the needle movement.
17. Using the oculars, slowly lower the injection needle until it comes into a sharp focus. The solution inside the needle will have a bright fluorescent signal. The needle will appear rounded if you are centered away from the tip on the body of

the glass capillary, but will focus as you lower the needle and translate it horizontally to focus on the tip.

18. Switch to the LSM imaging mode, and using the TPMT make sure both your cells and injection needle are in focus. If you need to change the z-plane of the stage to bring your cells into focus, significantly raise up the needle first, focus the cells, and then slowly lower the needle back down.
19. To perform an injection, lower the microinjection needle until you visually see the cell membrane of the target cell slightly deform and that the needle has entered the cell.
20. Press the limit button on the Injectman joystick unit. This sets the z-limit where the needle is currently located as the location where the injection will occur. You will not be able to manually move the joystick lower than this z-position unless you push the limit button again to remove the current set z-limit.
21. Raise the needle and move it to a new cell. Lower the needle until it hovers just over the top of the new target cell membrane.
22. Push the inject button or the button on the top of the joystick to inject the target cell using the current injection pressure and time settings. The injection needle will raise up and move backwards at a 45° angle, and then lower down at the same angle to pierce the cell.
23. Use your co-injection signal to verify that material was successfully delivered to the target cell.
24. Continue moving around your cell sample injecting cells. Raise the needle up before any large movements of the sample. Because your sample is likely not

completely flat due to variations in the coverglass thickness and the amount of vacuum grease used to attach the coverglass to the traction chamber, it may be necessary to reset the injection z-limit for different regions of your sample.

25. If the injection needle becomes clogged, use the home button to retract the needle out of the solution and press the clean button to push through a high burst of pressurized air. Use the home button to return the needle back to your sample. Note: If you move the needle with the joystick unit after retracting it, the home function will not work to return the needle. Repeatedly using the home feature to retract and lower the needle can also be used to remove debris that are stuck to the needle exterior.
26. If your needle breaks or becomes clogged and needs replacement:
    a. Use the home button to retract the needle out of the solution.
    b. Tilt the injection motor unit attached to the microscope backwards.
    c. Press the menu button until it prompts you to change the capillary.
    d. Remove the old injection needle.
    e. Fill a new injection needle with solution.
    f. Return to step 8, and proceed through the protocol.
27. To turn off the microinjection unit:
    a. Use the home button to retract the needle out of the solution.
    b. Tilt the injection motor unit attached to the microscope backwards.
    c. Press the menu button until it prompts you to change the capillary.
    d. Remove the injection needle.

e. Firmly press and hold the standby button for 3 seconds on the FemtoJet injector unit until you hear a loud exhaust as the pressure is bled out of the diaphragm. The FemtoJet inject unit will prompt you to wait, and then enter standby mode.
f. Turn off the FemtoJect inject unit using the switch on the back.
g. Disconnect the pressure tubing.
h. Press the standby button on the Injectman microinjector unit until the display dims.

Other Notes:

- The FemtoJet injector unit will record the number of injections you have performed. It is the "n" number on the screen.
- The menu button on the FemtoJet injector unit can be used to enter into various menus and change advanced settings. Use the knobs on the front of the unit to cycle through menu options.
- The Pos 1/Pos 2 buttons on the Injectman Unit are memory keys that can be used to save positions. Pushing the button saves the position. Pushing the button at the saved position removes it.

APPENDIX E

PROTOCOL FOR LOCAL SUBCELLULAR PERMEABILITY ASSAY

Adapted from Dubrovskyi et al., 2013.

A. Biotinylated Gelatin Synthesis:

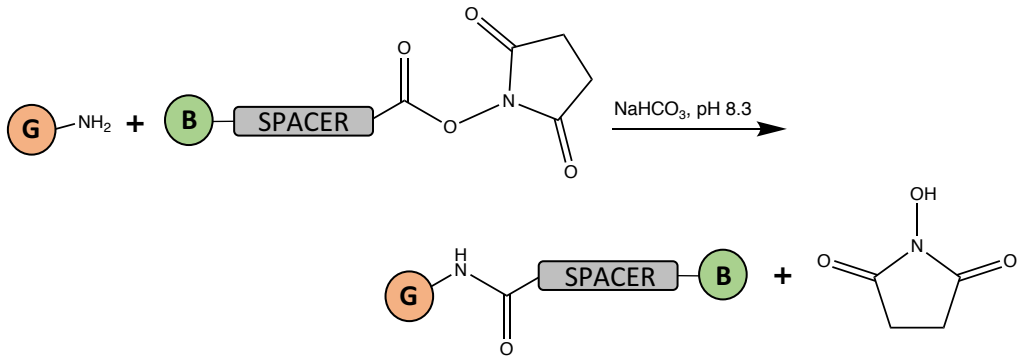

B. Biotin-Streptavidin Interaction:

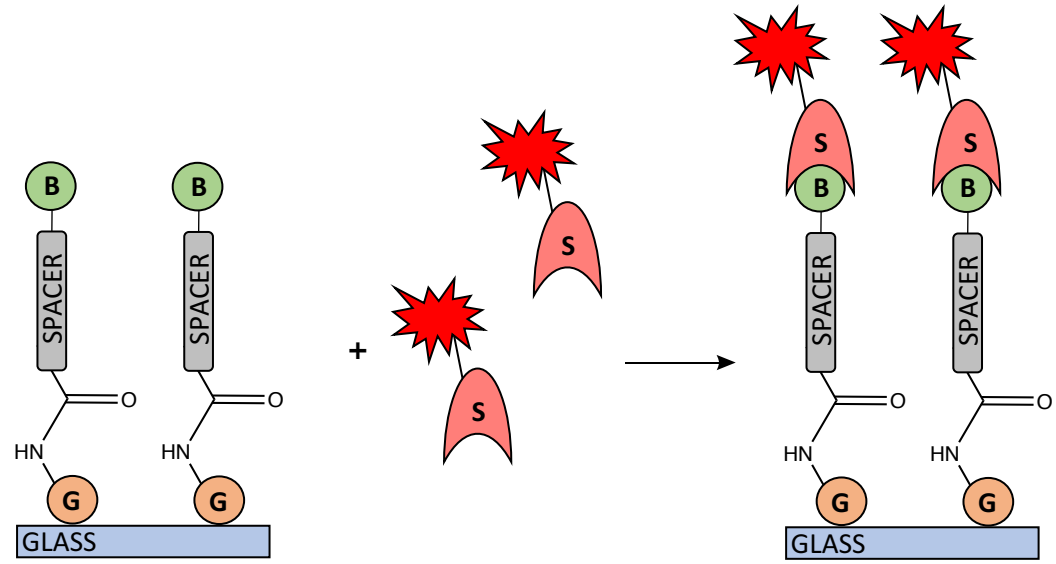

Materials:

Type A porcine gelatin

0.1 mol/L $NaHCO_3$, pH 8.3 buffer

EZ-Link NHS-LC-LC-Biotin (Cat. #21343, Thermo Scientific)

DMSO

Hot/stir plate and stir bar

Water bath

Centrifuge

Protocol for Synthesis of Biotinylated Gelatin:

1. Allow the NHS-biotin to warm to room temperature.
2. Prepare a 70 ºC water bath.
3. Prepare a 10 mg/mL gelatin solution in 0.1 mol/L $NaHCO_3$, pH 8.3 and dissolve the gelatin by heating the solution in the water bath with continuous stirring.
    a. Example: 600 mg gelatin in 60 mL of $NaHCO_3$, buffer
4. Centrifuge the gelatin solution for 5 min at 10,000 x g at room temperature to clarify.
5. Dissolve the EZ-link biotin in DMSO at 5.7 mg/mL and mix by pipetting up and down.
    a. Example: 28.5 mg EZ-link biotin in 5 mL DMSO
6. Combine the biotin and gelatin solutions in a 1:10 ratio for a final biotin concentration of 0.57 mg/mL biotin.
    a. Example: 45 mL of gelatin from #4 and 5 mL of biotin from #6

7. React for 1 hour at room temperature to conjugate the biotin to the gelatin.
8. Prepare 3 mL aliquots of the biotinylated gelatin and store at -20 ºC.

Materials:

0.57 mg/mL biotinylated gelatin aliquots, stored at -20 ºC

0.1 mol/L $NaHCO_3$, pH 8.3 buffer

Parafilm

Activated 22 x 22 coverglass or PA gels on 22 x 22 coverglass

6 well plate

PBS

Protocol for Coating Coverglass with Biotinylated Gelatin for Cell Studies:

1. Thaw biotinylated gelatin aliquots in a 37 ºC water bath for 10 minutes.
2. Add 0.1 mol/L $NaHCO_3$ buffer for a final protein concentration of 0.25 mg/mL.
    a. Example: 3.35 mL buffer per 3 mL aliquot.
3. Create 200 µL drops of the protein solution on Parafilm.
4. Invert coverlass onto the liquid drop with the activated side (or PA gel) touching the protein solution and incubate for 30 minutes at room temperature.
5. Place coverglass in a 6 well plate and rinse with PBS.
6. Proceed to cell culture.

Materials:

Confluent cell monolayers cultured on a biotinylated gelatin substrate

Alexa Fluor 568 streptavidin

Cell culture media, warmed to 37 ºC

PBS

3.7 % formaldehyde in PBS

Protocol for Localized Subcellular Permeability Assay:

1. Prepare a 25 μg/mL solution of Alexa Fluor 568 streptavidin in warm cell culture media.
2. Remove the culture media from samples and add 2 mL of the streptavidin containing media.
3. Incubate 5 minutes.
4. Wash samples 2x with 3 mL PBS.
5. Fix samples with 3.7% PFA.
6. Proceed to cell staining
7. Visualize stained cellular structures and the fluorescent biotin-streptavidin signal.

APPENDIX F

PROTOCOLS FOR PLASMID AND LENTIVIRUS MOLECULR BIOLOGY

Contents:

F.1 Process Flow

1. Pick gene of interest.
2. Choose plasmid source.
    a. Addgene (Type of vector dictates where in the process flow you begin)
    b. cDNA
3. Primer design
4. Convert mRNA to cDNA
5. Generate the plasmid (i.e. with overlapping PCR)
    a. Sample 1: Overlapping PCR to create construct of interest
        i. Overlapping PCR for fusion constructs
        ii. Amplification PCR
        iii. PCR cleanup
        iv. Restriction digest
        v. Agarose gel electrophoresis
        vi. Agarose gel extraction
        vii. Preparation of LB + Ampicillin agar plates
        viii. Ligation
        ix. Transformation
        x. Sequencing
    b. Sample 2: Modify an existing plasmid (i.e. replace a fluorescent tag)
        i. Amplification PCR for replacement sequence
        ii. PCR cleanup
        iii. Restriction digest

iv. Agarose gel electrophoresis

v. Agarose gel extraction

vi. Ligation

vii. Transformation

viii. Sequencing

6. Preparation of LB + Ampicillin broth
7. Inoculation
8. Midiprep
9. Transfection
10. Lentiviral concentration
11. Transduction

F.2 Primer Design

1. Find the reference sequence for the gene of interest.
    a. NCBI has reference sequences for many genes:
    http://www.ncbi.nlm.nih.gov/gene
    b. Under NCBI Reference Sequences:
        i. NM = DNA sequence referring to mRNA
        ii. NP = DNA sequence referring to polypeptide (final protein)
    c. Many proteins undergo processing. Click on NM to view the mRNA.
        i. CDS = Coding sequence (ORFs), excluding introns and 5'/3' UTR (click to highlight in the sequence)
        ii. Sig_peptide = DNA sequence referring to the signaling portion of the peptide
            1. If you want to change the N-terminus region, this could interfere with the signaling peptide function (i.e. secretion).
        iii. Mat_peptide = DNA sequence referring to the mature peptide
    d. To find the protein structure:
        i. UniProt (http://www.uniprot.org/) provides information on protein structure.
    e. Efficiency of transfection is inversely related to the plasmid size.
2. Manipulate the mRNA gene sequence in ApE plasmid editing software.
    a. http://biologylabs.utah.edu/jorgensen/wayned/ape/
    b. Example: Adding GFP to the C-terminus
    c. Copy the desired mRNA into a new file in ApE.

i. Annotate features with “Features” → “New Feature”

ii. Highlight restriction sites with “Enzymes” → “Highlight”

d. [if needed] Delete unnecessary stop codons (TAA, TAG, TGA).

e. [if adding a GFP reporter] Open the eGFP sequence (brighter than GFP) and copy the sequence at end of the mRNA sequence.

i. Do not include the “ATG” sequence because the gene already has a start codon from the fusion protein mRNA. Keep the stop codon after the eGFP sequence.

f. Check existing restriction sites within your plasmid and the desired mRNA insert using the enzyme tab.

i. Open the graphic maps and highlight unique restriction sites.

1. You need 1 unique restriction site before and after the inserted sequence.

ii. Only use restriction enzymes that have 1 restriction site within the polyclonal site.

g. Copy the entire [fusion] gene sequence into your plasmid between your two unique restriction sites that are also not present within your [fusion] sequence.

h. It is good practice to check the amino acid sequence of your construct. Select the sequence you would like to translate, and click “ORFs” and “Translate” to view the amino acid sequence.

i. Adding a **Kozak** sequence can improve protein expression if placed directly before the start codon: **GCCGCC** (ATG).

3. Designing primers for amplification.
    a. The melting temperature of the primers is an important parameter.
        i. Increasing the length of the DNA increases the melting temperature: generally want ~20 nucleotides.
        ii. Increasing the GC content of the DNA increases the melting temperature: generally want ~50%.
        iii. The melting temperature of the primers should be similar: generally around ~60 °C is optimal.
    b. Also avoid three CG nucleotides at the beginning or end of a primer because it reduces the binding specificity.
    c. Add a kozak sequence before the annealing sequence on the forward primer (if desired).
    d. Add restriction sites for future digestion with restriction enzymes.
    e. Add additional overhang 4-6 base pairs (length required depends on the specific restriction enzyme) of random A,T nucleotides (decreases the T_m).
    f. Example forward primer:
        i. Overhang – XbaI – Cozak – 1st 20 NTs
        ii. atta – TCTAGA – gccacc – "1st 20 NTs"
    g. Example reverse primer:
        i. Reverse complement of [Last 20 NTs – EcoRI – overhang]
        ii. Reverse Complement of ["Last 20 NTs" – GAATTC – atta]

4. Designing primers for sequencing:
    a. Generally, the 1st 50 base pairs after the primer are noisy, the next 800 base pairs are reliable, and the signal is noisy and unreliable beyond 800 base pairs.
    b. Design multiple primers from the plasmid sequence regions of interest such that the entire construct is sequenced.
    c. Addgene has standard primer sequences listed for specific lentiviral backbones and their features.
5. Order primers from Integrated DNA Technologies (IDT).
    a. 25 nm DNA oligo
    b. Standard desalting

F.3 Conversion of mRNA to cDNA

Materials:

RNA to cDNA EcoDry™ Premix (Oligo dT) kit (Clontech Cat. #639543)

1-5 µg RNA

20 µL endotoxin free water

PCR machine

Nanodrop

Microcentrifuge

Protocol for Conversion of mRNA to cDNA:

1. Measure mRNA using the nanodrop and calculate the volume needed to obtain 1-5 µg of total mRNA.
    a. Example: 406.6 ng/µL → 5 µL mRNA
    b. 230 nm peak = salt contamination
    c. 280 nm peak = protein concentration (benzene rings)
2. Dilute mRNA to a final volume of 20 µL.
    a. Example: 5 µL mRNA = 15 µL nuclease free water
3. Add 20 µL of RNA dilution to each tube of EcoDry premix that is needed.
4. Pipette up and down several times to dissolve the pellet, then cap the tube(s).
5. Spin briefly in a centrifuge.
6. Use the PCR Machine to conduct the reaction:
    a. Incubate at 42 °C for 60 minutes.
    b. Stop the reaction by heating at 70 °C for 10 minutes.

7. Store cDNA at -20 °C (4 °C is fine for use the next day).

F.4 PCR Amplification

Materials:

100 ng template DNA

10 μM primers (forward & reverse) (order from IDT, 25 nmole DNA oligo, standard desalting)

dNTP mixture (New England Biolabs Cat. #N0447S)

DNA polymerase

a. Taq (New England Biolabs Cat. #M0273L)
b. PFU (Agilent Technologies Cat. #600255-52)
c. LA Taq (Clontech Cat. #RR02AG)
d. Phusion (New England Biolabs Cat. #M0530S)

Polymerase buffer

a. Taq: 10x standard Taq buffer
b. PFU: 10x cloned PFU reaction buffer
c. LA Taq: 2x LA Taq GC buffers
d. Phusion: 5x standard and GC Phusion buffer

Nuclease free water

PCR machine

Microcentrifuge

Protocol for PCR Amplification:

1. Reconstitute lyophilized primers (if necessary).
    a. Spin lyophilized DNA at 12,000 rpm for 1 min.
    b. Reconstitute with autoclaved water to 100 µM (stock solution).
        i. Example: DNA amount = 27.4 nmol, add 274 µL water to get 100 µM
    c. Shake to mix.
    d. Complete a short spin after mixing (5,000 rpm).
    e. Dilute primers to a working solution of 10 µM.
        i. Example: Add 180 µL of water to 20 µL of primer
        ii. This is good for ~1 month.
2. Create a PCR master mix.
    a. In order add: water, template, primers, dNTPs, buffer.
        i. Keep enzymes cold in a cryosafe box (-20 °C).
        ii. Buffer should be thawed completely and mixed via inversion.
    b. Aliquot master mix to PCR tubes.
    c. Add polymerases.
        i. The pipette tip should only touch the interface of the enzyme stored in viscous glycerol. You do not want excess polymerase on the pipette tip to avoid star activity (reduced specificity).

d. Example reaction mix: Phusion polymerase:

i.	Template (100 ng)	1 uL
ii.	Forward primer (10 μM)	5 μL
iii.	Reverse primer (10 μM)	5 μL
iv.	dNTPs (10 mM)	1 μL
v.	5x Phusion buffer	10 μL
vi.	Phusion	1 μL
vii.	Nulcease free water	27 μL
viii.	**Total volume**	**50 μL**

3. Run PCR as per the polymerase specific protocol, which can be optimized from NEB software available online.
    a. Modify extension time to fit the product size and polymerase speed (i.e. Taq is slower than Phusion).
    b. Cycle 3 is a final extension cycle to complete any fragments that were not completely synthesized.
4. Notes:
    a. The annealing temperature for Taq should be 4-5° lower than the melting temperature for the primers **without** the restriction site. Use what the API software predicts without the restriction sites and not what IDT reports on the primers.
    b. The annealing temperature for Phusion can be the melting temperature.
    c. In general, the annealing temperature should be 4-5 °C lower than melting temperature of primers.

i. Higher temperatures drive specificity of primer binding.
ii. Lower temperatures allow DNA to bind.
iii. Useful tool: http://tmcalculator.neb.com/#!/

d. A Taq/PFU mixture mixes a high efficiency enzyme with a slow, accurate enzyme (mix 1:1 ratio).
    i. Taq is the most common and a very efficient enzyme: 1 kB/min. Can amplify difficult templates.
    ii. PFU is slow, but very accurate: 800 bp/min. Has an error checking function.
e. Phusion from New England Biolabs is a very accurate and very fast enzyme (if it works, use it!).
    i. Sometimes it will not bind GC rich templates.
    ii. Very fast: 1 kB/15 s
f. LA Taq is a last resort enzyme for difficult transcripts.
    i. It is good for templates that are difficult, but an expensive enzyme.
g. Hot Start
    i. Add the enzyme after 30 seconds of denaturing.
    ii. Avoids non-specific amplification of DNA by enzymes at lower temperatures.

F.5 Agarose Gel Electrophoresis

Materials:

DNA

Ethidium Bromide – intercalating agent that is carcinogenic

1x TAE electrophoresis buffer

Agarose powder

6x Loading dye (Invitrogen Cat #XR0611)

1 kB Plus DNA ladder (Invitrogen Cat #10787018)

Erlenmeyer flask (designated for ethidium bromide)

Graduated cylinder

Gel casting tray and combs

Hot plate (for extraction)

Microwave

Surgical blade

UV trans-illuminator

Protocol for Agarose Gel Electrophoresis:

1. Prepare 50 mL of 1x TAE electrophoresis buffer and pour it into the Erlenmeyer flask.
    a. TAE buffer can be reused 2-3 times for verification gels.
    b. Use fresh TAE buffer if performing gel extraction for a purified product.
2. Make an agarose gel of the appropriate wt%.

a. Measure and the add appropriate amount of agarose powder to 1x TAE buffer.
    i. Example: 0.8 % agarose gel:
        1. ~60 mL of 1x TAE buffer
        2. 0.48 g agarose
    ii. The amount of agarose is dependent on the desired resolution of the gel.
    iii. A 0.8 % agarose gel is versatile with the ability to separate fragments from 0.5 – 12 kB.
b. Heat up the agarose solution in the microwave.
    i. Heat for 30 seconds, swirl, heat for 30 seconds.
c. Allow the agarose solution to cool until it is warm enough to hold.
    i. The warm agarose solution can be cooled by running cold tap water along the outside of the flask.
d. Add ethidium bromide to the warm (40 – 50 °C) agarose solution.
    i. Do NOT add ethidium bromide to hot agarose (Volatile ethidium bromide becomes a carcinogenic fume!).
    ii. Add a 10,000 fold dilution of 5 mg/mL ethidium bromide.
        1. Example: 6 µL to 60 mL of agarose solution
    iii. Store extra ethidium bromide in foil (it is a fluorescent molecule).
e. Pour the warm agarose solution into the gel casting tray and add combs.
f. Allow the gel to solidify at RT for at least 1 hour OR at 4 °C (cold room) for 30 minutes.

g. Once the gel is solidified:
    i. Remove combs.
    ii. Cut the gel to separate each half and to only include the desired number of lanes.
    iii. Store extra gel pieces at 4 °C in an empty pipette tip box with 1x TAE buffer with 1:10,000 ethidium bromide (extra gels are good for ~1 week).

3. Place the gel in the electrophoresis unit and cover with 1x TAE buffer.
4. Prepare DNA samples.
    a. For simple verification:
        i. Add 1 µL of DNA to 5 µL of 6x loading dye.
        ii. Mix loading dye and DNA on parafilm.
    b. For gel extraction, use wide lanes and 40 µL of DNA and 5 µL of loading dye.
        i. Electrophoresis is constrained by lanes that can only hold 50 µL volume.
        ii. Separate lanes by 1 empty lane to avoid contamination.
        iii. Load with the tip at the bottom of the well to avoid losing sample.
    c. Add 2-3 µL of 1 kB plus DNA ladder to an empty well.
        i. To dilute a stock ladder (1 µg/µL to 100 ng/µL), mix the following:
            1. 50 µL of [1 µg/µL] stock ladder
            2. 450 µL of nuclease-free water

3. 100 µL of 6x loading dye

5. Turn on the electricity to the electrophoresis unit.
    a. Run black (negative) to red (positive).
    b. Run at high voltage (120 V) for detection.
    c. Run at low voltage (80 or 100 V) for gel extraction.
        i. If the voltage is too high, buffer gets hot and DNA can diffuse out.
6. If performing gel extraction, heat a hot plate to 50 °C.
7. Run the gel for the desired level of separation and view it on the UV trans-illuminator.
    a. For verification, excellent separation is not essential.
        i. View DNA at short wavelengths (302 nm).
    b. Gel extraction requires excellent separation to prevent isolating non-specific amplified products.
    c. DO NOT view DNA that you want to use under short wavelengths for long time periods, as this can crosslink the DNA.

F.6 Agarose Gel Extraction

Materials:

Agarose gel with separated bands

QIAquick® Gel Extraction Kit (Qiagen Cat. #28704)

(or kit components purchased/prepared individually)

Nuclease-free water

Ethanol

1.5 mL Micro-centrifuge tubes

2 mL collection tubes

Hot Plate

Surgical blade

UV trans-illuminator

UV glasses

Nanodrop

Microcentrifuge

Protocol for Agarose Gel Extraction:

1. Image the gel under UV trans-illuminator.
    a. Gel extraction requires excellent separation to prevent isolating non-specific amplified products.
    b. Do NOT view DNA that you want to use under short wavelengths for long time periods, as this can crosslink the DNA.
2. Cut the gel to isolate individual bands for extraction.

a. Clean the UV trans-illuminator and surgical blade with ethanol before cutting to avoid contamination.
b. Label a micro-centrifuge tube for each lane you are extracting before cutting.
c. Put on a face shield or UV protective glasses.
d. Cut the desired product out of the gel at long λ UV (365 nm).
e. Trim off all extra gel fragments (including below and above well) because extra gel lowers the yield.

3. Weigh the gel fragment containing the DNA (use an empty centrifuge tube as blank) and assume a density of 1 mg/μL.
4. Add 3 volumes of Buffer QG buffer per 1 volume of gel.
    a. Example: Assume 100 mg ≈ 100 μL
        i. DNA in gel = 120 mg
        ii. Add 360 μL QG buffer
5. Incubate the DNA and QG buffer tube at 50 °C for at least 5 minutes to digest completely.
    a. At this time also put nuclease-free water to warm for elution.
        i. Place a tube with nuclease-free water (at least 50 μL) into the hot plate at 50 °C.
6. Add 1 volume of isopropanol to the tube and mix by inverting (Do NOT vortex because it will shear the DNA).
7. Perform a quick spin to bring liquid down from the lid.
8. Place a QIAquick spin column (silica column) into a 2 mL collection tube.

9. Pipette the sample into the spin column (binds DNA to spin column).
    a. Centrifuge for 1 minute at 12,000 rpm.
    b. Discard flow-through.
    c. If the sample volume exceeds 750 µL, load the remaining volume and spin again.
10. Add 300 µL of Buffer QG to the spin column (removes traces of agarose).
    a. Centrifuge for 1 minute at 12,000 rpm.
    b. Discard flow-through.
11. Add 700 µL of Buffer PE or DNA wash buffer (washes unwanted primers, salts, enzymes, unincorporated nucleotides, agarose, dyes, ethidium bromide, oils, and detergents).
    a. Centrifuge for 1 minute at 12,000 rpm.
    b. Discard flow-through.
    c. Repeat wash, spin, and discard flow-through.
12. Spin empty tube for 1 minute at 12,000 rpm (removes traces of Buffer PE).
13. Swap the collection tube for a clean, new micro-centrifuge tube.
14. Add [20 µL] of warmed nuclease-free water (or buffer EB) into the spin column to elute the DNA.
    a. Water needs to be between pH 7.0 and 8.5 to achieve maximum elution efficiency.
    b. Allow the water to sit for a couple minutes (2 – 5 minutes) before spinning.
    c. Centrifuge for 1 minute at 12,000 rpm.

d. Keep flow-through, discard column.

e. [Adjust volume of water for elution to tune concentration].

15. Measure DNA concentration with the nanodrop and label the side of the tube with the value.

    a. Store DNA at -20 °C as DNA may degrade in the absence of a buffering agent.

        i. Particularly important if the elution is done with water.

F.7 PCR Clean-up and Restriction Enzyme Digestion

Materials:

PCR product

Omega E.Z.N.A. Cycle Pure PCR Cleanup Kit (Cat. # D6493-01)

Restriction enzymes (available from New England Biolabs)

Restriction enzyme buffer, ex. Cutsmart buffer (often included with enzyme purchase)

Nuclease free water

Clean microcentrifuge collection tube

Microcentrifuge

Protocol for PCR Clean-up and Restriction Enzyme Digestion:

1. PCR Cleanup: Changes the solvent of a PCR product so it is optimal for subsequent digestion reactions.
    a. Warm nuclease free water for elution to 60 °C.
    b. Add 5 volumes of buffer CP (guanine chloride) (kit) to 1 volume PCR product. Mix by pipetting.
        i. Example: 500 µL CP for 100 µL PCR product
    c. Add DNA to the silica column (kit).
    d. Spin at 12,000 rpm for 1 min. Discard flow-through.
    e. Wash salt off DNA by adding 700 µL DNA wash buffer (kit) to the spin column.
    f. Spin at 12,000 rpm for 1 min. Discard flow-through.
    g. Repeat wash with 700 µL DNA wash buffer (kit).

h. Spin at 12,000 rpm for 1 min. Discard flow-through.

i. Spin at 12,000 rpm for 1 min (empty spin).

j. Transfer the silica column to a clean microcentrifuge tube.

k. Elute DNA with warm nuclease free (60 °C) water.

i. The volume of elution water is dependent on the subsequent restriction digest reaction. A typical elution volume is 35 µL.

ii. Add water directly onto the filter membrane (not onto the side of the tube).

iii. Incubate water in the filter for 10 minutes.

iv. Spin at 12,000 rpm for 1 min. Keep flow-through.

2. Prepare the restriction digest reaction in a 1.7 mL micro-centrifuge tube (total reaction volume 40 µL).

a. Add 33 µL of the PCR product to the microcentrifuge tube.

i. Digestion of plasmids (which are often more concentrated) require less DNA, can use 10 µg.

ii. Add 10 - 12 µg of DNA if the concentration is known.

b. Add 4 µL of 10x CutSmart buffer.

c. Add 1.5 µL of restriction enzyme 1 (i.e. XbaI).

d. Add 1.5 µL of restriction enzyme 2 (i.e. EcoR1).

e. Add nuclease-free water to reach a final reaction volume of 40 µL.

f. Incubate reaction overnight at 37 °C.

i. Invert tube (gently, so the liquid remains suspended).

ii. The liquid should be at the top of the inverted tube so there is no evaporation and condensation.

iii. Can incubate the reaction in a cell culture or bacterial incubator.

F.8 Plasmid Ligation

Materials:

T4 DNA Ligase (stored in CryoSafe box) (New England Biolabs Cat. #M0202)

10x Ligation buffer (comes with ligase)

Ice bucket with ice

DNA substrate

Nuclease free water

Protocol for Plasmid Ligation:

1. Thaw ligation buffer on ice.
    a. Temperature sensitive because it contains ATP which can degrade.
    b. Aliquot stock solution into 10 μL aliquots if working with new buffer to avoid freeze/thaw cycles.
2. Determine volume of insert and backbone for ligation.
    a. The mass ratio of insert : backbone should be at least 3 : 1
        i. Example: Fix backbone at 100 ng. If the backbone is 3x as large as the insert, 100 ng of the insert will yield a 3 : 1 ratio of insert : backbone.
        ii. Increasing the ratio improves the likelihood of forcing the insert into the backbone (can use 9 : 1).
3. Set up the ligation reaction (total reaction volume = 10 μL).
    a. Mix backbone and insert first.
    b. Subsequently add water, buffer, and ligase

i. Avoid dipping pipette into glycerol. High amounts of glycerol in the reaction mixture lead to star activity (reduced specificity).

c. Example: Ligation Reaction

i.	Backbone (9200 bp, 71 ng/ µL)	1.5 µL
ii.	Insert (3100 bp, 65.6 ng/ µL)	4.5 µL
iii.	Nuclease free water	2 µL
iv.	Ligation buffer (stored on ice)	1 µL
v.	T4 DNA Ligase (stored in cryosafe box)	1 µL
vi.	**Total volume**	**10 µL**

4. React at room temperature 3-4 hours or overnight.

F.9 Plasmid Sequencing

Materials:

Sequencing tubes (VWR Cat. #16466-052)

Sequencing primers (Common Common primer sequences for lentiviral backbones are available on Addgene or can be designed for your insert F.2)

Protocol for Plasmid Sequencing (at Cornell):

1. Label sequencing tubes numerically on the caps and sides, i.e. 1, 2, 3, etc. In your notebook, document the details of each sample.
    a. Only one primer per tube.
    b. Forward and reverse sequencing primers go in separate tubes.
2. Combine 1 μg of plasmid DNA with ~8 pmole of primer.
    a. 1 μL of 10 mM plasmid stock is okay.
3. Add nuclease-free water to a final volume of 18 μL.
4. Submit an online order with an approved account number at:
    a. https://cores.lifesciences.cornell.edu/userdev/placeorder.php
    b. http://www.biotech.cornell.edu/brc/genomics-facility
5. Drop-off the physical samples in a Ziploc bag to 147 Biotech from 8:00 am to 4:00 pm, Monday-Friday.
    a. Results will be emailed.
6. Analyze the results using a sequence similarity BLAST search.
    a. NCBI Blast Search
    b. First 50 base pairs are noise

F.10 Fabrication of LB Broth

Materials:

Sodium chloride (NaCl) (VWR Cat. #BDH8014-500G)

Tryptone (EMD Cat. #1.07213.1000)

Yeast extract (EMD Cat. #1.03753.0500)

Ampicillin

0.2 μm sterile syringe filter

Sterile conical tube

Syringe

1 L bottle

Bunsen burner

Protocol for Fabrication of LB Broth:

1. Measure 1 L of DI water and add it to the 1 L bottle.
2. Weigh and add the following:
    a. 10 g NaCl
    b. 10 g Tryptone
    c. 5 g Yeast extract
3. Swirl to mix.
4. Autoclave the bottle on the liquid cycle.
5. [Prepare sterile Ampicillin if needed]
    a. Add 1 g Ampicillin to 10 mL DI water.
    b. Shake and stir to dissolve.

    c. Sterile filter with a 0.2 μm syringe filter into a sterile conical tube.
    d. Aliquot Ampicillin and store at -20 °C.
6. Allow the autoclaved broth to cool to ~40 °C (able to hold).
7. Turn on a Bunsen burner.
8. Working near the flame, add a 1/1000 dilution of Ampicillin. Or other appropriate antibiotic.
    a. Example: 200 μL Ampicillin for 200 mL broth.
9. Wrap the LB broth + Ampicillin bottle in aluminum foil to protect from light and store at 4 °C in the cold room.
    a. Ampicillin is good for 2-3 months in solution in the cold room (degrades via hydrolysis).

F.11 Fabrication of Agar Plates

Materials:

Sterile 100 mm Petri dishes

Sodium chloride (NaCl) (VWR Cat. #BDH8014-500G)

Tryptone (EMD Cat. #1.07213.1000)

Yeast extract (EMD Cat. #1.03753.0500)

Agar (Fisher Cat. #A360-500)

Ampicillin

0.2 μm sterile syringe filter

Sterile conical tube

Syringe

1 L bottle

Bunsen burner

Protocol for Fabrication of Agar Plates:

1. Measure 200 mL DI water and add it to the 1 L bottle.
2. Weigh and add the following:
    a. 2 g NaCl
    b. 2 g Tryptone
    c. 1 g Yeast extract
    d. 3 g Agar
3. Swirl to mix.
4. Autoclave the bottle on the liquid cycle.

5. [Prepare sterile Ampicillin if needed]
    a. Add 1 g Ampicillin to 10 mL DI water.
    b. Shake and stir to dissolve.
    c. Sterile filter with a 0.2 µm syringe filter into a sterile conical tube.
    d. Aliquot Ampicillin.
6. Allow the autoclaved broth to cool to ~40 °C (able to hold).
7. Lay out Petri dishes on a clean bench surface near a Bunsen burner.
8. Turn on a Bunsen burner.
9. Working near the flame, add a 1/1000 dilution of Ampicillin. Or other appropriate antibiotic.
    a. Example: 200 µL Ampicillin for 200 mL broth.
10. Working near the flame, add the LB + Ampicillin agar solution to the Petri dishes by pouring or using a serological pipette.
    a. Pour enough volume to cover the bottom of the plate and cover.
    b. Allow petri dishes to solidify while covered for 1 hour.
    c. Invert dishes and allow them to cool completely, several hours to overnight.
    d. Store dishes in saran wrap and aluminum foil at 4 °C.

F.12 Bacterial Transformation

Materials:

Max Efficiency DH5α Competent Cells (store at -80 °C)

(Thermo Fisher Cat. #18258 – 012)

Ligation product plasmid

pUC19 control DNA

SOC media

42 °C water bath

LB + Ampicillin agar plates (or other appropriate antibiotic)

Ethanol

Dry ice

Bunsen burner

Bacterial incubator

Protocol for Bacterial Transformation:

1. Warm LB + Ampicillin agar plates in a 37 °C bacterial incubator.
2. Warm SOC medium to room temperature.
3. Thaw competent cells on ice.
    a. Put the ligation product on ice (in the reaction microcentrifuge tube).
    b. Put a positive control microcentrifuge tube on ice (if using).
4. Pipette 50 μL competent cells into the ligation product (and positive control tube if using).

a. Do NOT mix. Cell are extremely fragile cells. Expel slowly while moving tip through the solution volume.
b. Make 50 µL aliquots of the remaining competent cell stock.
    i. Refreeze unused cell aliquots in a dry ice/ethanol bath for 5 minutes.
    ii. Return frozen competent cells to the -80 °C freezer.

5. Add 5 µL (50 pg) pUC19 control DNA to the positive control tube (if using).
    a. If the competent cell kit is new:
        i. Aliquot the stock pUC19 control DNA
        ii. 11 µL aliquots
        iii. Return to -80 °C freezer
6. Incubate cells on ice for 30 minutes.
7. Heat shock cells in a 42 °C water bath for 45 seconds. Do not shake cells.
8. Incubate cells on ice for 2 minutes.
9. Turn on a Bunsen burner.
10. Working near the flame, add 100 µL of SOC media to the cells.
11. Shake tubes at 225 rpm at 37 °C for 1 hour in the bacterial incubator.
12. Turn on a Bunsen burner.
13. Working near a flame, spread all the reaction volume per tube onto a LB + Ampicillin agar plate (use a different antibiotic if necessary for a particular plasmid).
    a. Bend the pipette tip on the inside of a Petri dish cover.

b. Use the bent pipette tip to pipette the cell volume and spread it without scraping the agar.

c. Allow the liquid on the agar surface to dry near the flame.

14. Incubate **inverted** petri dishes overnight at 37 °C in a bacterial incubator.

    a. Maximum incubation time should be ~18 hours to avoid satellite colonies.

15. Store agar plates with bacterial colonies at 4 °C.

F.13 Inoculation and Bacterial Expansion

Materials:

50% sterile glycerol

LB + Ampicillin broth (or LB broth with appropriate antibiotic)

Bacterial colonies on agar plate, live culture, or frozen bacterial stock

100% ethanol

Autoclaved 250 mL Erlenmeyer flask

17 x 100 mm culture tube

50 mL conical tube

Bunsen burner

Bacterial incubator

Centrifuge

Protocol for Inoculation and Bacterial Expansion:

1. Prepare a 50% sterile glycerol stock, if necessary.
    a. Combine equal parts water and glycerol, and sterile filter.
2. Autoclave a 250 mL Erlenmeyer flask for each bacterial culture.
3. Turn on a Bunsen burner.
4. Working near the flame add LB + Ampicillin to each culture tube.
    a. Use 2 mL of LB + Ampicillin if expanding to a larger culture volume.
    b. Use 5 mL of LB + Ampicillin if subsequently performing a mini-prep
5. Add bacteria to the culture.
    a. Dip tweezers in 100 % ethanol and pass over the flame twice to sterilize.

b. Use tweezers to pick up a sterile 200 µL (yellow) pipette tip.
c. Touch a single bacterial colony on an agar plate with the pipette tip OR scrape the pipette tip across the top of a frozen glycerol stock.
d. Drop the tip into the culture tube and cap the tube.
e. Incubate the culture overnight while shaking at 225-250 RPM at 37 °C.

6. If needed, prepare a frozen bacterial stock**.**
    a. Turn on a Bunsen burner.
    b. Working near the flame, add 800 µL of bacterial culture to a sterile 1.5 mL microcentrifuge tube.
        i. Use a P1000 with a clear tip to "pick-up" the yellow tip that was expelled in the overnight culture. This avoids contaminating your pipette by dipping it into the bacterial culture.
    c. Add 200 µL of sterile, 50% glycerol.
    d. Mix and store at -80 °C.
7. Inoculate a 100 mL culture.
    a. Turn on the Bunsen burner.
    b. Add 100 mL of LB + Ampicillin to each Erlenmeyer flask.
    c. Add bacteria to the Erlenmeyer flask:
        i. Frozen source:
            1. Scrape the pipette tip across the top of a frozen glycerol stock.
            2. Pipette within the flask, but do not expel pipette tip in the culture (less sterile).

ii. Live bacterial culture source:

1. Add 100 µL of bacterial culture to the Erlenmeyer flask.

d. Loosely cap the Erlenmeyer flask with sterile foil.

e. Incubate the culture overnight with shaking at 225 RPM at 37 °C.

8. Pellet bacteria.

a. Pour 50 mL of the bacterial culture into a 50 mL conical tube.

b. Spin at 4000 rpm for 8 minutes. Discard supernatant.

c. Pour the remaining 50 mL of culture into the same 50 mL conical tube.

d. Spin at 4000 rpm for 8 minutes. Discard supernatant.

e. Invert tubes onto a kimwipe to remove excess liquid.

f. Store at -20 °C or proceed directly to a Midiprep.

F.14 Midiprep

Materials:

NucleoBond Xtra Midi EF (Machery-Nagel Cat. #740420.10)

Isopropyl alcohol

Endotoxin free water

Ice bucket with ice

Microwave

Centrifuge

Protocol for Midiprep:

1. Add 8 mL re-suspension buffer (Buffer RES-EF) to a bacterial pellet in a 50 mL conical tube.
    a. To prepare the re-suspension buffer in a new kit:
        i. Add 1 mL of re-suspension buffer to RNAse (lyophilized powder) and mix.
        ii. Add RNase to the re-suspension buffer.
        iii. Wash the RNAse tube with re-suspension buffer and add it back into the re-suspension buffer bottle.
        iv. Store re-suspension buffer at 4 °C.
2. Vortex until the bacterial pellet is gone.
3. Add 8 mL lysis buffer (Buffer LYS-EF) to the conical tube.
    a. Gently invert 5x to mix.
    b. Incubate for 5 minutes at room temperature.

4. Add 8 mL neutralization buffer (Buffer NEU-EF).
    a. Gently invert until the solution is colorless.
    b. Incubate on ice for 5 minutes to precipitate.
5. Add 15 mL equilibration buffer to the rim of the column filter (Buffer EQU-EF).
    a. Poke the column bottom through a Styrofoam container, over a collection bin.
6. Invert the precipitated solution in the tube 3 times to homogenize the solution.
    a. Pour the solution into a labeled column filter tube.
    b. Allow the solution to filter via gravity.
7. Wash the column with 5 mL filter wash buffer (Buffer FIL-EF).
    a. Allow the solution to filter via gravity.
8. Remove and dispose the filter.
9. Wash the column (without the filter) with 35 mL Buffer ENDO-EF.
    a. Allow the solution to filter via gravity.
10. Wash the column (without the filter) with 15 mL Buffer Wash-EF.
11. Elute the plasmid into a clean 15 mL conical tube with 5 mL of warmed Buffer ELU-EF.
    a. Warm elution buffer in the microwave with 10 second spurts until it is around 50 °C (remember to loosen the cap when heating).
12. Measure the initial eluted plasmid DNA concentration with the nanodrop.
    a. Blank with Buffer ELU-EF.
    b. A reading of zero does not necessarily mean your prep failed, just that you may have lower yield.

13. Add 3.5 mL of room temperature isopropyl alcohol to the eluted plasmid and vortex thoroughly. Incubate for 3 minutes to allow the DNA to precipitate.
    a. Increase the incubation to 30 minutes at -20 °C if you want a higher yield.
    b. Pre-cool the centrifuge for Step #14 to 4 °C.
14. Centrifuge to precipitate the plasmid at 4 °C for 30 minutes.
    a. Speed must be greater than 4,500 x g, preferably greater than 15,000 x g.
15. Vacuum off supernatant.
16. Wash plasmid pellet with 2 mL of DNA wash buffer.
    a. Shake to mix. Do not attempt to re-suspend pellet.
    b. Incubate at room temperature for 2 minutes.
    c. Prepare DNA wash buffer in a new kit by adding 21 mL of 200-proof ethanol.
17. Spin to precipitate the plasmid at 4 °C for 5 minutes (same speed as step #14).
18. Vacuum off the supernatant.
19. Dry the DNA pellet in a vacuum chamber for 10 minutes.
20. Re-suspend the pellet with endotoxin free water.
    a. The resuspension volume is dependent on the expected yield.
        i. Typically varies between 100-400 µL.
    b. Transfer plasmid to a clean, new microcentrifuge tube.
        i. Pipette with P1000 to avoid shearing the DNA with P200
21. Measure the plasmid DNA concentration and label the side of the tube with the value.

F.15 Transfection

Materials:

T75 of HEK293 (293T) Cells at approximately 70% confluence

TransIT-LT1 reagent (store at 4 °C) (Mirus Cat. #2304 or #2300)

Opti-MEM reduced serum media (Invitrogen Cat. #31985-062)

Lentiviral plasmid with gene of interest

Helper plasmid #1: pSPAX2

Helper plasmid #2: pMD2G

Complete DMEM media

Protocol for Transfection:

1. Use the table below to determine the amount of media, DNA, and reagent required for the culture vessel being used.
    a. Source: https://www.mirusbio.com/

Culture vessel	96-well plate	48-well plate	24-well plate	12-well plate	6-well plate	10-cm dish	T75 flask
Surface area	0.35 cm^2	1.0 cm^2	1.9 cm^2	3.8 cm^2	9.6 cm^2	59 cm^2	75 cm^2
Complete growth medium	92 µl	263 µl	0.5 ml	1.0 ml	2.5 ml	15.5 ml	19.7 ml
Serum-free medium	9 µl	26 µl	50 µl	100 µl	250 µl	1.5 ml	1.9 ml
DNA (1µg/µl stock)	0.1 µl	0.26 µl	0.5 µl	1 µl	2.5 µl	15 µl	19 µl
*Trans*IT-LT1 Reagent	0.3 µl	0.78 µl	1.5 µl	3 µl	7.5 µl	45 µl	57 µl

2. In the biosafety cabinet, assuming a T75 flask for transfection:
    a. Add 1.9 mL of Opti-MEM reduced serum media to a 15 mL conical tube.
    b. Warm the TransIT-LT1 reagent to room temperature, vortex gently.
    c. Add 60 µL of TransIT-LT1 reagent to the same conical tube.

d. Incubate the mixture at room temperature for 10 minutes.

3. In the biosafety cabinet, mix the 3 plasmids to form a complex:
    a. Need a 10 : 7.5 : 2.5 **mass** ratio of: target plasmid : pSPAX2 : pMD2G
        i. Total volume should be approximately 19 µL of 1 µg/µL DNA (ratios are easier if you assume 20 µg of total DNA are needed).
        ii. Example:
            1. pFUWATP = 1260.6 ng/µL = 7.9 µL
            2. pSPAX2 = 786.2 ng/µL = 9.5 µL
            3. pMD2G = 855.3 ng/µL = 2.9 µL
    b. Mix the calculated volumes of the target plasmid and both helper plasmids in a new microcentrifuge tube.
        i. Incubate the plasmid complex at room temperature for 30 minutes.
    c. Following the 30 minute incubation, add the plasmid complex to the media containing the TransIT-LT1 reagent. Incubate for 10 minutes.
    d. During incubations, change the media on the HEK293 cells.
4. Transfection of HEK293 cells.
    a. The T75 flask should have 20 mL of fresh DMEM media.
    b. Tilt the flask back to expose cells from the media. Pipette the TransIT-LT1/plasmid complex directly onto the exposed HEK293 cells.
    c. Incubate 24-72 hours in the mammalian cell incubator to harvest the lentivirus particles.
5. Harvest lentivirus over the next 72 hours
    a. Approximately 10 mL of media lasts 1 day in a T75

i. At 48 hours collect 20 mL of media containing secreted lentiviral particles and replace with 10 mL of fresh complete DMEM media. Store collected media with lentiviral particles at 4 °C.

ii. At 24 hours following the first harvest, collect the media containing the secreted lentiviral particles.

F.16 Lentiviral Concentration

Materials:

HEK293 spent media containing lentivirus

Lenti-X concentrator **(**Clontech Cat. #631231)

Sterile PBS

Syringe

0.45 µm syringe filter (Syringe filter should be PVDF, cellulose acetate, or polyethersulfone. DO NOT use nitrocellulose, because it binds surface proteins on the lentiviral envelope and destroys the product)

Ice bucket with ice

Centrifuge

Protocol for Lentiviral Concentration:

1. Perform work in a biosafety cabinet.
2. Combine HEK293 spent media volumes into a single 50 mL conical tube.
3. Filter spent media through a 0.45 µm syringe filter into a new sterile 50 mL conical tube.
4. Thoroughly mix the Lenti-X concentrator by shaking.
5. Add 1 volume of Lenti-X concentrator to 3 volumes of clarified supernatant.
    a. Example:
        i. 30 mL supernatant
        ii. 10 mL Lenti-X concentration
6. Mix by inversion.

7. Incubate on ice or 4 °C for 30 minutes to overnight (based on your schedule, no difference for yield).
8. Centrifuge at 1,500 x g for 45 minutes at 4 °C (Reinhart-King centrifuge).
    a. Lentiviral particles should form an off-white pellet.
9. Carefully vacuum aspirate the supernatant.
10. Gently re-suspend the pellet in $1/10^{th}$ to $1/100^{th}$ of the original spent media volume in sterile PBS.
    a. i.e. Spent media volume = 30 mL, 1 mL sterile PBS is appropriate.
    b. Avoid introducing bubbles.
11. Immediately aliquot and store the lentivirus particles at -80 °C.
    a. Additional freeze thaw cycle will reduce efficiency of the virus by 50%.

F.17 Transduction

Materials:

Low passage target cells (T25 or T75) at 40 – 60 % confluence

Polybrene (store at -20 °C) (Santa Cruz Biotechnology Cat. #SC-134220)

Target cell complete media

Protocol for Transduction:

1. Work in sterile biosafety cabinet.
2. Choose the MOI (Multiplicity of infection, refers to the ratio of vector particles to target cells).
    a. Increasing the MOI can increase the transduction efficiency.
    b. Too much virus can be toxic.
    c. It is suggested to use greater than 1 : 1 vector : target cells but less than 100 : 1 (10 : 1 is a good starting point).
    d. If you do not know the concentration of virus, it is useful to try high and low concentrations. You want the lowest amount of virus needed to get 100% efficiency.
3. Mix the transduction reagents.
    a. Used a reduced volume of growth media during transduction.
    b. Add 3 mL (T25) or 6 mL (T75) of the target cell media to a 15 mL conical tube.
    c. Add a 1/1000 dilution of 10 mg/mL Polybrene.
        i. Example: 3 μL in 3 mL

d. Add the appropriate volume of lentivirus.

4. Transduction:
    a. Aspirate off spent media from the target cells.
    b. Pipette the lentivirus/polybrene/media mixture over the cells.
    c. Change the media in 12 to 24 hours.
        i. Polybrene can be harmful to cells.
5. Check fluorescence in 24 to 48 hours.
    a. Often weak fluorescence is observed at 24 hours.
    b. Much greater expression and fluorescence are present at 48 hours.
6. Culture cells normally. Expand and freeze down the transduced cell stock.
    a. Perform antibiotic selection if necessary to increase transduction efficiency.

APPENDIX G

LIST OF PUBLICATIONS

Cornell

Published

1. **Lampi MC**, Guvendiren M, Burdick JA, Reinhart-King CA. Photopatterned Hydrogels to Investigate the Endothelial Cell Response to Matrix Stiffness Heterogeneity. ACS Biomaterials Science & Engineering. 2017 Jan 4.
2. Rahman A, Carey SP, Kraning-Rush CM, Goldblatt ZE, Bordeleau F, **Lampi MC**, Lin DY, García AJ, Reinhart-King CA. Vinculin regulates directionality and cell polarity in two-and three-dimensional matrix and three-dimensional microtrack migration. Molecular Biology of the Cell. 2016 May 1;27(9):1431-41.
3. **Lampi MC**, Faber CJ, Huynh J, Bordeleau F, Zanotelli MR, Reinhart-King CA. Simvastatin Ameliorates Matrix Stiffness-Mediated Endothelial Monolayer Disruption. PloS one. 2016 Jan 13;11(1):e0147033.
4. Kohn JC*, **Lampi MC***, Reinhart-King CA. Age-related vascular stiffening: causes and consequences. Frontiers in Genetics. 2015 Mar 30;6:112.

   *denotes equal contribution
5. Alcoser TA, Bordeleau F, Carey SP, **Lampi MC**, Kowal DR, Somasegar S, Varma S, Shin SJ, Reinhart-King CA. Probing the biophysical properties of primary breast tumor-derived fibroblasts. Cellular and Molecular Bioengineering. 2015 Mar 1;8(1):76-85.

6. Kraning-Rush CM, Carey SP, **Lampi MC**, Reinhart-King CA. Microfabricated collagen tracks facilitate single cell metastatic invasion in 3D. Integrative Biology. 2013;5(3):606-616.

Working Papers

7. Goldblatt ZE*, Miller JP*, Li J, VanderBurgh JA, **Lampi MC**, King, MR, Reinhart-King, CA. Regulation of ATP generation during metastatic cell migration by collagen architecture, *in revision.*

   *denotes equal contribution.

8. **Lampi MC** and Reinhart-King, CA. Therapeutically targeting increased extracellular matrix mechanics to attenuate disease: From molecular targets to clinical trials, *in submission.*
9. Lin S, **Lampi MC**, Reinhart-King CA, Wang J, Nelscon C, Gu L. Eigenstrain as a Mechanical Set-Point of Cells, *in submission*.
10. Armiger T, **Lampi MC**, Islam M, Reinhart-King, CA, Dahl KN. Measuring intracellular force within monolayers by tracking sub-nuclear sensors, *in submission*.
11. Carey SP, Goldblatt ZE, Braun A, Hapach L**, Lampi MC**, Martin KE, Reinhart-King CA. Phenotypic isolation and characterization of differentially invasive tumor cell subpopulations, *in preparation.*

Prior to Cornell

1. **Lampi MC**, Wu X, Schilke KF, McGuire J. Structural attributes affecting peptide entrapment in PEO brush layers. Colloids and Surfaces B: Biointerfaces. 2013 Jun 1;106:79-85.

REFERENCES

1. D. Mozaffarian, E. J. Benjamin, A. S. Go, D. K. Arnett, M. J. Blaha, M. Cushman, S. R. Das, S. De Ferranti, J. P. Després, H. J. Fullerton, V. J. Howard, M. D. Huffman, C. R. Isasi, M. C. Jiménez, S. E. Judd, B. M. Kissela, J. H. Lichtman, L. D. Lisabeth, S. Liu, R. H. MacKey, D. J. Magid, D. K. McGuire, E. R. Mohler, C. S. Moy, P. Muntner, M. E. Mussolino, K. Nasir, R. W. Neumar, G. Nichol, L. Palaniappan, D. K. Pandey, M. J. Reeves, C. J. Rodriguez, W. Rosamond, P. D. Sorlie, J. Stein, A. Towfighi, T. N. Turan, S. S. Virani, D. Woo, R. W. Yeh, M. B. Turner, Heart disease and stroke statistics-2016 update a report from the American Heart Association, *Circulation* **133**, e38–e48 (2016).

2. A. J. Lusis, Atherosclerosis, *Nature* **407**, 233–41 (2000).

3. K. F. Fox, M. R. Cowie, D. a Wood, a J. Coats, J. S. Gibbs, S. R. Underwood, R. M. Turner, P. a Poole-Wilson, S. W. Davies, G. C. Sutton, Coronary artery disease as the cause of incident heart failure in the population, *Eur. Heart J.* **22**, 228–36 (2001).

4. G. K. Hansson, Inflammation, atherosclerosis, and coronary artery disease, *N. Engl. J. Med.* **352**, 1685–1695 (2005).

5. P. K. Shah, Mechanisms of plaque vulnerability and rupture, *J. Am. Coll. Cardiol.* **41**, S15–S22 (2003).

6. H. C. McGill, C. A. McMahan, E. E. Herderick, G. T. Malcom, R. E. Tracy, J. P. Strong, the P. D. of A. in Y. (PDAY) R. Group, Origin of atherosclerosis in childhood and adolescence, *Am. J. Clin. Nutr.* **72**, 1307s–1315s (2000).

7. A. Benetos, B. Waeber, J. Izzo, G. Mitchell, L. Resnick, R. Asmar, M. Safar, Influence of age, risk factors, and cardiovascular and renal disease on arterial stiffness: Clinical applications, *Am. J. Hypertens.* **15**, 1101–1108 (2002).

8. H. C. Stary, Evolution and progression of atherosclerotic lesions in coronary arteries of children and young adults, *Arteriosclerosis* **9**, I19-32 (1989).

9. S. Sukriti, M. Tauseef, P. Yazbeck, D. Mehta, Mechanisms regulating endothelial permeability, *Pulm. Circ.* **4**, 535–51 (2014).

10. A. Siflinger-Birnboim, P. J. del Vecchio, J. A. Cooper, F. A. Blumenstock, J. M. Shepard, A. B. Malik, Molecular sieving characteristics of the cultured endothelial monolayer, *J. Cell. Physiol.* **132**, 111–117 (1987).

11. Y. Komarova, A. B. Malik, Regulation of endothelial permeability via paracellular and transcellular transport pathways, *Annu. Rev. Physiol.* **72**, 463-493 (2010).

12. P. Libby, Inflammation in atherosclerosis, *Nature* **420**, 868–74 (2002).

13. I. Tabas, K. J. Williams, J. Borén, Subendothelial lipoprotein retention as the initiating process in atherosclerosis: Update and therapeutic implications, *Circulation* **116**, 1832–1844 (2007).

14. K. Skalén, M. Gustafsson, E. K. Rydberg, L. M. Hultén, O. Wiklund, T. L. Innerarity, J. Borén, Subendothelial retention of atherogenic lipoproteins in early atherosclerosis, *Nature* **417**, 750–4 (2002).

15. R. Stocker, J. F. Keaney, Role of oxidative modifications in atherosclerosis, *Physiol. Rev.* **84**, 1381–478 (2004).

16. S. D. Cushing, J. A. Berliner, A. J. Valente, M. C. Territo, M. Navab, F. Parhami, R. Gerrity, C. J. Schwartz, A. M. Fogelman, Minimally modified low density lipoprotein induces monocyte chemotactic protein 1 in human endothelial cells and smooth muscle cells, *Proc Natl Acad Sci U S A* **87**, 5134–5138 (1990).

17. J. A. Berliner, M. C. Territo, A. Sevanian, S. Ramin, Jeong Ai Kim, B. Bamshad, M. Esterson, A. M. Fogelman, Minimally modified low density lipoprotein stimulates monocyte endothelial interactions, *J. Clin. Invest.* **85**, 1260–1266 (1990).

18. A. Takei, Y. Huang, M. F. Lopes-Virella, Expression of adhesion molecules by human endothelial cells exposed to oxidized low density lipoprotein. Influences of degree of oxidation and location of oxidized LDL, *Atherosclerosis* **154**, 79–86 (2001).

19. J. Mestas, K. Ley, Monocyte-Endothelial Cell Interactions in the Development of Atherosclerosis *Trends Cardiovasc. Med.* **18**, 228–232 (2008).

20. P. Tontonoz, L. Nagy, J. G. A. Alvarez, V. A. Thomazy, R. M. Evans, PPARγ Promotes Monocyte/Macrophage Differentiation and Uptake of Oxidized LDL, *Cell* **93**, 241–252 (1998).

21. S. O. Rahaman, D. J. Lennon, M. Febbraio, E. A. Podrez, S. L. Hazen, R. L. Silverstein, A CD36-dependent signaling cascade is necessary for macrophage foam cell formation, *Cell Metab.* **4**, 211–221 (2006).

22. E. A. Podrez, E. Poliakov, Z. Shen, R. Zhang, Y. Deng, M. Sun, P. J. Finton, L. Shan, M. Febbraio, D. P. Hajjar, R. L. Silverstein, H. F. Hoff, R. G. Salomon, S. L. Hazen, A novel family of atherogenic oxidized phospholipids promotes macrophage foam cell formation via the scavenger receptor CD36 and is enriched in atherosclerotic lesions, *J. Biol. Chem.* **277**, 38517–38523 (2002).

23. R. G. Gerrity, The role of the monocyte in atherogenesis: I. Transition of blood-borne monocytes into foam cells in fatty lesions, *Am. J. Pathol.* **103**, 181–190 (1981).

24. F. K. Swirski, M. Nahrendorf, Leukocyte behavior in atherosclerosis, myocardial infarction, and heart failure, *Science* **339**, 161–166 (2013).

25. E. G. Nabel, Biology of the impaired endothelium, *Am. J. Cardiol.* **68**, 6C–8C (1991).

26. R. Ross, J. Masuda, E. W. Raines, A. M. Gown, S. Katsuda, M. Sasahara, L. T. Malden, H. Masuko, H. Sato, Localization of PDGF-B protein in macrophages in all phases of atherogenesis, *Science* **248**, 1009-1012 (1990).

27. E. W. Raines, PDGF and cardiovascular disease, *Cytokine Growth Factor Rev.* **15**, 237–254 (2004).

28. H. Hao, G. Gabbiani, M.-L. Bochaton-Piallat, Arterial Smooth Muscle Cell Heterogeneity, *Arterioscler. Thromb. Vasc. Biol.* **23**, 1510-1520 (2003).

29. A. C. Doran, N. Meller, C. A. McNamara, Role of Smooth Muscle Cells in the Initiation and Early Progression of Atherosclerosis, *Arterioscler. Thromb. Vasc. Biol.* **28**, 812-819 (2008).

30. M. Y. Chang, S. Potter-Perigo, C. Tsoi, A. Chait, T. N. Wight, Oxidized low density lipoproteins regulate synthesis of monkey aortic smooth muscle cell proteoglycans that have enhanced native low density lipoprotein binding properties, *J. Biol. Chem.* **275**, 4766–4773 (2000).

31. P. J. Little, L. Tannock, K. L. Olin, A. Chait, T. N. Wight, Proteoglycans synthesized by arterial smooth muscle cells in the presence of transforming growth factor-beta1 exhibit increased binding to LDLs, *Arterioscler. Thromb. Vasc. Biol.* **22**, 55–60 (2002).

32. G. Wolfbauer, J. M. Glick, L. K. Minor, G. H. Rothblat, Development of the smooth muscle foam cell: uptake of macrophage lipid inclusions, *Proc. Natl. Acad. Sci. U. S. A.* **83**, 7760–7764 (1986).

33. Y. Vengrenyuk, H. Nishi, X. Long, M. Ouimet, N. Savji, F. O. Martinez, C. P. Cassella, K. J. Moore, S. A. Ramsey, J. M. Miano, E. A. Fisher, Cholesterol loading reprograms the microRNA-143/145-Myocardin axis to convert aortic smooth muscle cells to a dysfunctional macrophage-like phenotype, *Arterioscler. Thromb. Vasc. Biol.* **35**, 535–546 (2015).

34. J. X. Rong, M. Shapiro, E. Trogan, E. A. Fisher, Transdifferentiation of mouse aortic smooth muscle cells to a macrophage-like state after cholesterol loading, *Proc. Natl. Acad. Sci.* **100**, 13531–13536 (2003).

35. E. Thorp, I. Tabas, Mechanisms and consequences of efferocytosis in advanced atherosclerosis, *J. Leukoc. Biol.* **86**, 1089–1095 (2009).

36. M. C. H. Clarke, T. D. Littlewood, N. Figg, J. J. Maguire, A. P. Davenport, M. Goddard, M. R. Bennett, Chronic apoptosis of vascular smooth muscle cells accelerates atherosclerosis and promotes calcification and medial degeneration, *Circ. Res.* **102**, 1529–1538 (2008).

37. Z. S. Galis, G. K. Sukhova, M. W. Lark, P. Libby, Increased expression of matrix metalloproteinases and matrix degrading activity in vulnerable regions of human atherosclerotic plaques, *J. Clin. Invest.* **94**, 2493–2503 (1994).

38. R. Virmani, A. P. Burke, J. T. Willerson, A. Farb, J. Narula, F. D. Kolodgie (Editors), The Vulnerable Atherosclerotic Plaque: Strategies for Diagnosis and Management, *Wiley & Sons,* 2007.

39. A. Palotie, K. Tryggvason, L. Peltonen, H. Seppä, Components of subendothelial aorta basement membrane. Immunohistochemical localization and role in cell attachment, *Lab. Invest.* **49**, 362–370 (1983).

40. R. H. Kramer, K. G. Bensch, P. M. Davison, M. A. Karasek, Basal lamina formation by cultured microvascular endothelial cells, *J. Cell Biol.* **99**, 692–698 (1984).

41. H. C. Stary, D. H. Blankenhorn, A. B. Chandler, S. Glagov, J. Insull Jr., M. Richardson, M. E. Rosenfeld, S. A. Schaffer, C. J. Schwartz, W. D. Wagner, A definition of the intima of human arteries and of its atherosclerosis-prone regions. A report from the Committee on Vascular Lesions of the Council on Arteriosclerosis, American Heart Association, *Circulation* **85**, 391–405 (1992).

42. P. Farand, A. Garon, G. E. Plante, Structure of large arteries: Orientation of elastin in rabbit aortic internal elastic lamina and in the elastic lamellae of aortic media, *Microvasc. Res.* **73**, 95–99 (2007).

43. R. Ross, J. A. Glomset, Atherosclerosis and the arterial smooth muscle cell: Proliferation of smooth muscle is a key event in the genesis of the lesions of atherosclerosis, *Science* **180**, 1332–1339 (1973).

44. D. Bergel, The dynamic elastic properties of the arterial wall, *J. Physiol.* **156**, 458–469 (1961).

45. M. K. O'Connell, S. Murthy, S. Phan, C. Xu, J. Buchanan, R. Spilker, R. L. Dalman, C. K. Zarins, W. Denk, C. A. Taylor, The three-dimensional micro- and nanostructure of the aortic medial lamellar unit measured using 3D confocal and electron microscopy imaging, *Matrix Biol.* **27**, 171–181 (2008).

46. R. J. Rizzo, W. J. McCarthy, S. N. Dixit, M. P. Lilly, V. P. Shively, W. R. Flinn, J. S. Yao, Collagen types and matrix protein content in human abdominal aortic aneurysms, *J. Vasc. Surg.* **10**, 365–73 (1989).

47. J. T. Powell, N. Vine, M. Crossman, On the accumulation of D-aspartate in elastin and other proteins of the ageing aorta, *Atherosclerosis* **97**, 201–208 (1992).

48. M. R. Roach, A. C. Burton, The reason for the shape of the distensibility curves of arteries, *Can. J. Biochem. Physiol.* **35**, 681–690 (1957).

49. A. J. Schriefl, G. Zeindlinger, D. M. Pierce, P. Regitnig, G. A. Holzapfel, Determination of the layer-specific distributed collagen fibre orientations in human thoracic and abdominal aortas and common iliac arteries, *J. R. Soc. Interface* **9**, 1275–1286 (2012).

50. P. B. Dobrin, Mechanical properties of arteries, *Physiol. Rev.* **58**, 265–324 (1978).

51. J. E. Wagenseil, N. L. Nerurkar, R. H. Knutsen, R. J. Okamoto, D. Y. Li, R. P. Mecham, Effects of elastin haploinsufficiency on the mechanical behavior of mouse arteries, *Am. J. Physiol. Heart Circ. Physiol.* **289**, H1209–H1217 (2005).

52. J. C. Lasheras, The Biomechanics of Arterial Aneurysms, *Annu. Rev. Fluid Mech.* **39**, 293–319 (2007).

53. J. E. Wagenseil, R. P. Mecham, Elastin in large artery stiffness and hypertension, *J. Cardiovasc. Transl. Res.* **5**, 264–273 (2012).

54. J. W. Baynes, S. R. Thorpe, Role of oxidative stress in diabetic complications: A new perspective on an old paradigm, *Diabetes* **48**, 1–9 (1999).

55. E. Fonck, G. G. Feigl, J. Fasel, D. Sage, M. Unser, D. A. Rüfenacht, N. Stergiopulos, Effect of aging on elastin functionality in human cerebral arteries, *Stroke* **40**, 2552–2556 (2009).

56. Q. Yu, J. Zhou, Y. C. Fung, Neutral axis location in bending and Young's modulus of different layers of arterial wall, *Am. J. Physiol.* **265**, H52–H60 (1993).

57. A. Pandit, X. Lu, C. Wang, G. S. Kassab, Biaxial elastic material properties of porcine coronary media and adventitia, *Am. J. Physiol. Heart Circ. Physiol.* **288**, H2581–H2587 (2005).

58. X. Lu, A. Pandit, G. S. Kassab, Biaxial incremental homeostatic elastic moduli of coronary artery: two-layer model, *Am. J. Physiol. Heart Circ. Physiol.* **287**, H1663–H1669 (2004).

59. S. Sen, S. Subramanian, D. E. Discher, Indentation and adhesive probing of a cell membrane with AFM: theoretical model and experiments, *Biophys. J.* **89**, 3203–3213 (2005).

60. A. Buxboim, K. Rajagopal, A. E. X. Brown, D. E. Discher, How deeply cells feel: methods for thin gels, *J. Phys. Condens. Matter* **22**, 194116 (2010).

61. G. A. Holzapfel, T. C. Gasser, R. W. Ogden, A new constitutive framework for arterial wall mechanics and a comparative study of material models, *J. Elast.* **61**, 1–48 (2000).

62. X. Lu, J. Yang, J. B. Zhao, H. Gregersen, G. S. Kassab, Shear modulus of porcine coronary artery: contributions of media and adventitia, *Am. J. Physiol. Heart Circ. Physiol.* **285**, H1966–H1975 (2003).

63. J. Huynh, N. Nishimura, K. Rana, J. M. Peloquin, J. P. Califano, C. R. Montague, M. R. King, C. B. Schaffer, C. A. Reinhart-King, Age-Related Intimal Stiffening Enhances Endothelial Permeability and Leukocyte Transmigration, *Sci. Transl. Med.* **3**, 112ra122 (2011).

64. C. A. Reinhart-King, M. Dembo, D. A. Hammer, The dynamics and mechanics of endothelial cell spreading, *Biophys. J.* **89**, 676–689 (2005).

65. A. J. Engler, M. A. Griffin, S. Sen, C. G. Bönnemann, H. L. Sweeney, D. E. Discher, Myotubes differentiate optimally on substrates with tissue-like stiffness: Pathological implications for soft or stiff microenvironments, *J. Cell Biol.* **166**, 877–887 (2004).

66. P. N. Patel, C. K. Smith, C. W. Patrick, Rheological and recovery properties of poly(ethylene glycol) diacrylate hydrogels and human adipose tissue, *J. Biomed. Mater. Res. - Part A* **73**, 313–319 (2005).

67. J. D. Wallace, R. C. Cuneo, P. A. Lundberg, T. Rosén, J. O. L. Jørgensen, S. Longobardi, N. Keay, L. Sacca, J. S. Christiansen, B. Å. Bengtsson, P. H. Sönksen, Responses of markers of bone and collagen turnover to exercise, growth hormone (GH) administration, and GH withdrawal in trained adult males, *J. Clin. Endocrinol. Metab.* **85**, 124–133 (2000).

68. A. Lundkvist, E. Lilleodden, W. Siekhaus, J. Kinney, L. Pruitt, M. Balooch, Viscoelastic Properties of Healthy Human Artery Measured in Saline Solution by AFM-Based Indentation Technique, *MRS Proc.* **436** (1996).

69. S. E. Greenwald, J. E. Moore, A. Rachev, T. P. Kane, J. J. Meister, Experimental investigation of the distribution of residual strains in the artery wall, *J. Biomech. Eng.* **119**, 438–444 (1997).

70. Z. J. Samila, S. A. Carter, The effect of age on the unfolding of elastin lamellae and collagen fibers with stretch in human carotid arteries, *Can. J. Physiol. Pharmacol.* **59**, 1050–1057 (1981).

71. H. Wolinsky, S. Glagov, A lamellar unit of aortic medial structure and function in mammals, *Circ. Res.* **20**, 99–111 (1967).

72. P. Dobrin, A. Rovick, Influence of vascular smooth muscle on contractile mechanics and elasticity of arteries, *Am. J. Physiol.* **217**, 1644–51 (1969).

73. D. Tremblay, R. Cartier, R. Mongrain, R. L. Leask, Regional dependency of the vascular smooth muscle cell contribution to the mechanical properties of the pig ascending aortic tissue, *J. Biomech.* **43**, 2228–51 (2010).

74. C. L. Berry, S. E. Greenwald, J. F. Rivett, Static mechanical properties of the developing and mature rat aorta, *Cardiovasc. Res.* **9**, 669–679 (1975).

75. R. Rezakhaniha, A. Agianniotis, J. T. C. Schrauwen, A. Griffa, D. Sage, C. V. C. Bouten, F. N. Van De Vosse, M. Unser, N. Stergiopulos, Experimental investigation of collagen waviness and orientation in the arterial adventitia using confocal laser scanning microscopy, *Biomech. Model. Mechanobiol.* **11**, 461–473 (2012).

76. H. Chen, Y. Liu, M. N. Slipchenko, X. Zhao, J. X. Cheng, G. S. Kassab, The layered structure of coronary adventitia under mechanical load, *Biophys. J.* **101**, 2555–2562 (2011).

77. S. Laurent, P. Boutouyrie, R. Asmar, I. Gautier, B. Laloux, L. Guize, P. Ducimetiere, A. Benetos, Aortic stiffness is an independent predictor of all-cause and cardiovascular mortality in hypertensive patients, *Hypertension* **37**, 1236–1241 (2001).

78. G. F. Mitchell, S.-J. Hwang, R. S. Vasan, M. G. Larson, M. J. Pencina, N. M. Hamburg, J. A. Vita, D. Levy, E. J. Benjamin, Arterial stiffness and cardiovascular events: The Framingham Heart Study, *Circulation* **121**, 505–511 (2010).

79. A. A. Laogun, R. G. Gosling, In vivo arterial compliance in man, *Clin. Phys. Physiol. Meas.* **3**, 201–212 (1982).

80. R. Asmar, A. Benetos, G. London, C. Hugue, Y. Weiss, J. Topouchian, B. Laloux, M. Safar, Aortic Distensibility in Normotensive, Untreated Hypertensive Patients, *Blood Press.* **4**, 48–54 (1995).

81. J. J. van der Heijden-Spek, J. A. Staessen, R. H. Fagard, A. P. Hoeks, H. A. Boudier, L. M. van Bortel, Effect of age on brachial artery wall properties differs from the aorta and is gender dependent: a population study, *Hypertension* **35**, 637–642 (2000).

82. T. J. M. Schlatmann, A. E. Becker, Histologic changes in the normal aging aorta: Implications for dissecting aortic aneurysm, *Am. J. Cardiol.* **39**, 13–20 (1977).

83. M. O'Rourke, Pulsatile arterial haemodynamics in hypertension, *Aust. N. Z. J. Med.* **6**, 40–8 (1976).

84. A. Avolio, D. Jones, M. Tafazzoli-Shadpour, Quantification of alterations in structure and function of elastin in the arterial media, *Hypertension* **32**, 170–175 (1998).

85. S. E. Greenwald, Ageing of the conduit arteries, *J. Pathol.* **211**, 157–172 (2007).

86. D. W. Urry, Neutral sites for calcium ion binding to elastin and collagen: a charge neutralization theory for calcification and its relationship to atherosclerosis, *Proc. Natl. Acad. Sci. U. S. A.* **68**, 810–814 (1971).

87. D. W. Urry, T. Ohnishi, Calcium ion binding to carbonyls of elastin hexapeptide, *Bioinorg. Chem.* **3**, 305–313 (1974).

88. C. M. Otto, B. K. Lind, D. W. Kitzman, B. J. Gersh, D. S. Siscovick, Association of aortic-valve sclerosis with cardiovascular mortality and morbidity in the elderly, *N. Engl. J. Med.* **341**, 142–147 (1999).

89. R. J. Elliott, L. T. McGrath, Calcification of the human thoracic aorta during aging, *Calcif. Tissue Int.* **54**, 268–273 (1994).

90. V. Gaillard, D. Casellas, C. Seguin-Devaux, H. Schohn, M. Dauça, J. Atkinson, I. Lartaud, Pioglitazone improves aortic wall elasticity in a rat model of elastocalcinotic arteriosclerosis, *Hypertension* **46**, 372–379 (2005).

91. R. W. Thompson, B. T. Baxter, MMP inhibition in abdominal aortic aneurysms. Rationale for a prospective randomized clinical trial, *Ann. N. Y. Acad. Sci.* **878**, 159–178 (1999).

92. Yasmin, S. Wallace, C. M. McEniery, Z. Dakham, P. Pusalkar, K. Maki-Petaja, M. J. Ashby, J. R. Cockcroft, I. B. Wilkinson, Matrix metalloproteinase-9 (MMP-9), MMP-2, and serum elastase activity are associated with systolic hypertension and arterial stiffness, *Arterioscler. Thromb. Vasc. Biol.* **25**, 372–378 (2005).

93. M. Wang, G. Takagi, K. Asai, R. G. Resuello, F. F. Natividad, D. E. Vatner, S. F. Vatner, E. G. Lakatta, Aging increases aortic MMP-2 activity and angiotensin II in nonhuman primates, *Hypertension* **41**, 1308–1316 (2003).

94. D. D. Bonnema, C. S. Webb, W. R. Pennington, R. E. Stroud, A. E. Leonardi, L. L. Clark, C. D. McClure, L. Finklea, F. G. Spinale, M. R. Zile, Effects of Age on Plasma Matrix Metalloproteinases (MMPs) and Tissue Inhibitor of Metalloproteinases (TIMPs), *J. Card. Fail.* **13**, 530–540 (2007).

95. V. C. Myers, W. W. Lang, Some Chemical Changes in the Human Thoracic Aorta Accompanying the Aging Process, *J. Gerontol.*, 441–444 (1946).

96. E. L. Kanabrocki, I. G. Fels, E. Kaplan, Calcium, cholesterol and collagen levels in human aortas, *J. Gerontol.* **15**, 383–387 (1960).

97. T. Toda, N. Tsuda, I. Nishimori, D. E. Leszczynski, F.A. Kummerow, Morphometrical analysis of the aging process in human arteries and aorta, *Acta Anat. (Basel).* **106**, 35–44 (1980).

98. N.R. Davis, R.A. Anwar, On the Mechanism of Formation of Desmosine and Isodesmosine Cross-Links of Elastin, *J. Am. Chem. Soc.* **92**, 3778–3782 (1970).

99. R. John, J. Thomas, Chemical compositions of elastins isolated from aortas and pulmonary tissues of humans of different ages, *Biochem. J.* **127**, 261–269 (1972).

100. M. Watanabe, T. Sawai, H. Nagura, K. Suyama, Age-related alteration of cross-linking amino acids of elastin in human aorta, *Tohoku J. Exp. Med.* **180**, 115–130 (1996).

101. B. S. Fleenor, K. D. Marshall, C. Rippe, D. R. Seals, Replicative Aging Induces Endothelial to Mesenchymal Transition in Human Aortic Endothelial Cells: Potential Role of Inflammation, *J. Vasc. Res.* **49**, 59–64 (2012).

102. S. R. Greenberg, The association of medial collagenous tissue with atheroma formation in the aging human aorta as revealed by a special technique, *Histol. Histopathol.* **1**, 323–326 (1986).

103. B. S. Fleenor, K. D. Marshall, J. R. Durrant, L. A. Lesniewski, D. R. Seals, Arterial stiffening with ageing is associated with transforming growth factor-β1-related changes in adventitial collagen: reversal by aerobic exercise, *J. Physiol.* **588**, 3971–3982 (2010).

104. T. J. Sims, L. M. Rasmussen, H. Oxlund, A. J. Bailey, The role of glycation cross-links in diabetic vascular stiffening, *Diabetologia* **39**, 946–951 (1996).

105. E. D. Schleicher, E. Wagner, A. G. Nerlich, Increased accumulation of the glycoxidation product N(epsilon)-(carboxymethyl)lysine in human tissues in diabetes and aging, *J. Clin. Invest.* **99**, 457–468 (1997).

106. G. L. Bakris, A. J. Bank, D. A. Kass, J. M. Neutel, R. A. Preston, S. Oparil, Advanced glycation end-product cross-link breakers: A novel approach to cardiovascular pathologies related to the aging process, *Am. J. Hypertens.* **17**, (2004).

107. D. R. Sell, V. M. Monnier, Molecular basis of arterial stiffening: Role of glycation-a mini-review, *Gerontology* **58**, 227–237 (2012).

108. R. Bucala, K. J. Tracey, A. Cerami, Advanced glycosylation products quench nitric oxide and mediate defective endothelium-dependent vasodilatation in experimental diabetes, *J. Clin. Invest.* **87**, 432–438 (1991).

109. R. De Caterina, P. Libby, H. B. Peng, V. J. Thannickal, T. B. Rajavashisth, M. A. Gimbrone, W. S. Shin, J. K. Liao, Nitric oxide decreases cytokine-induced endothelial activation: Nitric oxide selectively reduces endothelial expression of adhesion molecules and proinflammatory cytokines, *J. Clin. Invest.* **96**, 60–68 (1995).

110. B. Xu, R. Chibber, D. Ruggiero, E. Kohner, J. Ritter, A. Ferro, Impairment of vascular endothelial nitric oxide synthase activity by advanced glycation end products, *FASEB J* **17**, 1289–1291 (2003).

111. B. Xu, Y. Ji, K. Yao, Y. X. Cao, A. Ferro, Inhibition of human endothelial cell nitric oxide synthesis by advanced glycation end-products but not glucose: relevance to diabetes, *Clin. Sci. (Lond).* **109**, 439–446 (2005).

112. C. J. Mullarkey, D. Edelstein, M. Brownlee, Free radical generation by early glycation products: a mechanism for accelerated atherogenesis in diabetes, *Biochem. Biophys. Res. Commun.* **173**, 932–939 (1990).

113. J. L. Wautier, C. Zoukourian, O. Chappey, M. P. Wautier, P. J. Guillausseau, R. Cao, O. Hori, D. Stern, A. M. Schmidt, Receptor-mediated endothelial cell dysfunction in diabetic vasculopathy. Soluble receptor for advanced glycation end products blocks hyperpermeability in diabetic rats, *J. Clin. Invest.* **97**, 238–243 (1996).

114. M. P. Wautier, O. Chappey, S. Corda, D. M. Stern, A. M. Schmidt, J. L. Wautier, Activation of NADPH oxidase by AGE links oxidant stress to altered gene expression via RAGE, *Am. J. Physiol. Endocrinol. Metab.* **280**, E685–E694 (2001).

115. A. Bierhaus, S. Chevion, M. Chevion, M. Hofmann, P. Quehenberger, T. Illmer, T. Luther, E. Berentshtein, H. Tritschler, M. Müller, P. Wahl, R. Ziegler, P. P. Nawroth, Advanced glycation end product-induced activation of NF-kappaB is suppressed by alpha-lipoic acid in cultured endothelial cells, *Diabetes* **46**, 1481–1490 (1997).

116. L. Park, K. G. Raman, K. J. Lee, Y. Lu, L. J. Ferran, W. S. Chow, D. Stern, A. M. Schmidt, Suppression of accelerated diabetic atherosclerosis by the soluble receptor for advanced glycation endproducts, *Nat. Med.* **4**, 1025–1031 (1998).

117. H. Tanaka, F. A. Dinenno, K. D. Monahan, C. M. Clevenger, C. A. DeSouza, D. R. Seals, Aging, habitual exercise, and dynamic arterial compliance, *Circulation* **102**, 1270–1275 (2000).

118. D. R. Seals, C. A. Desouza, A. J. Donato, H. Tanaka, Habitual exercise and arterial aging, *J. Appl. Physiol.* **105**, 1323–1332 (2008).

119. J. R. Santos-Parker, T. J. LaRocca, D. R. Seals, Aerobic exercise and other healthy lifestyle factors that influence vascular aging, *Adv. Physiol. Educ.* **38**, 296-307 (2014).

120. K. E. Ferrier, T. K. Waddell, C. D. Gatzka, J. D. Cameron, A. M. Dart, B. A. Kingwell, Aerobic Exercise Training Does Not Modify Large-Artery Compliance in Isolated Systolic Hypertension, *Hypertension* **38**, 222-226 (2001).

121. F. Dimeo, N. Pagonas, F. Seibert, R. Arndt, W. Zidek, T. H. Westhoff, Aerobic exercise reduces blood pressure in resistant hypertension, *Hypertension* **60**, 653–658 (2012).

122. J. C. Kohn, A. Chen, S. Cheng, D. R. Kowal, M. R. King, C. A. Reinhart-King, Mechanical heterogeneities in the subendothelial matrix develop with age and decrease with exercise, *J. Biomech.* **49**, 1447–1453 (2016).

123. T. Nosaka, H. Tanaka, I. Watanabe, M. Sato, M. Matsuda, Influence of regular exercise on age-related changes in arterial elasticity: mechanistic insights from wall compositions in rat aorta, *Can. J. Appl. Physiol.* **28**, 204–212 (2003).

124. S. Maeda, M. Iemitsu, T. Miyauchi, S. Kuno, M. Matsuda, H. Tanaka, Aortic stiffness and aerobic exercise: Mechanistic insight from microarray analyses, *Med. Sci. Sports Exerc.* **37**, 1710–1716 (2005).

125. H. Langberg, D. Skovgaard, L. J. Petersen, J. Bulow, M. Kjaer, Type I collagen synthesis and degradation in peritendinous tissue after exercise determined by microdialysis in humans, *J. Physiol.* **521 Pt 1**, 299–306 (1999).

126. A. Radauceanu, F. Moulin, W. Djaballah, P. Y. Marie, F. Alla, B. Dousset, J. M. Virion, J. Capiaumont, G. Karcher, E. Aliot, F. Zannad, Residual stress ischaemia is associated with blood markers of myocardial structural remodelling, *Eur. J. Heart Fail.* **9**, 370–376 (2007).

127. M. Brownlee, H. Vlassara, A. Kooney, P. Ulrich, A. Cerami, Aminoguanidine prevents diabetes-induced arterial wall protein cross-linking, *Science* **232**, 1629–1632 (1986).

128. B. Corman, M. Duriez, P. Poitevin, D. Heudes, P. Bruneval, A. Tedgui, B. I. Levy, Aminoguanidine prevents age-related arterial stiffening and cardiac hypertrophy, *Proc. Natl. Acad. Sci. U. S. A.* **95**, 1301–1306 (1998).

129. B. I. Freedman, J. P. Wuerth, K. Cartwright, R. P. Bain, S. Dippe, K. Hershon, A. D. Mooradian, B. S. Spinowitz, Design and baseline characteristics for the aminoguanidine clinical trial in overt type 2 diabetic nephropathy (ACTION II), *Control. Clin. Trials* **20**, 493–510 (1999).

130. T. Soulis, S. Sastra, V. Thallas, S. B. Mortensen, M. Wilken, J. T. Clausen, O. J. Bjerrum, H. Petersen, J. Lau, G. Jerums, E. Boel, M. E. Cooper, A novel inhibitor of advanced glycation end-product formation inhibits mesenteric vascular hypertrophy in experimental diabetes, *Diabetologia* **42**, 472–479 (1999).

131. A. Nenna, F. Nappi, S. S. Avtaar Singh, F. W. Sutherland, F. Di Domenico, M. Chello, C. Spadaccio, Pharmacologic Approaches Against Advanced Glycation End Products (AGEs) in Diabetic Cardiovascular Disease, *Res. Cardiovasc. Med.* **4**, e26949 (2015).

132. S. Vasan, X. Zhang, A. Kapurniotu, J. Bernhagen, S. Teichberg, J. Basgen, D. Wagle, D. Shih, I. Terlecky, R. Bucala, A. Cerami, J. Egan, P. Ulrich, An agent cleaving glucose-derived protein crosslinks in vitro and in vivo, *Nature* **382**, 275–278 (1996).

133. T. Kim, D. A. Spiegel, The unique reactivity of N-phenacyl-derived thiazolium salts toward α-dicarbonyl compounds, *Rejuvenation Res.* **16**, 43–50 (2013).

134. B. H. Wolffenbuttel, C. M. Boulanger, F. R. Crijns, M. S. Huijberts, P. Poitevin, G. N. Swennen, S. Vasan, J. J. Egan, P. Ulrich, A. Cerami, B. I. Lévy, Breakers of advanced glycation end products restore large artery properties in experimental diabetes, *Proc. Natl. Acad. Sci. U. S. A.* **95**, 4630–4634 (1998).

135. W. C. Little, M. R. Zile, D. W. Kitzman, W. G. Hundley, T. X. O'Brien, R. C. Degroof, The effect of alagebrium chloride (ALT-711), a novel glucose cross-link breaker, in the treatment of elderly patients with diastolic heart failure, *J. Card. Fail.* **11**, 191–195 (2005).

136. M. H. Oudegeest-Sander, M. G. M. O. Rikkert, P. Smits, D. H. J. Thijssen, A. P. J. van Dijk, B. D. Levine, M. T. E. Hopman, The effect of an advanced glycation end-product crosslink breaker and exercise training on vascular function in older individuals: A randomized factorial design trial, *Exp. Gerontol.* **48**, 1509–1517 (2013).

137. K. P. Chandra, A. Shiwalkar, J. Kotecha, P. Thakkar, A. Srivastava, V. Chauthaiwale, S. K. Sharma, M. R. Cross, C. Dutt, Phase I Clinical Studies of the Advanced Glycation End-product (AGE)-Breaker TRC4186, *Clin. Drug Investig.* **29**, 559–575 (2009).

138. G. Cheng, L.-L. Wang, L. Long, H.-Y. Liu, H. Cui, W.-S. Qu, S. Li, Beneficial effects of C36, a novel breaker of advanced glycation endproducts cross-links, on the cardiovascular system of diabetic rats, *Br. J. Pharmacol.* **152**, 1196–1206 (2007).

139. M. F. O'Rourke, J. A. Staessen, C. Vlachopoulos, D. Duprez, G. E. Plante, Clinical applications of arterial stiffness; definitions and reference values, *Am. J. Hypertens.* **15**, 426–444 (2002).

140. R. M. Weisbrod, T. Shiang, L. Al Sayah, J. L. Fry, S. Bajpai, C. A. Reinhart-King, H. E. Lob, L. Santhanam, G. Mitchell, R. A. Cohen, F. Seta, Arterial stiffening precedes systolic hypertension in diet-induced obesity, *Hypertension* **62**, 1105–1110 (2013).

141. K. K. Quevedo, Aortic stiffness, blood pressure progression, and incident hypertension, *Cardiol. Rev.* **28**, (2012).

142. D. Kothapalli, S. L. Liu, Y. H. Bae, J. Monslow, T. Xu, E. A. Hawthorne, F. J. Byfield, P. Castagnino, S. Rao, D. J. Rader, E. Puré, M. C. Phillips, S. Lund-Katz, P. A. Janmey, R. K. Assoian, Cardiovascular Protection by ApoE and ApoE-HDL Linked to Suppression of ECM Gene Expression and Arterial Stiffening, *Cell Rep.* **2**, 1259–1271 (2012).

143. J. A. Maedeker, K. V. Stoka, S. A. Bhayani, W. S. Gardner, L. Bennett, J. D. Procknow, M. C. Staiculescu, T. A. Walji, C. S. Craft, J. E. Wagenseil, Hypertension and decreased aortic compliance due to reduced elastin amounts do not increase atherosclerotic plaque accumulation in Ldlr-/- mice, *Atherosclerosis* **249**, 22–29 (2016).

144. A. B. Jaffe, A. Hall, Rho GTPases: biochemistry and biology, *Annu. Rev. Cell Dev. Biol.* **21**, 247–69 (2005).

145. J. Bos, H. Rehmann, A. Wittinghofer, GEFs and GAPs: Critical Elements in the Control of Small G Proteins, *Cell* **129**, 865–877 (2007).

146. R. G. Hodge, A. J. Ridley, Regulating Rho GTPases and their regulators, *Nat. Rev. Mol. Cell Biol.* **17**, 496–510 (2016).

147. C. M. L. Beckers, V. W. M. Van Hinsbergh, G. P. Van Nieuw Amerongen, Driving Rho GTPase activity in endothelial cells regulates barrier integrity, *Thromb. Haemost.* **103**, 40–55 (2010).

148. T. R. Stankiewicz, D. A. Linseman, Rho family GTPases: key players in neuronal development, neuronal survival, and neurodegeneration, *Front. Cell. Neurosci.* **8**, 314 (2014).

149. G. P. van Nieuw Amerongen, C. M. L. Beckers, I. D. Achekar, S. Zeeman, R. J. P. Musters, V. W. Van Hinsbergh, Involvement of Rho kinase in endothelial barrier maintenance, *Arterioscler. Thromb. Vasc. Biol.* **27**, 2332–2339 (2007).

150. M. Amano, M. Ito, K. Kimura, Y. Fukata, K. Chihara, T. Nakano, Y. Matsuura, K. Kaibuchi, Phosphorylation and Activation of Myosin by Rho-associated, *J. Biol. Chem.* **271**, 20246–20249 (1996).
151. K. Burridge, K. Wennerberg, Rho and Rac Take Center Stage, *Cell* **116**, 167–179 (2004).

152. E. C. Lessey, C. Guilluy, K. Burridge, From mechanical force to RhoA activation, *Biochemistry* **51**, 7420–7432 (2012).

153. G. P. van Nieuw Amerongen, S. van Delft, M. A. Vermeer, J. G. Collard, V. W. M. van Hinsbergh, Activation of RhoA by Thrombin in Endothelial Hyperpermeability: Role of Rho Kinase and Protein Tyrosine Kinases, *Circ. Res.* **87**, 335–340 (2000).

154. M. Aslam, C. Tanislav, C. Troidl, R. Schulz, C. Hamm, D. Gündüz, cAMP controls the restoration of endothelial barrier function after thrombin-induced hyperpermeability via Rac1 activation, *Physiol. Rep.* **2**, e12175 (2014).

155. Y. A. Komarova, K. Kruse, D. Mehta, A. B. Malik, Protein Interactions at Endothelial Junctions and Signaling Mechanisms Regulating Endothelial Permeability, *Circ. Res.* **120**, 179-206 (2017).

156. E. E. Sander, J. P. Ten Klooster, S. Van Delft, R. A. Van Der Kammen, J. G. Collard, Rac downregulates Rho activity: Reciprocal balance between both GTPases determines cellular morphology and migratory behavior, *J. Cell Biol.* **147**, 1009–1021 (1999).

157. Y. Ohta, J. H. Hartwig, T. P. Stossel, FilGAP, a Rho- and ROCK-regulated GAP for Rac binds filamin A to control actin remodelling, *Nat. Cell Biol.* **8**, 803–814 (2006).

158. A. Hall, Rho GTPases and the control of cell behavior, *Biochem. Soc. Trans.* **33**, 891–895 (2005).

159. N. Daneshjou, N. Sieracki, G. P. van Nieuw Amerongen, M. A. Schwartz, Y. A. Komarova, A. B. Malik, Rac1 functions as a reversible tension modulator to stabilize VE-cadherin trans-interaction, *J. Cell Biol.* **208**, 23–32 (2015).

160. S. M. Dudek, J. R. Jacobson, E. T. Chiang, K. G. Birukov, P. Wang, X. Zhan, J. G. N. Garcia, Pulmonary endothelial cell barrier enhancement by sphingosine 1-phosphate. Roles for cortactin and myosin light chain kinase, *J. Biol. Chem.* **279**, 24692–24700 (2004).

161. I. Timmerman, N. Heemskerk, J. Kroon, A. Schaefer, J. Van Rijssel, M. Hoogenboezem, J. van Unen, J. Goedhart, T. W. J. Gadella, T. Yin, Y. Wu, S. Huveneers, J. D. van Buul, J. van Rijssel, J. Van Unen, J. Goedhart, T. W. J. G. Jr, A local VE-cadherin/Trio-based signaling complex stabilizes endothelial junctions through Rac1, *J. Cell Sci.* **128**, 3041–3054 (2015).

162. R. Ramchandran, D. Mehta, S. M. Vogel, M. K. Mirza, P. Kouklis, A. B. Malik, Critical role of Cdc42 in mediating endothelial barrier protection in vivo, *Am. J. Physiol. - Lung Cell. Mol. Physiol.* **295**, L363-L369 (2008).

163. D. M. Barry, K. Xu, S. M. Meadows, Y. Zheng, P. R. Norden, G. E. Davis, O. Cleaver, Cdc42 is required for cytoskeletal support of endothelial cell adhesion during blood vessel formation in mice, *Development* **142**, 3058-3070 (2015).

164. P. Kouklis, Cdc42 Regulates the Restoration of Endothelial Barrier Function, *Circ. Res.* **94**, 159–166 (2004).

165. M. J. Paszek, V. M. Weaver, The tension mounts: Mechanics meets morphogenesis and malignancy, *J. Mammary Gland Biol. Neoplasia* **9**, 325–342 (2004).

166. A. L. Sieminski, R. P. Hebbel, K. J. Gooch, The relative magnitudes of endothelial force generation and matrix stiffness modulate capillary morphogenesis in vitro, *Exp. Cell Res.* **297**, 574–584 (2004).

167. M. J. Paszek, N. Zahir, K. R. Johnson, J. N. Lakins, G. I. Rozenberg, A. Gefen, C. A. Reinhart-King, S. S. Margulies, M. Dembo, D. Boettiger, D. A. Hammer, V. M. Weaver, Tensional homeostasis and the malignant phenotype, *Cancer Cell* **8**, 241–254 (2005).

168. A. J. Engler, S. Sen, H. L. Sweeney, D. E. Discher, Matrix Elasticity Directs Stem Cell Lineage Specification, *Cell* **126**, 677–689 (2006).

169. F. Calvo, N. Ege, A. Grande-Garcia, S. Hooper, R. P. Jenkins, S. I. Chaudhry, K. Harrington, P. Williamson, E. Moeendarbary, G. Charras, E. Sahai, Mechanotransduction and YAP-dependent matrix remodelling is required for the generation and maintenance of cancer-associated fibroblasts, *Nat. Cell Biol*. **15**, 637–646 (2013).

170. S. R. Caliari, M. Perepelyuk, E. M. Soulas, G. Y. Lee, R. G. Wells, J. A. Burdick, Gradually softening hydrogels for modeling hepatic stellate cell behavior during fibrosis regression, *Integr. Biol.* **8**, 720–728 (2016).

171. M. Guvendiren, J. A. Burdick, Stiffening hydrogels to probe short- and long-term cellular responses to dynamic mechanics, *Nat. Commun.* **3**, 792 (2012).

172. J. Peloquin, J. Huynh, R. M. Williams, C. A. Reinhart-King, Indentation measurements of the subendothelial matrix in bovine carotid arteries, *J. Biomech.* **44**, 815–821 (2011).

173. D. E. Discher, P. Janmey, Y.L. Wang, Tissue cells feel and respond to the stiffness of their substrate, *Science* **310**, 1139–1143 (2005).

174. B. D. Hoffman, C. Grashoff, M. A. Schwartz, Dynamic molecular processes mediate cellular mechanotransduction, *Nature* **475**, 316–323 (2011).

175. M. T. Breckenridge, R. A. Desai, Mi. T. Yang, J. Fu, C. S. Chen, Substrates with Engineered Step Changes in Rigidity Induce Traction Force Polarity and Durotaxis, *Cell. Mol. Bioeng.* **7**, 26–34 (2014).

176. J. D. Humphrey, E. R. Dufresne, M. A. Schwartz, Mechanotransduction and extracellular matrix homeostasis, *Nat. Rev. Mol. Cell Biol.* **15**, 802–812 (2014).

177. A. del Rio, R. Perez-Jimenez, R. Liu, P. Roca-Cusachs, J. M. Fernandez, M. P. Sheetz, Stretching Single Talin Rod Molecules Activates Vinculin Binding, *Science* **323**, 638-641 (2009).

178. J. D. Humphries, P. Wang, C. Streuli, B. Geiger, M. J. Humphries, C. Ballestrem, Vinculin controls focal adhesion formation by direct interactions with talin and actin, *J. Cell Biol.* **179**, 1043–1057 (2007).

179. L. Trichet, J. Le Digabel, R. J. Hawkins, S. R. K. Vedula, M. Gupta, C. Ribrault, P. Hersen, R. Voituriez, B. Ladoux, Evidence of a large-scale mechanosensing mechanism for cellular adaptation to substrate stiffness, *Proc. Natl. Acad. Sci. U. S. A.* **109**, 6933–6938 (2012).

180. M. Dembo, Y. L. Wang, Stresses at the cell-to-substrate interface during locomotion of fibroblasts, *Biophys. J.* **76**, 2307–2316 (1999).

181. M. T. Yang, N. J. Sniadecki, C. S. Chen, Geometric Considerations of Micro- to Nanoscale Elastomeric Post Arrays to Study Cellular Traction Forces, *Adv. Mater.* **19**, 3119–3123 (2007).

182. J. H. C. Wang, J. S. Lin, Cell traction force and measurement methods, *Biomech. Model. Mechanobiol.* **6**, 361-371 (2007).

183. S. Huveneers, M. J. Daemen, P. L. Hordijk, Between Rho(k) and a Hard Place: The Relation Between Vessel Wall Stiffness, Endothelial Contractility, and Cardiovascular Disease, *Circ. Res.* **116**, 895–908 (2015).

184. A. A. Birukova, X. Tian, I. Cokic, Y. Beckham, M. L. Gardel, K. G. Birukov, Endothelial barrier disruption and recovery is controlled by substrate stiffness, *Microvasc. Res.* **87**, 50–57 (2013).

185. K. M. Stroka, H. Aranda-Espinoza, Endothelial cell substrate stiffness influences neutrophil transmigration via myosin light chain kinase-dependent cell contraction, *Blood* **118**, 1632–1640 (2011).

186. J. L. MacKay, D. A. Hammer, Stiff substrates enhance monocytic cell capture through E-selectin but not P-selectin, *Integr. Biol.* **8**, 68-72, (2016).

187. V. Maruthamuthu, B. Sabass, U. S. Schwarz, M. L. Gardel, Cell-ECM traction force modulates endogenous tension at cell-cell contacts, *Proc. Natl. Acad. Sci. U. S. A.* **108**, 4708–4713 (2011).

188. Z. Liu, J. L. Tan, D. M. Cohen, M. T. Yang, N. J. Sniadecki, S. A. Ruiz, C. M. Nelson, C. S. Chen, Mechanical tugging force regulates the size of cell-cell junctions, *Proc. Natl. Acad. Sci. U. S. A.* **107**, 9944–9949 (2010).

189. A. K. Barry, N. Wang, D. E. Leckband, Local VE-cadherin mechanotransduction triggers long-ranged remodeling of endothelial monolayers, *J. Cell Sci.* **128**, 1341–51 (2015).

190. S. Huveneers, J. de Rooij, Mechanosensitive systems at the cadherin–F-actin interface, *J. Cell Sci.* **126**, 403-413 (2013).

191. S. Yonemura, Y. Wada, T. Watanabe, A. Nagafuchi, M. Shibata, alpha-Catenin as a tension transducer that induces adherens junction development, *Nat Cell Biol* **12**, 533–542 (2010).

192. B. Geiger, J. P. Spatz, A. D. Bershadsky, Environmental sensing through focal adhesions, *Nat. Rev. Mol. Cell Biol.* **10**, 21–33 (2009).

193. Q. le Duc, Q. Shi, I. Blonk, A. Sonnenberg, N. Wang, D. Leckband, J. de Rooij, Vinculin potentiates E-cadherin mechanosensing and is recruited to actin-anchored sites within adherens junctions in a myosin II–dependent manner, *J. Cell Biol.* **189**, 1107–1115 (2010).

194. S. Huveneers, J. Oldenburg, E. Spanjaard, G. van der Krogt, I. Grigoriev, A. Akhmanova, H. Rehmann, J. de Rooij, R. J. de, Vinculin associates with endothelial VE-cadherin junctions to control force-dependent remodeling, *J. Cell Biol.* **196**, 641–652 (2012).

195. A. A. Birukova, A. S. Shah, Y. Tian, N. Moldobaeva, K. G. Birukov, Dual role of vinculin in barrier-disruptive and barrier-enhancing endothelial cell responses, *Cell. Signal.* **28**, 541–551 (2016).

196. J. Oldenburg, G. van der Krogt, F. Twiss, A. Bongaarts, Y. Habani, J. A. Slotman, A. Houtsmuller, S. Huveneers, J. de Rooij, VASP, zyxin and TES are tension-dependent members of Focal Adherens Junctions independent of the α-catenin-vinculin module, *Sci. Rep.* **5**, 17225 (2015).

197. K. L. Mui, C. S. Chen, R. K. Assoian, The mechanical regulation of integrin–cadherin crosstalk organizes cells, signaling and forces, *J. Cell Sci.* **129**, 1093–1100 (2016).

198. J. C. Wang, M. Bennett, Aging and atherosclerosis: Mechanisms, functional consequences, and potential therapeutics for cellular senescence, *Circ. Res.* **111**, 245–259 (2012).

199. M. F. O'Rourke, Arterial aging: pathophysiological principles, *Vasc. Med.* **12**, 329–41 (2007).

200. J. C. Kohn, M. C. Lampi, C. A. Reinhart-King, Age-Related Vascular Stiffening: Causes and Consequences, *Front. Genet.* **6** (2015).

201. F. U. S. Mattace-Raso, T. J. M. van der Cammen, A. Hofman, N. M. van Popele, M. L. Bos, M. A. D. H. Schalekamp, R. Asmar, R. S. Reneman, A. P. G. Hoeks, M. M. B. Breteler, J. C. M. Witteman, Arterial stiffness and risk of coronary heart disease and stroke: the Rotterdam Study, *Circulation* **113**, 657–663 (2006).

202. S. Oberoi, U. J. Schoepf, M. Meyer, T. Henzler, G. W. Rowe, P. Costello, J. W. Nance, Progression of Arterial Stiffness and Coronary Atherosclerosis: Longitudinal Evaluation by Cardiac CT, *Am. J. Roentgenol.* **200**, 798–804 (2013).

203. J. P. Califano, C. A. Reinhart-King, A Balance of Substrate Mechanics and Matrix Chemistry Regulates Endothelial Cell Network Assembly, *Cell. Mol. Bioeng.* **1**, 122–132 (2008).

204. J. P. Califano, C. A. Reinhart-King, The effects of substrate elasticity on endothelial cell network formation and traction force generation, *Conf. Proc. IEEE Eng. Med. Biol. Soc.* **2009**, 3343–3345 (2009).

205. B. N. Mason, A. Starchenko, R. M. Williams, L. J. Bonassar, C. A. Reinhart-King, Tuning three-dimensional collagen matrix stiffness independently of collagen concentration modulates endothelial cell behavior, *Acta Biomater.* **9**, 4635–4644 (2013).

206. J. P. Califano, C. A. Reinhart-King, Substrate Stiffness and Cell Area Predict Cellular Traction Stresses in Single Cells and Cells in Contact, *Cell. Mol. Bioeng.* **3**, 68–75 (2010).

207. A. A. Birukova, D. Burdette, N. Moldobaeva, J. Xing, P. Fu, K. G. Birukov, Rac GTPase is a hub for protein kinase A and Epac signaling in endothelial barrier protection by cAMP, *Microvasc. Res.* **79**, 128–138 (2010).

208. K. Lee, F. Forudi, G. M. Saidel, M. S. Penn, Alterations in internal elastic lamina permeability as a function of age and anatomical site precede lesion development in apolipoprotein E-null mice, *Circ. Res.* **97**, 450–456 (2005).

209. R. Ross, Atherosclerosis--an inflammatory disease, *N. Engl. J. Med.* **340**, 115–126 (1999).

210. R. Krishnan, D. D. Klumpers, C. Y. Park, K. Rajendran, X. Trepat, J. van Bezu, V. W. M. van Hinsbergh, C. V Carman, J. D. Brain, J. J. Fredberg, J. P. Butler, G. P. van Nieuw Amerongen, Substrate stiffening promotes endothelial monolayer disruption through enhanced physical forces, *Am. J. Physiol. Cell Physiol.* **300**, C146-C154 (2011).

211. C. S. Chen, Mechanotransduction - a field pulling together?, *J. Cell Sci.* **121**, 3285–3292 (2008).

212. J. Davignon, Beneficial cardiovascular pleiotropic effects of statins, *Circulation* **109**, III39-I43 (2004).

213. C.Y. Wang, P.Y. Liu, J. K. Liao, Pleiotropic effects of statin therapy: molecular mechanisms and clinical results, *Trends Mol. Med.* **14**, 37–44 (2008).

214. M. Takemoto, J. K. Liao, Pleiotropic effects of 3-hydroxy-3-methylglutaryl coenzyme a reductase inhibitors, *Arterioscler. Thromb. Vasc. Biol.* **21**, 1712–1719 (2001).

215. G. O'Driscoll, D. Green, R. R. Taylor, Simvastatin, an HMG-coenzyme A reductase inhibitor, improves endothelial function within 1 month*, Circulation* **95**, 1126-1131 (1997).

216. M. A. Albert, E. Danielson, N. Rifai, P. M. Ridker, Effect of statin therapy on C-reactive protein levels: the pravastatin inflammation/CRP evaluation (PRINCE): a randomized trial and cohort study, *JAMA,* **286**, 64-70 (2001).

217. S. S. Levinson, Rosuvastatin to prevent vascular events in men and women with elevated C-reactive protein - An analysis, *J. Clin. Ligand Assay* **31**, 25–28 (2008).

218. T. R. Pedersen, J. Kjekshus, K. Berg, T. Haghfelt, O. Faergeman, G. Thorgeirsson, K. Pyorala, T. Miettinen, L. Wilhelmsen, A. G. Olsson, H. Wedel, K. Kristianson, H. Thomsen, E. Nordero, B. Thomsen, K. Lyngborg, G. S. Andersen, F. Nielsen, U. Talleruphuus, A. Mcnair, K. Egstrup, E. H. Simonsen, I. Simonsen, H. Vejbychristensen, L. Sommer, P. O. Eidner, E. Klarholt, A. Henriksen, K. Mellemgaard, J. Launbjerg, P. Freuergaard, L. Nielsen, E. B. Madsen, H. Ibsen, U. Andersen, H. Enemark, J. Haarbo, B. Martinsen, C. G. Dahlstrom, L. Thyrring, K. Thomassen, G. Jensen, S. L. Rasmussen, N. Skov, K. N. Hansen, M. L. Larsen, B. Haastrup, I. Hjaere, A. Thuroe, A. Et, Randomized trial of cholesterol-lowering in 4444 patients with coronary-heart-disease - the scandinavian simvastatin survival study (4s), *Lancet* **344**, 1383–1389 (1994).

219. J. Shepherd, S. M. Cobbe, I. Ford, C. G. Isles, A. R. Lorimer, P. W. MacFarlane, J. H. McKillop, C. J. Packard, Prevention of coronary heart disease with pravastatin in men with hypercholesterolemia. West of Scotland Coronary Prevention Study Group, *N. Engl. J. Med.* **333**, 1301-1308, (1995).

220. U. Laufs, M. Endres, F. Custodis, K. Gertz, G. Nickenig, J. K. Liao, M. Böhm, Suppression of endothelial nitric oxide production after withdrawal of statin treatment is mediated by negative feedback regulation of rho GTPase gene transcription, *Circulation* **102**, 3104–3110 (2000).

221. W. Chen, S. Pendyala, V. Natarajan, J. G. N. Garcia, J. R. Jacobson, Endothelial cell barrier protection by simvastatin: GTPase regulation and NADPH oxidase inhibition, *Am. J. Physiol. Lung Cell. Mol. Physiol.* **295**, L575-L583 (2008).

222. Y. Rikitake, J. K. Liao, Rho GTPases, statins, and nitric oxide, *Circ. Res.* **97**, 1232–1235 (2005).

223. H. Xiao, X. Qin, D. Ping, K. Zuo, Inhibition of Rho and Rac Geranylgeranylation by Atorvastatin Is Critical for Preservation of Endothelial Junction Integrity, *PLoS One* **8**, (2013).

224. J. R. Jacobson, S. M. Dudek, K. G. Birukov, S. Q. Ye, D. N. Grigoryev, R. E. Girgis, J. G. N. Garcia, Cytoskeletal activation and altered gene expression in endothelial barrier regulation by simvastatin, *Am. J. Respir. Cell Mol. Biol.* **30**, 662–670 (2004).

225. G. P. van Nieuw Amerongen, M. A. Vermeer, P. Nègre-Aminou, J. Lankelma, J. J. Emeis, V. W. van Hinsbergh, Simvastatin improves disturbed endothelial barrier function, *Circulation* **102**, 2803–2809 (2000).

226. R. J. Gerson, J. S. MacDonald, A. W. Alberts, D. J. Kornbrust, J. A. Majka, R. J. Stubbs, D. L. Bokelman, Animal safety and toxicology of simvastatin and related hydroxy-methylglutaryl-coenzyme A reductase inhibitors, *Am. J. Med.* **87**, 28S–38S (1989).

227. P. A. Todd, K. L. Goa, Simvastatin. A review of its pharmacological properties and therapeutic potential in hypercholesterolaemia, *Drugs* **40**, 583–607 (1990).

228. M. M. Sadeghi, M. Collinge, R. Pardi, J. R. Bender, Simvastatin modulates cytokine-mediated endothelial cell adhesion molecule induction: involvement of an inhibitory G protein, *J. Immunol.* **165**, 2712–2718 (2000).

229. G. P. van Nieuw Amerongen, M. A. Vermeer, P. Negre-Aminou, J. Lankelma, J. J. Emeis, V. W. M. van Hinsbergh, Simvastatin Improves Disturbed Endothelial Barrier Function, *Circulation* **102**, 2803–2809 (2000).

230. M. Chrzanowska-Wodnicka, K. Burridge, Rho-stimulated contractility drives the formation of stress fibers and focal adhesions, *J. Cell Biol.* **133**, 1403–1415 (1996).

231. J. L. Tan, J. Tien, D. M. Pirone, D. S. Gray, K. Bhadriraju, C. S. Chen, Cells lying on a bed of microneedles: an approach to isolate mechanical force, *Proc. Natl. Acad. Sci. U. S. A.* **100**, 1484–1489 (2003).

232. S. Tojkander, G. Gateva, P. Lappalainen, Actin stress fibers--assembly, dynamics and biological roles, *J. Cell Sci.* **125**, 1855–64 (2012).

233. K. G. Birukov, A. A. Birukova, S. M. Dudek, A. D. Verin, M. T. Crow, X. Zhan, N. DePaola, J. G. N. Garcia, Shear stress-mediated cytoskeletal remodeling and cortactin translocation in pulmonary endothelial cells, *Am. J. Respir. Cell Mol. Biol.* **26**, 453–464 (2002).

234. T. Uruno, J. Liu, P. Zhang, Y. Fan, C. Egile, R. Li, S. C. Mueller, X. Zhan, Activation of Arp2/3 complex-mediated actin polymerization by cortactin, *Nat. Cell Biol.* **3**, 259–266 (2001).

235. S. A. Weed, Y. Du, J. T. Parsons, Translocation of cortactin to the cell periphery is mediated by the small GTPase Rac1, *J. Cell Sci.* **111**, 2433–2443 (1998).

236. P. V. Vaitkevicius, J. L. Fleg, J. H. Engel, F. C. O'Connor, J. G. Wright, L. E. Lakatta, F. C. Yin, E. G. Lakatta, Effects of age and aerobic capacity on arterial stiffness in healthy adults, *Circulation* **88**, 1456–1462 (1993).

237. D. K. Arnett, G. W. Evans, W. A. Riley, Arterial stiffness: a new cardiovascular risk factor?, *Am. J. Epidemiol.* **140**, 669–82 (1994).

238. A. V. Sima, C. S. Stancu, M. Simionescu, Vascular endothelium in atherosclerosis, *Cell Tissue Res.* **335**, 191–203 (2009).

239. D. Aronson, Cross-linking of glycated collagen in the pathogenesis of arterial and myocardial stiffening of aging and diabetes, *J. Hypertens.* **21**, 3–12 (2003).

240. A. Cordle, J. Koenigsknecht-Talboo, B. Wilkinson, A. Limpert, G. Landreth, Mechanisms of statin-mediated inhibition of small G-protein function, *J. Biol. Chem.* **280**, 34202–34209 (2005).

241. R. Kou, J. Sartoretto, T. Michel, Regulation of Rac1 by simvastatin in endothelial cells: differential roles of AMP-activated protein kinase and calmodulin-dependent kinase kinase-beta, *J. Biol. Chem.* **284**, 14734–14743 (2009).

242. R. Szulcek, C. M. L. Beckers, J. Hodzic, J. de Wit, Z. Chen, T. Grob, R. J. P. Musters, R. D. Minshall, V. W. M. van Hinsbergh, G. P. van Nieuw Amerongen, Localized RhoA GTPase activity regulates dynamics of endothelial monolayer integrity, *Cardiovasc. Res.* **99**, 471–482 (2013).

243. B. Wojciak-Stothard, A. J. Ridley, Shear stress-induced endothelial cell polarization is mediated by Rho and Rac but not Cdc42 or PI 3-kinases, *J. Cell Biol.* **161**, 429–439 (2003).

244. E. Tzima, M. A. Del Pozo, S. J. Shattil, S. Chien, M. A. Schwartz, Activation of integrins in endothelial cells by fluid shear stress mediates Rho-dependent cytoskeletal alignment, *EMBO J.* **20**, 4639–4647 (2001).

245. P. L. Hordijk, Regulation of NADPH oxidases: The role of Rac proteins, *Circ. Res.* **98**, 453–462 (2006).

246. D. Choquet, D. P. Felsenfeld, M. P. Sheetz, Extracellular matrix rigidity causes strengthening of integrin-cytoskeleton linkages, *Cell* **88**, 39–48 (1997).

247. J. A. Florian, J. R. Kosky, K. Ainslie, Z. Pang, R. O. Dull, J. M. Tarbell, Heparan sulfate proteoglycan is a mechanosensor on endothelial cells, *Circ. Res.* **93**, e136–e142 (2003).

248. F. Ali, M. Zakkar, K. Karu, E. A. Lidington, S. S. Hamdulay, J. J. Boyle, M. Zloh, A. Bauer, D. O. Haskard, P. C. Evans, J. C. Mason, Induction of the cytoprotective enzyme heme oxygenase-1 by statins is enhanced in vascular endothelium exposed to laminar shear stress and impaired by disturbed flow, *J. Biol. Chem.* **284**, 18882–18892 (2009).

249. B. M. Kaess, M. G. Larson, N. M. Hamburg, J. A. Vita, D. Levy, E. J. Benjamin, R. S. Vasan, G. F. Mitchel, Aortic stiffness, blood pressure progression, and incident hypertension, *J. Am. Med. Assoc.* **308**, 875–881 (2012).

250. K. M. Stroka, H. N. Hayenga, H. Aranda-Espinoza, Human Neutrophil Cytoskeletal Dynamics and Contractility Actively Contribute to Trans-Endothelial Migration, *PLoS One* **8**, (2013).

251. P. Lu, V. M. Weaver, Z. Werb, The extracellular matrix: A dynamic niche in cancer progression, *J. Cell Biol.* **196**, 395-406 (2012).

252. M. Brownlee, A. Cerami, H. Vlassara, Advanced Glycosylation End Products in Tissue and the Biochemical Basis of Diabetic Complications, *N. Engl. J. Med.* **318**, 1315–1321 (1988).

253. P. A. Janmey, R. T. Miller, Mechanisms of mechanical signaling in development and disease, *J. Cell Sci.* **124**, 9-18 (2010).

254. N. M. van Popele, D. E. Grobbee, M. L. Bots, R. Asmar, J. Topouchian, R. S. Reneman, A. P. Hoeks, D. A. van der Kuip, A. Hofman, J. C. Witteman, Association between arterial stiffness and atherosclerosis: The Rotterdam Study, *Stroke* **32**, 454–460 (2001).

255. A. P. Avolio, S. G. Chen, R. P. Wang, C. L. Zhang, M. F. Li, M. F. O'Rourke, Effects of aging on changing arterial compliance and left ventricular load in a northern Chinese urban community, *Circulation* **68**, 50-58 (1983).

256. B. E. Sumpio, J. Timothy Riley, A. Dardik, Cells in focus: endothelial cell, *Int. J. Biochem. Cell Biol.* **34**, 1508–1512 (2002).

257. C. D. Buckley, J. Tan, K. L. Anderson, D. Hanein, N. Volkmann, W. I. Weis, W. J. Nelson, A. R. Dunn, The minimal cadherin-catenin complex binds to actin filaments under force, *Science* **346,** 1254211 (2014).

258. M. C. Lampi, C. J. Faber, J. Huynh, F. Bordeleau, M. R. Zanotelli, C. A. Reinhart-King, Simvastatin ameliorates matrix stiffness-mediated endothelial monolayer disruption, *PLoS One* **11**, (2016).

259. S. V. Plotnikov, A. M. Pasapera, B. Sabass, C. M. Waterman, Force Fluctuations within Focal Adhesions Mediate ECM-Rigidity Sensing to Guide Directed Cell Migration, *Cell* **151**, 1513-1527, (2012).

260. B. C. Isenberg, P. A. DiMilla, M. Walker, S. Kim, J. Y. Wong, Vascular smooth muscle cell durotaxis depends on substrate stiffness gradient strength, *Biophys. J.* **97**, 1313–1322 (2009).

261. R. A. Marklein, J. A. Burdick, Spatially controlled hydrogel mechanics to modulate stem cell interactions, *Soft Matter* **6**, 136-143 (2010).

262. J. A. Burdick, C. Chung, X. Jia, M. A. Randolph, R. Langer, Controlled Degradation and Mechanical Behavior of Photopolymerized Hyaluronic Acid Networks, *Biomacromolecules* **6**, 386–391 (2005).

263. M. Guvendiren, S. Yang, J. A. Burdick, Swelling-Induced Surface Patterns in Hydrogels with Gradient Crosslinking Density, *Adv. Funct. Mater.* **19**, 3038–3045 (2009).

264. M. Ahearne, Y. Yang, A. J. El Haj, K. Y. Then, K.K. Liu, Characterizing the viscoelastic properties of thin hydrogel-based constructs for tissue engineering applications, *J. R. Soc. Interface* **2**, 455–463 (2005).

265. M. J. Dalby, M. O. Riehle, H. Johnstone, S. Affrossman, A. S. G. Curtis, In vitro reaction of endothelial cells to polymer demixed nanotopography, *Biomaterials* **23**, 2945–2954 (2002).

266. M. F. A. Cutiongco, S. H. Goh, R. Aid-Launais, C. Le Visage, H. Y. Low, E. K. F. Yim, Planar and tubular patterning of micro and nano-topographies on poly(vinyl alcohol) hydrogel for improved endothelial cell responses, *Biomaterials* **84**, 184–195 (2016).

267. T. Gillessen, F. Gillessen, H. Sieberth, P. Hanrath, B. Heintz, Age-related changes in the elastic properties of the aortic tree in normotensive patients: investigation by intravascular ultrasound, *Eur. J. Med. Res.* **1**, 144–148 (1995).

268. E. de Groot, G. K. Hovingh, A. Wiegman, P. Duriez, A. J. Smit, J.C. Fruchart, J. J. P. Kastelein, Measurement of Arterial Wall Thickness as a Surrogate Marker for Atherosclerosis, *Circulation* **109**, III33-III38 (2004).

269. J. M. Ruddy, J. A. Jones, F. G. Spinale, J. S. Ikonomidis, Regional Heterogeneity within the Aorta: Relevance to Aneurysm Disease, *J. Thorac. Cardiovasc. Surg.* **136**, 1123–1130 (2008).

270. U. S. Schwarz, M. L. Gardel, United We Stand – integrating the actin cytoskeleton and cell–matrix adhesions in cellular mechanotransduction, *J. Cell Sci.* **125**, 3051–3060 (2012).

271. V. Vogel, M. Sheetz, Local force and geometry sensing regulate cell functions, *Nat. Rev. Mol. Cell Biol.* **7**, 265–275 (2006).

272. J. G. N. Garcia, F. Liu, A. D. Verin, A. Birukova, M. A. Dechert, W. T. Gerthoffer, J. R. Bamberg, D. English, Sphingosine 1-phosphate promotes endothelial cell barrier integrity by Edg-dependent cytoskeletal rearrangement, *J. Clin. Invest.* **108**, 689–701 (2001).

273. J. Millán, R. J. Cain, N. Reglero-Real, C. Bigarella, B. Marcos-Ramiro, L. Fernández-Martín, I. Correas, A. J. Ridley, Adherens junctions connect stress fibres between adjacent endothelial cells, *BMC Biol.* **8**, (2010), 10.1186/1741-7007-8-11.
.

274. S. Hu, J. Chen, B. Fabry, Y. Numaguchi, A. Gouldstone, D. E. Ingber, J. J. Fredberg, J. P. Butler, N. Wang, Intracellular stress tomography reveals stress focusing and structural anisotropy in cytoskeleton of living cells, *Am. J. Physiol. Cell Physiol.* **285**, C1082-C1090 (2003).
275. E. T. Valent, G. P. van Nieuw Amerongen, V. W. M. van Hinsbergh, P. L. Hordijk, Traction force dynamics predict gap formation in activated endothelium, *Exp. Cell Res.* **347**, 161–170 (2016).

276. Y. Cai, N. Biais, G. Giannone, M. Tanase, G. Jiang, J. M. Hofman, C. H. Wiggins, P. Silberzan, A. Buguin, B. Ladoux, M. P. Sheetz, Nonmuscle Myosin IIA-Dependent Force Inhibits Cell Spreading and Drives F-Actin Flow, *Biophys. J.* **91**, 3907–3920 (2006).

277. Y. Cai, O. Rossier, N. C. Gauthier, N. Biais, M.-A. Fardin, X. Zhang, L. W. Miller, B. Ladoux, V. W. Cornish, M. P. Sheetz, Cytoskeletal coherence requires myosin-IIA contractility, *J. Cell Sci.* **123**, 413-423 (2010).

278. A. A. Birukova, F. T. Arce, N. Moldobaeva, S. M. Dudek, J. G. N. Garcia, R. Lal, K. G. Birukov, Endothelial permeability is controlled by spatially defined cytoskeletal mechanics: AFM force mapping of pulmonary endothelial monolayer, *Nanomedicine* **5**, 30 (2009).

279. H. Delanoë-Ayari, R. Al Kurdi, M. Vallade, D. Gulino-Debrac, D. Riveline, Membrane and acto-myosin tension promote clustering of adhesion proteins, *Proc. Natl. Acad. Sci. U. S. A.* **101**, 2229–2234 (2004).

280. A. Kris, R. D. Kamm, A. L. Sieminski, VASP involvement in force-mediated adherens junction strengthening, *Biochem. Biophys. Res. Commun.* **375**, 134–138 (2008).

281. A. K. Barry, H. Tabdili, I. Muhamed, J. Wu, N. Shashikanth, G. A. Gomez, A. S. Yap, C. J. Gottardi, J. de Rooij, N. Wang, D. E. Leckband, α-Catenin cytomechanics – role in cadherin-dependent adhesion and mechanotransduction, *J. Cell Sci.* **127**, 1779-1791 (2014).

282. E. Tzima, M. Irani-Tehrani, W. B. Kiosses, E. Dejana, D. A. Schultz, B. Engelhardt, G. Cao, H. DeLisser, M. A. Schwartz, A mechanosensory complex that mediates the endothelial cell response to fluid shear stress, *Nature* **437**, 426–431 (2005).

283. World Health Organization, Cardiovascular diseases: Fact sheet No. 317, *Geneva* (2015).

284. J. P. Califano, C. A. Reinhart-King, Matrix Mechanics and Cell Contractility in Angiogenesis, *Springer*, 143-160 (2013).

285. J.J. Chiu, S. Chien, Effects of disturbed flow on vascular endothelium: pathophysiological basis and clinical perspectives, *Physiol. Rev.* **91**, 327–387 (2011).

286. M. J. Levesque, R. M. Nerem, The elongation and orientation of cultured endothelial cells in response to shear stress, *J. Biomech. Eng.* **107**, 341–347 (1985).

287. J. C. Kohn, D. W. Zhou, F. Bordeleau, A. L. Zhou, B. N. Mason, M. J. Mitchell, M. R. King, C. A. Reinhart-King, Cooperative Effects of Matrix Stiffness and Fluid Shear Stress on Endothelial Cell Behavior, *Biophys. J.* **108**, 471–478 (2015).

288. S. R. Caliari, M. Perepelyuk, B. D. Cosgrove, S. J. Tsai, G. Y. Lee, R. L. Mauck, R. G. Wells, J. A. Burdick, Stiffening hydrogels for investigating the dynamics of hepatic stellate cell mechanotransduction during myofibroblast activation, *Sci. Rep.* **6**, 21387 (2016).

289. C. M. Lo, H. B. Wang, M. Dembo, Y. L. Wang, Cell movement is guided by the rigidity of the substrate, *Biophys. J.* **79**, 144–152 (2000).

290. S. R. Caliari, J. A. Burdick, A practical guide to hydrogels for cell culture, *Nat. Meth.* **13**, 405–414 (2016).

291. B. D. Fairbanks, M. P. Schwartz, C. N. Bowman, K. S. Anseth, Photoinitiated polymerization of PEG-diacrylate with lithium phenyl-2,4,6-trimethylbenzoylphosphinate: polymerization rate and cytocompatibility, *Biomaterials* **30**, 6702–6707 (2009).

292. K. R. Levental, H. Yu, L. Kass, J. N. Lakins, M. Egeblad, J. T. Erler, S. F. T. Fong, K. Csiszar, A. Giaccia, W. Weninger, M. Yamauchi, D. L. Gasser, V. M. Weaver, Matrix Crosslinking Forces Tumor Progression by Enhancing Integrin Signaling, *Cell* **139**, 891–906 (2009).

293. D. J. Quick, K. S. Anseth, Gene Delivery in Tissue Engineering: A Photopolymer Platform to Coencapsulate Cells and Plasmid DNA, *Pharm. Res.* **20**, 1730–1737 (2003).

294. D. J. Quick, K. S. Anseth, DNA delivery from photocrosslinked PEG hydrogels: Encapsulation efficiency, release profiles, and DNA quality, *J. Control. Release* **96**, 341–351 (2004).

295. R. Cruz-Acuña, A. J. García, Synthetic hydrogels mimicking basement membrane matrices to promote cell-matrix interactions, *Matrix Biol.* **57**–**58**, 324–333 (2017).

296. A. M. Kloxin, M. W. Tibbitt, K. S. Anseth, Synthesis of photodegradable hydrogels as dynamically tunable cell culture platforms, *Nat. Protoc.* **5**, 1867–1887 (2010).

297. D. D. McKinnon, T. E. Brown, K. A. Kyburz, E. Kiyotake, K. S. Anseth, Design and Characterization of a Synthetically Accessible, Photodegradable Hydrogel for User-Directed Formation of Neural Networks, *Biomacromolecules* **15**, 2808–2816 (2014).

298. R. V Ulijn, N. Bibi, V. Jayawarna, P. D. Thornton, S. J. Todd, R. J. Mart, A. M. Smith, J. E. Gough, Bioresponsive hydrogels, *Mater. Today* **10**, 40–48 (2007).

299. S. E. Greenwald, Ageing of the conduit arteries, *J. Pathol.* **211**, 157–172 (2007).

300. D. E. Conway, M. T. Breckenridge, E. Hinde, E. Gratton, C. S. Chen, M. A. Schwartz, Fluid shear stress on endothelial cells modulates mechanical tension across VE-cadherin and PECAM-1, *Curr. Biol.* **23**, 1024–30 (2013).

301. A. Abu Taha, M. Taha, J. Seebach, H. J. Schnittler, ARP2/3-mediated junction-associated lamellipodia control VE-cadherin-based cell junction dynamics and maintain monolayer integrity, *Mol. Biol. Cell* **25**, 245–256 (2014).

302. A. Labernadie, T. Kato, A. Brugues, X. Serra-Picamal, S. Derzsi, E. Arwert, A. Weston, V. Gonzalez-Tarrago, A. Elosegui-Artola, L. Albertazzi, J. Alcaraz, P. Roca-Cusachs, E. Sahai, X. Trepat, A mechanically active heterotypic E-cadherin/N-cadherin adhesion enables fibroblasts to drive cancer cell invasion, *Nat. Cell. Biol.* **19**, 224–237 (2017).

303. O. Dubrovskyi, A. A. Birukova, K. G. Birukov, Measurement of local permeability at subcellular level in cell models of agonist- and ventilator-induced lung injury, *Lab. Invest.* **93**, 254–63 (2013).

304. C. Grashoff, B. D. Hoffman, M. D. Brenner, R. Zhou, M. Parsons, M. T. Yang, M. A. McLean, S. G. Sligar, C. S. Chen, T. Ha, M. A. Schwartz, Measuring mechanical tension across vinculin reveals regulation of focal adhesion dynamics, *Nature* **466**, 263–266 (2010).

305. A. Kumar, M. Ouyang, K. Van den Dries, E. J. McGhee, K. Tanaka, M. D. Anderson, A. Groisman, B. T. Goult, K. I. Anderson, M. A. Schwartz, Talin tension sensor reveals novel features of focal adhesion force transmission and mechanosensitivity, *J. Cell Biol.* **213**, 371-383 (2016).

306. B. MB, R. Harris, F. SW, Does this patient have breast cancer? The screening clinical breast examination: Should it be done? How?, *JAMA* **282**, 1270–1280 (1999).

307. S. Sidney, C. P. Quesenberry, M. G. Jaffe, M. Sorel, M. N. Nguyen-Huynh, L. H. Kushi, A. S. Go, J. S. Rana, Recent trends in cardiovascular mortality in the United States and public health goals, *JAMA Cardiol.* **1**, 594–599 (2016).

308. V. M. Monnier, G. T. Mustata, K. L. Biemel, O. Reihl, M. O. Lederer, D. Zhenyu, D. R. Sell, Cross-linking of the extracellular matrix by the maillard reaction in aging and diabetes: an update on "a puzzle nearing resolution", *Ann. N.Y. Acad. Sci.* **1043,** 533–544 (2005).

309. A. M. Handorf, Y. Zhou, M. A. Halanski, W.J. Li, Tissue Stiffness Dictates Development, Homeostasis, and Disease Progression, *Organogenesis* **11**, 1–15 (2015).

310. M. W. Pickup, J. K. Mouw, V. M. Weaver, The extracellular matrix modulates the hallmarks of cancer, *EMBO Rep.* **15**, 1243–1253 (2014).

311. C. Frantz, K. M. Stewart, V. M. Weaver, The extracellular matrix at a glance, *J. Cell Sci.* **123**, 4195-4200 (2010).

312. J. Y. Rho, R. B. Ashman, C. H. Turner, Young's modulus of trabecular and cortical bone material: Ultrasonic and microtensile measurements, *J. Biomech.* **26**, 111–119 (1993).

313. A. Samani, J. Zubovits, D. Plewes, Elastic moduli of normal and pathological human breast tissues: an inversion-technique-based investigation of 169 samples, *Phys. Med. Biol*. **52**, 1565–1576 (2007).

314. I. D. Campbell, M. J. Humphries, Integrin Structure, Activation, and Interactions, *Cold Spring Harb. Perspect. Biol.* **3**, (2011).

315. B. Hinz, S. H. Phan, V. J. Thannickal, A. Galli, M.L. Bochaton-Piallat, G. Gabbiani, The Myofibroblast: One Function, Multiple Origins, *Am. J. Pathol.* **170**, 1807–1816 (2007).

316. F. Klingberg, B. Hinz, E. S. White, The myofibroblast matrix: implications for tissue repair and fibrosis, *J. Pathol.* **229**, 298–309 (2013).

317. A. Biernacka, M. Dobaczewski, N. G. Frangogiannis, TGF-β signaling in fibrosis, *Growth Factors* **29**, 196–202 (2011).

318. D. R. Edwards, G. Murphy, J. J. Reynolds, S. E. Whitham, A. J. Docherty, P. Angel, J. K. Heath, Transforming growth factor beta modulates the expression of collagenase and metalloproteinase inhibitor, *EMBO J.* **6**, 1899–1904 (1987).

319. P. J. Wipff, D. B. Rifkin, J. J. Meister, B. Hinz, Myofibroblast contraction activates latent TGF-B1 from the extracellular matrix, *J. Cell Biol.* **179**, 1311–1323 (2007).

320. C. M. Kraning-Rush, J. P. Califano, C. A. Reinhart-King, Cellular traction stresses increase with increasing metastatic potential, *PLoS One* **7**, (2012).

321. I. Acerbi, L. Cassereau, I. Dean, Q. Shi, A. Au, C. Park, Y. Y. Chen, J. Liphardt, E. S. Hwang, V. M. Weaver, Human breast cancer invasion and aggression correlates with ECM stiffening and immune cell infiltration, *Integr. Biol.* **7**, 1120–1134 (2015).

322. R. J. Akhurst, A. Hata, Targeting the TGFβ signalling pathway in disease, *Nat. Rev. Drug Discov* **11**, 790–811 (2012).

323. C.H. Heldin, Targeting the PDGF signaling pathway in tumor treatment, *Cell Commun. Signal.* **11**, (2013).

324. A. S. Selvaggio, P. W. Noble, Pirfenidone Initiates a New Era in the Treatment of Idiopathic Pulmonary Fibrosis, *Annu. Rev. Med.* **67**, 487–495 (2016).

325. C.H. Heldin, Targeting the PDGF Signaling Pathway in the Treatment of Non-Malignant Diseases, *J. Neuroimmune Pharmacol.* **9**, 69–79 (2014).

326. D. Schuppan, Y. O. Kim, Evolving therapies for liver fibrosis, *J. Clin. Invest.* **123**, 1887–1901 (2013).

327. A. D. Keefe, S. Pai, A. Ellington, Aptamers as therapeutics, *Nat. Rev. Drug Discov.* **9**, 537–550 (2010).

328. J. Barman, Targeting cancer cells using aptamers: cell-SELEX approach and recent advancements, *RSC Adv.* **5**, 11724–11732 (2015).

329. E. W. M. Ng, D. T. Shima, P. Calias, E. T. Cunningham, D. R. Guyer, A. P. Adamis, Pegaptanib, a targeted anti-VEGF aptamer for ocular vascular disease, *Nat. Rev. Drug Discov.* **5**, 123–132 (2006).

330. H. Qiu, B. Tian, R. G. Resuello, F. F. Natividad, A. Peppas, Y.T. Shen, D. E. Vatner, S. F. Vatner, C. Depre, Sex-specific regulation of gene expression in the aging monkey aorta, *Physiol. Genomics* **29**, 169-180 (2007).

331. R. A. DeFilippis, H. Chang, N. Dumont, J. T. Rabban, Y.-Y. Chen, G. V Fontenay, H. K. Berman, M. L. Gauthier, J. Zhao, D. Hu, J. J. Marx, J. A. Tjoe, E. Ziv, M. Febbraio, K. Kerlikowske, B. Parvin, T. D. Tlsty, CD36 Repression Activates a Multicellular Stromal Program Shared by High Mammographic Density and Tumor Tissues, *Cancer Discov.* **2**, 826–839 (2012).

332. P. D. Arora, N. Narani, C. A. McCulloch, The compliance of collagen gels regulates transforming growth factor-beta induction of alpha-smooth muscle actin in fibroblasts, *Am. J. Pathol.* **154**, 871–82 (1999).

333. P. C. Georges, J.J. Hui, Z. Gombos, M. E. McCormick, A. Y. Wang, M. Uemura, R. Mick, P. A. Janmey, E. E. Furth, R. G. Wells, Increased stiffness of the rat liver precedes matrix deposition: implications for fibrosis, *Am. J. Physiol. Gastrointest. Liver Physiol.* **293**, G1147-G1154 (2007).

334. S. C. Wei, L. Fattet, J. H. Tsai, Y. Guo, V. H. Pai, H. E. Majeski, A. C. Chen, R. L. Sah, S. S. Taylor, A. J. Engler, J. Yang, Matrix stiffness drives epithelial-mesenchymal transition and tumour metastasis through a TWIST1-G3BP2 mechanotransduction pathway, *Nat. Cell. Biol.* **17**, 678–688 (2015).

335. L. Santhanam, E. C. Tuday, A. K. Webb, P. Dowzicky, J. H. Kim, Y. J. Oh, G. Sikka, M. Kuo, M. K. Halushka, A. M. Macgregor, J. Dunn, S. Gutbrod, D. Yin, A. Shoukas, D. Nyhan, N. A. Flavahan, A. M. Belkin, D. E. Berkowitz, Decreased S-Nitrosylation of Tissue Transglutaminase Contributes to Age-Related Increases in Vascular Stiffness, *Circ. Res.* **107**, 117-125 (2010).

336. N. Agnihotri, K. Mehta, Transglutaminase-2: evolution from pedestrian protein to a promising therapeutic target, *Amino Acids* **49**, 425–439 (2017).

337. R. Issa, X. Zhou, C. M. Constandinou, J. Fallowfield, H. Millward-Sadler, M. D. A. Gaca, E. Sands, I. Suliman, N. Trim, A. Knorr, M. J. P. Arthur, R. C. Benyon, J. P. Iredale, Spontaneous recovery from micronodular cirrhosis: Evidence for incomplete resolution associated with matrix cross-linking, *Gastroenterology* **126**, 1795–1808 (2004).

338. A. Nenna, C. Spadaccio, M. Lusini, L. Ulianich, M. C. and F. Nappi, Basic and Clinical Research Against Advanced Glycation End Products (AGEs): New Compounds to Tackle Cardiovascular Disease and Diabetic Complications, *Recent Adv. Cardiovasc. Drug Discov.* **10**, 10–33 (2015).

339. J. V. Valencia, M. Mone, C. Koehne, J. Rediske, T. E. Hughes, Binding of receptor for advanced glycation end products (RAGE) ligands is not sufficient to induce inflammatory signals: lack of activity of endotoxin-free albumin-derived advanced glycation end products, *Diabetologia* **47**, 844–852 (2004).

340. M. Hori, M. Yagi, K. Nomoto, R. Ichijo, A. Shimode, T. Kitano, Y. Yonei, Experimental models for advanced glycation end product formation using albumin, collagen, elastin, keratin and proteoglycan, *Anti-Aging Med.* **9**, 125–134 (2012).

341. S. Yamagishi, K. Taguchi, K. Fukami, DNA-aptamers raised against AGEs as a blocker of various aging-related disorders, *Glycoconj. J.* **33**, 683–690 (2016).

342. S. Maeda, T. Matsui, A. Ojima, M. Suematsu, K. Kaseda, Y. Higashimoto, R. Yamakawa, S. Yamagishi, DNA Aptamer Raised against Advanced Glycation End Products Prevents Abnormalities in Electroretinograms of Experimental Diabetic Retinopathy, *Ophthalmic Res.* **54**, 175–180 (2015).

343. J. Uribarri, Restriction of Dietary Glycotoxins Reduces Excessive Advanced Glycation End Products in Renal Failure Patients, *J. Am. Soc. Nephrol.* **14**, 728–731 (2003).

344. C. Couppé, R. B. Svensson, J.-F. Grosset, V. Kovanen, R. H. Nielsen, M. R. Olsen, J. O. Larsen, S. F. E. Praet, D. Skovgaard, M. Hansen, P. Aagaard, M. Kjaer, S. P. Magnusson, Life-long endurance running is associated with reduced glycation and mechanical stress in connective tissue, *Age.* **36**, 9665 (2014).

345. H. E. Barker, T. R. Cox, J. T. Erler, The rationale for targeting the LOX family in cancer, *Nat. Rev. Cance.r* **12**, 540–552 (2012).

346. A. Bondareva, C. M. Downey, F. Ayres, W. Liu, S. K. Boyd, B. Hallgrimsson, F. R. Jirik, The Lysyl Oxidase Inhibitor, β-Aminopropionitrile, Diminishes the Metastatic Colonization Potential of Circulating Breast Cancer Cells, *PLoS One* **4**, (2009).

347. F. Bordeleau, B. N. Mason, E. M. Lollis, M. Mazzola, M. R. Zanotelli, S. Somasegar, J. P. Califano, C. Montague, D. J. LaValley, J. Huynh, N. Mencia-Trinchant, Y. L. Negrón Abril, D. C. Hassane, L. J. Bonassar, J. T. Butcher, R. S. Weiss, C. A. Reinhart-King, Matrix stiffening promotes a tumor vasculature phenotype, *Proc. Natl. Acad. Sci.* **114**, 492–497 (2017).

348. S. B. Liu, N. Ikenaga, Z.-W. Peng, D. Y. Sverdlov, A. Greenstein, V. Smith, D. Schuppan, Y. Popov, Lysyl oxidase activity contributes to collagen stabilization during liver fibrosis progression and limits spontaneous fibrosis reversal in mice, *FASEB J.* **30**, 1599–1609 (2016).

349. H. R. Keiser, A. Sjoerdsma, Studies on beta-aminopropionitrile in patients with scleroderma, *Clin. Pharmacol. Ther.* **8**, 593–602 (1967).

350. A. B. Benson, Z. A. Wainberg, J. R. Hecht, D. Vyushkov, H. Dong, J. Bendell, F. Kudrik, A Phase II Randomized, Double-Blind, Placebo-Controlled Study of Simtuzumab or Placebo in Combination with Gemcitabine for the First-Line Treatment of Pancreatic Adenocarcinoma, *Oncol.* **22**, 241-e15 (2017).

351. G. Raghu, K. K. Brown, H. R. Collard, V. Cottin, K. F. Gibson, R. J. Kaner, D. J. Lederer, F. J. Martinez, P. W. Noble, J. W. Song, A. U. Wells, T. P. M. Whelan, W. Wuyts, E. Moreau, S. D. Patterson, V. Smith, S. Bayly, J. W. Chien, Q. Gong, J. J. Zhang, T. G. O'Riordan, Efficacy of simtuzumab versus placebo in patients with idiopathic pulmonary fibrosis: a randomised, double-blind, controlled, phase 2 trial, *Lancet Respir. Med.* **5**, 22–32 (2017).

352. RCSB Protein Data Bank (available at http://www.rcsb.org).

353. T. R. Cox, A. Gartland, J. T. Erler, Lysyl Oxidase, a Targetable Secreted Molecule Involved in Cancer Metastasis, *Cancer Res.* **76**, 188-192 (2016).

354. N. Chan, A. Willis, N. Kornhauser, M. M. Ward, S. B. Lee, E. Nackos, B. R. Seo, E. Chuang, T. Cigler, A. Moore, D. Donovan, M. Vallee Cobham, V. Fitzpatrick, S. Schneider, A. Wiener, J. Guillaume-Abraham, E. Aljom, R. Zelkowitz, J. D. Warren, M. E. Lane, C. Fischbach, V. Mittal, L. Vahdat, Influencing the Tumor Microenvironment: A Phase II Study of Copper Depletion Using Tetrathiomolybdate in Patients with Breast Cancer at High Risk for Recurrence and in Preclinical Models of Lung Metastases, *Clin. Cancer Res.* **23**, 666-676 (2017).

355. J. W. Keillor, K. Y. P. Apperley, Transglutaminase inhibitors: a patent review, *Expert Opin. Ther. Pat.* **26**, 49–63 (2016).

356. N. L. Occleston, S. O'Kane, N. Goldspink, M. W. J. Ferguson, New therapeutics for the prevention and reduction of scarring, *Drug Discov. Today* **13**, 973–981 (2008).

357. K. C. Olsen, A. P. Epa, A. A. Kulkarni, R. M. Kottmann, C. E. McCarthy, G. V Johnson, T. H. Thatcher, R. P. Phipps, P. J. Sime, Inhibition of Transglutaminase 2, a Novel Target for Pulmonary Fibrosis, by Two Small Electrophilic Molecules, *Am. J. Respir. Cell Mol. Biol.* **50**, 737–747 (2014).

358. N. Daneshpour, M. Griffin, R. Collighan, Y. Perrie, Targeted delivery of a novel group of site-directed transglutaminase inhibitors to the liver using liposomes: a new approach for the potential treatment of liver fibrosis, *J. Drug Target.* **19**, 624–631 (2011).

359. B. Fingleton, MMPs as therapeutic targets – still a viable option?, *Semin. Cell Dev. Biol.* **19**, 61–68 (2008).

360. K. J. Isaacson, M. Martin Jensen, N. B. Subrahmanyam, H. Ghandehari, Matrix-metalloproteinases as targets for controlled delivery in cancer: An analysis of upregulation and expression, *J. Control. Release* (2017).

361. S. Cabrera, M. Gaxiola, J. L. Arreola, R. Ramírez, P. Jara, J. D'Armiento, T. Richards, M. Selman, A. Pardo, Overexpression of MMP9 in macrophages attenuates pulmonary fibrosis induced by bleomycin, *Int. J. Biochem. Cell Biol.* **39**, 2324–2338 (2007).

362. Q. Yu, I. Stamenkovic, Cell surface-localized matrix metalloproteinase-9 proteolytically activates TGF-β and promotes tumor invasion and angiogenesis, *Genes Dev.* **14**, 163–176 (2000).

363. M. J. P. Arthur, Reversibility of liver fibrosis and cirrhosis following treatment for hepatitis C, *Gastroenterology* **122**, 1525–1528 (2002).

364. A. Haage, I. C. Schneider, Cellular contractility and extracellular matrix stiffness regulate matrix metalloproteinase activity in pancreatic cancer cells, *FASEB J.* **28**, 3589–3599 (2014).

365. R. E. Vandenbroucke, C. Libert, Is there new hope for therapeutic matrix metalloproteinase inhibition?, *Nat. Rev. Drug Discov.* **13**, 904–927 (2014).

366. S. Shuster, G. I. Frost, A. B. Csoka, B. Formby, R. Stern, Hyaluronidase reduces human breast cancer xenografts in SCID mice, *Int. J. Cancer* **102**, 192–197 (2002).

367. R. H. Alvarez, C. Savulsky, A. Almonte, D. Xing, N. Lokker, D. Chondros, A randomized, open-label, multicenter, phase 1b/2 study of eribulin mesylate in combination with PEGylated recombinant human hyaluronidase in patients with human epidermal growth factor receptor 2-negative, high-hyaluronan metastatic breast cancer, *Cancer Res.* **77**, (2017).

368. S. R. Hingorani, W. P. Harris, T. E. Seery, L. Zheng, D. Sigal, A. E. Hendifar, F. S. Braiteh, M. Zalupski, A. D. Baron, N. Bahary, A. Wang-Gillam, N. K. LoConte, G. M. Springett, P. S. Ritch, A. F. Hezel, W. W. Ma, V. G. Bathini, X. W. Wu, P. Jiang, A. J. Bullock, Interim results of a randomized phase II study of PEGPH20 added to nab-paclitaxel/gemcitabine in patients with stage IV previously untreated pancreatic cancer, *J. Clin. Oncol.* **34**, 439 (2016).

369. T. Yeung, P. C. Georges, L. A. Flanagan, B. Marg, M. Ortiz, M. Funaki, N. Zahir, W. Ming, V. Weaver, P. A. Janmey, Effects of substrate stiffness on cell morphology, cytoskeletal structure, and adhesion, *Cell Motil. Cytoskeleton* **60**, 24–34 (2005).

370. W. Guo, F. G. Giancotti, Integrin signalling during tumour progression, *Nat. Rev. Mol. Cell Biol.* **5**, 816–826 (2004).

371. S. K. Mitra, D. D. Schlaepfer, Integrin-regulated FAK–Src signaling in normal and cancer cells, *Curr. Opin. Cell Biol.* **18**, 516–523 (2006).

372. J. S. Desgrosellier, D. A. Cheresh, Integrins in cancer: biological implications and therapeutic opportunities, *Nat. Rev. Cancer* **10**, 9–22 (2010).

373. H. B. Schiller, M.R. Hermann, J. Polleux, T. Vignaud, S. Zanivan, C. C. Friedel, Z. Sun, A. Raducanu, K.E. Gottschalk, M. Théry, M. Mann, R. Fässler, β1- and αv-class integrins cooperate to regulate myosin II during rigidity sensing of fibronectin-based microenvironments, *Nat. Cell Biol*. **15**, 625–636 (2013).

374. A. W. Orr, M. H. Ginsberg, S. J. Shattil, H. Deckmyn, M. A. Schwartz, R. Hynes, Ed. Matrix-specific Suppression of Integrin Activation in Shear Stress Signaling, *Mol. Biol. Cell* **17**, 4686–4697 (2006).

375. Y. Boucher, L. T. Baxter, R. K. Jain, Interstitial Pressure Gradients in Tissue-isolated and Subcutaneous Tumors: Implications for Therapy, *Cancer Res.* **50**, 4478-4484 (1990).

376. B. Suki, J. H. T. Bates, Extracellular matrix mechanics in lung parenchymal diseases, *Respir. Physiol. Neurobiol.* **163**, 33–43 (2008).

377. N. C. Henderson, D. Sheppard, Integrin-mediated regulation of TGFβ in fibrosis, *Biochim. Biophys. Acta* **1832**, 891–896 (2013).

378. N. I. Reed, H. Jo, C. Chen, K. Tsujino, T. D. Arnold, W. F. DeGrado, D. Sheppard, The αvβ1 integrin plays a critical in vivo role in tissue fibrosis, *Sci. Transl. Med.* **7**, 288ra79 (2015).

379. L. A. Koopman Van Aarsen, D. R. Leone, S. Ho, B. M. Dolinski, P. E. McCoon, D. J. LePage, R. Kelly, G. Heaney, P. Rayhorn, C. Reid, K. J. Simon, G. S. Horan, N. Tao, H. A. Gardner, M. M. Skelly, A. M. Gown, G. J. Thomas, P. H. Weinreb, S. E. Fawell, S. M. Violette, Antibody-Mediated Blockade of Integrin αvβ6 Inhibits Tumor Progression in vivo by a Transforming Growth Factor-β–Regulated Mechanism, *Cancer Res.* **68**, 561-570 (2008).

380. S. Minagawa, J. Lou, R. I. Seed, A. Cormier, S. Wu, Y. Cheng, L. Murray, P. Tsui, J. Connor, R. Herbst, C. Govaerts, T. Barker, S. Cambier, H. Yanagisawa, A. Goodsell, M. Hashimoto, O. J. Brand, R. Cheng, R. Ma, K. J. McKnelly, W. Wen, A. Hill, D. Jablons, P. Wolters, H. Kitamura, J. Araya, A. J. Barczak, D. J. Erle, L. F. Reichardt, J. D. Marks, J. L. Baron, S. L. Nishimura, Selective Targeting of TGF-β Activation to Treat Fibroinflammatory Airway Disease, *Sci. Transl. Med.* **6**, 241ra79 (2014).

381. R. Stupp, M. E. Hegi, T. Gorlia, S. C. Erridge, J. Perry, Y.K. Hong, K. D. Aldape, B. Lhermitte, T. Pietsch, D. Grujicic, J. P. Steinbach, W. Wick, R. Tarnawski, D.-H. Nam, P. Hau, A. Weyerbrock, M. J. B. Taphoorn, C.C. Shen, N. Rao, L. Thurzo, U. Herrlinger, T. Gupta, R.D. Kortmann, K. Adamska, C. McBain, A. A. Brandes, J. C. Tonn, O. Schnell, T. Wiegel, C.Y. Kim, L. B. Nabors, D. A. Reardon, M. J. van den Bent, C. Hicking, A. Markivskyy, M. Picard, M. Weller, Cilengitide combined with standard treatment for patients with newly diagnosed glioblastoma with methylated MGMT promoter (CENTRIC EORTC 26071-22072 study): a multicentre, randomised, open-label, phase 3 trial, *Lancet Oncol.* **15**, 1100–1108 (2014).

382. M. Parri, P. Chiarugi, Rac and Rho GTPases in cancer cell motility control, *Cell Commun. Signal.* **8**, (2010).

383. C. A. Street, B. A. Bryan, Rho Kinase Proteins—Pleiotropic Modulators of Cell Survival and Apoptosis, *Anticancer Res.* **31**, 3645–3657 (2011).

384. G. L. Verdine, L. D. Walensky, The Challenge of Drugging Undruggable Targets in Cancer: Lessons Learned from Targeting BCL-2 Family Members, *Clin. Cancer Res.* **13**, 7264-7270 (2007).

385. E. Lemichez, K. Aktories, Hijacking of Rho GTPases during bacterial infection, *Exp. Cell Res.* **319**, 2329–2336 (2013).

386. C.Y. Wang, P.Y. Liu, J. K. Liao, Pleiotropic effects of statin therapy: molecular mechanisms and clinical results, *Trends Mol. Med.* **14**, 37–44 (2008).

387. K. L. Watts, E. M. Sampson, G. S. Schultz, M. A. Spiteri, Simvastatin Inhibits Growth Factor Expression and Modulates Profibrogenic Markers in Lung Fibroblasts, *Am. J. Respir. Cell Mol. Biol.* **32**, 290–300 (2005).
388. S. Pisanti, P. Picardi, E. Ciaglia, A. D'Alessandro, M. Bifulco, Novel prospects of statins as therapeutic agents in cancer, *Pharmacol. Res.* **88**, 84–98 (2014).

389. M. L. Kutys, K. M. Yamada, Rho GEFs and GAPs: Emerging integrators of extracellular matrix signaling, *Small GTPases* **6**, 16–19 (2015).

390. X. Shang, F. Marchioni, N. Sipes, C. R. Evelyn, M. Jerabek-Willemsen, S. Duhr, W. Seibel, M. Wortman, Y. Zheng, Rational Design of Small Molecule Inhibitors Targeting RhoA Subfamily Rho GTPases, *Chem. Biol.* **19**, 699–710 (2012).

391. X. Shang, F. Marchioni, C. R. Evelyn, N. Sipes, X. Zhou, W. Seibel, M. Wortman, Y. Zheng, Small-molecule inhibitors targeting G-protein–coupled Rho guanine nucleotide exchange factors, *Proc. Natl. Acad. Sci. U. S. A.* **110**, 3155–3160 (2013).

392. F. Bai, F. Morcos, R. R. Cheng, H. Jiang, J. N. Onuchic, Elucidating the druggable interface of protein−protein interactions using fragment docking and coevolutionary analysis, *Proc. Natl. Acad. Sci.* **113**, E8051–E8058 (2016).

393. C. Guilluy, V. Swaminathan, R. Garcia-Mata, E. T. O'Brien, R. Superfine, K. Burridge, The Rho GEFs LARG and GEF-H1 regulate the mechanical response to force on integrins, *Nat. Cell Biol.* **13**, 722–727 (2011).

394. R. S. Knipe, A. M. Tager, J. K. Liao, The Rho Kinases: Critical Mediators of Multiple Profibrotic Processes and Rational Targets for New Therapies for Pulmonary Fibrosis, *Pharmacol. Rev.* **67**, 103-117 (2014).

395. S. S. Htwe, B. H. Cha, K. Yue, A. Khademhosseini, A. J. Knox, A. M. Ghaemmaghami, Role of ROCK Isoforms in Regulation of Stiffness Induced Myofibroblast Differentiation in Lung Fibrosis, *Am. J. Respir. Cell Mol. Biol.* ***56***, 772-783 (2017).

396. J. Shi, L. Wei, Rho kinases in cardiovascular physiology and pathophysiology: the effect of fasudil, *J. Cardiovasc. Pharmacol.* **62**, 341–54 (2013).

397. C. Hahmann, T. Schroeter, Rho-kinase inhibitors as therapeutics: from pan inhibition to isoform selectivity, *Cell. Mol. Life Sci.* **67**, 171–177 (2010).

398. C. Vennin, V. T. Chin, S. C. Warren, M. C. Lucas, D. Herrmann, A. Magenau, P. Melenec, S. N. Walters, G. del Monte-Nieto, J. R. W. Conway, M. Nobis, A. H. Allam, R. A. McCloy, N. Currey, M. Pinese, A. Boulghourjian, A. Zaratzian, A. A. S. Adam, C. Heu, A. M. Nagrial, A. Chou, A. Steinmann, A. Drury, D. Froio, M. Giry-Laterriere, N. L. E. Harris, T. Phan, R. Jain, W. Weninger, E. J. McGhee, R. Whan, A. L. Johns, J. S. Samra, L. Chantrill, A. J. Gill, M. Kohonen-Corish, R. P. Harvey, A. V Biankin, T. R. J. Evans, K. I. Anderson, S. T. Grey, C. J. Ormandy, D. Gallego-Ortega, Y. Wang, M. S. Samuel, O. J. Sansom, A. Burgess, T. R. Cox, J. P. Morton, M. Pajic, P. Timpson, Transient tissue priming via ROCK inhibition uncouples pancreatic cancer progression, sensitivity to chemotherapy, and metastasis, *Sci. Transl. Med.* **9**, eaai8504 (2017).

399. S. K. Wang, R. T. Chang, An emerging treatment option for glaucoma: Rho kinase inhibitors, *Clin. Ophthalmol.* **8**, 883–890 (2014).

400. K. P. Garnock-Jones, Ripasudil: First Global Approval, *Drugs* **74**, 2211–2215 (2014).

401. S. Boland, O. Defert, J. Alen, A. Bourin, K. Castermans, N. Kindt, N. Boumans, L. Panitti, S. Van de Velde, I. Stalmans, D. Leysen, 3-[2-(Aminomethyl)-5-[(pyridin-4-yl)carbamoyl]phenyl] benzoates as soft ROCK inhibitors, *Bioorg. Med. Chem. Lett.* **23**, 6442–6446 (2013).

402. F. J. Sulzmaier, C. Jean, D. D. Schlaepfer, FAK in cancer: mechanistic findings and clinical applications, *Nat. Rev. Cancer* **14**, 598–610 (2014).

403. V. M. Golubovskaya, Targeting FAK in human cancer: from finding to first clinical trials, *Front. Biosci.* **19**, 687–706 (2014).

404. B. Y. Lee, P. Timpson, L. G. Horvath, R. J. Daly, FAK signaling in human cancer as a target for therapeutics, *Pharmacol. Ther.* **146**, 132–149 (2015).

405. Y. Mimura, H. Ihn, M. Jinnin, Y. Asano, K. Yamane, K. Tamaki, Constitutive Phosphorylation of Focal Adhesion Kinase Is Involved in the Myofibroblast Differentiation of Scleroderma Fibroblasts, *J. Invest. Dermatol.* **124**, 886–892 (2005).

406. V. J. Thannickal, D. Y. Lee, E. S. White, Z. Cui, J. M. Larios, R. Chacon, J. C. Horowitz, R. M. Day, P. E. Thomas, Myofibroblast Differentiation by Transforming Growth Factor-β1 Is Dependent on Cell Adhesion and Integrin Signaling via Focal Adhesion Kinase, *J. Biol. Chem.* **278**, 12384–12389 (2003).

407. D. K. Treiber, N. P. Shah, Ins and Outs of Kinase DFG Motifs, *Chem. Biol.* **20**, 745–746 (2013).

408. D. Lietha, M. J. Eck, Crystal Structures of the FAK Kinase in Complex with TAE226 and Related Bis-Anilino Pyrimidine Inhibitors Reveal a Helical DFG Conformation, *PLoS One* **3**, (2008).

409. V. M. Golubovskaya, S. Figel, B. T. Ho, C. P. Johnson, M. Yemma, G. Huang, M. Zheng, C. Nyberg, A. Magis, D. A. Ostrov, I. H. Gelman, W. G. Cance, A small molecule focal adhesion kinase (FAK) inhibitor, targeting Y397 site: 1-(2-hydroxyethyl) -3, 5, 7-triaza-1-azoniatricyclo [3.3.1.1 3,7]decane; bromide effectively inhibits FAK autophosphorylation activity and decreases cancer cell viability, clonogenicity and tumor growth in vivo, *Carcinogenesis* **33**, 1004–1013 (2012).

410. S. Dupont, L. Morsut, M. Aragona, E. Enzo, S. Giulitti, M. Cordenonsi, F. Zanconato, J. Le Digabel, M. Forcato, S. Bicciato, N. Elvassore, S. Piccolo, Role of YAP/TAZ in mechanotransduction, *Nature* **474**, 179–183 (2011).

411. F. Liu, D. Lagares, K. M. Choi, L. Stopfer, A. Marinković, V. Vrbanac, C. K. Probst, S. E. Hiemer, T. H. Sisson, J. C. Horowitz, I. O. Rosas, L. E. Fredenburgh, C. Feghali-Bostwick, X. Varelas, A. M. Tager, D. J. Tschumperlin, Mechanosignaling through YAP and TAZ drives fibroblast activation and fibrosis, *Am. J. Physiol. Lung Cell. Mol. Physiol.* **308**, L344-L357 (2015).

412. B. Z. Stanger, Quit your YAPing: a new target for cancer therapy, *Genes Dev.* **26**, 1263–1267 (2012).

413. X. Varelas, P. Samavarchi-Tehrani, M. Narimatsu, A. Weiss, K. Cockburn, B. G. Larsen, J. Rossant, J. L. Wrana, The Crumbs Complex Couples Cell Density Sensing to Hippo-Dependent Control of the TGF-β-SMAD Pathway, *Dev. Cell* **19**, 831–844 (2010).

414. G. Sorrentino, N. Ruggeri, V. Specchia, M. Cordenonsi, M. Mano, S. Dupont, A. Manfrin, E. Ingallina, R. Sommaggio, S. Piazza, A. Rosato, S. Piccolo, G. Del Sal, Metabolic control of YAP and TAZ by the mevalonate pathway, *Nat. Cell. Biol* **16**, 357–366 (2014).

415. Y. Liu-Chittenden, B. Huang, J. S. Shim, Q. Chen, S.-J. Lee, R. A. Anders, J. O. Liu, D. Pan, Genetic and pharmacological disruption of the TEAD–YAP complex suppresses the oncogenic activity of YAP, *Genes Dev.* **26**, 1300–1305 (2012).

416. S. Jiao, H. Wang, Z. Shi, A. Dong, W. Zhang, X. Song, F. He, Y. Wang, Z. Zhang, W. Wang, X. Wang, T. Guo, P. Li, Y. Zhao, H. Ji, L. Zhang, Z. Zhou, A Peptide Mimicking VGLL4 Function Acts as a YAP Antagonist Therapy against Gastric Cancer, *Cancer Cell* **25**, 166–180 (2017).

417. I. Mannaerts, S. B. Leite, S. Verhulst, S. Claerhout, N. Eysackers, L. F. R. Thoen, A. Hoorens, H. Reynaert, G. Halder, L. A. van Grunsven, The Hippo pathway effector YAP controls mouse hepatic stellate cell activation, *J. Hepatol.* **63**, 679–688 (2015).

418. X. Huang, N. Yang, V. F. Fiore, T. H. Barker, Y. Sun, S. W. Morris, Q. Ding, V. J. Thannickal, Y. Zhou, Matrix Stiffness–Induced Myofibroblast Differentiation Is Mediated by Intrinsic Mechanotransduction, *Am. J. Respir. Cell Mol. Biol.* **47**, 340–348 (2012).

419. L. A. Johnson, E. S. Rodansky, A. J. Haak, S. D. Larsen, R. R. Neubig, P. D. R. Higgins, Novel Rho/MRTF/SRF Inhibitors Block Matrix-stiffness and TGF-β–Induced Fibrogenesis in Human Colonic Myofibroblasts, *Inflamm. Bowel Dis.* **20**, 154–165 (2014).

420. M. A. Scharenberg, B. E. Pippenger, R. Sack, D. Zingg, J. Ferralli, S. Schenk, I. Martin, R. Chiquet-Ehrismann, TGF-β-induced differentiation into myofibroblasts involves specific regulation of two MKL1 isoforms, *J. Cell Sci.* **127**, 1079-1091 (2014).

421. C. R. Evelyn, S. M. Wade, Q. Wang, M. Wu, J. A. Iñiguez-Lluhí, S. D. Merajver, R. R. Neubig, CCG-1423: a small-molecule inhibitor of RhoA transcriptional signaling, *Mol. Cancer Ther.* **6**, 2249-2260 (2007).

422. K. Hayashi, B. Watanabe, Y. Nakagawa, S. Minami, T. Morita, H. Ariga, Ed. RPEL Proteins Are the Molecular Targets for CCG-1423, an Inhibitor of Rho Signaling, *PLoS One* **9**, (2014).

423. F. Bordeleau, J. P. Califano, Y. L. Negrón Abril, B. N. Mason, D. J. LaValley, S. J. Shin, R. S. Weiss, C. A. Reinhart-King, Tissue stiffness regulates serine/arginine-rich protein-mediated splicing of the extra domain B-fibronectin isoform in tumors, *Proc. Natl. Acad. Sci.* **112**, 8314–8319 (2015).

424. V. R. Babaev, F. Porro, M. F. Linton, S. Fazio, F. E. Baralle, A. F. Muro, Absence of regulated splicing of fibronectin EDA exon reduces atherosclerosis in mice, *Atherosclerosis* **197**, 534–540 (2008).

425. E. Balza, L. Borsi, G. Allemanni, L. Zardi, Transforming growth factor β regulates the levels of different fibronectin isoforms in normal human cultured fibroblasts, *FEBS Lett.* **228**, 42–44 (1988).

426. K. Le, B. S. Prabhakar, W. Hong, L. Li, Alternative splicing as a biomarker and potential target for drug discovery, *Acta Pharmacol. Sin.* **36**, 1212–1218 (2015).

427. N. Wang, J. D. Tytell, D. E. Ingber, Mechanotransduction at a distance: mechanically coupling the extracellular matrix with the nucleus, *Nat. Rev. Mol. Cell Biol.* **10**, 75–82 (2009).

428. D. E. Ingber, Tensegrity I. Cell structure and hierarchical systems biology, *J. Cell Sci.* **116**, 1157-1173 (2003).

429. G. R. Fedorchak, A. Kaminski, J. Lammerding, Cellular Mechanosensing: Getting to the nucleus of it all, *Prog. Biophys. Mol. Biol.* **115**, 76–92 (2014).

430. J. Swift, I. L. Ivanovska, A. Buxboim, T. Harada, P. C. D. P. Dingal, J. Pinter, J. D. Pajerowski, K. R. Spinler, J.-W. Shin, M. Tewari, F. Rehfeldt, D. W. Speicher, D. E. Discher, Nuclear Lamin-A Scales with Tissue Stiffness and Enhances Matrix-Directed Differentiation, *Science* **341**, 1240104 (2013).

431. A. T. Bertrand, S. Ziaei, C. Ehret, H. Duchemin, K. Mamchaoui, A. Bigot, M. Mayer, S. Quijano-Roy, I. Desguerre, J. Lainé, R. Ben Yaou, G. Bonne, C. Coirault, Cellular microenvironments reveal defective mechanosensing responses and elevated YAP signaling in LMNA-mutated muscle precursors, *J. Cell Sci.* **127**, 2873-2884 (2014).

432. S. H. Park, S. Y. Kim, C. H. Suh, S. S. Lee, K. W. Kim, S. J. Lee, M.-G. Lee, What we need to know when performing and interpreting US elastography, *Clin. Mol. Hepatol.* **22**, 406–414 (2016).

433. S. R. Cherry, R. D. Badawi, J. S. Karp, W. W. Moses, P. Price, T. Jones, Total-body imaging: Transforming the role of positron emission tomography, *Sci. Transl. Med.* **9**, eaaf6169 (2017).

434. C. M. McEniery, Yasmin, I. R. Hall, A. Qasem, I. B. Wilkinson, J. R. Cockcroft, Normal Vascular Aging: Differential Effects on Wave Reflection and Aortic Pulse Wave Velocity: The Anglo-Cardiff Collaborative Trial (ACCT), *J. Am. Coll. Cardiol.* **46**, 1753–1760 (2005).

435. B. Y. Hsu, Y. H. Bae, K. L. Mui, S.-L. Liu, R. K. Assoian, S. Kumar, Ed. Apolipoprotein E3 Inhibits Rho to Regulate the Mechanosensitive Expression of Cox2, *PLoS One* **10**, (2015).

436. U. Laufs, J. K. Liao, Post-transcriptional Regulation of Endothelial Nitric Oxide Synthase mRNA Stability by Rho GTPase, *J. Biol. Chem.* **273**, 24266–24271 (1998).

437. Y. Kureishi, Z. Luo, I. Shiojima, A. Bialik, D. Fulton, D. J. Lefer, W. C. Sessa, K. Walsh, The HMG-CoA reductase inhibitor simvastatin activates the protein kinase Akt and promotes angiogenesis in normocholesterolemic animals, *Nat. Med.* **6**, 1004–1010 (2000).

438. H. Saito, Y. Minamiya, S. Saito, J. Ogawa, Endothelial Rho and Rho kinase regulate neutrophil migration via endothelial myosin light chain phosphorylation, *J. Leukoc. Biol.* **72**, 829–836 (2002).

439. A. Strey, A. Janning, H. Barth, V. Gerke, Endothelial Rho signaling is required for monocyte transendothelial migration, *FEBS Lett.* **517**, 261–266 (2002).

440. J. Huynh, F. Bordeleau, C. M. Kraning-Rush, C. A. Reinhart-King, Substrate stiffness regulates PDGF-induced circular dorsal ruffle formation through MLCK, *Cell. Mol. Bioeng.* **6**, 138–147 (2013).

441. P. P. Provenzano, P. J. Keely, Mechanical signaling through the cytoskeleton regulates cell proliferation by coordinated focal adhesion and Rho GTPase signaling, *J. Cell Sci.* **124**, 1195–1205 (2011).

442. X. Q. Brown, E. Bartolak-Suki, C. Williams, M. L. Walker, V. M. Weaver, J. Y. Wong, Effect of substrate stiffness and PDGF on the behavior of vascular smooth muscle cells: Implications for atherosclerosis, *J. Cell. Physiol.* **225**, 115–122 (2010).

443. Y. Sun, L.-T. Jiang, R. Okada, J. Fu, UV-Modulated Substrate Rigidity for Multiscale Study of Mechanoresponsive Cellular Behaviors, *Langmuir* **28**, 10789–10796 (2012).

444. I. T. Hoffecker, W. Guo, Y. Wang, Assessing the spatial resolution of cellular rigidity sensing using a micropatterned hydrogel-photoresist composite, *Lab Chip* **11**, 3538–3544 (2011).

445. M. Arnold, E. A. Cavalcanti-Adam, R. Glass, J. Blümmel, W. Eck, M. Kantlehner, H. Kessler, J. P. Spatz, Activation of Integrin Function by Nanopatterned Adhesive Interfaces, *ChemPhysChem* **5**, 383–388 (2004).

446. L. Wang, J.Y. Luo, B. Li, X. Y. Tian, L.J. Chen, Y. Huang, J. Liu, D. Deng, C. W. Lau, S. Wan, D. Ai, K. L. K. Mak, K. K. Tong, K. M. Kwan, N. Wang, J.J. Chiu, Y. Zhu, Y. Huang, Integrin-YAP/TAZ-JNK cascade mediates atheroprotective effect of unidirectional shear flow, *Nature* **540**, 579–582 (2016).

447. C. A. Reinhart-King, M. Dembo, D. A. Hammer, Cell-cell mechanical communication through compliant substrates, *Biophys. J.* **95**, 6044–6051 (2008).